NATIONAL TECHNICAL UNIVERSITY OF ATHENS

School of Naval Architecture and Marine Engineering

Shipbuilding Technology Laboratory

DIPLOMA THESIS

Study of the Corrosion Behavior of S560 and S700 Steels

Mitsika Evrydiki

Supervisor: Professor Nicholas Tsouvalis

Examination Committee:

A. Karantonis, Assoc. Profesor, School of Chemical Engineering

M. Samuelides, Professor, School of Naval Architecture and Marine Engineering

N. Tsouvalis, Professor, School of Naval Architecture and Marine Engineering

Athens, March 2021

Acknowledgements

I want to express my gratitude towards my supervisor Prof. Nicholas Tsouvalis for assigning this thesis to me, guiding me throughout my studies and helping me whenever needed.

I would also like to thank Prof. Antonis Karantonis for his valuable advice on the electrochemical techniques, which were essential for the purposes of this study.

I want to express my gratitude to Mrs. Theodora Tsiourva, for presenting me the idea of this thesis, for guiding and helping me in all stages of its implementation, and for all the bibliography and the scientific knowledge she provided. Most importantly, I am very grateful for having the chance to know her as a person, even though we had to work remotely during these difficult months of COVID pandemic quarantine. I consider Mrs. Tsiourva to be a great person of good quality.

I also want to thank my fellow colleague Alexandros Ziakas, who helped me in the beginning with the laboratory procedures and gladly shared his advice and knowledge with me.

I would also like to thank my parents and my siblings for encouraging and supporting me in every way throughout my studies, and last but not least, my friends who made this challenging journey more enjoyable and gave me the strength to keep going.

Introduction

One of the most challenging topics of research in the marine field, in the last years, is the reduction of the weight, which mainly affects the fuel consumption and the payload capacity of the ship. The introduction of high-performance steels called High Strength Low Alloy (HSLA) aim to achieve this objective. Fatigue Crack Arresters (FCA) are HSLA steels with better fatigue performance and they possess a satisfying combination of strength, toughness, formability and weldability while exhibiting high yielding point.

However, the application of these steel needs to be studied concerning several issues i.e. fatigue performance and corrosion behavior, in comparison with conventional steel AH36.

The present thesis studies the corrosion behavior of HSLA structural steels S560 and S700 and compares them with the conventional shipbuilding High Strength steel AH36.

The steel specimens were provided by FINCANTIERI Shipbuilding Company, through SSAB Steel Company, in the frame of RAMSSES EU funded project. Shipbuilding Technology Laboratory participates in this project as partner.

Electrochemical techniques were employed, applying DC and AC perturbation techniques, in particular; Open Circuit Potential, Linear Polarization, Potentiodynamic Polarization, Cyclic Polarization and Electrochemical Impedance Spectroscopy, accompanied by study of the microstructure and micro-hardness of both specimens. The experiments were performed in simulated seawater solution 3.5% NaCl. All the experiments were performed in the Shipbuilding Technology Laboratory, employing the relevant infrastructure, Potentiostat with FRA (Frequency Response Analyzer), Optical Microscope and Scanning Electron Microscope.

The present thesis consists of two main aspects. The first one is the Study of the Metal Alloys, including metallography, chemical analysis and micro-hardness measurements, accompanied with the relevant literature study on the production processes of steels and the contribution of their alloy elements to their final properties. The second one, which is also the most significant, is the Study of Corrosion Behavior, including a thoroughgoing theoretical study on the corrosion mechanism, concerning the Thermodynamic and the Kinetic background of the phenomenon, along with the fundamentals of the electrochemical techniques. The experimental results of these studies, are presented in detail for S560 and S700 steels separately, then comparatively with each other and finally, compared to AH36, along with the relevant conclusions. In the appendix, the reader may find detailed experimental results of the electrochemical experiments.

Abstract

The main objective of the present thesis is the study of the corrosion behavior of the HSLA S560 and S700 structural steels. This study investigates the corrosion performance of these steels as an alternative to conventional steel AH36 for specific applications on the ship.

To this purpose, electrochemical techniques were employed, applying DC and AC techniques. In particular five electrochemical techniques were used for this study; Open Circuit Potential (OC), Potentiodynamic Polarization (PP) – including Linear Polarization (LPR), Tafel Extrapolation and Cyclic Polarization (CP) – and Electrochemical Impedance Spectroscopy (EIS).

The main objective was accompanied by study of the microstructure of S560 and S700, including optical observations – Optical Microscopy and Scanning Electron Microscopy – and measurements of their micro-hardness and their chemical composition. Completing the above, their production process was also taken into account in order to arrive into sound conclusions.

The experiments performed showed that the mechanism of corrosion, is well described by an increase of current density with increasing potential in the anodic region, indicating active corrosion behavior without evident passivation. Both metals present similar anodic dissolution determined by charge transfer (activation polarization) for long ranges of potential (CP) and long times of EIS experiment (24 hours) until the formation of oxide film that limits the dissolution. The cathodic polarization is determined by O_2 diffusion, meaning that the phenomenon is controlled by concentration polarization further than equilibrium. S700 present faster transition from equilibrium to concentration polarization than S560.

The corrosion parameters obtained prove no significant differences among S560 S700 and AH36, concerning the Potentiodynamic Polarization Experiments (DC), as the corrosion current (i_{corr}) values are similar for these three steels. However, EIS Experiments (AC) revealed that both of the studied specimens, S560 and S700, appear to have lower corrosion susceptibility compared to AH36. Between S560 and S700, the latter presents higher corrosion resistance, which can be attributed to the harder microstructure of S700, consisting of tempered martensite and bainite, along with ferrite. Moreover, S700 implies the formation of oxide film that limits the dissolution, in opposition to S560 that does not exhibit such behavior. These differences between the results of DC and AC experiments, can be explained by the difference of the perturbation applied on the specimens.

The aforementioned results prove that concerning the corrosion performance S700 can be introduced as an alternate material for specific areas on the ship. Whereas, it is essential to study the corrosion behavior in combination with fatigue performance.

Περίληψη

Στόχος της παρούσας διπλωματικής είναι η μελέτη της συμπεριφοράς σε διάβρωση των χαλύβων υψηλής αντοχής και χαμηλής κραμάτωσης S560 και S700. Η μελέτη αυτή διερευνά την απόδοση των δύο αυτών χαλύβων σε διάβρωση, ως εναλλακτικές του συμβατικού χάλυβα AH36 για συγκεκριμένες εφαρμογές στο πλοίο.

Για το σκοπό αυτό, εφαρμόστηκαν ηλεκτροχημικές τεχνικές, με την εφαρμογή συνεχούς και εναλλασσόμενου ρεύματος. Συγκεκριμένα, εφαρμόστηκαν οι τεχνικές του Δυναμικού Ανοιχτού Κυκλώματος, της Γραμμικής Πόλωσης, της Ποτενσιοδυναμικής Πόλωσης, της Φασματοσκοπίας Ηλεκτροχημικής Εμπέδησης και της Κυκλικής Πόλωσης.

Εκτός από τη διάβρωση μελετήθηκε και η μικροδομή του S560 και του S700, με οπτική παρατήρηση, μέσω Οπτικής και Ηλεκτρονικής Μικροσκοπίας, καθώς και με μετρήσεις της μικροσκληρότητας και της χημικής τους σύστασης. Στα παραπάνω, λήφθηκε υπόψη η διαδικασία παραγωγής κάθε χάλυβα προκειμένου να εξαχθούν ασφαλή συμπεράσματα.

Τα πειράματα που διεξήχθησαν έδειξαν ότι ο μηχανισμός της διάβρωσης περιγράφεται από αύξηση της πυκνότητας ρεύματος με αύξηση του δυναμικού στην ανοδική περιοχή, υποδεικνύοντας έτσι δραστική συμπεριφορά χωρίς εμφανή παθητικοποίηση. Τόσο ο S560 όσο και ο S700 παρουσιάζουν παρόμοια ανοδική διάλυση η οποία ελέγχεται από το φαινόμενο της πόλωση ενεργοποίησης, ακόμα και για μεγάλο εύρος δυναμικού (Κυκλική Πόλωση) και χρόνου στα πειράματα της Φασματοσκοπίας Ηλεκτροχημικής Εμπέδησης (24 ωρών), έως τη δημιουργία ενός στρώματος οξειδίων στην επιφάνειά τους, που εμποδίζει την περεταίρω διάλυση. Η καθοδική πόλωση καθορίζεται από το φαινόμενο της διάχυση οξυγόνου, δηλαδή ελέγχεται από το φαινόμενο της πόλωσης συγκέντρωσης. Ο S700 παρουσιάζει πιο γρήγορη μετάβαση από την κατάσταση ισορροπίας στην πόλωση συγκέντρωσης σε σχέση με τον S560.

Οι παράμετροι της διάβρωσης που εξήχθησαν από τα πειράματα αποδεικνύουν ότι δεν υπάρχει ουσιαστική διαφορά των δύο μελετώμενων χαλύβων σε σύγκριση με τον AH36 (κοινός ναυπηγικός χάλυβας), όσον αφορά στα πειράματα Ποτενσιοδυναμικής Πόλωσης (συνεχούς ρεύματος), καθώς η πυκνότητα ρεύματος διάβρωσης παρουσιάζει παρόμοιες τιμές και για τους τρεις χάλυβες. Παρ' όλα αυτά, τα πειράματα της Ηλεκτροχημικής Εμπέδησης (εναλλασσόμενου ρεύματος) απέδειξαν πως οι δύο χάλυβες, S560 και S700, φαίνεται να έχουν υψηλότερη αντοχή στη διάβρωση σε σύγκριση με τον AH36. Μεταξύ των S560 και S700, ο τελευταίος παρουσιάζει καλύτερη συμπεριφορά, η οποία μπορεί να αποδοθεί στη σκληρότερη μικροδομή του, που αποτελείται από επαναφερμένο μαρτενσίτη, μπαινίτη και φερρίτη. Επιπλέον, τα πειράματα της εμπέδησης έδειξαν ότι στον S700 σχηματίζεται προστατευτικό στρώμα οξειδίου που περιορίζει την περαιτέρω διάλυση του μετάλλου.

Τα αποτελέσματα αποδεικνύουν ότι όσον αφορά την συμπεριφορά των χαλύβων έναντι της διάβρωσης, ο S700 θα μπορούσε να αποτελέσει εναλλακτικό υλικό σε ορισμένα σημεία του πλοίου. Ωστόσο, είναι σημαντικό να μελετηθεί η συμπεριφορά σε διάβρωση σε συνθήκες κόπωσης.

Contents

Steels in Marine Industry

Introduction

Steel is the backbone of the modern society. Nowadays, there is a rapidly growing demand for new kind of steel products that use less resources, are more energy efficient, take higher payloads and emit less CO_2 over their entire lifecycle.

The need for lighter and stronger marine structures led the steel industry towards steel grades with better structural performance. High Strength Low Alloy (HSLA) steels is one way of addressing these challenges and depending their grade they can make the final metal structure stronger, lighter, safer and more sustainable. Their high strength and consistent properties mean they can be used as thinner plates, thereby diminishing the weight of the metal structure, while maintaining high levels of performance.

This chapter is an introduction to the HSLA steels S560 and S700, which are studied in the present thesis. At first, the properties of High Strength (HS) and High Strength Low Alloy (HSLA) steels are presented, while the impact of the alloy elements on steels is described. Afterwards, the process of their production is analyzed and how this affects their microstructure and their final properties.

In the last paragraph (1.4), the basic characteristics and the chemical composition of the two examined samples, S560 and S700, are reported, based on their standards and their data sheets. Finally, their mechanical properties, obtained from their production process, are presented in detail, in comparison to the shipbuilding steel AH36, which is the most usual steel employed in shipbuilding.

1.1. The Evolution of Steel

The development of steel can be traced back 4000 years to the beginning of the Iron Age. Proving to be harder and stronger than bronze, which had previously been the most widely used metal, iron began to displace bronze in weaponry and tools. For the following few thousand years, however, the quality of iron produced would depend as much on the ore available as on the production methods.

By the 17th century, iron's properties were well understood, but increasing urbanization in Europe demanded a more versatile structural metal. And by the 19th century, the amount of iron being consumed by expanding railroads provided metallurgists with the financial incentive to find a solution to iron's brittleness and inefficient production processes. Undoubtedly, though, the most breakthrough in steel history came in 1856 when Henry Bessemer developed an effective way to use oxygen to reduce the carbon content in iron: **The modern steel industry was born** [Bell, 2020].

Steel, in particular heavy plates, is the most important input material for heavy steel structures. Therefore it is obvious that the improvement of the efficiency of steel products in design, fabrication and service life of a steel structure is a key element to develop also the efficiency of the steel structure. One way of gaining this advantages is offered by the use of higher strength steel, which can be defined as a product with a yield strength higher than 355 MPa.

The need for lighter and stronger marine structures leads the industry towards steel grades with better structural performance. Steel industry develops steels with higher yield stress and in general better mechanical properties. This allows the use of plates with lower thickness, resulting in a significant reduction in the weight of the overall metal structure which enables an increase in payload capacity and affects the engine's requirements, leading to considerable savings in fuel consumption. Under special constructional circumstances such higher strength steel enables the designer to reduce cross-sections saving also considerable fabrication time and costs by smaller welds. Furthermore, also higher strength steels with a good structural safety in particular against brittle fracture and excellent fabrication properties (welding) already exist [Schröter and Willms, 2010].

Steel industry has developed High-Strength Low-Alloy (HSLA) steels grades which have been already adopted by the civil engineering, in structures like bridges, cranes etc. The advantages of these steels have attracted the interest of shipbuilding industry and several efforts are made towards this direction. HSLA steel grades exhibit a favorable strength-to-weight ratio when compared to conventional steel grades, such as the shipbuilding steel AH36 High-Strength (HS). HSLA steels have already been used in offshore oil and gas structures and they could fulfill the new policies in marine transportation.

1.2. Steels in Marine Industry

1.2.1. High Strength Steels

High Strength (HS) steels present higher yield and tensile strength than common carbon steels and they are able to reduce the weight of the structure. They also present better performance in buckling and fatigue. High hardenability, ductility (in order to avoid brittle fractures), good weldability, and high strength are some of their mechanical properties. Different type of HS steels, according to their chemical composition (in particular their carbon content) and their production process, offer different benefits. Thus, increase of carbon will improve the material's strength, but it will also reduce its weldability. Thus, a wide variety of High Strength steels are offered by the steel industry, each one used for specific applications.

According to European standards, HS steels are manufactured in two ways. The first is through **quenching and tempering (Q&T)**, acquiring minimum yield strength of 1100 MPa. The second is through **thermo-mechanical controlled process (TMCP)**, where the minimum yield strength is almost 500 MPa and offers high weldability [Gogou, 2012], [Sastri, 2015], [Ziakas, 2020].

1.2.2. High Strength Low Alloy Steels

High-strength low-alloy (HSLA) steels, or micro-alloyed steels, contain small amounts of alloying elements, which enhance strength through the formation of stable carbides, nitrides and carbonitrides, effecting the steel's hardenability. Yield strength in HSLA steels is two or even three times higher than that of plain carbon-manganese steel. These steels present better mechanical properties and greater resistance to atmospheric corrosion than conventional carbon steels, and are designed to meet specific mechanical properties, such as a yield strength greater than 275 MPa. The chemical composition of a specific HSLA steel may vary for different product thicknesses to acquire mechanical property requirements through the production process. The main advantage of HSLA steels is that they present better weldability and weldment toughness due to lower carbon content. Moreover, due to their high yield strength they present crack arrest properties and higher strength, so they can be used in thinner dimensions resulting in lighter structures. All of the above contribute to cost savings in in material, transport and better workability of the material.

The HSLA steels possess the proper chemical composition, consisting of the suitable alloying elements and they are subjected to certain **thermo-mechanical treatmen**t, such as hot rolling process, to achieve the proper combination of strength, toughness, ductility, formability and weldability. These are acquired through ferrite grain refinement and precipitation of microalloyed carbonitride particles (the precise process is explained in paragraph 1.3.2.). Some alloy elements, such as Mo, Ni, Cr, and Mn also contribute in the improvement of hardenability, whereas other alloy elements, such as Nb, Ti, and V contribute in achieving a more fine-grained structure [Morrison, 2000], [Chakrabati, 2007], [Krinis, 2020]. The impact of the alloying elements is discussed in detail in the next paragraph (1.2.3.).

1.2.3. Impact of alloy elements

In order to ensure the performance of high-strength ship plates, micro-alloying technology is adopted. The addition to iron-carbon alloys of elements such as nickel, silicon and manganese, which do not form carbides in competition with cementite, does not basically alter the microstructures formed after transformation. However, in the case of strong carbide-forming elements such as molybdenum, chromium and tungsten, cementite will be replaced by the appropriate alloy carbides, often at relatively low alloying element concentrations. Still stronger carbide-forming elements such as niobium, titanium and vanadium are capable of forming alloy carbides preferentially at alloying concentrations less than 0.1 wt% [Bhadeshia and Honeycombe, 2017]. It would, therefore, be expected that the microstructures of steels containing these elements would be radically altered.

Undoubtedly, not only the addition of alloying elements contributes to the change of the properties of a metal, but also its production process. For example by adding Nb, V, Ti and other alloying elements to the steel, combined with the controlled rolling process, the grain is refined and the toughness is improved, but this aspect is going to be presented in chapter 1.3

The way in which each alloy element affects steel will be described in the following paragraphs [Gladman, 1997], [Skobir, 2011], [BorTec] , in alphabetical order.

Aluminum (Al) is deoxidizer element, which reduces the grain coarsening and ageing in heating, while providing of grain refining. In low percentages of aluminum, the microstructure consists mostly of ferrite and acicular ferrite, whereas in higher percentages, the microstructure consists of upper bainite, negatively affecting the hardness of the material.

Boron (B) even in small amounts (0.001 - 0.003 %) can increase hardenability. However, boronsteel is not easy to find, as it only makes up to 0.003% of the alloy steels. It increases the hardenability of low and medium carbon steels in the most effective way. Also, in low-alloyed steels, the existence of boron nitride suspends the separation in the boundaries of the ferrite grains.

Carbon (C) is the basic alloy element for steel. Increase of the carbon contents, increase the hardness and the resistance. However, the tensile strength and yield point increase up to 0,8% carbon. The fracture toughness increases above this value and the hardness does not increase anymore at the end of a heat treatment, due to any residual austenite. The carbon amount of steels adversely affects such properties as ductility, forgeability and weldability and most important high carbon steels might present cracking risk in the heat treatment.

Chromium (Cr) is one of the most popular alloying metals for steel due to its hardness and corrosion resistance. Higher chromium contents of 4- 18% result in better corrosion resistance. When Cr is added at values up to 25%, it creates an oxide layer on the material's surface, therefore ensuring resistance to corrosion and adding a bright appearance to materials. It also

increases the tensile strength and heat resistance, but it can also lead to tempering brittle or decrease the ductility. As the Mn increases, the Cr must be reduced to avoid the formation of bainite against acicular ferrite.

Manganese (Mn) is a deoxidizer and a degasifier element which is used in combination with S and P. Manganese offers reduced brittleness and improved forgeability, tensile strength, and resistance to wear. Manganese reacts with S, resulting in manganese sulfides, which prevents the formation of iron sulfides and enhances the forgeability/ weldability of the steel. Manganese is also added for better hardenability, as it leads to slower quenching rates in such techniques and helps the remove of O2 in molten pools. Mn enhances the formation of acicular ferrite (AF) when Mn is approximately 1%. However, when Mn is 1.4-1.8% higher fragility occurs. These higher percentages lead to the formation of bainite and the decrease of fragility. As the amount of Mn increases, the material strength and toughness increase as well (highest values at 1.4% Mn).

Molybdenum (Mo) increases strength, hardness, hardenability, toughness, as well as creep resistance and strength at elevated temperatures. It improves machinability and resistance to corrosion, and it intensifies the effects of other alloying elements. At amounts equal to 0.2-0.3% Mo contributes to the formation of acicular ferrite, at higher percentages, while it increases the formation of bainite, and at 0.5% Mo completely eliminates acicular ferrite. A combination of molybdenum and titanium significantly contributes in the formation of acicular ferrite.

Nickel (Ni) increases strength and impacts toughness/ hardness without sacrificing ductility. When introduced in suitable quantities in high-chromium (stainless) steels, it increases resistance to corrosion and scaling at elevated temperatures, resulting in increased hardness. Austenitic stainless steels are mostly known for their high content in nickel and chromium.

Niobium (Nb) causes grain refining and increases the yield strength. It also increases the hardness due to its ability to increase the carbide. However, both Nb and V can cause problems with hardness. Small amounts of Nb (<0.02%) and V (<0.05%) don't affect hardness, depending on the concentration of Mn and the cooling rate.

Nitrogen (N) has the ability to increase the hardness of the material like carbon but it does not affect the microstructure. The amount of N must always be lower than 0.007%- below this level, its percentage is dependent on the present concentrations of Al and Ti. Although it increases the mechanical and corrosion resistance, it causes ageing at the same time.

Oxygen (O) affects the entire microstructure of the material: at small concentrations leads to bainitic formation while in high concentrations leads to Widmanstätten ferrite. Generally, the better concentration of oxygen is 0.03-0.06% and for the HSLA steels. 0.02 - 0.035% oxygen

concentration lead to the formation of acicular ferrite and present the best mechanical properties of the material.

Phosphorus (P) is an element which has a hazardous impact, because it decreases toughness. While it increases steel's resistance and hardenability, it decreases its ductility and impact strength. This impact is more clearly seen in high carbon steels. While it enhances the corrosion resistance of steel, it is to be kept as low as possible. The fewness of phosphor, along with sulfur, is the first criterion in terms of material quality.

Silicon (Si) has also deoxidizing properties. It is always used in amounts lower than 0.5% because it leads to the reduction of the yield strength. It also enhances the resistance and hardenability of material without decreasing its ductility and toughness since it is dissolved in the ferrite. Steels which contain high Si offer also high heat resistance. In general, it increases the hardenability, abrasion resistance, and elasticity, while the grain size of steel increases as the silicon amount increases.

Sulfur (S) is an undesired element and needs to be eliminated. As the sulfur amount increases, its ductility and impact strength decrease perpendicular to forming. When it is not balanced with manganese, it causes fragility in contact with heat, decreasing weldability and hardenability. The combination of O and S causes inclusions inside the material, whereas the increase of S limits the formation of acicular ferrite and reduces the material's hardness/toughness.

Titanium (Ti) is used as a stabilizing element in stainless steels. It improves corrosion resistance and weldability and provides grain refining. Small amounts of titanium in addition the existence of C-Mn contributes to the formation of acicular ferrite. The addition of Ti increases the toughness while slightly decreasing the ductility. Since Titanium is a rare element on Earth, this alloying element can be up to 200 times more expensive than regular carbon steel.

Vanadium (V) is a grain reducer alloying element for steels. Even in concentration of 0.1%, it substantially prevents grain coarsening during process. Moreover, it increases the heat resistance, as well as hardness depth. It provides increased strength specifically at cutting parts, and is therefore effective in maintaining the forms of cutting edges for a long period.

Wolfram (W) increases the resistance of steel. It also enhances strength, wear resistance, hardness, and toughness. Furthermore, wolfram steels have superior hot-working and greater cutting efficiency at elevated temperatures. It is specifically in high-speed steels, tool steels, and heat treatable steels.

1.3. Production Process of Steels

Various ways of steel production are available nowadays and their chemical composition, in each case, differs considerably. It can be seen that **not only the alloy elements** but also the **production process** of heavy plates has fundamental impact on the final properties of a steel product, through producing different microstructures. Therefore, the various heat treatments used for the production techniques which exist today for heavy plates will be described.

1.3.1. Microstructure Formation through Heat Treatments

Along with the addition of chemical elements, heat treatment is probably the most important process in controlling the properties of a mental. It involves heating solid metal to a defined temperature, followed by a suitable cooling rete, in order to achieve the desired material properties.

Heat treatments are primarily conducted to either soften or harden the steel, depending on its final applications and manufacturing process. The softening treatment is often referred to as a **conditioning process** and will lower strength and hardness while increasing toughness and ductility. Conditioning includes two heat treatments called annealing and normalizing. The **hardening process** does the opposite. It increases strength and hardness while lowering toughness and ductility. This includes two processes called quenching and tempering and age hardening. The specific heat treatment used in manufacturing will depend on the metal chemistry, the size of the part and the required properties [Metallurgy Data, 2020].

The three **main structures** that are achievable through heat treatment are **pearlite**, **bainite** and **martensite**, whose typical structure are shown in Figure 1.1, Figure 1.2 and Figure 1.3, respectively.
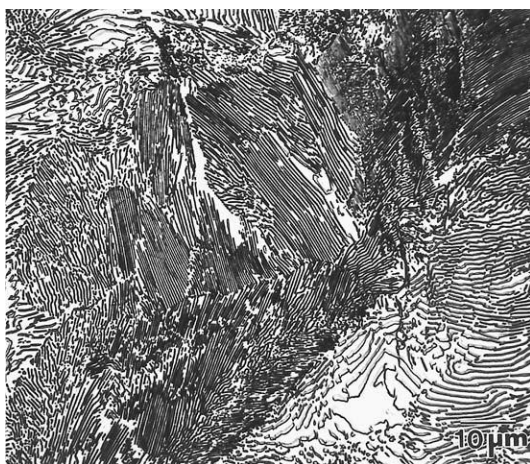
Figure 1.1: **Pearlite** (Microstructure of a fully pearlitic steel rail. 4% picral etch. 1000x). [Bramfitt and Benscoter, 2002]
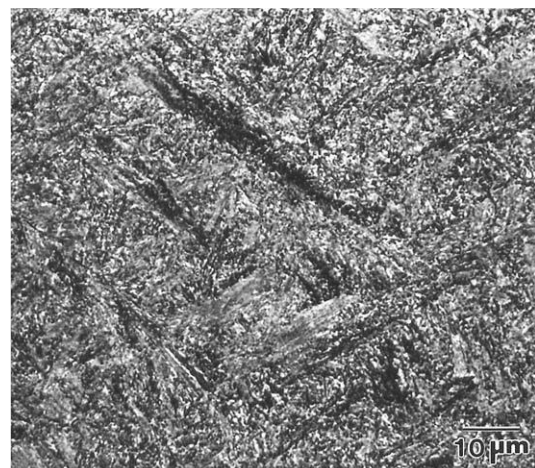
Figure 1.2: **Bainite** (A fully bainitic microstructure. 4% picral etch. 1000x). [Bramfitt and Benscoter, 2002]

*Figure 1.3: **Martensite** (A fully martensitic microstructure. Sodium metabisulfite etch.1000x). [Bramfitt and Benscoter, 2002]*

For the majority of heat treatments we cool from the <u>austenitic temperature region</u> (γ-austenite) which is shown in the Iron-Carbon Equilibrium Diagram in Figure 1.4, which provides the structures formed under slow cooling in iron, as a function of temperature and carbon content. The austenitic region is where most of the alloying additions go back into solution. As we cool through the <u>transformation region</u> (α-ferrite + γ-austenite), different structures are possible to be created by altering the cooling rate.

Figure 1.4: Iron-Carbon Equilibrium Diagram. Austenitic region is the γ – region and transformation region is the α+γ – region.

To achieve **pearlite**, the softest structure, slowly cooling is needed so that this structure is formed. To achieve **martensite**, the hardest structure, it is crucial to cool quickly enough to ensure that pearlite or bainite is not formed. **Bainite** lays at a medium cooling rate in between pearlite and martensite and it is of medium hardness. Depending on the cooling rate these iron carbide particles can be more elongated, com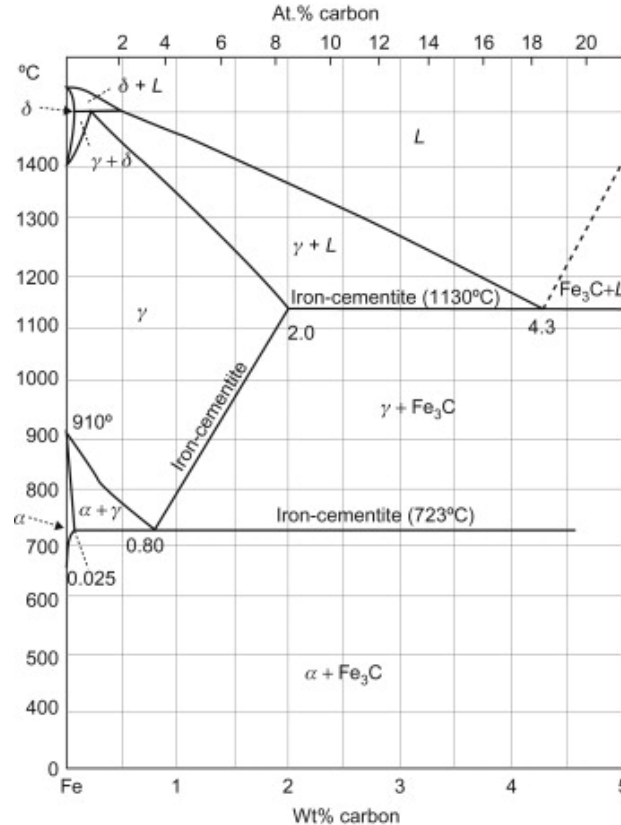posing **upper bainite**, which is the slower cooled of the two structures. The other, **lower bainite**, forms at faster cooling rates and contains ferrite with finer disc like particles of iron carbide [Metallurgy Data, 2020].

Generally, the higher the **alloy content** the easier it is to form martensite and this ability to form martensite is known as hardenability, meaning a steel with low hardenability requires a faster cooling rate to attain the same hardness at a given location than a steel with high hardenability [Metallurgy Data, 2020]. The speed of these cooling rate depends on the given steel composition and there are various diagrams (Continuous Colling Transformation – CTT and Time Temperature Transformation – TTT) that help to predict the different structures formed.

1.3.2. Production Process

Higher strength plates can be produced by various production processes which also influence the final use and mechanical properties of the steel. The **thermomechanical rolling** process is mostly applied for the production of higher strength plates as thereby also good fabrication and utilization properties can be guaranteed. Such plates are today produced up to a yield strength of 500 MPa and have gained special attentiveness in large span landmark bridges. But also other fields of applications, such as industrial buildings or medium span bridges, can profit from these materials. Furthermore, some extra high-strength steel with a yield strength up to 690 MPa is sometimes used for special structural elements of bridges and buildings. These steels are produced by a **quenching and tempering** process. Figure 1.5 summarizes the historical development of higher strength steel grades during the last decades.
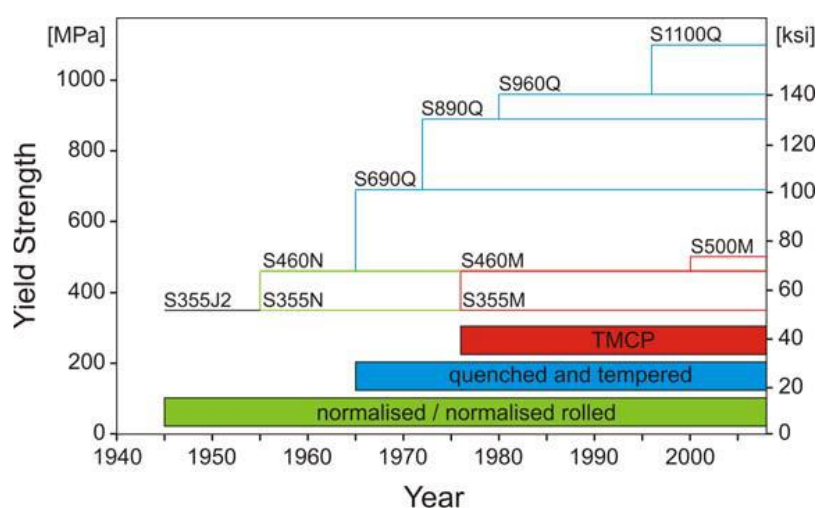

Figure 1.5: Historical development of production processes for rolled steel products. [Schröter and Willms, 2010]

Weldable structural steels are delivered in the conditions (shown in Figure 1.6):

- **Normalized** (N),

- **Thermo-Mechanical Controlled Processed** (TMCP) and

- **Quenched** and **Tempered** (QT).

For steel grades of moderate strength and toughness requirements, a classical **hot rolling** and **normalizing** (N) of the steel is sufficient to obtain the necessary mechanical values (processes A and B, respectively, in Figure 1.6).

Thermomechanical rolling (TM or TMCP) creates an extremely fine grained microstructure by a skilled combination of rolling steps at particular temperatures and a close temperature control (processes D – G in Figure 1.6). The gain in strength obtained by the grain refinement allows to reduce effectively the carbon and alloy content of the TM-steel compared to normalized steel of the same grade.

By **quenching** and **tempering** (QT) structural steels can reach a yield strength of up to 1,100 MPa. This heat treatment (process C in Figure 1.6) applied subsequent to hot rolling, consists of an austenitisation, followed by quenching and finally tempering.

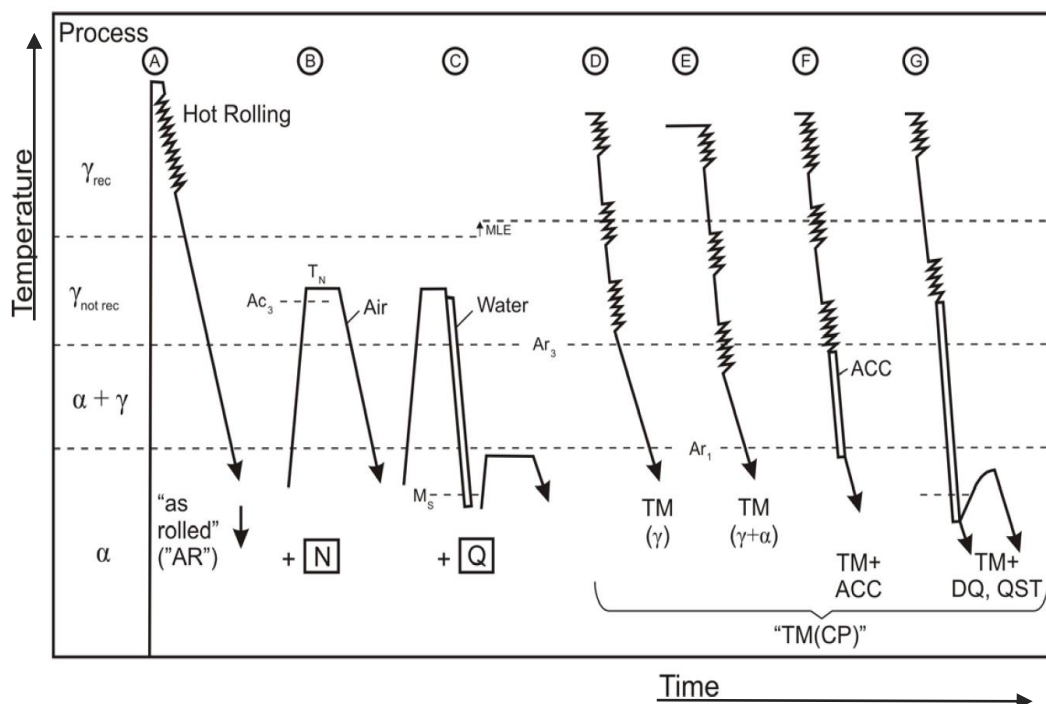In the following paragraphs, these processes are analyzed in detail.

Figure 1.6: Schematic temperature-time-procedures used in plate production: normalized (process A+B), quenched and tempered (process A+C) and different TMCP processes (D - G). [Schröter and Willms, 2010]

1.3.2.1. Normalized Steels

As earlier mentioned, Normalizing (N) is a conditioning treatment and it can be used to obtain the final properties of a steel or as an intermediate step in order to ensure that the material would not crack following rolling, casting, forming or forging. It can also be used to get the material into a state to aid in machining. The material is heated to the austenite range and then is slow cooled in still air.

A normalized structure can also be tempered to alter the properties slightly. Any gases that need removing, for example hydrogen, will be done as part of this process. This treatment leave the material **homogeneous**, **soft** and **ductile**. Due to the slow cooling rates present in normalizing, a **pearlite** structure is likely to form. Pearlite consists of alternate laths of iron carbide (Fe_3C), also known as cementite, and pure iron structure called ferrite (α). During cooling the austenite (γ) which has a higher solubility for carbon starts to turn to ferrite. But because this ferrite cannot accommodate the higher concentration of carbon, the structure develops in alternate laths of cementite and ferrite. This pearlite is often present with ferrite, and depending on the carbon content, the pearlite and ferrite will be present in different ratios. If the cooling rate is too fast for pearlite but not quick enough to produce martensite, **bainite** will form. Initially ferrite is produced, but because the cooling rate is quicker than pearlite, the structure does not form in laths of ferrite and iron carbide. But instead, the iron carbide starts to precipitate from the remaining (carbon rich) austenite forming a structure that consists of ferrite and particles of iron carbide. Depending on the <u>cooling rate</u> these iron carbide particles can be more elongated, composing **upper bainite**, which is the slower cooled of the two structures. The other, **lower bainite**, forms at faster cooling rates and contains ferrite with finer disc like particles of iron carbide [Metallurgy Data, 2020].

By this process route weldable structural steels up to S460N are produced. In Figure 1.6, a typical process of heat treatment is presented schematically. Hot rolling is generally carried out at high temperatures above 950°C (process A). By **reheating** the hot rolled plates to some 900°C followed by **free cooling** in air a refined microstructure of ferrite and pearlite (process B) is obtained, as shown in Figure 1.7. However with this process a higher strength of steel plates is mostly related to higher alloying contents influencing weldability in a negative way.
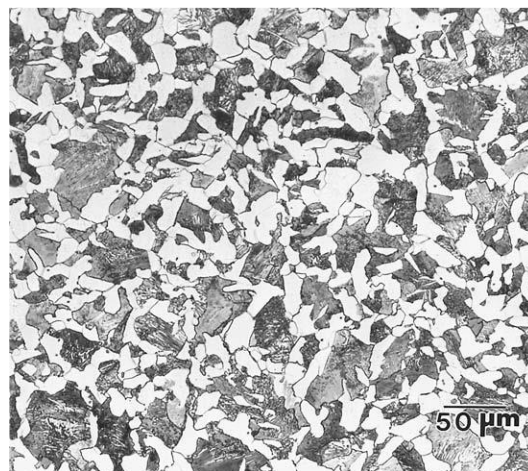

Figure 1.7: Microstructure of a typical normalized AISI/SAE 1040 steel bar showing uniformity of ferrite (light) and pearlite (dark). 2% nital and 4% picral etch. 200x [Bramfitt and Benscoter, 2002].

1.3.2.2. Thermo-Mechanical Controlled Processed Steels

Historically, the rolling of steel, like other hot deformation processes, was carried out primarily to achieve a specific external shape (e.g. plate or strip) and the mechanical properties of the finished product were largely imparted by virtue of the effects of alloying elements and subsequent heat treatment. Initially, therefore, hot rolling was usually carried out at temperatures as high as possible in the austenitic (γ) region, where the steel is softest and the upper limit tended to be governed by practical limitations, for example, operating at such high temperatures, costs, pressures on productivity, etc. Conventional hot rolling(*Figure 1.8*a), e.g. of pre-World War II C-Mn steels, made little attempt to control the rolling conditions and usually finished in the range 1050-900 °C depending on product thickness [Kirkwood, 2020].

Following unfortunate instances of brittle failure of hot rolled plates in ships' hulls during the last world war, the 1950s witnessed many attempts to improve toughness, both by changes in steelmaking practices and, more interestingly, by the introduction of what we now call 'controlled rolling'. At that time, it was beginning to be appreciated that the ductile to brittle transition temperature of steel could be greatly improved by the refinement of ferrite (α) grain size. This could be achieved either by the normalizing of aluminum treated steels or by **controlled**, lower temperature, **hot rolling** to further refine the austenite at temperatures still above the Ar_3 (the temperature, during cooling, at which austenite begins to transform to ferrite) but down to 800 °C (Figure 1.8b), [Kirkwood, 2020].
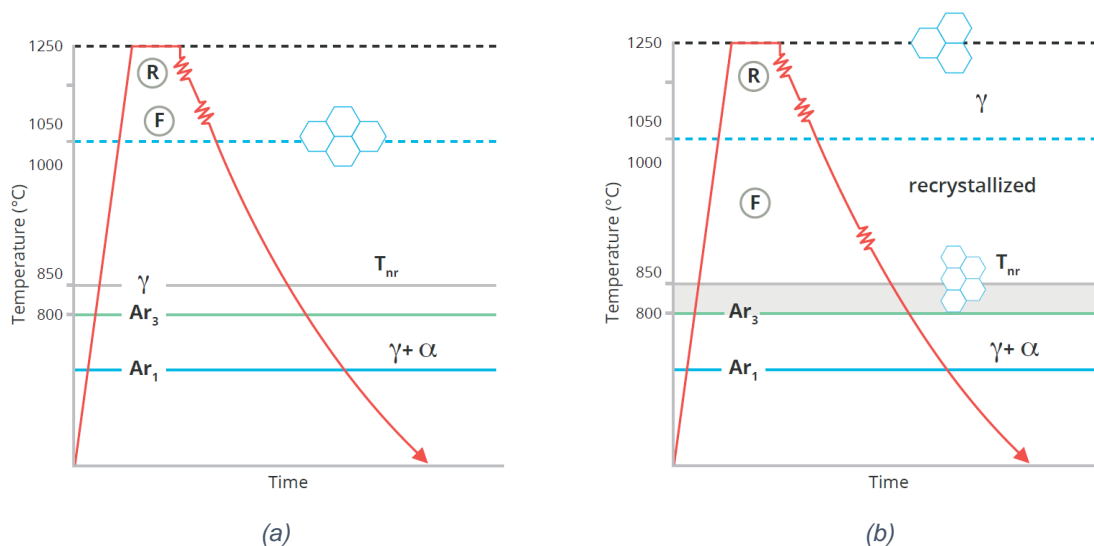
Figure 1.8: C-Mn steel produced by (a) hot rolling, (b) controlled rolling. R indicates the initial deformation stages of the slab or 'roughing' and F denotes the 'finishing' rolling stages. [Kirkwood, 2020]

Depending on the chemical composition, the required strength and toughness properties and the plate thickness the "rolling schedule" is individually designed. Especially for thick plates an **accelerated cooling** after the final rolling pass is beneficial for the achievement of the most suitable microstructure as it forces the transformation of the **elongated austenite** grains before recrystallization can happen. For very thick plates and higher yield strength grades a **tempering process** can be used after the accelerated cooling [Schröter and Willms, 2010]. In recent years, it has become more common to utilize the term Thermomechanical Controlled Processing (TMCP), which implies the use of a combination of various features of controlled

rolling, modifications to slab reheating and interpass holding temperatures, and some form of accelerated cooling following the completion of the rolling process [Kirkwood, 2020].

Figure 1.9: Schematic diagram of the influence of accelerated cooling on the microstructure of HSLA steel. [Kirkwood, 2020]
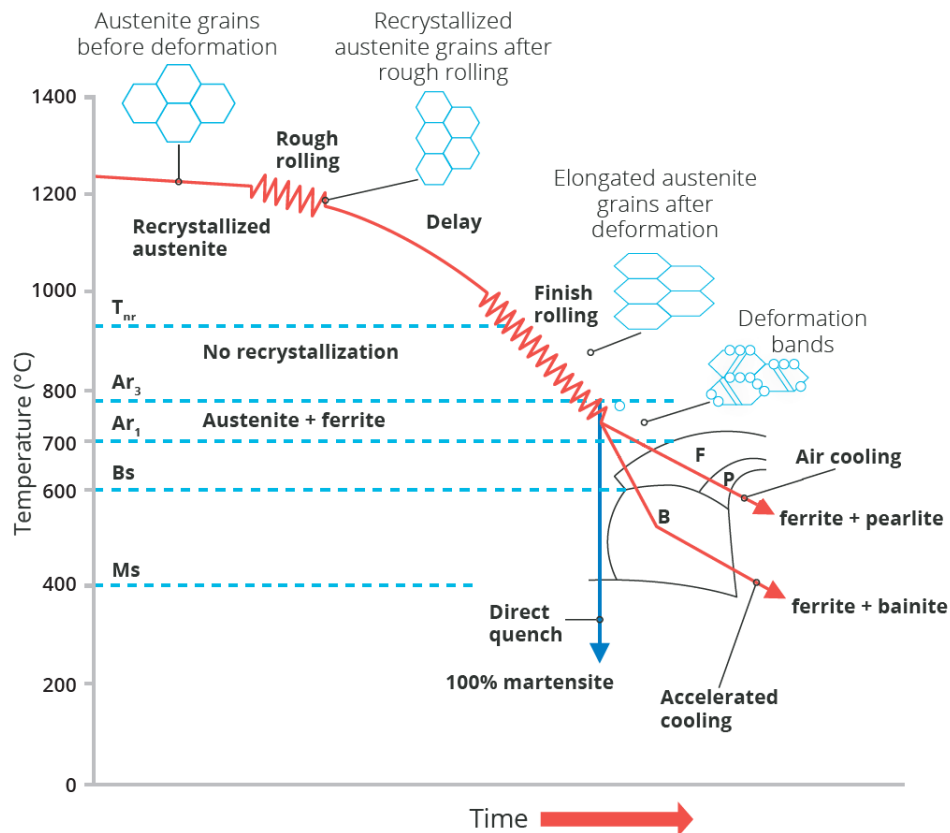
The improved weldability that results from the leaner steel composition is the most significant advantage of TM-plates, compared with conventional steel grades of the same thickness. Their outstanding suitability for welding is characterized by two main features: on the one hand, preheating of thicker TM-plates can be significantly reduced or omitted completely, which allows significant savings in fabrication time and costs. On the other hand, TM plates exhibit high toughness values and low hardening values in the heat affected zone (HAZ) after welding [Schröter, 2004]. These effects are due to the very low alloying contents (in particular carbon contents) which can be reached by this special rolling process.

At this point, it is worth comparing, through Table 1.1, the typical alloying content of a **conventional steel** (S355J2+N), with that of a **TM-steel** of the same yield strength (S355ML). This table also indicates the values for the mostly used carbon equivalents, formulas which are used to judge the influence of the alloying elements on weldability. It can be seen that TMCP rolled steel shows much smaller carbon equivalents than normalized steel grades of the same yield strength.

Table 1.1: Comparison of chemical compositions (according to standards and production of 50 mm plate thickness) between a normalized S355J2+N and a TMCP rolled S355ML. [Schröter and Willms, 2010]

	S 355 J2+N		S 355 ML	
	acc. EN 10025-2	typ. analysis	acc. EN 10025-4	typ. analysis
C	≤ 0,22	0,17	≤ 0,14	0,08
Si	≤ 0,55	0,45	≤ 0,50	0,35
Mn	≤ 1,60	1,50	≤ 1,60	1,53
P	≤ 0,025	0,018	≤ 0,025	0,012
S	≤ 0,025	0,015	≤ 0,020	0,005
Nb	-	-	≤ 0,05	0,02
V	-	-	≤ 0,10	-
Mo	-	-	≤ 0,10	-
Ni	-	-	≤ 0,50	-
CE	≤ 0,47	0,42	≤ 0,40	0,34
Pcm		0,26		0,17
CET		0,32		0,24

$$CE = C + Mn/6 + (Cr + Mo + V)/5 + (Ni+Cu)/15 \ ;$$
$$Pcm = C + Si/30 + (Mn + Cu + Cr)/20 + Ni/60 + Mo/15 + V/10 + 5B$$
$$CET = C + (Mn + Mo)/10 + (Cr + Cu)/20 + Ni/40)$$

Furthermore, TMCP rolled steel has an excellent toughness behavior Figure 1.10 illustrates that the transition temperature between brittle and tough fracture behavior, which is often defined by the temperature, where a Charpy-V impact energy of 27 J is attained, can be significantly reduced by TMCP rolling in comparison to a conventional steel grade S355J2+N.
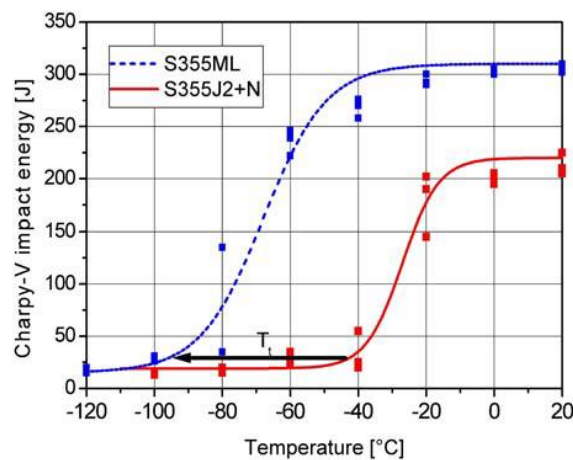
Figure 1.10: Comparison of the Charpy-V-temperature transition curve for a conventional normalized steel S355J2+N and a TMCP rolled steel S355ML. [Schröter and Willms, 2010]

Thus, a reserve is given in order to ensure also outstanding **toughness properties in the heat affected zone** of the weld. As an example Figure 1.11 shows the Charpy-V-temperature transition curve of an S355ML measured in the heat affected zone in distance of 2 mm to the fusion line. It can be seen that even at –50°C a good toughness level can be reached resulting in a high safety of the welded joint against brittle fracture. Furthermore, good toughness levels in the heat affected zone are a prerequisite for the application of welding processes with high heat input. Thus, also the efficiency of the welding process can be increased by using TMCP rolled material [Schröter and Willms, 2010].

Figure 1.11: Charpy-V-temperature transition curve in the heat affected zone of a S355ML after welding with submerged arc welding (3.0 kJ/mm). [Schröter and Willms, 2010]

Due to the higher carbon content and the risk of hydrogen-induced cracking a conventional **S355J2+N** in thickness above 30 mm is normally **preheated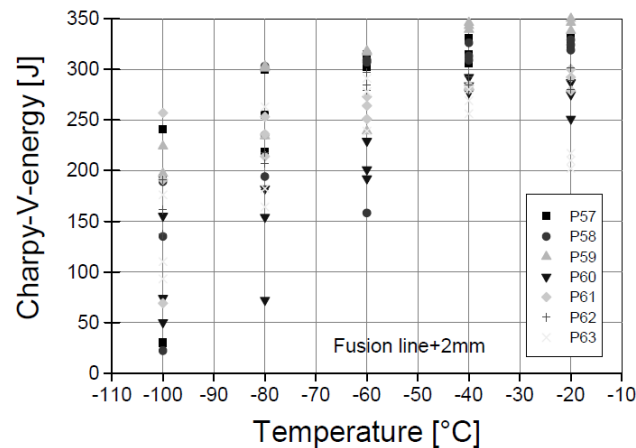** prior to welding. Due to its low alloying content, **TM-steel S355M** is normally **not preheated** if EN 1011-2 is applied for the calculation of preheating temperatures.

The economic benefit of avoiding preheating is clear: A time- and money consuming step in the fabrication process of steel structures can be avoided and the production efficiency of the workshop be increased (Hever & Schröter, 2003). But this is not only a matter of economics. Also in terms of job safety avoiding preheating is a benefit. Welding in narrow box sections is the daily work of a welder on site. Reducing preheating temperatures results in better working conditions, better welding results and higher efficiency. So, in this case, TM-steel is the best choice.

One big advantage of **TMCP rolling technique** is that even higher strength grades can be produced by an appropriate heat treatment without considerably increasing the alloying content. Thus Figure 1.12 shows the mechanical properties of two steel plates of the same chemical compositions but with **different treatments after rolling**. By applying an especially harsh cooling – the so-called heavy accelerated cooling – the yield and ultimate strength of the steel plates can be increased without any change of the chemical composition.
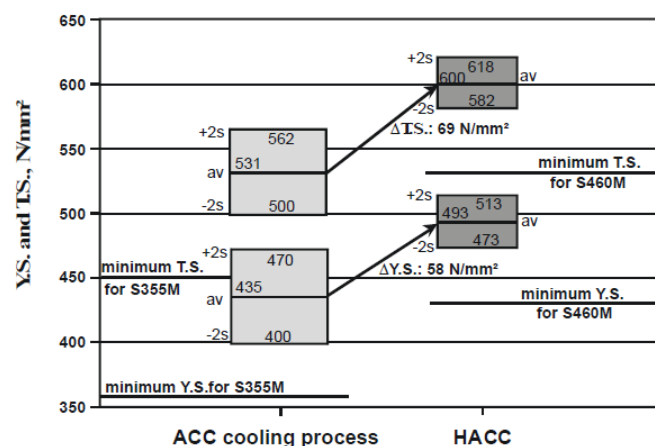

Figure 1.12: Tensile strength and yield strength of two TMCP-rolled steel plates with the same chemical compositions but with different cooling speed after rolling. [Schröter and Willms, 2010]

15

In this way, even a steel with a minimum yield strength of 460 MPa can be produced with acceptable carbon equivalents for best weldability. For instance, an S460M steel shows a carbon equivalent of 0.40 – 0.42 % which may be lower than that for a conventional S355J2+N.

As a result, S460M enables the reduction of preheating temperatures in comparison to a conventional S460N. Furthermore, in most cases even for this higher-strength steel grade preheating can be omitted completely if special conditions on the welding process are fulfilled, as in particular the usage of low-hydrogen consumables (hydrogen content: HD) such as thoroughly dried basic electrodes. Figure 1.13 compares the necessary preheating temperatures for a S460M and S460N steel.
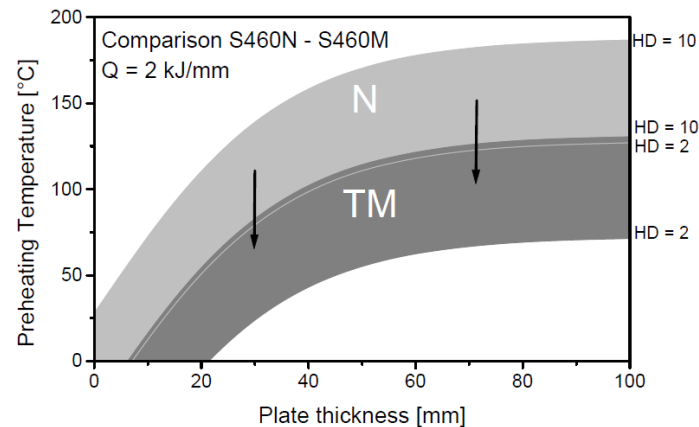
Figure 1.13: Comparison of preheating temperatures according to EN 1011 between normalized steel S460N and higher strength steel S460M. [Schröter and Willms, 2010]

In order to reduce the danger of embrittlement in the heat-affected zone, steels unsusceptible to ageing are needed. The **insusceptibility for ageing** is shown on the material by notch impact tests on cold formed and artificially aged material. Figure 1.14 shows that the notch impact temperature - transition curve moves towards higher temperatures when the steel is being aged, but relatively low transition temperatures can still be found even under this hard test conditions.
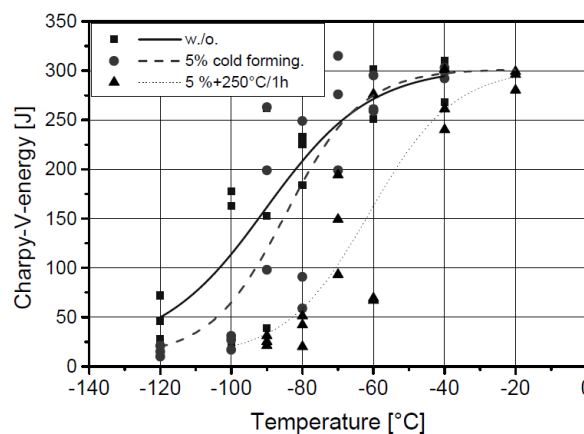
Figure 1.14: Charpy-V temperature transition curves for an S500M steel without cold forming, with additional cold forming and cold forming with additional artificial ageing. [Schröter and Willms, 2010]

At this point it is worth mentioning that thermomechanically rolled steels meet the requirements of European Standards ***EN 10149 – 2: "Hot rolled products made of high yield strength steels for cold forming – Part 2: Technical delivery conditions for thermomechanically rolled steels"***.

EN 10149-2 is the European Standard for hot-rolled flat products made of high yield strength thermo-mechanically rolled steels for cold forming. Steels encompassed by this specification have minimum yield strengths ranging from 315 MPa to 460 MPa for thicknesses ranging from 1.5 mm up to 20 mm. The specification also covers steel grades having minimum yield strengths of 500 to 700 MPa in thicknesses of 1.5 to 16 mm [European Standards].

1.3.2.3. Quenched and Tempered Plates

Steels of 690 MPa yield became commercial about three decades ago. They were, like today, essentially produced by water quenching and tempering (QT). Nowadays QT-plates with a yield strength over 1,100 MPa have become commercial.

Quench & Tempering is probably the widest used of the heat treatments to harden a steel. The material is heated to the austenitic range, which for HS steels is usually somewhere between 900 to 960°C [Schröter F. and Willms R. 2010], and held at this temperature until the material is fully transformed to **austenite**. This hold time takes into account the dimensions of the component. It is then removed from the furnace and submerged in an agitated, usually, liquid in a process called quenching. This causes changes in the microstructure, as the component cools rapidly down to around 200°C. This quenching causes none or very little carbon to precipitate as iron carbide. It produces a feather like structure called **martensite**, which distorts the internal structure. This additional stress makes it difficult for defects on the atomic scale, called dislocations, to move around in response to the applied load causing the material to become stronger. The formation of martensite is only achieved if the material exceeds a **critical cooling rate** [Metallurgy Data, 2020]. In order to suppress the formation of softer microstructure, essentially ferrite, during cooling, an accelerated cooling is necessary. The fastest cooling is obtained by exposing the plate surfaces to a rapid water stream. By such an operation the very surface is cooled to a temperature below 300 °C within a few seconds. In the core of the plate cooling is considerably slower and the cooling rate decreases with increasing plate thickness. Therefore the alloying concept of thicker quenched and tempered plates has to be adapted to ensure sufficient hardening in the plate core.

If we consider the mechanical properties in the as quenched condition, this operation **increases the hardness and strength** of the steel but drastically **decreases the ductility and toughness**. This means that the strength is considerably higher than required but the material is too brittle for most structural applications.

The aim of tempering is to soften the steel back achieving the desired combination of properties. By tempering the martensite, the supersaturation of carbon in the matrix is reduced by the precipitation of carbides leading to a relaxation in the atomistic scale. At the same heat treatment the high dislocation density associated with martensite formation is reduced [Schröter and Willms, 2010]. Tempering will considerably **improve toughness and ductility** while still maintaining a high strength level. It consists of heating the steel to a temperature below the austenitic range usually somewhere between 500 to 650°C and holding at this temperature for a specific time period. During this process the hard, brittle martensite

dissociate into ferrite and iron carbide, producing a structure called **tempered martensite** which has lots of fine particles dispersed through the ferrite. This will give a satisfactory combination of **strength, hardness, toughness and ductility** [Metallurgy Data, 2020]. Some amounts of lower bainite are also acceptable. The ratios of these properties can be refined through the time and temperature of the tempering.

A 60 mm thick S890QL **(EN 10025-6)** is chosen for example that shows the influence of tempering on the properties. *Figure 1.15* illustrates how the tensile properties are lowered with increasing temper parameter and Figure 1.16 the improvement of impact toughness, respectively.
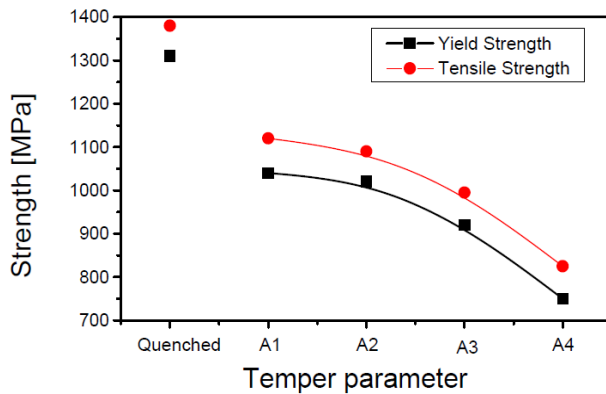

Figure 1.15: Influence of increasing tempering temperatures on the tensile properties of S890QL in 60 mm thickness. [Hanus, Schütz & Schütz, 2002]
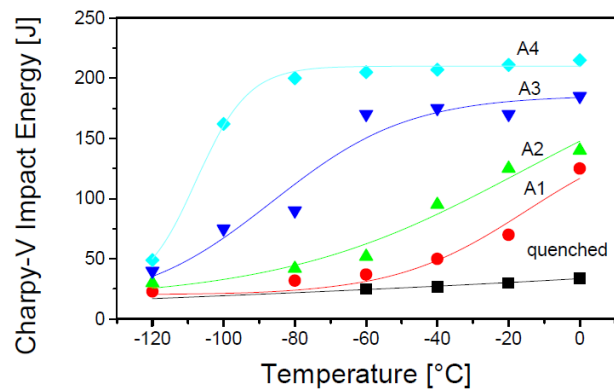
Figure 1.16: Influence of increasing tempering temperatures on the Charpy impact temperature transition of S890QL steel. [Schröter and Willms, 2010]

The tempering conditions must be adapted to the particular chemical composition of the steel. The higher the toughness and strength requirements the closer gets the permitted range for the tempering conditions.

It has already been mentioned that the alloying compositions of quenched and tempered steel increases with growing plate thickness in order to ensure a sufficient hardening of the plate in the core region. Therefore, it is obvious that the carbon equivalent of a quenched and tempered steel increases with the plate thickness. An example is given by *Table 1.2*.

Table 1.2: Typical carbon equivalents of S690QL steel.

Thickness [mm]	CE	CET [%]	Pcm
$t \leq 20$	0.42	0.30	0.26
$20 \leq t < 50$	0.59	0.37	0.31
$50 \leq t < 80$	0.66	0.39	0.32
$80 \leq t < 110$	0.72	0.41	0.34
$110 \leq t < 150$	0.79	0.44	0.35

Due to higher strength and carbon equivalents quenched and tempered steel grades of a yield strength of 690 MPa and more show a more sophisticated fabrication behavior than thermomechanically rolled steel grades.

At this point it is worth mentioning that quenched and tempered steels meet the requirements of European Standards ***EN 10025 – 6: "Hot rolled products of structural steels – Part 6: Technical delivery conditions for flat products of high yield strength structural steels in quenched and tempered condition"***

This document specifies technical delivery conditions for flat products of high yield strength alloy special steels. The steels specified in this document are applicable to hot-rolled flat products with a minimum nominal thickness of 3 mm and a maximum nominal thickness of 200 mm for grades S460, S500, S550, S620 and S690, a maximum nominal thickness of 125 mm for grades S890 and S960, in steels which, after quenching and tempering, have a specified minimum yield strength of 460 MPa to 960 MPa [European Standards].

1.4. Steels: S560 and S700

This diploma thesis is conducted in the frame of RAMSSES EU funded project. One of its objectives is the introduction of the HSLA steels in marine industry in order to reduce the ship weight (L.S.), which is one of the most challenging topic of research in the marine field in the last years, as L.S. mainly affects the fuel consumption and the payload capacity of the ship. Although the use of the HSLA steels can potentially achieve this objective of weight savings due to the better mechanical performances, compared with conventional steels, technical, economic and regulatory issues must be investigated carefully before reaching a massive use of these steel in the marine industry.

Compared to conventional steel, the HSLA steels can guarantee better static performances being their yielding point greater but also their long term behavior is better having generally better fatigue and corrosive performances. European shipbuilding industries like FINCANTIERI (largest shipbuilder in Europe, fourth largest in the world after the acquisition of Vard in 2013), are strongly interested in using specific HSLA steels, in addition to the commonly used AH36. These specific steels have the peculiarity of having a higher fatigue resistance than AH36. Therefore, FINCANTIERI is interested in introducing such steels to the shipbuilding industry, in order to replace AH36 with these steels in areas or parts of the metal structure that undergo high fatigue loads. Thus, in addition to their own properties, it is necessary to study the behavior of their welds (homogeneous and heterogeneous).

So, from SSAB, through FINCANTIERI Shipbuilding Company, we were provided two HSLA steel samples, S560 and S700, along with their certificates, which meet all the requirements of European standard **EN 10 204 – 3.1**: "*Metallic products – Inspection Certificate, Type 3.1*". This EN is a mill test report validated by the mill's in–house test department which has to be independent of the manufacturing department. This report certifies the chemical and mechanical features of a product and its compliance to the applicable norms and technical specifications.

These steels are also called FCA – Fatigue Crack Arresters, as they promise to have the ability to delay crack propagation which resulted by cyclic loadings. S560 and S700 offers a much higher yield and tensile strength, in compare to AH36, good weldability, and hardenability. So, they could potentially be used in these critical spots of the metal structure. Moreover, S560's ductility is not very lower than that of AH36, so, it could be used even in larger areas of the structure.

Both samples belong in cold-formed section of SSAB and they meet all the requirements of European standard **EN 10162**, which specifies dimensional and cross-sectional tolerances for cold rolled steel sections produced on roll-forming machines. This section of steels are lightweight, uniform and consistent products and they offer high strength-to-weight ratio. They are uniform and consistent products with smooth surface finish. Moreover, common jointing methods can be used (welding, bolting, adhesives, etc.). Another important advantage of these steels is that they are recyclable at end of life.

In the paragraphs below (1.4.1. and 1.4.2.) the main characteristics of both steels, S560 and S700 are presented. Furthermore, the certificate's results of the sent samples are presented in tabular form, as well as the standard values to which each grade of steel must comply.

1.4.1. S560 steel

SSAB Domex S560 is a **hot-rolled**, **cold-forming** steel at 560 MPa, high-strength low-alloy (**HSLA**) steel that features consistent quality as it is produced under rigorous quality control. A well-balanced analysis with a fine grain structure produced through **thermomechanical rolling** creates a steel with first-class mechanical and cold-forming properties. Together with the steel's high purity, these properties make for good bending and cutting characteristics and a steel that can be welded using all standard methods. Thus, S560 could be a good choice when looking for high productivity and high-quality end products. Typical applications include a wide range of fabricated components and steel structures.

The delivery condition of S560 is thermomechanically rolled. The plates are delivered with non-pickled or pickled surface and with mill or cut edge condition. S560 meets or exceeds the requirements of S420MC in **EN 10149-2** (paragraph 1.3.2.2.). Due to its fabrication (cold forming steel), S560 is not suited for heat treatments at temperatures above 580°C, since the material then may lose its guaranteed properties. Moreover, it has good welding, cold forming and cutting performance.

More specifically, S560 steel's characteristics, according to the corresponding standards and the sample's certificate, are presented in the tables below.

Table 1.3: Mechanical properties in the longitudinal direction of S560.

Mechanical Properties		S560 (standard)	S560 (certificate)
Thickness	[mm]	6.01 - 15	10
Yield strength Re	[min MPa]	560	459
Tensile strength Rm	[MPa]	480 - 620	548
Elongation A% (50mm)	[min %]	20	25,0

Table 1.4: Impact properties of S560 sample employing longitudinal Charpy V- notch test.

Impact Properties		S560 (standard)	S560 (certificate)
Thickness	[mm]	6.01 - 15	10
Test temperature	[ºC]	-20	-20
Minimum impact energy	[J]	40	233

In the following table (Table 1.5) the chemical composition of S560 is presented along with the Carbon Equivalent percentage (CEV and CET) which is an empirical value in weight percent, relating the combined effects of different alloying elements used in the making of carbon steels to an equivalent amount of carbon. There are several commonly used equations for expressing Carbon Equivalent. Two examples of such mathematical formulae are:

$$CEV = C + \frac{Mn}{6} + \frac{Cr + Mo + V}{5} + \frac{Cu + Ni}{15} \tag{1.1}$$

$$CET = C + \frac{Mn + Mo}{10} + \frac{Cr + Cu}{20} + \frac{Ni}{40} \tag{1.2}$$

Table 1.5: Chemical composition of S560 and Carbon Equivalent (CE) percentage.

Chemical Composition

		S560 (standard)	**S560 (certificate)**
Thickness [mm]		1.8 - 15	10
C	(max %)	0.1	0.063
Si	(max %)	0.03	0.01
Mn	(max %)	1.5	1.36
P	(max %)	0.025	0.01
S	(max %)	0.01	0.003
Al$_{tot}$	(min %)	0.015	0.038
Nb	(max %)	0.09	0.041
V	(max %)	0.2	0.01
Ti	(max %)	0.15	0
Cr	(max %)		0.02
Cu	(max %)		0.01
Ni	(max %)		0.04
Mo	(max %)		0
B	(max %)		0.0001
N	(max %)		0.004
Carbon Equivalent			
CEV		0.25	0.30
CET		0.18	

1.4.2. S700 steel

SSAB Strenx S700 (grade E) is a **HSLA** structural steel with a minimum yield strength of 650-700 MPa depending on thickness. S700 has obtained its mechanical properties by **quenching and subsequent tempering** and meets the requirements of **EN 10 025-6** (paragraph 1.3.2.3.) for the S690 grade and thicknesses.

S700 E (complies with S690QL) is available in plate thicknesses of 4-160 mm and meet or exceed the requirements of EN 10149-2. Its benefits include very good bendability and surface quality, weldability with excellent HAZ strength and toughness, exceptional consistency within a plate guaranteed by close tolerances and high impact toughness which provides for good resistance to fractures. Typical applications include demanding load-bearing structures in the lifting, handling and transportation segments.

The delivery condition of S700 is **Quenched** and **Tempered**. The plates are delivered with sheared or thermally cut edges or untrimmed edges after agreement. Due to its fabrication (cold-formed) the properties of the delivery condition **cannot be retained after exposure to temperatures in excess of 580ºC**, since the material then may lose its guaranteed properties.

More specifically, S700 steel's characteristics, according to the corresponding standards and the sample's certificate, are presented in the tables below.

Table 1.6: Mechanical properties in the longitudinal direction of S700 sample.

Mechanical Properties		S700 (standard)	S700 (certificate)
Thickness	[mm]	4.0 - 53.0	20
Yield strength Re	[min MPa]	700	785.5
Tensile strength Rm	[MPa]	780 - 930	826.5
Elongation A% (50mm)	[min %]	14	16.5

Table 1.7: Impact properties of S700 sample employing longitudinal Charpy V- notch test.

Impact Properties		S700 (standard)	S700 (certificate)
Thickness	[mm]	4.0 - 53.0	20
Test temperature	[ºC]	-40	-40
Minimum impact energy	[J]	69	211

In the following table (Table 1.8) the chemical composition of S700 is presented along with the Carbon Equivalent percentage (CEV and CET) calculated according to equation (1.1) and (1.2).

Table 1.8: Chemical composition of S700 and Carbon Equivalent (CE) percentage according to its standards and its certificate.

Chemical Composition

		S700 (standard)	**S700 (certificate)**
Thickness [mm]		4.0 – 53.0	20
C	(max %)	0.2	0.14
Si	(max %)	0.6	0.3
Mn	(max %)	1.6	1.15
P	(max %)	0.02	0.012
S	(max %)	0.01	0.001
Al_{tot}	(min %)		0.0345
Nb	(max %)		0.001
V	(max %)		0.013
Ti	(max %)		0.0085
Cr	(max %)	0.8	0.295
Cu	(max %)	0.3	0.01
Ni	(max %)	2	0.065
Mo	(max %)	0.7	0.172
B	(max %)	0.005	0.001
N	(max %)		0.002
Zr	(max %)		0.002
Carbon Equivalent			
CEV		0.52	0.43
CET		0.36	0.29

1.4.3. AH36 steel

At this point, it is considered important to mention some of the properties of the shipbuilding steel AH36 in order to compare them with those of the specimens that we received from FINCANTIERI, S560 and S700, and are the subject of this study.

ABS Steels are types of structural steel which are standardized by the American Bureau of Shipping for use in shipbuilding [Rules for Building and Classing Steel Vessels, American Bureau of Shipping, 1990]. ABS steels come many grades in **ordinary-strength** and two levels of **higher-strength** specifications.

Ordinary-strength ABS shipbuilding steel comes in a number of grades, A, B, D, E, DS, and CS. Yield point for all ordinary-strength ABS steels is specified as 235 MPa, except for ABS A in thicknesses of greater than 25 mm which has yield strength of 225 MPa, and cold flange rolled sections, which have yield strength of 205 MPa. Ultimate tensile strength of ordinary strength alloys is 400-490 MPa, except for ABS A shapes and bars with 400-550 MPa, and cold flanged sections with 380-450 MPa. The various grades have slightly differing alloy chemical ingredients, and differing fracture toughness.

Higher-strength ABS shipbuilding steel comes in six grades of two strengths, AH32, DH32, EH32, AH36, DH36, and EH36. The 32 grades have yield strength of 315 MPa, and ultimate tensile strength of 440-590 MPa. The 36 grades have yield strength of 355 MPa, and ultimate tensile strength of 490-620 MPa.

All of these steels have been engineered to be optimal long-lived shipbuilding steels. ABS does permit the use of other steels in shipbuilding, but discourages it, and requires more detailed engineering analysis [ABS, 2010].

AH36 is the most commonly used steel in shipbuilding industry and has a tensile strength of **355 MPa**. It is produced through hot rolling and normalizing (paragraph 1.3.2.1.). More specifically AH36 steel's mechanical properties, according to the corresponding standards, are presented in the following tables. S560 and S700 steels' properties are also mentioned in these tables for comparison purposes.

Table 1.9: Mechanical properties in the longitudinal direction of S560, S700 and AH36 according to their standards.

Mechanical Properties		AH36	S560	S700
Thickness	[mm]	4 - 260	6.01 - 15	4.0 - 53.0
Yield strength Re	[min MPa]	355	560	700
Tensile strength Rm	[MPa]	480 - 620	480 - 620	780 - 930
Elongation A% (50mm)	[min %]	21-22	20	14

Table 1.10: Impact properties of S560, S700 and AH36 according to their standards employing longitudinal Charpy V- notch test.

Impact Properties		AH36	S560	S700
Thickness	[mm]	≤ 50	6.01 - 15	4.0 - 53.0
Test temperature	[ºC]	0	-20	-40
Minimum impact energy	[J]	34	40	69

In the following table (Table 1.11) the chemical composition of S700 is presented along with the Carbon Equivalent percentage (CEV and CET) calculated according to equation (1.1) and (1.2).

Table 1.11: Chemical composition of S560, S700 and AH36 and Carbon Equivalent (CE) percentage according to their standards.

Chemical Composition		AH36	S560	S700
C	(max %)	0.18	0.10	0.20
Si	(max %)	0.5	0.03	0.6
Mn	(max %)	1.60	1.50	1.60
P	(max %)	0.035	0.025	0.02
S	(max %)	0.035	0.01	0.01
Al_{tot}	(min %)	0.015	0.015	
Nb	(max %)	0.05	0.09	
V	(max %)	0.1	0.2	
Ti	(max %)	0.02	0.15	
Cr	(max %)	0.2		0.8
Cu	(max %)	0.35		0.3
Ni	(max %)	0.4		2
Mo	(max %)	0.08		0.7
B	(max %)			0.005
Carbon Equivalent				
CEV		0.38	0.25	0.52
CET			0.18	0.36

References – Chapter 1

[1]   **American Bureau of Shipping**, (2010), <u>Steel Vessel Rules, Part 2 - Materials and Welding</u>, (Chapter 1, Sections 2 and 3), Houston.

[2]   **Bell T.**, (2020), <u>The History of Steel: From Iron Age to Electric Arc Furnaces</u>, (website: https://www.thoughtco.com/steel-history-2340172), Carleton University - University of British Columbia.

[3]   **Bhadeshia H., Honeycombe R.**, (2016), <u>Steels: Microstructure and Properties</u>, 4th Ed., Elsevier Science and Technology Books, Cambridge.

[4]   **BorTec**, <u>Common Alloying Elements for Steel and their Effects</u>.

[5]   **Bramfitt L.B., Benscoter O.A.**, (2002), <u>Metallographer's Guide: Practices and Procedures for Irons and Steels</u>, ASM International, The Materials Information Society, United States of America.

[6]   **Chakrabati D**, (2007), <u>Development of bimodal grain structures and their effect on toughness in HSLA steel</u>, (PhD Thesis), University of Birmingham.

[7]   **European Standards** (website: www.en-standard.eu/)

[8]   **Gladman T.,** (1997), <u>The physical metallurgy of microalloyed steels</u>, 1st edition, The University Press, Cambridge.

[9]   **Gogou E.,** (2012), <u>Use of High Strength Steel Grades for Economical Bridge Design</u>, (Thesis Master), Delft University.

[10]   **Hanus F., Hubo R.**, (1999), <u>Flame straightening of thermomechanically rolled structural steel</u>, Steel Research 70 (475): 193-197.

[11]   **Hanus. F., Schütz, J., Schütz W.**, (2002), <u>One step further - 500 MPa yield strength steel for offshore constructions</u>, Proceedings of 21st Intern Conference on Offshore Mechanics and Arctic Engineering Oslo - Norway.

[12]   **Kakaei K., Esrafili M., Ehsani A.,** (2019), <u>Interface Science and Technology vol. 27: Graphene Surfaces: Particles and Catalysts</u>, Interface Science and Technology, Elsevier.

[13]   **Kirkwood P.R.**, (2020), <u>Thermomechanical Controlled Processing (TMCP) Delivering the Advantages of Niobium Technology</u>, Technical Briefing, CBMM.

[14]   **Krinis I.,** (2020), <u>Corrosion Susceptibility of AH36 and S690 Steel Weldments</u>, (Thesis), School of Naval Architecture and Marine Engineering, National Technical University of Athens.

[15]   **Metallurgy Data,** (2020), <u>Heat Treatment - Types (Including Annealing), Process and Structures (Principles of Metallurgy)</u>, YouTube video.

[16]   **Morrison W.B.,** (2000), <u>Overview of Microalloying in Steels</u>, academia.edu

[17]   **Pantelis D.I., Chrysoulakis G.**, (2008), <u>Materials Science and Technology</u>, (in Greek: Επιστήμη και Τεχνολογία των Μεταλλικών Υλικών), Second Edition, Papasotiriou, Athens.

[18]   **Pantelis D.I., Tsiourva D.E.**, (2012), <u>Corrosion and Protection of Shipbuilding and Mechanical Constructions</u>, (in Greek: Διάβρωση Και Προστασία Ναυπηγικών Κατασκευών), School of Naval Architecture and Marine Engineering, National Technical University of Athens.

[19]   **Pantelis D.I., Tsiourva D.E.**, (2017), <u>Trends in Oil and Gas Corrosion Research and Technologies</u>, Chapter 10, Shipbuilding Technology Laboratory, School of Naval Architecture and Marine Engineering, National Technical University of Athens, Greece.

[20]   **Sastri V.S.**, (2015), Challenges in Corrosion: Costs, Causes, Consequences and Control, John Wiley & Sons.

[21]   **Schröter F.**, (2004), <u>Steels for modern steel construction and offshore applications</u>, 10th Nordic Steel Construction Conference, Copenhagen.

[22]   **Schröter F., Willms R.**, (2010), <u>Welding and fatigue in high performance steel</u>, Dillinger Publications, Germany.

[23]   **Skobir D.A.**, (2011), <u>High-Strength Low-Alloy (HSLA) Steels</u>, Institute of Metals and Technology.

[24]   **Zhen-jia Xie, Cheng-jia Shang, Xue-lin Wang, Xue-min Wang, Gang Han, Raja-devesh-kumar Misra**, (2020), <u>Recent progress in third-generation low alloy steels developed under M^3 microstructure control</u>, International Journal of Minerals, Metallurgy and Materials (Vol. 27, No.1), Springer.

[25]   **Ziakas A.**, (2020), <u>Corrosion Behavior of AH36 and S460 Steel Weldments</u>, (Thesis), School of Naval Architecture and Marine Engineering, National Technical University of Athens.

Science of Corrosion

Introduction

Corrosion is an inevitable issue in maritime industry. Each part of the ship, from its hull, to the stiffeners, pipelines, tanks, plates, and their weldments are continuously subjected to highly corrosive conditions and environments. Thus, the study of the corrosion science, along with the mechanisms undergo this phenomenon, is a very important for the structural design and constitutes the main purpose of this thesis.

The corrosion process is based on electrochemical reactions consisting of oxidation of metallic materials and reduction of environmental substances. The oxidation and reduction can be described in electrochemistry, which includes charge transfer reactions at the metal/environment interface and movement of charged particles of ions in the environment and electrons in the metal.

Thermodynamics gives an understanding of the energy changes involved in the electrochemical reactions of corrosion, which provide the driving force and control the spontaneous direction of the reactions. Nevertheless, when corrosion is possible, thermodynamics cannot predict the rate, which, along with the actual extent of corrosion, are governed by Kinetic laws.

This chapter of the present thesis analyzes the phenomenon of corrosion, beginning from what is defined as corrosion and in what light it is studied. Then the nature of corrosion is examined, along with the reactions that occur during this phenomenon. Finally, the most extensive piece of this chapter is devoted to explaining the thermodynamic and kinetic background of corrosion.

2.1. Definition and Classification

Corrosion is defined as a physicochemical interaction between a metallic material and its environment that results in changes in the properties of the metal, and that may lead to significant impairment of the function of the metal, the environment or the technical system, of which these form a part (ISO 8044, 1986).

Corrosion phenomena can be classified according to the type of corroding medium acting on the metal. Corrosion in nonelectrolytic media is distinguished from that in electrolytic media. The former include dry hot gases, organic liquids (e.g., gasoline), and molten metals. Electrolytic media are most diverse, and include ambient air (with moisture and other components), water (seawater, tap water) and aqueous solutions (acids, alkalies, salt solutions), moist soil (for underground pipelines, piles, etc.), melts, and nonaqueous electrolyte solutions.

Corrosion phenomena can also be classified according to the visible aspects of corrosive attack. This may be general (continuous), affecting all of the exposed surface of a metallic object, or localized. General corrosion can be uniform and nonuniform. Depending on the width and depth of the segments affected by localized corrosion, we may speak of spot, pit (large or small), or subsurface corrosion. Often, intercrystalline corrosion is encountered, which propagates in the zones between individual metal crystallites. Cracks develop between or in individual crystals in the case of stress corrosion cracking. Certain types of corrosion are selective. Thus, corrosion cracking is observed primarily in the case of alloys and only when these are in contact with particular media. Corrosion is often enhanced by various extraneous effects. Stress corrosion cracking can occur under appreciable mechanical loads or internal stresses; corrosion fatigue develops under prolonged cyclic mechanical loads. Other factors are fretting and cavitation in a liquid (impact of the liquid) [Bagotsky, 2006]. Galvanic corrosion can also occur in a metal when it is in electrical contact with another, which is nobler than the first one, in the presence of an electrolyte. Some of the aforementioned types of corrosion are shown schematically in Figure 2.1.
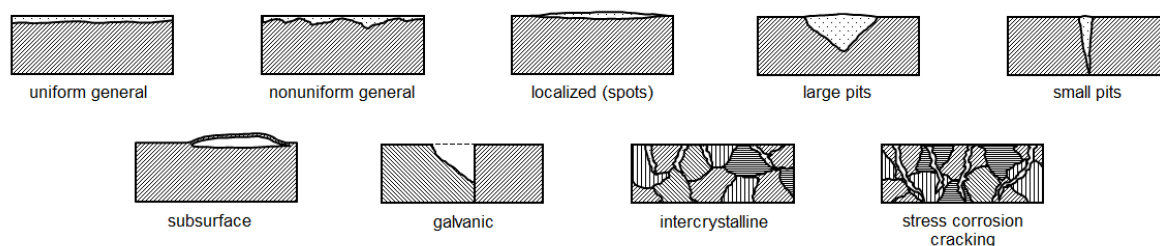

Figure 2.1: Types of metallic corrosion.

There are four main reasons to study corrosion. Three of these reasons are based on societal issues regarding (i) human life and safety, (ii) the cost of corrosion, and (iii) conservation of materials. The fourth reason is that corrosion is inherently a difficult phenomenon to understand, and its study is in itself a challenging and interesting pursuit.

2.2. Corrosion Science and Engineering

Corrosion science is an interdisciplinary area embracing <u>chemistry</u>, <u>materials science</u>, and <u>mechanics</u>, as shown in Figure 2.2. The study of aqueous corrosion processes involves the intersection of chemistry and materials science. But the science of mechanics must be added to understand mechanically assisted corrosion processes, such as stress-corrosion cracking and corrosion fatigue.
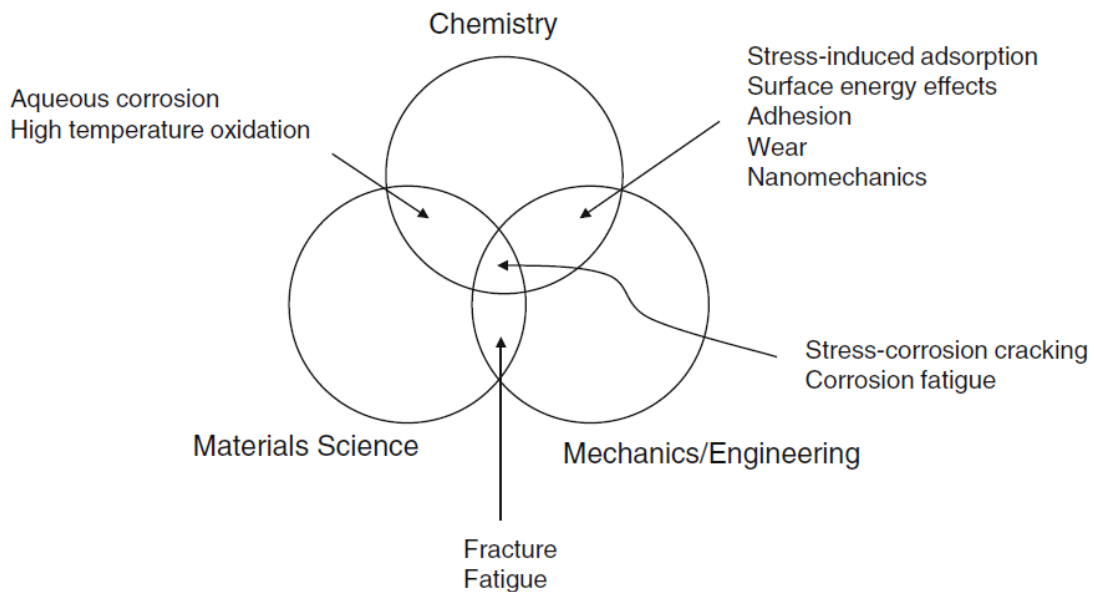

Figure 2.2: Schematic relationship between corrosion science and corrosion engineering and the large number of variables which can be operative when corrosion occurs. [McCafferty, 2010]

Corrosion science is the study of the chemical and metallurgical processes that occur during corrosion. **Corrosion engineering** is the design and application of the methods to prevent corrosion. Ideally, science should be married to engineering so as to invent new and better methods of prevention and apply existing methods more intelligently and effectively. However, scientists are sometimes devoted to the pursuit of pure knowledge, with little or no perspective on the possible applications of their work. On the other hand, engineers often apply time-honored methods with little or no understanding of the principles behind them. One of the objectives of this thesis is to encourage further cooperation in both engineering and science.

2.3. Electrochemical Nature of Aqueous Corrosion

Corrosion (from Latin corrodere, "gnaw to pieces") of **metals** is the spontaneous chemical (oxidative) destruction of metals under the effect of their **environment**. Most often it follows an electrochemical mechanism, where anodic dissolution (oxidation) of the metal and cathodic reduction of an oxidizing agent occur as coupled reactions. Sometimes a chemical mechanism is also observed [Bagotsky, 2006].

The aforementioned couple reactions, either the oxidation or reduction, are called half-cell reactions and component of a redox reaction. A half reaction is obtained by considering the change in oxidation states of individual substances involved in the redox reaction.

2.3.1. Anodic Reactions

Anodic reaction is a half-reaction of oxidization which means the release of electrons or an increase in the oxidation state of an atom, an ion, or of certain atoms in a molecule. A corroding metal, M, turns into metal ions, M^{n+}, and simultaneously losses electrons, e^-, where n is the number of the electrons lost. The general form of this reaction is

$$M \rightarrow M^{n+} + ne^- \tag{2.1}$$

An examples of anodic reaction, is this of ferrum, Fe,

$$Fe_{(s)} \rightarrow Fe^{2+}_{(aq)} + 2e^- \tag{2.2}$$

where the notations (s), (aq), and (l) refer to the solid, aqueous, and liquid phases, respectively. A schematic representation of the reaction (2.2) is shown in Figure 2.3.
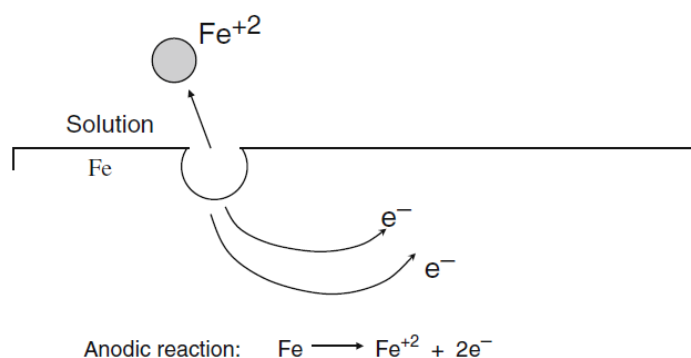

Figure 2.3: Example of an anodic reaction – the dissolution of iron. [McCafferty, 2010]

At this point, it is worth mentioning that not all anodic reactions are corrosion reactions, i.e. there is not a loss of metal. However, in each anodic reaction there is a charge transfer, through

the electron exchange. This observation allows the following scientific definition of corrosion: ***Corrosion is the simultaneous transfer of mass and charge across a metal/solution interface.***

2.3.2. Cathodic Reactions

The processes of oxidation and reduction occur simultaneously and cannot happen independently of one another. According to this, cathodic reactions are half-cell reactions of reduction. There is gain of electrons (electrons are consumed by the reaction) or a decrease in the oxidation number of the given species (a reduction in oxidation state). The general form of a reduction reaction is

$$\mathbf{Ox + ne^- \rightarrow Re} \tag{2.3}$$

The most common cathodic reaction in corrosion is the reduction of two hydrogen ions at a surface to form one molecule of hydrogen gas:

$$\mathbf{2H^+_{(aq)} + 2e^- \rightarrow H_{2\,(g)}} \tag{2.4}$$
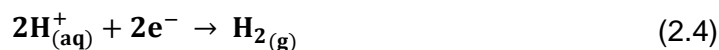
This is the predominant cathodic reaction in **acidic solutions**. A schematic representation of this reaction, is presented in Figure 2.4.
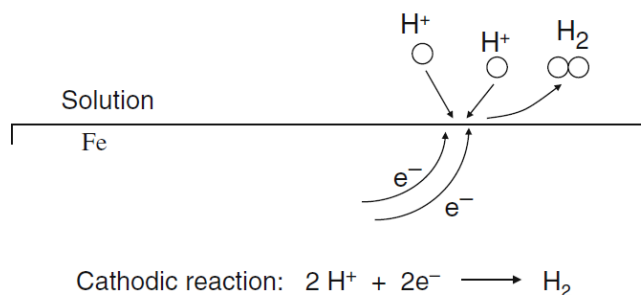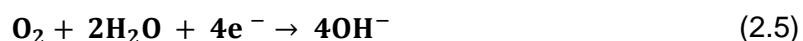

Figure 2.4: Example of a cathodic reaction – hydrogen evolution on iron immersed in an acid solution. [McCafferty, 2010]

Another common cathodic reaction is the reduction of dissolved oxygen in **neutral** or **alkaline solutions**

$$\mathbf{O_2 + 2H_2O + 4e^- \rightarrow 4OH^-} \tag{2.5}$$

or **in acidic solutions**

$$\mathbf{O_2 + 4H^+ + 4e^- \rightarrow 2H_2O} \tag{2.6}$$

When none of the above cathodic reactions occur, water reduces

$$2H_2O + 2e^- \rightarrow H_2 + 2OH^- \tag{2.7}$$

which is equal to reaction (2.4), assuming that water dissociates to H^+ and OH^- and subtracting two OH^- from each side of the reaction[Pantelis and Tsiourva, 2012].

2.3.3. Coupled Electrochemical Reactions

On a corroding metal surface, anodic and cathodic reactions occur in a coupled manner at different places on the metal surface. Figure 2.5 illustrates this behavior for an iron surface immersed in an acidic aqueous environment. At certain sites on the iron surface, iron atoms pass into solution as Fe^{2+} ions by equation (2.2). The two electrons produced by this anodic half-cell reaction are consumed elsewhere on the surface to reduce two hydrogen ions to one H_2 molecule by equation (2.4).
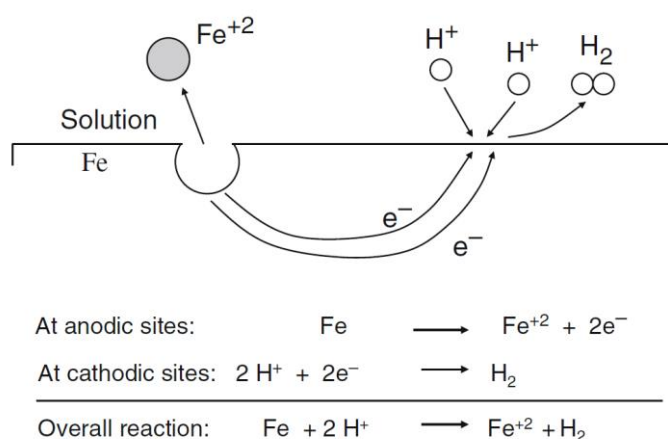

Figure 2.5: Coupled electrochemical reactions occurring at different sites on the same metal surface for iron in an acid solution. The electrons lost by the oxidation of Fe atoms are consumed in the reduction of two H^+ ions to form hydrogen gas (H_2). [McCafferty, 2010]

The reason that two different electrochemical half-cell reactions can occur on the same metal surface lies in the heterogeneous nature of a metal surface. Polycrystalline metal surfaces contain an array of site energies due to the existence of various crystal faces (i.e., grains) and grain boundaries. In addition, there can be other defects such as edges, steps, kink sites, screw dislocations, and point defects. Moreover, there can be surface contaminants due to the presence of impurity metal atoms or to the adsorption of ions from solution so as to change the surface energy of the underlying metal atoms around the adsorbate. Some of these effects are illustrated in Figure 2.6.
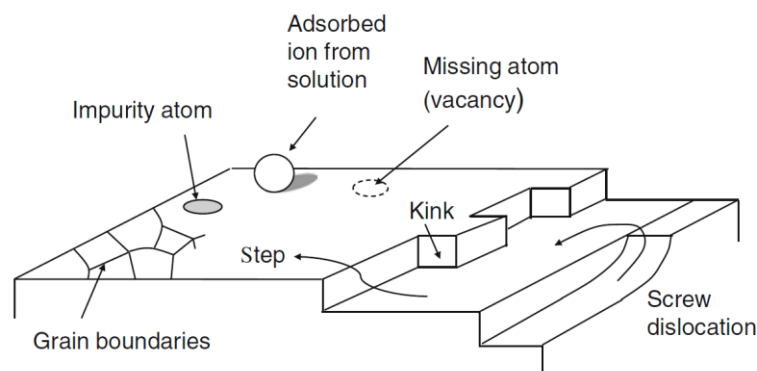
Figure 2.6: The heterogeneous nature of a metal surface showing various types of imperfections. [McCafferty, 2010]

Metal atoms at the highest energy sites are most likely to pass into solution. These high-energy sites include atoms located at the edges and corners of crystal planes, for example. Stressed surfaces also contain atoms that are reactive because they have a less stable crystalline environment. When a metal is cold worked or shaped, the metal lattice becomes strained, and atoms located in the strained regions tend to go into solution more readily than do atoms in unstrained regions. Once the process of metal dissolution process begins, a new energy distribution of sites is established. Then, the positions of anodic and cathodic surface sites change randomly with time so that the overall effect is uniform corrosion of the metal.

As shown in Figure 2.5, the sum of the two half-cell reactions, the anodic (2.2) and the cathodic (2.4), constitutes the overall chemical reaction

$$\textbf{Fe}_{(s)} + \textbf{2H}^+_{(aq)} \rightarrow \textbf{Fe}^{2+}_{(aq)} \rightarrow \textbf{H}_{2(g)} \qquad (2.8)$$
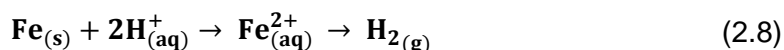
Figure 2.5 illustrates the four conditions which are necessary for corrosion to occur. These are the following:

1. An anodic reaction.
2. A cathodic reaction.
3. A metallic path of contact between anodic and cathodic sites.
4. The presence of an electrolyte.

An electrolyte is a solution which contains dissolved ions capable of conducting a current. The most common electrolyte is an aqueous solution, i.e., water containing dissolved ions; but other liquids, such as liquid ammonia, can function as electrolytes.

2.4. Thermodynamics of Corrosion

Thermodynamics gives an understanding of the **energy changes** involved in the electrochemical reactions of corrosion. These energy changes provide the driving force and control the spontaneous direction for a chemical reaction. Thus, thermodynamics shows how conditions may be adjusted to make corrosion possible or impossible.

Nevertheless, when corrosion is possible, thermodynamics cannot predict the rate; corrosion may range from fast to very slow. The **rate** of the reaction and the actual **extent** of corrosion is governed by kinetic laws (see paragraph 2.5) [Jones, 1995].
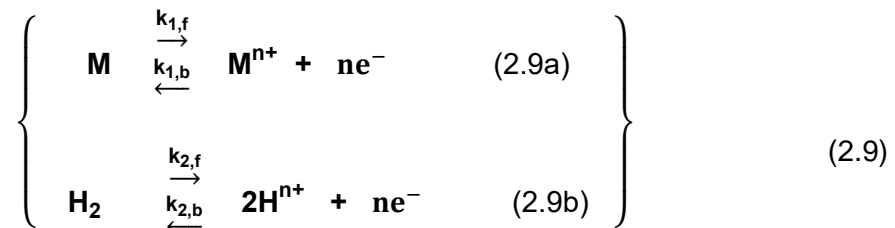
2.4.1. Nature of Corrosion

Corrosion is a phenomenon in which a material lowers its Free Energy (enthalpy). Therefore, it is a natural process, involving spontaneous chemical reactions. When a material interacts with its environment, and the total energy of this system is not at the least level possible, then corrosion occurs. At this point chemical reactions take place.

Metals in specific, corrode because they are more stable in their oxide form. Before mining, metals are found under the earth as ores. There, most of them are oxides, sulfides and silicates. This means that iron for example, that is found as an oxide, contains much more stored energy as pure iron than as iron oxide. Thus, iron will react with its environment whenever possible, in order to release all this energy and become more stable.

The amount of energy that each metal needs after its extraction from earth, in order to convert it from the oxide to the pure metal, varies for each different metallic element, and so does the stored energy it will reserve afterwards. This is the reason why some metals tend to corrode easily while others will not corrode at all.

2.4.2. Reactions and Terminology

Considering a case of a corrosive environment (containing hydrogen forming into hydrogen ions), the reactions that will happen on the interface of a metal that will be exposed to that environment are the following [Pantelis and Tsiourva, 2012],

$$
\left\{
\begin{array}{l}
M \quad \underset{k_{1,b}}{\overset{k_{1,f}}{\rightleftarrows}} \quad M^{n+} + ne^{-} \qquad (2.9a) \\[3em]
H_2 \quad \underset{k_{2,b}}{\overset{k_{2,f}}{\rightleftarrows}} \quad 2H^{n+} + ne^{-} \qquad (2.9b)
\end{array}
\right\} \qquad (2.9)
$$

In the above reactions $k_{1,f}$ and $k_{1,b}$ are the reaction rate coefficients for the forward (f) and the backward (b) reaction respectively, of (2.9a). The same applies for $k_{2,f}$ and $k_{2,b}$ with respect to reaction (2.9b).

The values of k of a specific reaction are obtained through the Arrhenius equation, as follows:

$$\mathbf{k = c \cdot e^{-E_\alpha/R \cdot T}} \tag{2.10}$$

In the above definition k corresponds to the reaction of activation energy E_α and temperature T, where:

- E_α : the activation energy (necessary energy) for the reaction of the respective k

- n : the number of electrons transferred

- Me : the metallic atoms that react on the surface (either in mol or mol/volume unit)

- H_2 : the hydrogen molecules that are formed or cleaved (either in mol or mol/volume unit)

- c : the pro-exponential factor (constant)

- R : is the universal gas constant so that R = 8.3144598 J/(mol·K)

- T : is the temperature in Kelvin (K) at which the reaction of the respective k takes place

Reactions (2.9) show the possible reactions that may appear on the metallic surface.

- Oxidation is the reaction when "n" electrons are given up, so ne^- appears at the products.

- Reduction is the reaction when "n" electrons are bounded, so ne^- appears at the reactants.

When the forward reaction rate equals the backwards reaction rate, in reaction (2.9a), then the metal is in equilibrium. The same applies for hydrogen in reaction (2.9b). When the metallic surface is exposed to a corrosive environment (an environment that contains an amount of hydrogen), and corrosion appears, then reactions (2.9) are not in equilibrium anymore.

However, the system will have to be in equilibrium, which means that the total reaction rate of both reactions will be the same. Specifically, supposing that the metal corrodes in a way that only the forward reaction happens (oxidation), then the rate at which the metal oxidizes will have to equal the rate of the hydrogen evolution. This is chemically translated as:

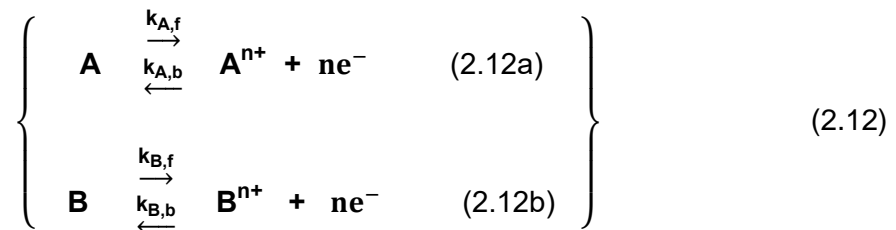$$[\mathbf{M}] \cdot \mathbf{k_{1,f}} = [\mathbf{H^{n+}}] \cdot \mathbf{k_{2,b}} \tag{2.11}$$

It is now shown how the metal cannot be in its ground state when a corrosive environment appears. The metal has to stop keeping the equilibrium in reaction (2.9a), and start giving up electrons in order to achieve equilibrium in the system of (2.9).

All of the above correspond to a simplified approach of corrosion phenomenon. In reality there are more reactions and more substances that control the problem, but even then, the oxidation-reduction systems will behave accordingly.

In terms of corrosion, "anodic reaction" is the reaction of oxidation, and the material giving up the electrons is called "anode". Similarly, "cathodic reaction" is the reaction of reduction, and the material that gains the electrons is called "cathode". The interface of the metal and the environment is called corroding surface [Traka, 2015].

2.4.3. Thermodynamics Principles

Considering an electrochemical system constituted of the following reactions (similar to equations 2.9):

$$
\left\{
\begin{array}{l}
A \underset{k_{A,b}}{\overset{k_{A,f}}{\rightleftarrows}} A^{n+} + ne^- \qquad (2.12a) \\[2em]
B \underset{k_{B,b}}{\overset{k_{B,f}}{\rightleftarrows}} B^{n+} + ne^- \qquad (2.12b)
\end{array}
\right\} \qquad (2.12)
$$

where the reaction rate coefficients k in the above reactions (2.12) are defined as in equation (2.10). However, here they correspond to the activation energies E_α and temperatures T of this particular case. This means that $k_{A,f}$ and $k_{B,f}$ correspond to the rates at which substances A and B form into ions A^{n+} and B^{n+} respectively. Likewise, $k_{A,b}$ and $k_{B,b}$ correspond to the rates at which ions A^{n+} and B^{n+} form to substances A and B, respectively.

The electrochemical cell can be considered as a system operating under constant pressure, **p**, and temperature, **T**. Assuming the system is isolated, i.e. it does not interact with its surroundings in any way, and so mass and energy remains constant within the system, then the total energy should remain constant. The law of the conservation of energy, in this case, takes the form of the first thermodynamic law:

$$\textbf{First Thermodynamic Law}: \quad \Delta U = Q - W \qquad (2.13)$$

The above equation (2.13) states that the change in the internal energy, **ΔU**, of a closed system is equal to the amount of heat, **Q**, supplied to the system minus the amount of work, **W**, consumed by the system on its surroundings.

Assuming that the system of reactions (2.12) constitute a **reversible** process (ideal situation), then the second thermodynamic law can also be applied:

$$\text{Second Thermodynamic Law}: \quad dQ = T \cdot dS \quad \Rightarrow \quad Q = \int_V T \cdot dS \qquad (2.14)$$

where **S** is the entropy.

The work, W, produced in the system is constituted from the mechanical, W_{mech}, and the electrical, W_{el}, work. For a reversible process, the mechanical work due to the change in volume, **V**, is the integral of pressure with respect to volume, so:

$$W = W_{mech} + W_{el} = \int_V p \cdot dV + W_{el} \qquad (2.15)$$

Having made the assumption that the electrochemical system operates under constant pressure, p, and temperature, T, then equations (2.14) and (2.15) become:

$$\left\{ \begin{array}{c} W = p \cdot \Delta V + W_{el} \\ \\ Q = T \cdot \Delta S \end{array} \right\} \qquad (2.16)$$

Substituting equation (2.16) into (2.13), the electrical work is expressed as:

$$W_{el} = -\Delta U + T \cdot \Delta S - p \cdot \Delta V \qquad (2.17)$$

By definition, the change on **free Gibbs energy** is given by the following equation:

$$G = U + p \cdot V - T \cdot S \qquad (2.18a)$$

Then the total differential of G in (2.18a):

$$dG = dU + p \cdot dV + V \cdot dp - T \cdot dS - dT \cdot S \qquad (2.18b)$$

For constant pressure, p, and temperature, T, the integration of equation (2.18b) gives:

$$\int_V dG = \int_V dU + \int_V p \cdot dV + \int_V dp \cdot V - \int_V T \cdot dS - \int_V dT \cdot S \;\Rightarrow$$

$$\xRightarrow{dT=0, \; dp=0} \qquad \Delta G = \Delta U + p \cdot dV - T \cdot dS \qquad (2.18c)$$

From equations (2.17) and (2.18c):

$$\Delta G = -W_{el} \qquad (2.19)$$

Equation (2.19) denotes that the change in Gibbs free energy for the electrochemical system is given by the total electrical work produced. [Karantonis, 2015], [Pantelis and Tsiourva, 2012]

2.4.4. Half - cell Potential

Electrode potential (Half - cell Potential), E, in electrochemistry, is the difference on the electrochemical potentials between two elements A and B that are in contact. This potential difference is the electromotive force causing the reactions of equations (2.12), on the interface between A and B [Pantelis and Tsiourva, 2012].

The maximum electrical work, W_{el}, that the system can produce is equal to the charge passing through the electrochemical cell multiplied by the potential difference between the two electrodes, at equilibrium. Hence, the electrical work for **n** moles of charged particles (i.e. $nN_A = n\ 6.023 \times 10^{23}$ particles) is:

$$W_{el} = n \cdot e_0 \cdot N_A \cdot E_{eq} \qquad (2.20a)$$

where:

- e_0 = q = 1.602×10^{-19} C is the elementary electric charge,
- N_A = 6.023×10^{23} mol^{-1} is the Avogadro constant and
- E_{eq} is the potential difference between the two electrodes at equilibrium.

Setting F = e$_0$ N$_A$, where, the equation (2.20a) becomes:

$$\mathbf{W_{el}} = \ \mathbf{n \cdot F \cdot E_{eq}}$$
(2.20b)

where:

➢ **n**: the moles of electrons reacting and
➢ **F**= 96485.33 C·mol^{-1} the Faraday's constant which represents the magnitude of electric charge per mole of electrons (or equivalents).

Substituting equation (2.19) in (2.20b), it is obtained:

$$\mathbf{\Delta G} \ = \ - \mathbf{n \ \cdot \ F \ \cdot \ E_{eq}}$$
(2.21)

Thus, that is the fundamental relationship, in which a charge, nF, taken reversibly at equilibrium through a potential, E, corresponds to an energy change, ΔG. The negative sign in the above equation (2.21) conforms the convention that a positive potential, E, results in a negative free energy change, ΔG, for a spontaneous reaction. Last but not least, it is worth mentioning that equation (2.21) associates Gibbs energy with the potential difference, E$_{eq}$, if only the electrochemical reaction is reversible under constant pressure and temperature [Karantonis, 2015].

Whenever corrosion appears on a metallic surface, there is a specific value of potential, in which the corroding surface is expected to find equilibrium and thus stabilize. This value depends on the metal, the environment and the conditions under which corrosion takes place. For each metal, a value of this potential, called half – cell potential, has been specified under experiments that have been conducted. Of course, the measured potentials correspond to a specific environment (electrolyte) and specific conditions (temperature and concentration of hydrogen or other oxidizers) [Pantelis and Tsiourva, 2012].

In practice, the electrochemical half – cell potentials (equilibrium potentials) that are commonly used, are the differences measured between the potential of the metal and the potential of the standard hydrogen electrode, when the metal is being corroded by purified water with 3.5% NaCl, under 25°C. These potentials are known as potentials versus Standard Hydrogen Electrode – SHE (presented in detail in paragraph 2.4.6.2.).

When ion activity, α, is different than unity and temperature, T, different than 25ºC, the **Nernst Equation** is used. This equation relates the reduction potential of an electrochemical reaction (half-cell or full cell reaction) to the standard electrode potential, temperature, and activities (often approximated by concentrations, C) of the chemical species undergoing reduction and oxidation. More specifically, standard thermodynamics says that the actual **Gibbs free energy**, **ΔG**, is related to the free energy change under **standard state ΔG⁰** by the relationship:

$$\Delta G = \Delta G^0 + R\,T\,\ln Q \qquad (2.22)$$

where **R**= 8.314 J K⁻¹ mol⁻¹ is the universal gas constant. **Q** is the **reaction quotient**, a quantity that provides a measurement of the relative quantities of products and reactants present in a reaction mixture for a reaction with well-defined overall stoichiometry, at a particular point in time. Mathematically, is defined as the ratio of the ion or <u>molecule activities</u>, α, of the product (**Reduced**) species over those of the reactant (**Oxidized**) species involved in the chemical reaction, taking stoichiometric coefficients, v, of the reaction into account as exponents of the concentrations.

$$Q_{(t)} = \frac{\prod_i^{\text{products}} \alpha_{i\ (t)}^{v_i}}{\prod_j^{\text{reactants}} \alpha_{j\ (t)}^{v_j}} \qquad (2.23a)$$

Usually, the activities of molecules or ions dissolved in solution are assumed to be the same as their <u>molar concentrations</u>, C, thus, in this case, the reaction coefficient Q equals to

$$Q_{(t)} = \frac{C_{\text{Reduced}(t)}}{C_{\text{Oxidized}(t)}} \qquad (2.23b)$$

In **equilibrium**, the reaction quotient, Q, is constant over time and is equal to the **equilibrium constant**, $K^0 = \frac{k_f}{k_b}$, where k_f and k_b are the forward and backward rate constants, as mentioned earlier. Moreover, due to the fact that the reaction is in equilibrium, the concentrations on the electrode's surface are equal to those in the bulk of the solution, i.e. $C_{\text{Oxidized}} = C_O^*$ and $C_{\text{Reduced}} = C_R^*$.

$$Q = \frac{C_R^*}{C_O^*} \qquad (2.23c)$$

The cell potential, E, associated with the electrochemical reaction is defined as the decrease in Gibbs free energy per coulomb of charge transferred, which leads to the

relationship (**2.21**) and through equation (**2.22**) we are led to the **Nernst Equation**, which for an electrochemical half-cell is:

$$E_{eq} = E_{eq}^0 - \frac{R\,T}{n\,F} \cdot \ln Q \overset{2.23c}{\Longrightarrow}$$

$$E_{eq} = E_{eq}^0 + \frac{R\,T}{n\,F} \cdot \ln \frac{C_O^*}{C_R^*} \tag{2.24}$$

where C_O^* and C_R^* are the concentrations of the oxidized and the reduced species, respectively, at equilibrium, on the electrode's surface (which are equal to those in the bulk of the solution due to the fact that the reaction is in equilibrium). Inert alia, the Nernst Equation expresses the dependence of the electrode's equilibrium potential as to the composition of the electrolyte solution. [Karantonis, 2020] [Skoulikidis and Vasiliou, 2007] [Toshiaki, 2018]

2.4.5. Charged Interfaces

Interfaces are formed at the physical boundary between two phases. So, the interface between the metal **electrode** and the **electrolyte**, is of paramount interest to the study of corrosion. This paragraph shows how a potential difference originates across a metal/solution interface and discusses the concept of the electrode potential for use in subsequent chapters.

2.4.5.1. Electrolytes

An electrolyte, as previously mentioned, is a solution which contains dissolved ions capable of conducting a current. The interior of an electrolyte may consist of a variety of charged and uncharged species. An aqueous solution usually contains H_2O molecules, Na+ ions, Cl− ions and organic molecules (which may be present as impurities, biological entities, or may be intentionally added as a corrosion inhibitor).

In a sodium chloride NaCl solution, the electrolyte contains an equal concentration of Na+ ions and Cl− ions. In any volume element of solution, there is an equal number of positive and negative ions, and these ions are randomly distributed. Moreover, these ions are in constant motion migrating through the solution in a random walk. Thus, there is **no net charge** within any volume element of solution due to the existence of dissolved ions.

2.4.5.2. The Metal/Solution Interface

Immersion of a metal into a solution creates another type of S/L interface, the metal/solution interface which is quite complicated for several reasons.

First, the metal is a conductor of electricity. By connecting external leads to the metal (without immersing these leads into the aqueous solution) and then connecting the metal under study to an external device, we can supply electrons to the metal side of the metal/solution interface, or we can extract electrons from the metal side of the interface. Thus, the metal side of the interface can be charged negatively or positively, respectively. Second, chloride ions (and other inorganic anions) which are not surface active at solution/air interfaces are adsorbed at metal/solution interfaces. Third, the water molecule itself is adsorbed at metal/solution interfaces. Moreover, the water molecule being a dipole is oriented at the interface, as shown in Figure 2.7.
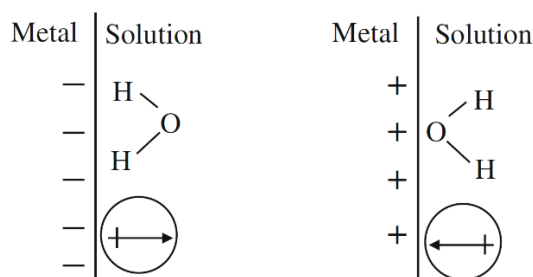
Figure 2.7: The orientation of water molecules at a metal/solution interface. **Left**: the "flop-down" orientation of the water dipole. **Right**: the "flip-up" orientation.

Fourth, the metal/solution interface is not always a stable one. If the metal corrodes, then the interface is neither chemically nor geometrically stable. Under freely corroding conditions, the metal surface supports both local anodic and local cathodic processes, as discussed in paragraph 2.3. Under these conditions, the metal/solution interface is a hubbub of activity. This statement needs to be examined more carefully by considering the character of water molecules in ionic solutions. Water molecules in the immediate vicinity of positive or negative ions are attracted toward the charge on the ion. The charge on the ion orients these nearest water molecules with the appropriate end of the dipole pointing toward the ion, as shown in Figure 2.8.
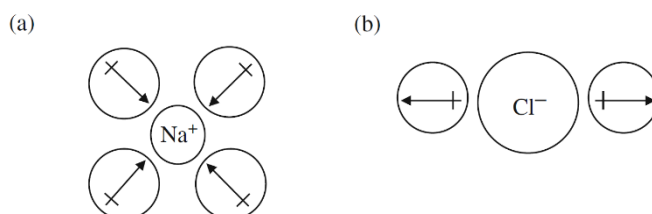
Figure 2.8: Primary waters of hydration for (**a**) Na+ ion, (**b**) Cl− anion. Primary hydration numbers are from Bockris and Reddy. [Bockris and Reddy, 1998]

Due to these ion-dipole forces, a certain number of water molecules become attracted to the central ion. Such water molecules are called primary **waters of hydration**. Located just outside the primary sheath of oriented water molecules is a secondary region of partially ordered water molecules, called secondary waters of hydration, which balance the localized oriented charge which has developed in the primary water sheath. Thus, the overall effect of ionic hydration is that there is no net charge due to ionic hydration. It can easily be shown that the number of water molecules located in primary water sheaths is a very small percentage of the total number of water molecules in solution.

2.4.5.3. The Electrical Double Layer

As previously reported, a metal in contact with an electrolyte, acts as an area where electricity current enters from an energy source into the metal or exits from it and goes to consumption. The above is defined as an **electrode**. During immersion of a metal electrode into an electrolyte an electrically charged interface is created, which is called **electrical double layer**. The metal side of the interface can be charged positively or negatively by withdrawing or providing electrons, as seen in paragraph 2.3. The charge on the metal side of the interface is balanced by a distribution of ions at the solution side of the interface [McCafferty, 2010].

The electrical double layer has evolved through the development of various models, but the most recent is the **Bockris−Devanathan−Müller model**, which embraces two important considerations, while maintaining all the features of the previous models of Gouy−Chapman and Stern.

Supposing that a metal is positively charged, the **Gouy−Chapman model** takes into account that a diffuse layer of negative ions partially balances the positive charge on the metal side of the interface. That is the diffuse part of the double layer. The **Stern model** also includes the case of absorption of anions or cations at the metal surface (as shown in Figure 2.7). The distance of closest approach of the ion is its radius, and the plane through the center of these adsorbed ions is called the **inner Helmholtz plane**. The excess charge at the metal surface is balanced in part by ions located in a Gouy−Chapman diffuse double layer, which exists outside the Helmholtz plane.
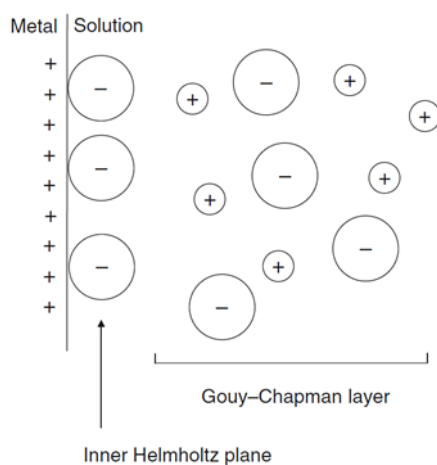
Figure 2.9: The Stern model of the electrical double layer at a metal/solution interface. [McCafferty, 2010]

The Bockris−Devanathan−Müller model takes into account the adsorption of water molecules at the metal/solution interface. For a positive charge on the metal side of the interface, water molecules are oriented with the negative ends of their dipoles toward the metal surface, as shown below in Figure 2.10. This model recognizes that water molecules and ions in solution compete for sites on the metal surface. The adsorption of the chloride ion, for example, may be considered a replacement reaction in which Cl^- ions replace water molecules adsorbed at the metal/solution interface. The plane through the center of these adsorbed ions is called the **inner Helmholtz plane** in this model. Moreover, one added feature of this model is that the charge introduced by the adsorption of anions at the metal surface is balanced in

part by counterions of the opposite charge. These counterions are not adsorbed on the metal surface, but exist in solution, and have associated with them their waters of hydration. The plane through the center of these counter ions is called the **outer Helmholtz plane**.
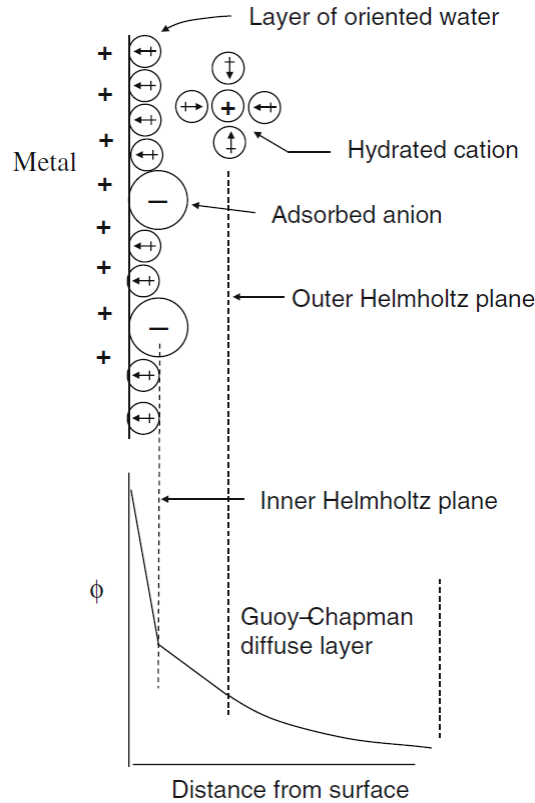

Figure 2.10: The Bockris−Devanathan−Müller model of the electrical double layer at a metal/solution interface.[Bockris and Devanathan, 1963]

As seen in Figure 2.9, there is a net charge within the diffuse part of the electrical double layer. This is in marked contrast to the interior of the solution, which, as shown earlier, does not exhibit a net charge. This difference in local chemical environments leads to the concept of the electrostatic potential. The **electrostatic potential** (at some point) is the work required to move a small positive unit charge from infinity to the point in question. This is a thought experiment for which:

1. the positive test charge is small enough not to perturb the existing electrical field;
2. the work involved is independent of the path taken.

The potential difference (between two points) is the work required to move a small unit positive charge between the two points, as shown below in Figure 2.11. The potential difference, ΔΦ, between A and B is given by:

$$\Delta\Phi_{BA} = \varphi_B - \varphi_A \tag{2.25}$$

where φ_B and φ_A are the electrostatic potentials at points B and A, respectively. The potential difference, $\Delta\Phi$, has the units of joules per coulomb, or volts.

Unit test charge
(small enough not to perturb
electrical field)

B   A
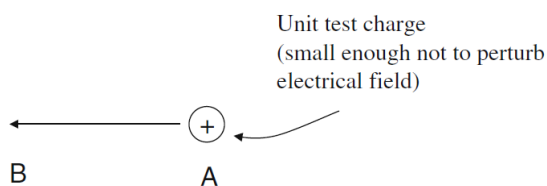
Figure 2.11: A positive unit test charge and the definition of a potential difference. [McCafferty, 2010]

A typical potential difference across the Helmholtz plane is of the order of 1 V. The thickness of the Helmholtz layer is about 10 Å (1 Å = 10^{-8} cm). This amounts to a field strength of 1×10^7 V/cm. This is a very high field strength and is, of course, the consequence of having a localized charge confined within the narrow region of the interface.

The significance of the electrical double layer (edl) to corrosion is that the edl is the origin of the potential difference across an interface and accordingly of the electrode potential. Changes in the electrode potential can produce changes in the rate of anodic (or cathodic) processes, as it will be seen in paragraph 2.5. Emerging (corroding) metal cations must pass across the edl outward into solution, and solution species (e.g., anions) which participate in the corrosion process must enter the edl from solution in order to attack the metal.

Thus, the properties of the edl control the corrosion process. The edl on a corroding metal can be modeled by a **capacitance** in parallel with a **resistance**, as shown in Figure 2.12. In this simple equivalent circuit, the **double layer capacitance C_{dl}** ensues because the edl at a metal surface is similar to a parallel plate capacitor. The **Faradaic resistance R_P** in parallel with this capacitance represents the resistance to charge transfer across the edl. The quantity R_P is inversely proportional to the specific rate constant for the half-cell reaction. The term **R_S** is the ohmic **resistance of the solution**.

Metal   Solution
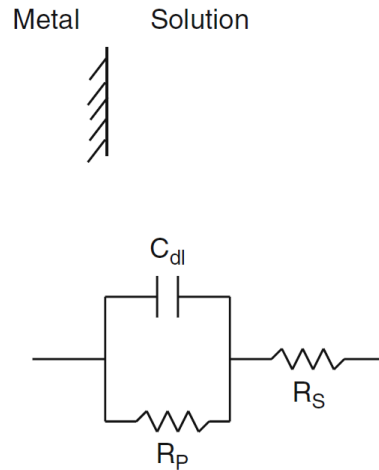
Figure 2.12: Simple equivalent circuit model of the electrical double layer. C_{dl} is the double layer capacitance, R_P is the resistance to charge transfer across the edl, and R_S is the ohmic resistance of the solution. [McCafferty, 2010]

2.4.6. Electrode Potential

2.4.6.1. The Potential Difference Across a Metal/Solution Interface

The idea of conceptually moving a test positive unit charge across the metal/solution interface is not of much practical help to us in the laboratory. We quickly realize that in order to measure the potential difference across the metal/solution interface of interest, we must create additional interfaces [Bockris and Reddy, 1998]. These new interfaces are necessary in order to connect the metal/solution interface of interest to the potential-measuring device so as to complete the electrical circuit.

In this regard, the metal of interest, *M*, connects (through a metal wire) to a second metal which is called **reference electrode**, *ref*, and forms a second metal/solution interface. A potential-measuring device is inserted in between. Through the solution, *S*, the electrical path is closed. It is demonstrated by Kirchhoff's second law (*the directed sum of the potential differences (voltages) around any closed loop is zero*) and by the fact that there is no net charge in the interior of solution, that the potential difference between the the M/S interface and the ref/S interface equals to:

$$V = \Delta\Phi_{M/S} - \Delta\Phi_{ref/S} \qquad (2.26)$$

2.4.6.2. Relative Electrode Potentials

The potential difference across a metal/solution interface is commonly referred to as an **electrode potential**. Equation (2.26) clearly shows that it is impossible to measure the

absolute electrode potential, but instead we measure the relative electrode potential in terms of a second interface, which is a standard reference electrode.

The hydrogen electrode is universally accepted as the primary standard (Standard Hydrogen Electrode - **SHE**) against which all electrode potentials are compared, for the reversible half-cell reaction:

$$2H^+_{(aq)} + 2e^- \rightleftharpoons H_{2(g)} \tag{2.27}$$

In the special case:

$$2H^+_{(aq,\ \alpha=1)} + 2e^- \rightleftharpoons H_{2(g,\ P=1atm)} \tag{2.28}$$
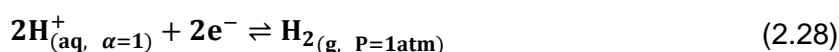
where α is the ion activity and P is the gas pressure, the half-cell potential is arbitrarily defined as **E⁰ = 0.000 V**. The subscript means that all species are in their standard states, which is unit activity for ions and 1 atm pressure for gases. For dilute solutions or solutions of moderate concentration (approximately 1 M or less), the activity can be approximated by the concentration of the solution.

As a result, in equation (2.26) $\Delta\Phi_{ref/S}$ is defined to be zero for a standard hydrogen electrode which satisfies the conditions in equation (2.27). Thus, by measuring electrode potentials relative to the standard hydrogen electrode, a series of standard electrode potentials can be developed for metals immersed in their own ions at unit activity.

An ordered listing of the standard half-cell potentials is called the electromotive force (emf) series. According to the Stockholm Convention of 1953, all of the half-cell reactions are written from left to right as reduction reactions. Metals located near the positive end of the emf series are more chemically stable than metals located near the bottom and they are referred to as "noble" metals (oxidation reaction is not favored), while metals near the negative end of the emf scale are called "active" metals (oxidation reaction is favored) [Vanysek, 2001].

According to SHE, some of the most typical reactions are:

$$Cu^+ + e^- \rightarrow Cu \qquad E° = \quad +0.342$$

$$2H^+ + 2e^- \rightarrow H_2 \qquad E° = \quad 0.000$$

$$Fe^{2+} + 2e^- \rightarrow Fe \qquad E° = \quad -0.447$$

$$Zn^{2+} + 2e^- \rightarrow Zn \qquad E° = \quad -0.762$$

$$Mg^{2+} + 2e^- \rightarrow Mg \qquad E° = \quad -2.372$$

Noble ↑

Active ↓

The electrode potential for a half-cell reaction for a metal immersed in a solution of its ions at some concentration other than unit activity is related to its SHE (at unit activity) by the Nernst Equation (2.24).

Although the standard hydrogen electrode is the reference electrode against which electrode potentials are defined; this reference electrode is not commonly used in the laboratory. The hydrogen electrode is inconvenient to use as it requires a constant external source of hydrogen gas. Instead of using the standard hydrogen electrode, other reference electrodes are commonly used in the laboratory. The **Saturated Calomel Electrode** (**SCE**) has long been used, especially in chloride solutions. Its construction is shown in Figure 2.13, and its half-cell reaction is:

$$\mathbf{Hg_2Cl_{2\,(s)} + 2e^- \rightleftharpoons 2Hg_{(s)} + 2Cl^-_{(aq,\ saturated)}} \tag{2.29}$$
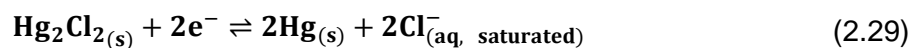
The electrode potential under these conditions at 25°C is **E = + 0.242 V**.
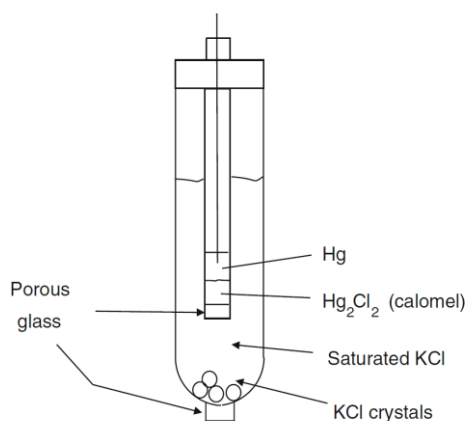
Figure 2.13: A saturated calomel reference electrode. [McCafferty, 2010]

2.5. Kinetics of Corrosion

As seen in the previous paragraph, thermodynamics are useful first to the corrosion behavior of many different systems. However, they do not give any information as to corrosion rates. Although a given reaction may be spontaneous, it does not necessarily proceed at a fast rate. The reaction may in fact proceed "slowly" rather than "quickly", but we cannot determine this difference from thermodynamics alone. [Jones, 1995]

This chapter deals with the rates of corrosion reactions. The corrosion rate of a given metal or alloy in its environment is a crucial factor in determining the lifetime of a material.

2.5.1. Faraday's Law

Corrosion rate does not depend on the difference of potential between anode and cathode, but mainly on the corrosion current. Electrochemical reactions either produce or consume electrons. Thus, the rate of electron flow, to or from a reacting interface, is a measure of reaction rate. Electron flow is conveniently measured as current, I, in Amperes, where 1 Ampere is equal to 1 Coulomb of charge (6.2×10^{18} electrons) per second.

As stated earlier, the process of corrosion involves simultaneous charge transfer and mass transfer across the metal/solution interface. The proportionality between mass loss m, in grams, and current I, in an anodic reaction, as in equation (2.9a), is given by **Faraday's Law**:

$$m = \frac{I \cdot t \cdot \alpha}{n \cdot F} \qquad (2.30)$$

where:

- ➢ I : the corrosion current
- ➢ t : the time,
- ➢ α : the atomic weight of the anode metal,
- ➢ n : the number of electrons exchanged of the anode metal and
- ➢ F : the Faraday's constant (96485.33289 Coulomb/mol, corresponds to the charge carried by one mole of electrons)

Dividing equation (2.30) through by time t and the anode's surface area A, yields the **corrosion rate** r:

$$r = \frac{m}{t \cdot A} = \frac{i \cdot \alpha}{n \cdot F} \qquad (2.31)$$

where i, defined as current density, equals to:

$$i = \frac{I}{A} \qquad (2.32)$$

Equation (2.31) shows a proportionality between mass loss per unit area per unit time (e.g., mg/dm^2/day) and current density (e.g., µA/cm^2). Current density rather than current is proportional to corrosion rate because the same current concentrated into a smaller surface area results in a larger corrosion rate. Corrosion rate is inversely proportional to area for the same dissolving current [Pantelis and Tsiourva, 2012].

Current density can be routinely measured to values as low as 10^{-9} A/cm^2 up to several A/cm^2. Thus, electrochemical measurements are very sensitive and convenient tools fir the study of corrosion in the laboratory and the field.

Units of penetration per unit time results from dividing equation (2.31) by the density, D, of the alloy. For corrosion rate in mils (0.001 in.) per year, mpy, equation (2.31) becomes [Jones, 1995]:

$$\mathbf{r} = \mathbf{0.129} \frac{\boldsymbol{\alpha} \cdot \mathbf{i}}{\mathbf{n} \cdot \mathbf{D}} \tag{2.33}$$

for units of i, µA/cm^2, and D, g/cm^3. The proportionality constant, 0.129, becomes 0.00327 and 3.27 for mm/yr and µM/υρ, respectively. A list of penetration rates equivalent to 1µA/cm2 appears in Figure 2.14:

Relative corrosion resistance	Corrosion rate (mils per year, mpy)	Corresponding corrosion current density from Faraday's law (in µA/cm^2)		
		Aluminum[a]	Iron[b]	Lead[c]
Outstanding	< 1	2.3	2.2	0.85
Excellent	1–5	2.3–12	2.2–11	0.8–4.3
Good	5–20	12–47	11–43	4.2–17
Fair	20–50	47–180	43–109	17–42
Poor	50–200	180–470	109–430	42–170
Unacceptable	> 200	> 470	> 430	> 170

[a]$Al \rightarrow Al^{3+} + 3e^-$
[b]$Fe \rightarrow Fe^{2+} + 2e^-$
[c]$Pb \rightarrow Pb^{2+} + 2e^-$

Figure 2.14: Relative severity of corrosion rates. [McCafferty, 2010]

Calculation of relation between penetration rate and current density for an alloy requires a determination of the equivalent weight, a/n, in equations (2.31) and (2.33) for the alloy. This alloy equivalent weight is a weight average of a/n for the major alloying elements in any given alloy. The recommended procedure for calculation of equivalent weight sums the fractional number of equivalents of alloying elements to determine the total **number of equivalents**, $\mathbf{N_{EQ}}$, which result from dissolving unit mass of the alloy. That is [Jones, 1995]:

$$\mathbf{N_{EQ}} = \sum \left(\frac{\mathbf{f_i}}{\boldsymbol{\alpha_i}/\mathbf{n_i}} \right) = \sum \left(\frac{\mathbf{f_i} \cdot \mathbf{n_i}}{\boldsymbol{\alpha_i}} \right) \tag{2.34}$$

where f_i, n_i and α_i are the mass fraction, the electrons exchanged and the atomic weight, respectively, of the ith alloying element (all minor elements below 1% are neglected). **Equivalent Weight**, **EW**, is then the reciprocal of N_{EQ}:

$$\mathbf{EW} = \mathbf{N_{EQ}}^{-1} \tag{2.35}$$

2.5.2. Units and Methods of Determining Corrosion Rate

Various units have been used to express corrosion rates. These include weight loss per unit area per unit time (e.g. g/cm^2 h), penetration rates (e.g. mpy), and electrochemical rates (e.g. $\mu A/cm^2$). There is no standard unit to express corrosion rates, and many different units have been used.

Corrosion rates for metals undergoing uniform corrosion can be determined by any of the following methods:

a. **Weight loss**, where previously weighed metal samples are exposed to corrosive environment, and when removed, any solid corrosion products must be detached from the metal surface and the loss in weight due to metallic corrosion is determined.
b. **Weight gain**, which is more suited to dry oxidation, where oxide films or products are more adherent and have the useful feature that the gain in weight can be measured continuously and without removal of the specimen from its environment.
c. **Chemical analysis of solution** as a function of time allows determination of the corrosion rate, due to the increase of the concentration in metal's dissolved cations.
d. **Gasometric techniques**, when one of the reaction products is a gas, such as the determination of volume of hydrogen release during the redox reaction.
e. **Thickness measurements** of a metal, as a function of time, is used to survey the practical corrosion behavior of a system in service, rather than as a laboratory technique. Thickness measurements are based on the response of a specimen to an ultrasonic or a magnetic signal.
f. **Electrical resistance probes**, where the increase in the electrical resistance, as a test metallic film or wire is thinned due to corrosion is measured.
g. **Inert marker method**, where an inert marker, such as ion-implanted Xe, is used in conjunction with the surface analysis technique of Rutherford backscattering (RBS).
h. **Electrochemical techniques**, some of which were used in our laboratory for this thesis and will be described in detail in the next chapter.

Each of the methods described above has an application in either the laboratory or the field. Concerning this methods only electrochemical techniques can provide insights into the underlying mechanism of corrosion and, in addition, offer the possibility of mitigating corrosion by controlling the electrode potential.

2.5.3. Electrochemical Polarization

Polarization, η, is the potential change, $E - e$, from the equilibrium half-cell electrode potential, e, caused by a net surface reaction rate for the half-cell reaction. For cathodic polarization, η_c, electrons are supplied to the surface, and a buildup in the metal due to the slow reaction rate causes the surface potential, E, to become negative to e. Hence, η_c is negative by definition. For the anodic polarization, electrons are removed from the metal, a deficiency results in a positive potential change due to the slow liberation of electrons by the surface reaction, and ηa must be positive. Polarization is classified into two types – activation and concentration; both are discussed in the sections that follow [Pantelis and Tsiourva, 2012].

2.5.3.1. Activation Polarization

When some step in the half-cell reaction controls the rate of charge (electron) flow, the reaction is said to be under activation or charge-transfer control, and activation polarization results. Hydrogen evolution by

$$2H^+ + 2e^- \rightarrow H_2 \qquad (2.36)$$

at a metal surface occurs, for example, in three major steps. First, H⁺ reacts with an electron from the metal,

$$H^+ + e^- \rightarrow H_{ads} \qquad (2.37)$$

to form an adsorbed hydrogen atom, H_{ads}, at the surface. Two of these adsorbed atoms must react in the second step to form the hydrogen molecule,

$$H_{ads} + H_{ads} \rightarrow H_2 \; . \qquad (2.38)$$

A third step requires sufficient molecules to combine and nucleate a hydrogen bubble on the surface. Any one of the steps can control the rate of reaction (2.36) and cause activation polarization.

The relation between activation polarization or overpotential, $\boldsymbol{\eta}$, and the rate of the reaction represented by current density, $\mathbf{i_\alpha}$ or $\mathbf{i_c}$, is:

$$\boldsymbol{\eta_\alpha} = \boldsymbol{\beta_\alpha} \cdot \log \frac{\mathbf{i_\alpha}}{\mathbf{i_0}} \qquad (2.39a)$$

for anodic polarization, and

$$\boldsymbol{\eta_c} = \boldsymbol{\beta_c} \cdot \log \frac{\mathbf{i_c}}{\mathbf{i_0}} \qquad (2.39b)$$

for cathodic polarization, where i_0 is the **exchange current density** (in A/cm^2), which is the rate of oxidation and reduction reactions at the electrode equilibrium state, expressed as current density. The equations (2.39) are called **Tafel equations** and the parameters $\boldsymbol{\beta_\alpha}$ and $\boldsymbol{\beta_c}$ are known as **the Tafel constants** for the half-call reaction.

For anodic overpotential, η_α is positive, and β_α must be positive, as a consequence. Similarly, for cathodic polarization, β_c is negative because η_c is negative. The anodic, i_α, and the cathodic, i_c, current densities flow in opposite directions. The Tafel relationship described by equations (2.39) have universally been observed by experiment for activation polarization.

Inspection of Tafel equations indicates that a plot of overpotential, η_{act}, versus $\log i$ is linear for both anodic and cathodic polarization, as shown in Figure 2.15. The slopes are given by the Tafel constants, which are assumed as ±0.1V per decade of current. For $\eta = 0$, either of equations (2.39) reduces to $i = i_0$. Below the reversible half-cell electrode potential (intersection of the two lines) the reduction of H$^+$ is favored, while above the same potential, the oxidation of H$_2$ is favored.
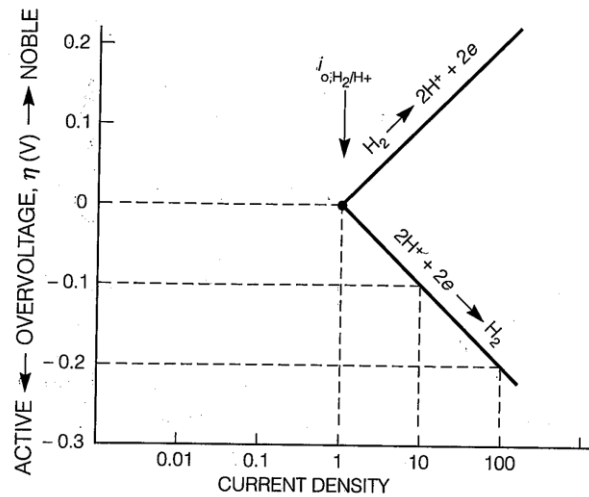
Figure 2.15: Activation overpotential showing Tafel behavior. [Fontana, 1986]

At the value of the equilibrium potential, the rate of oxidation is equal to the rate of reduction (intersection point). From Figure 2.15 it can be seen that the reaction rate (i_a or i_c) increases by one order of magnitude for overpotential change of + 0.1V for anodic polarization and -0.1V for cathodic polarization, respectively. Therefore, the reaction rate of an electrochemical reaction is very sensitive even to small changes in potential. The absolute values of β Tafel constants usually range from 0.03 to0.2V and may not be equal for anodic and cathodic reactions. However, +0.01 and -0.01V are reasonable estimates for $\boldsymbol{\beta_\alpha}$ and $\boldsymbol{\beta_c}$, respectively, for many purposes [Jones, 1995].

2.5.3.2. Concentration Polarization

At high rates, cathodic reduction reactions deplete the adjacent solution of the dissolved species being reduced. The concentration profile of H$^+$, for example, is shown schematically in Figure 2.16. C_B is the H$^+$ concentration profile of the uniform bulk solution, and δ is the thickness of the concentration gradient in solution. The half-call electrode potential e_{H^+/H_2} of

the depleted surface is given by the Nernst equation (2.24) as a function of H⁺ concentration or activity (H⁺):

$$e_{H^+/H_2} = e^o_{H^+/H_2} + \frac{2.3\,R\,T}{n\,F} \cdot \log \frac{(H^+)^2}{P_{H_2}} \tag{2.40}$$
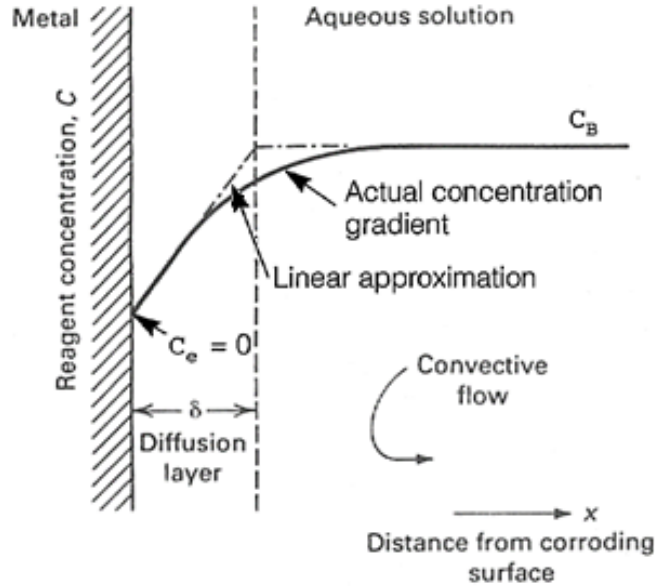
Figure 2.16: Concentration of H⁺ in solution near a surface controlled by concentration polarization.

It is apparent that the half-cell electrode potential, e, decreases as (H^+) is depleted at the surface. This decrease (potential change) is concentration polarization, η_{conc}, which is given as a function of current density by:

$$\eta_{conc} = \frac{2.3\,R\,T}{n\,F}\,\log\left[1 - \frac{i_c}{i_L}\right] \tag{2.41}$$

A plot of this equation in Figure 2.17a shows that η_{conc} is low until a limiting current density, i_L, is approached. i_L is the measure of a maximum reaction rate that cannot be exceeded because of a limited diffusion rate of H⁺ in solution.

The limiting current density, i_L, can be calculated from:

$$i_L = \frac{D_z\,n\,F\,C_B}{\delta} \tag{2.42}$$

where D_z is the diffusivity of the reacting species, z (H^+ in this case). Thus, i_L is increased by higher solution concentration, C_B; higher temperature, which increases D_z; and higher solution agitation, which decreases δ; as shown in Figure 2.17b.

For corrosion, concentration polarization is significant primarily for cathodic reduction processes. Concentration polarization for anodic oxidation during corrosion can usually be ignored because unlimited supply of metal atoms is available at the interface. Some concentration polarization of the anodic reaction is possible at very high corrosion rates or during intentional anodic dissolution by impressed currents (e.g. electrochemical machining or electrorefining), when rates are limited by transport of soluble oxidation products away from the surface [Jones, 1995].

(a)   (b)
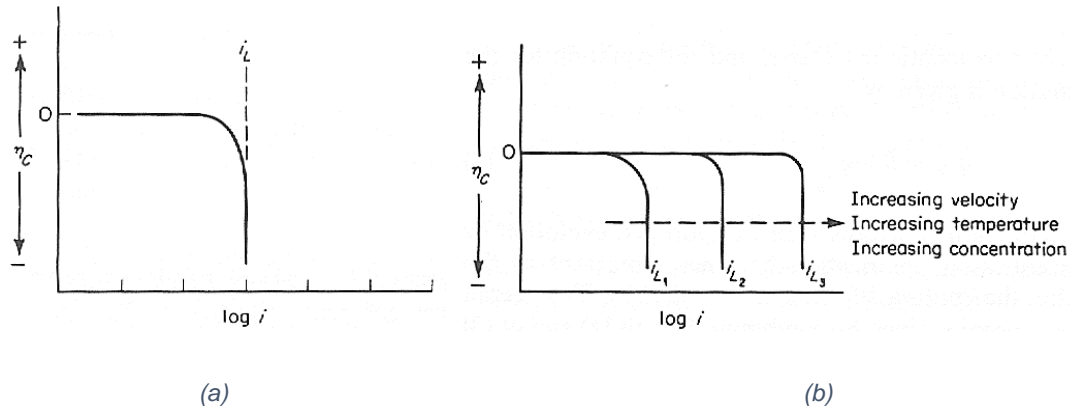
*Figure 2.17: Cathodic concentration polarization: **(a)** plotted versus reaction rate or current density; **(b)** effect of solution conditions.*

2.5.3.3. Combined Polarization

Total cathodic polarization, $\eta_{T,c}$, is the sum of activation and concentration polarization:

$$\eta_{T,c} = \eta_{act,c} + \eta_{conc,c} \tag{2.43}$$

which, from equations (2.39b and 2.41), can be expanded to:

$$\eta_{T,c} = \beta_c \, \log \frac{i_c}{i_0} + \frac{2.3\,R\,T}{n\,F} \, \log \left[1 - \frac{i_c}{i_L} \right] \tag{2.44}$$

Equation (2.44) is schematically shown in Figure 2.18.
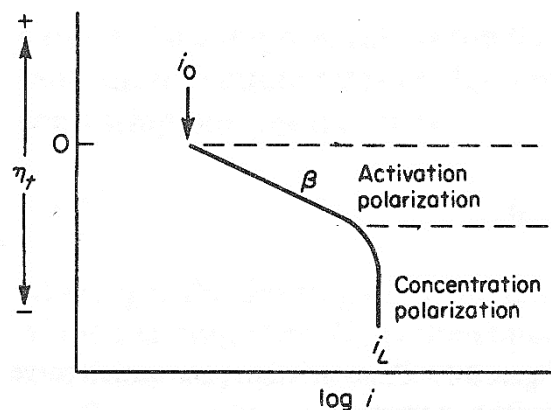
Figure 2.18: Cathodic combined polarization – Activation and concentration polarization.

Because concentration polarization is usually absent for **anodic polarization** of metal dissolution reaction, as mentioned in the previous paragraph, there remains:

$$\eta_{T,\alpha} = \eta_{act,\alpha} = \beta_\alpha \ \log\frac{i_\alpha}{i_0} \tag{2.45}$$

Actually, equation (2.45) is identical to (2.39a). Equations (2.44) and (2.45) are the fundamental equations for all electrochemical reactions [Pantelis and Tsiourva, 2012].

2.5.4. Mixed Potential Theory

The first comprehensive presentation of this theory was made by Wagner and Traud in 1938. The theory of mixed potential is based on two simple assumptions:

- Each electrochemical reaction can be divided into two or more sub-oxidation and reduction reactions.
- During an electrochemical reaction there can be no net charge accumulation.

The first assumption is obvious. It can be shown, experimentally, that electrochemical reactions consist of two or more individual oxidation and reduction reactions. The second assumption is an expression of the principle of conservation of charge, which means that a metal immersed in an electrolyte cannot spontaneously gain an electric charge. From the latter it follows that when corroding an electrically insulated metal specimen, the total rate of oxidation is equal to the total rate of reduction.

The theory of mixed potential, together with the kinetic equations mentioned above, form the basis of the modern kinetic theory of electrochemical reactions [Pantelis and Tsiourva, 2012].

58

The mixed potential theory can be applied in metal corroding in an acid solution. For example, when zinc is corroding in an acid solution, both the anodic,

$$\mathbf{Zn^{2+} + 2e^- \rightarrow Zn} \tag{2.46}$$

and cathodic,

$$\mathbf{2H^+ + 2e^- \rightarrow H_2} \tag{2.47}$$

half-cell reactions occur simultaneously on the surface. Each has its own half-call electrode potential and exchange current density, as shown in Figure 2.19. However, the two half-cell electrode potentials $e_{\mathbf{Zn/Zn^{2+}}}$ and $e_{\mathbf{H^+/H_2}}$ cannot coexist separately on an electrically conductive surface. Each must polarize or change potential to a common intermediate value, E_{corr}, which is called **corrosion potential.** E_{corr} is referred to as a **mixed potential** since it is a combination or mixture of the half-cell electrode potentials for reactions (2.46) and (2.47). Hydrogen is sometimes referred to as an **oxidizer** because it serves to "oxidize" the metal to dissolved cations by its reduction in the cathodic reaction (2.47).
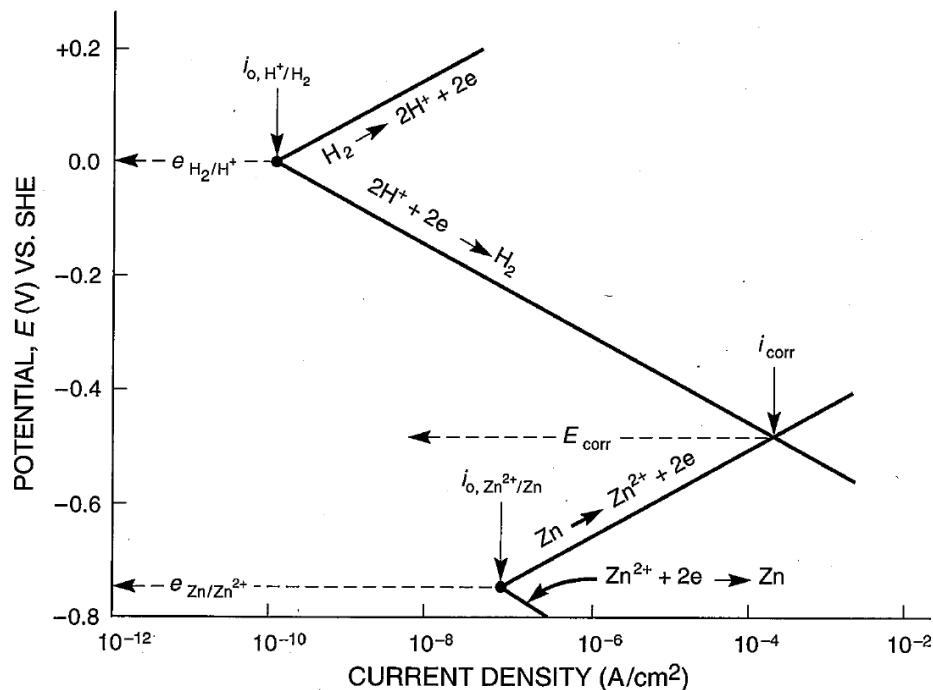
Figure 2.19: Polarization of anodic half-call reactions for zinc in acid solution to give a mixed potential, E_{corr}, and a corrosion rate (current density), i_{corr}. [Fontana, 1986]

As reaction (2.46) and (2.47) polarize on the same surface, the half-cell electrode potentials change respectively, according to:

$$\eta_\alpha = \beta_\alpha \, \log \frac{i_\alpha}{i_0} \tag{2.39a}$$

and

$$\eta_c = \beta_c \, \log \frac{i_c}{i_0} \tag{2.39b}$$

until they become equal at E_{corr}, as shown in Figure 2.19. Equation (2.39b) is identical to equation (2.44), assuming for the moment that concentration polarization is absent. The relationships (2.39a) and (2.39b) for the activation polarization of reactions (2.46) and (2.47) are linear on the semilog plot. Uniform average values of β_α and β_c are estimated at ±0.1V in this case. At E_{corr} the rates of the anodic (2.46) and the cathodic (2.47) reactions are equal. As indicated in Figure 2.19, at E_{corr}, the rate of anodic dissolution, i_α, is identical to the corrosion rate, i_{corr}, in terms of current density, and

$$i_c = i_\alpha = i_{corr} \tag{2.48}$$

Up to this point, **concentration polarization** was assumed **absent** in the preceding example. This is equivalent to assuming that the limiting diffusion current for the cathodic reduction process is substantially higher than the graphically derived corrosion current density. The assumption is invalid in many real situations, especially when **the concentration of the oxidizer is relatively low**, as shown by a decrease in C_B in equation (2.42) [Jones, 1995].
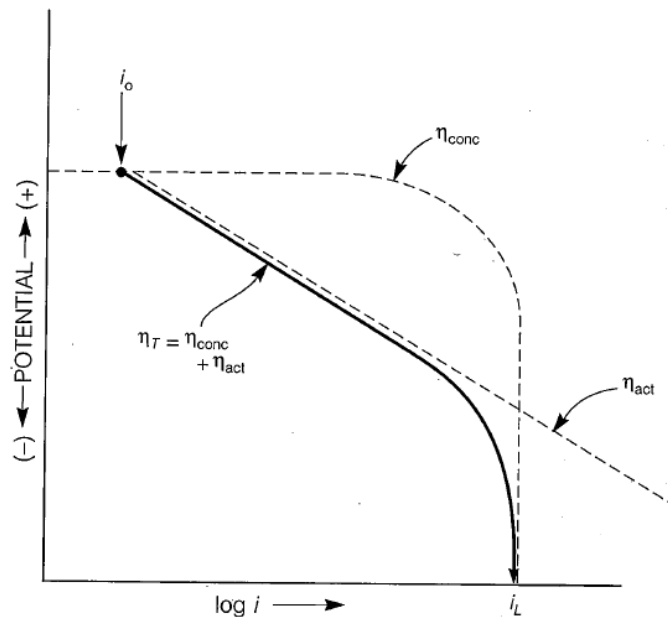
Figure 2.20: Combined polarization: sum of activation, n_{act}, and concentration, n_{conc}, polarization. [Jones, 1995]

Figure 2.20 shows a plot of equation (2.43 or 2.44), which is the sum of activation and concentration polarization contributions in the total cathodic polarization. When the reduction current density approaches i_L, **concentration polarization** takes over from activation polarization, and the corrosion rate becomes limited by the **diffusion of the oxidizer** from the bulk solution. At low cathodic polarization the reduction process is activation controlled, but at high polarization it is diffusion or concentration controlled.

A common example of corrosion controlled by concentration polarization is iron or steel in dilute aerated salt solution (e.g., seawater). The cathodic process is reduction of dissolved oxygen, according to

$$O_2 + 2H_2O + 4e^- \rightarrow 4OH^- \tag{2.49}$$

The maximum solubility of dissolved oxygen in water is relatively low, about 8 ppm at ambient temperature. In quiescent conditions, corrosion is controlled by **diffusion of dissolved oxygen to the steel surface**. However, if the solution is stirred, increasing i_L, a crossover is possible, as shown in Figure 2.21a, when i_L becomes greater than the anodic oxidation rate or current density, i_a. Corrosion rate, i_{corr}, increases with stirring (Figure 2.21b) but levels off and becomes independent of stirring rate, when $i_L > i_a$, and the reduction reaction becomes activation controlled.

(a)   (b)
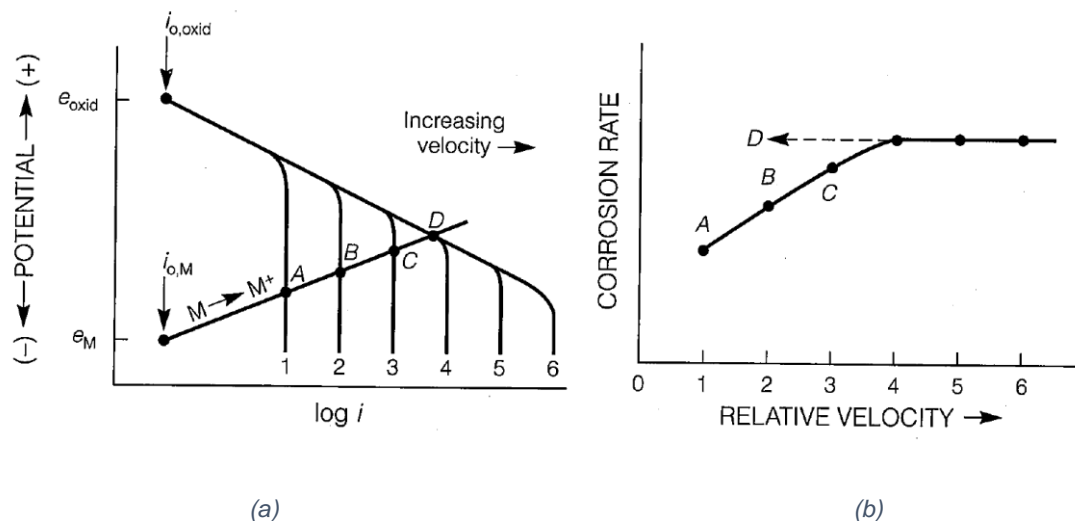
Figure 2.21: Effect of stirring during combined polarization: (a) on i_L, (b) on i_{corr}. [Jones, 1995]

Mixed potential theory was derived originally to explain experimental electrochemical laboratory measurements [Wanger and Traud, 1938]. However, the theory was presented ahead of the experimental principles which are given in the next chapter.

References – Chapter 2

[1] **Bagotsky V. S.** (2006), <u>Fundamentals of Electrochemistry</u>, 2nd ed., Wiley-Interscience, New Jersey & Canada.

[2] **Bockris J. O'M. & Reddy A. K. N.** (1977), <u>Modern Electrochemistry - Vol. 2</u>, Plenum Press, New York.

[3] **Bockris J. O'M. & Reddy A. K. N.** (1998), <u>Modern Electrochemistry – Vol.1</u>, 2nd ed., Plenum Press, New York (1st ed. 1977).

[4] **Bockris J. O'M., Devanathan M. A. V., & Müller K**. (1963), <u>Proceedings of the Royal Society, 274, 55</u>, London.

[5] **Fontana** M. G., (1986), <u>Corrosion Engineering</u>, 3rd ed., McGraw-Hill International.

[6] **Jones A. D.** (1995), <u>Principles and Prevention of Corrosion</u>, 2nd ed., Prentice Hall Publishing, University of Nevada, Reno, Nevada.

[7] **Karantonis A.**, (2015), <u>Basic Principles of Electrochemistry</u>, (in Greek:Βασικές Αρχές Ηλεκτροχημείας, Ελληνικά Ακαδημαϊκά Ηλεκτρονικά Συγγράμματα και Βοηθήματα), Athens.

[8] **Karantonis A.**, (2020), Electrochemical Principles of Corrosion of Metals, (in Greek: Ηλεκτροχημικές Αρχές της Διάβρωσης των Μετάλλων), NTUA, Athens.

[9] **McCafferty E.,** (2010), <u>Introduction to Corrosion Science</u>, Springer, Washington, DC.

[10] **Pantelis D.I., Chrysoulakis G.**, (2008), <u>Materials Science and Technology</u>, (in Greek: Επιστήμη και Τεχνολογία των Μεταλλικών Υλικών), Second Edition, Papasotiriou, Athens.

[11] **Pantelis D.I., Tsiourva D.E.**, (2012), <u>Corrosion and Protection of Shipbuilding and Mechanical Constructions</u>, (in Greek: <u>Διάβρωση Και Προστασία Ναυπηγικών Κατασκευών</u>), School of Naval Architecture and Marine Engineering, National Technical University of Athens.

[12] **Skoulikidis T. & Vasiliou P**., (2007), <u>Corrosion and Protection of Materials</u> (in greek: Διάβρωση και Προστασία Υλικών), Symeon, Athens.

[13] **Toshiaki O., Atsushi N., Masatoshi S., Koji F.,** (2018)**,** <u>Electrochemistry for Corrosion Fundamentals</u>, Springer, Singapore.

[14] **Traka K.** (2015), <u>Numerical Simulation of Electrochemical Behavior for Naval Steel Microstructure via Tafel Curves Extrapolation Method</u>, Diploma Thesis for the degree of Naval Architecture and Marine Engineering, National Technical University of Athens.

[15] **Vanysek P.** (2001), <u>CRC Handbook of Chemistry and Physics</u>, 82nd ed, D. R. Lide, Ed., CRC Press, Boca Raton, Florida.

[16] **Wanger C. & Traud W.**, (1938), <u>Concerning the Evaluation of Corrosion Reactions by Superposition of Electrochemical Partial Reactions and Concerning the Potential Formation on Mixed Electrodes</u>, Z. Electrochem., Vol. 44.

Principles of Electrochemical Techniques

Introduction

Electrochemical techniques serve as the most important tools for the determination of the corrosion behavior of the materials. Electrochemical signal relates to behavior in potential, current and electrical charge of a corroding electrode based on the electrochemical nature of the corrosion phenomenon. They can provide valuable results for the polarization resistance and corrosion rate, as well as for the corrosion mechanism that takes place. In corrosion engineering, they are used alone or in combination with accelerated corrosion techniques to determine the corrosion behavior of metallic materials.

In the present thesis five (5) electrochemical techniques were employed, for the configuration of the behavior of each steel sample under corrosive environment. These techniques are:

- **Open Circuit** (OC) **Potential**, which does not apply any voltage or current and simply measures the voltage difference between the Working electrode and the Reference electrode.

- **Linear Polarization Resistance** (LPR), which uses a single voltage scan in a range near the corrosion potential and provides the capability to calculate corrosion rate.

- **Potentiodynamic Polarization** (PP) with **Tafel Extrapolation** technique, which uses a single voltage scan in a range of potential around corrosion potential but greater than the LPR method and takes into account the linear segments of the anodic and cathodic branches of polarization, whose figures reveal the mechanism of corrosion of the employing system.

- **Electrochemical Impedance Spectroscopy** (EIS), measures impedance (Z) by applying a sinusoidal (ac) voltage across a cell and measuring the resulting ac current along with phase shifts between the ac voltage and ac current.

- **Cyclic Polarization** (CP), which utilizes a two-step voltage scan and is used to determine the tendency of a material to undergo surface pitting or crevice corrosion.

In Figure 4.23 these techniques are presented schematically along with some basic information of each one.
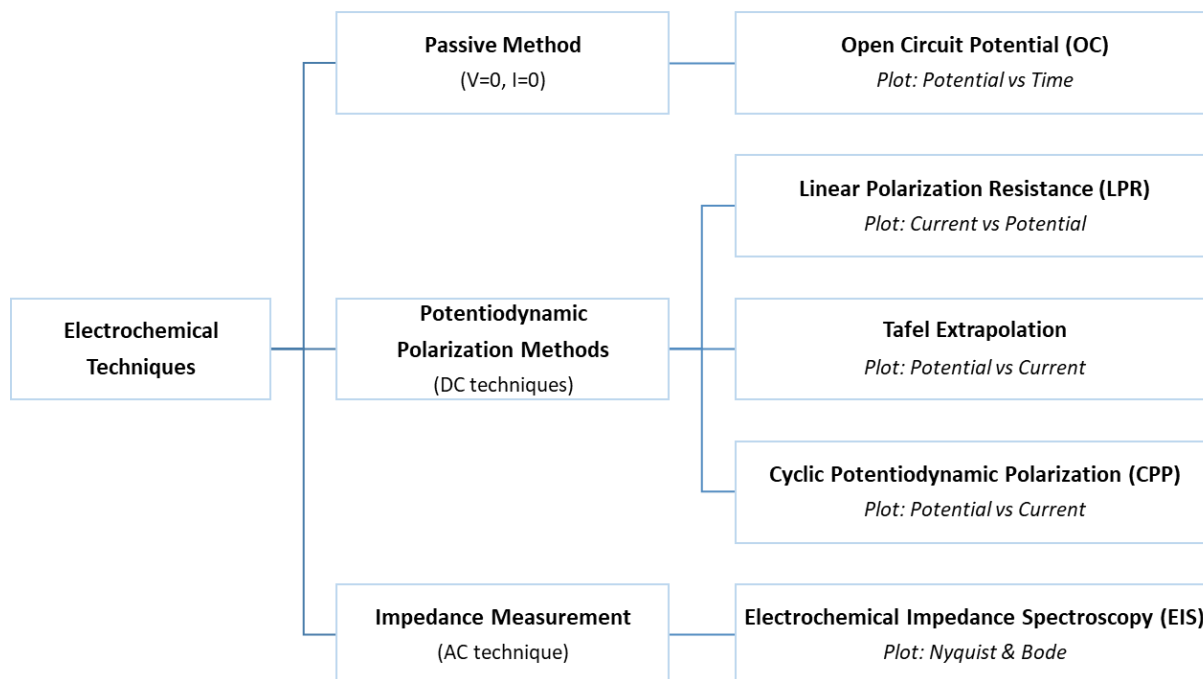
Figure 3.1: Categories of electrochemical techniques employed in the present thesis. The plot which depicts the results of each technique is also mentioned.

These electrochemical methods offer important advantages in the determination of the corrosion rate:

- Corrosion rates can be determined in a very short time, only a few minutes, whereas conventional methods, such as weight loss measurements, need several days or even more to produce results.

- These methods are sensitive and accelerating factors, e.g. elevated temperature, are not required in order to increase the rate of the reaction in the laboratory.

- Electrochemical Impedance Spectroscopy and Linear Polarization can be used repeatedly to measure consecutive corrosion rates on the same electrode, since this is a non-destructive method.

3.1. Open Circuit Potential

Open Circuit Potential (OCP or OC) is a passive method also known as open circuit voltage, zero-current potential, corrosion potential, equilibrium potential, or rest potential. Except of **stand-alone experiments**, it is often used to find the **resting potential of a system**, from which other experiments are based. In select experiments, such as impedance spectroscopy (EIS) or Linear Polarization Resistance (LPR), potential is set vs. OC instead of vs. reference.

Open Circuit Potential (OCP) is a passive experiment. By passive, the counter electrode (necessary to pass current through the cell) circuitry of the potentiostat is bypassed. In this mode, only the resting potential measured between reference and working electrode is measured. This is not to say that the chemical system is at equilibrium. In fact, some systems may be far from equilibrium and their passive potential changes as a function of homogeneous reactions. What makes OCP unique is that is is a purely electrolytic measurement, thermodynamically.

Researchers might want to know whether or not their electrochemical system is stable. OCP is one method that informs this question. A constant (generally, ±5 mV or less) OCP over long periods of time (minutes) indicates that the system may be stable or at least stable enough, thermodynamically, for a perturbation-based experiment. There is much greater analytical certainty in measurement based on a flat baseline than it is on a sloping baseline, especially if the sloping baseline is not well defined, modeled, or constant [PINEresearch], [Bard and Faulkner, 2001].

While measuring OC potential is a benign task for a potentiostat, it can still be a useful experiment. Since i=0, either by disconnecting the counter electrode or by placing a very high impedance resistor in its path as to prevent current passage, the E_{OC} is simply the potential difference between working and reference electrode, or

$$E_{OC} = E_{WE} - E_{RE} \qquad (3.1)$$

where E_{OC} is the potential measurement, E_{WE} and E_{RE} the potential of the working and the reference electrode, respectively. Therefore, a potentiostat can be used as a simple voltmeter, to measure the potential difference between two points.

The theory of OCP is very simple. There are also common references that describe the method in greater detail. Considering the general electrochemical reaction:

$$O + ne^- \rightleftharpoons R \qquad (3.2)$$

where O (Oxidizer) is reduced to R (Reducer) in an n electron transfer reaction, with formal (thermodynamic) potential E^0, by measuring the Open Circuit Potential, E, we can determine the ratio of O and R by invoking the **Nernst Equation**:

$$E = E^0 + \frac{R\,T}{n\,F} \ln \frac{C_O}{C_R} \tag{3.3}$$

where

- > **R** is the Universal Gas Constant (8.314 J K^{-1} mol^{-1}),
- > **T** is absolute temperature,
- > **n** is the number of electrons,
- > **F** is Faraday's Constant (96,485 C mol^{-1}),
- > **C$_O$** and **C$_R$** are the concentrations of the dissolved molecules or ions in the oxidized and reduced forms, respectively, at the surface of the electrode.

Open Circuit Potential experimental results are depicted in figures of potential (in Voltage) as a function of the elapsed time of the experiment (in second). An indicative plot of experimental results employing the Open Circuit Polarization method in two different samples of steels is shown in Figure 3.2 below, where it becomes apparent that after a certain period of time, the potential acquires an almost constant value which is the equilibrium potential for each electrode (metal).
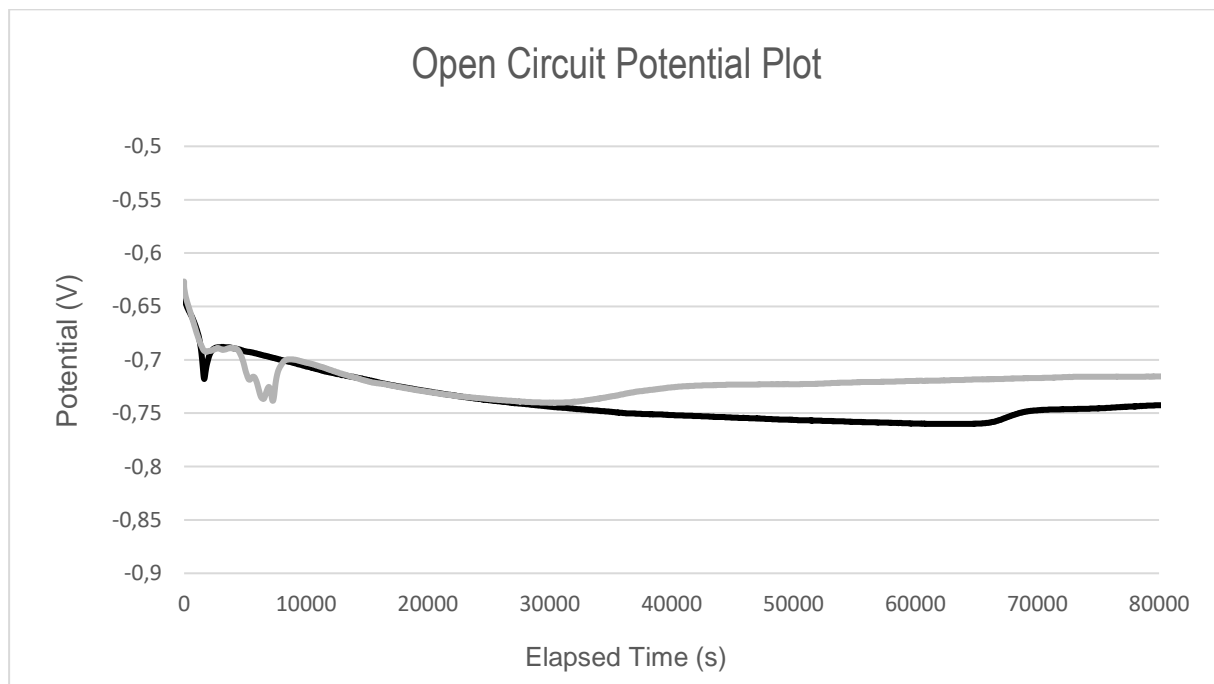
Figure 3.2: Indicative plot of Open Circuit Polarization method employed on two different metals for 24 hours.

3.2. Linear Polarization Resistance method

Linear Polarization Resistance (LPR) method is an electrochemical technique which offers rapid corrosion rate measurements, mainly employed in industrial monitoring corrosion operations. It can be used to characterize a material by scanning the current density – potential (i – E) domain [Berradja, 2019]. Researchers have observed that there is a linearity at the origin of the polarization curve, as shown in Figure 3.3, for polarization up to a few millivolts. The **slope** of this linear curve is **inversely proportional to the corrosion rate (CR)** and is called **polarization resistance R_P,**

$$\frac{di}{dE} = R_P \propto \frac{1}{CR} \tag{3.4}$$
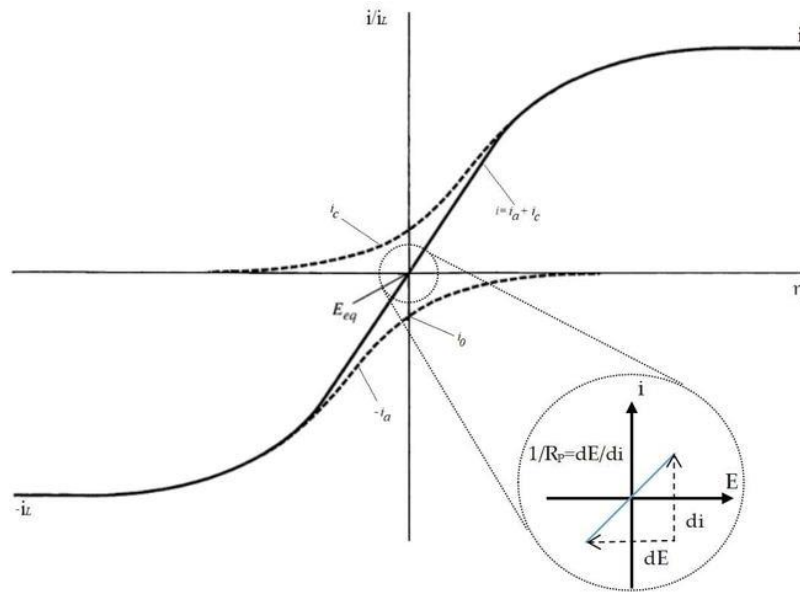
Figure 3.3: Current density (i) – overpotential (η) curves for the system where α = 0.5 and $i_{L,a} = -i_{L,c} = i_L$. Partial current densities: ia, ic (dashed line), i_L limit current density (horizontal line), and R_P the polarization resistance (enlarged area). [Berradja, 2019]

For a system in which electrode processes involve a slow reaction step at the electrode surface, the rate of reaction is limited by activation polarization (electrochemically explained in paragraph 2.5.3.1.). The relationship between the reaction rate, or net current density **i**, and the driving force for the reaction, or potential **E**, is given by the **Butler-Volmer equation**, which relates i, for a single electrode process, such as the oxidation of a metal,

$$M \rightarrow M^{n+} + ne^- \tag{3.5}$$

to E by the formula [Karantonis, 2020]:

$$i = i^0 \left[e^{\frac{\alpha n F}{R T}(E-E_{eq})} - e^{-\frac{(1-\alpha) n F}{R T}(E-E_{eq})} \right] = i^0 \left[e^{\frac{\alpha n F}{R T}\eta_{ct}} - e^{-\frac{(1-\alpha) n F}{R T}\eta_{ct}} \right] \tag{3.6}$$

where

- $\eta_{ct} = E - E_{eq}$: the overpotential, defined as the potential difference (voltage) between the electrode potential, E, and the equilibrium potential, E_{eq},
- i^0: the exchange current density (rate of either the forward or reverse half-cell reaction) at the equilibrium potential E_{eq},
- α: the transfer coefficient (usually close to 0.5, but must be between 0 and 1),
- **n**: the number of electrons transferred,
- **R**: the universal gas constant (8.314 J K^{-1} mol^{-1}),
- **F**: the Faraday constant (96485.33 C·mol^{-1}) and
- **T**: the absolute temperature.

The representation of the Butler-Volmer equation, as shown in Figure 3.3 and Figure 3.4 below, is called the polarization curve. It is worth mentioning that the **Butler-Volmer equation** is valid only when, under certain conditions, the concentrations of the oxidized species, $C_{O(x=0)}$, and the reduced species, $C_{R(x=0)}$, at the electrode's surface are almost equal to those in the bulk of the solution, i.e.

$$C_{O(x=0)} = C_O^*$$
(3.7a)

$$C_{R(x=0)} = C_R^*$$
(3.7b)

Conditions (3.7) apply when the system is under agitation or when the rate of the electrochemical reaction is much slower than the rate of mass transfer from the bulk of the solution to the electrode interface. More clearly, in Figure 3.4, the Butler-Volmer equation is shown (in black line) as a function of potential, E. The Butler-Volmer curve is the algebraic sum of the anodic and the cathodic current. Butler-Volmer equation as a function of the overpotential, η_{ct}, presents identical graph [Karantonis, 2020].
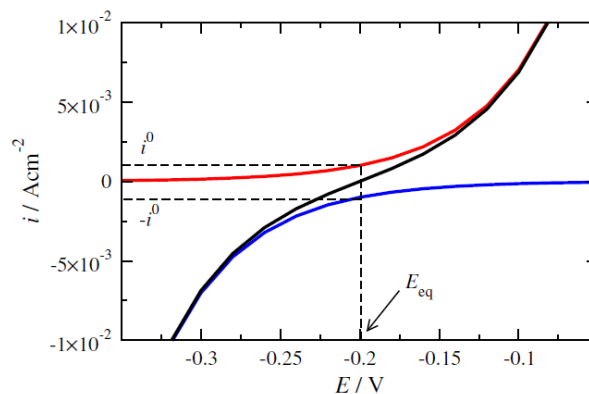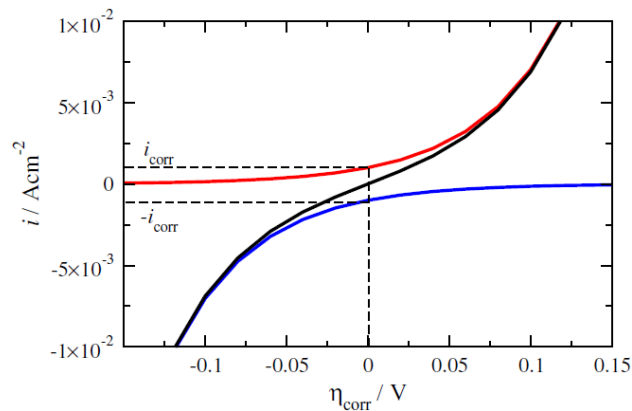

*Figure 3.4: Current density, i, dependence from potential, E, through Butler-Volmer equation (**black curve**). **Red curve** represent the anodic current and **blue curve** the cathodic, for n=1, α=0.5 and $i_0=10^{-3}$ A/cm^2. [Karantonis, 2020]*

The electrochemistry of corroding metals involves two or more half-cell reactions. Suppose there is a simple corrosion system, such as a corroding working metal (M) electrode immersed in a sulfuric acid solution. In addition to reaction (3.5), the following half-cell reaction also occurs:

$$2H^+ + 2e^- \rightarrow H_2 \tag{3.8}$$
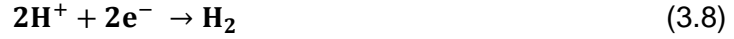
The dissolution of the M takes place in the acid electrolyte. At equilibrium, the total anodic rate is equal to the total cathodic rate. In this case, the net rate of either M dissolution or hydrogen evolution can be measured at the electrode potential of the steady-state freely corroding condition. This potential refers to the **corrosion potential**, **E_{corr}**, which lies between the equilibrium potentials of the two individual half-cell reactions. At E_{corr}, the net rate corresponds to the uniform corrosion rate, i_{corr}, at free corrosion condition. In such a system, the relationship between the overpotential, η_{corr}, and the current, i, flowing between the working electrode and the auxiliary counter electrode, is governed by the fundamental **Butler-Volmer** equation given as follows [Karantonis, 2020]:

$$i = i_{corr}\left[e^{\frac{\alpha_a\, n\, F}{R\, T}\eta_{corr}} - e^{-\frac{\alpha_c\, n\, F}{R\, T}\eta_{corr}}\right] \tag{3.9a}$$

where

> ➢ $\eta_{corr} = E - E_{corr}$: the corrosion overpotential between applied potential, E, minus corrosion potential, E_{corr},
> ➢ i_{corr}: the corrosion current density at the corrosion potential, E_{corr}, and
> ➢ α_a, α_c: the transfer coefficient (close to 0.5) for the anodic and the cathodic reactions, respectively.

Equation (3.9a) can also be written as

$$i = i_{corr}\left[e^{\frac{2.303}{\beta_a}\eta_{corr}} - e^{-\frac{2.303}{\beta_c}\eta_{corr}}\right] = i_{corr}\left[10^{\frac{\eta_{corr}}{\beta_a}} - 10^{-\frac{\eta_{corr}}{\beta_c}}\right] \tag{3.9b}$$

where $\beta_a = \frac{2.303\, R\, T}{\alpha_a\, n\, F}$ and $\beta_c = \frac{2.303\, R\, T}{\alpha_c\, n\, F}$ the Tafel exponents, whose equations are valid only when oxidation and reduction reactions are elementary, while the differ when are multi-stage reactions.

Examining the Butler-Volmer equation (3.6), or even better (3.9a) or (3.9b) for corrosion, some interesting results arise. According to LPR method, when corrosion overpotential, η_{corr}, tends to zero, i.e. **$E \approx E_{corr}$**, then the exponential terms can be developed in Taylor series and

only the linear ones maintained. Thus, the formula which relates current density, i, and potential, E (through overpotential, η_{corr}), becomes

$$\mathbf{i} = \frac{\mathbf{2.303\ i_{corr}\ (\beta_a + \beta_c)}}{\mathbf{\beta_a\ \beta_c}}\ \mathbf{\eta_{corr}}, \qquad \text{for } E \approx E_{corr} \qquad (3.10)$$

It is obvious that when overpotential is low, i.e. when potential is close to corrosion potential, the dependence of current density on corrosion overpotential is linear. In this way, the corrosion or polarization resistance, R_P, is expressed through equation (3.11) below and its unit is Ohm·cm^2.

$$\mathbf{R_P} = \frac{\mathbf{\beta_a\ \beta_c}}{\mathbf{2.303\ i_{corr}\ (\beta_a + \beta_c)}}, \qquad \text{for } E \approx E_{corr} \qquad (3.11)$$

Equation (3.11) is also known as the **Stern - Geary** equation [Roberge, 2000]. **High polarization resistance values** indicate **a small corrosion current**, i.e. a **low rate of mass loss**, and vice versa. As already mentioned, polarization resistance can be measured experimentally by alternating working electrode potential close to corrosion potential and recording the current density. The slope of the resulting curve is R_P^{-1}. Corrosion current density can, also, be calculated from equation (3.11) knowing β_a and β_c, which can be determined experimentally using potentiodynamic polarization electrochemical technique with Tafel extrapolation (paragraph 3.3).

In Figure 3.5 current density, i, dependence from the corrosion overpotential, n_{corr}, through Butler-Volmer equation, is shown, which is the algebraic sum of the anodic and the cathodic current, i_a and i_c, respectively. In Figure 3.6 the same curve is shown at higher magnification, where corrosion overpotential, η_{corr}, tends to zero. The linearity at the origin of the polarization curve can be observed and the slope or R_P^{-1} can be determined.

*Figure 3.5: Current density, i, dependence from the corrosion overpotential, n_{corr}, through Butler-Volmer equation (**black curve**). **Red curve** represent the anodic current and **blue curve** the cathodic, for n=1, α=0.5 and i0=10-3 A/cm^2. [Karantonis, 2020]*
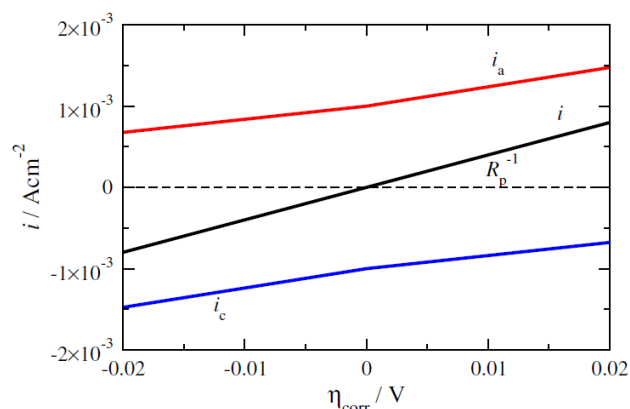
*Figure 3.6: Polarization resistance determination. **Red curve** represent the anodic current and **blue curve** the cathodic. [Karantonis, 2020]*

The examination of Butler-Volmer equation when corrosion overpotential, η_{corr}, receives large positive or negative values is going to be examined in the next paragraph (3.3) by Tafel extrapolation on Potentiodynamic Polarization curves.

3.2.1. Uncertain Tafel Constants

In *Figure 3.7* is shown that the extent of the linear part of the polarization depends mainly to the values of the Tafel constants. When relatively high values for the Tafel constants are chosen (such as $\beta_a = \beta_c = 0.118$ V, in Figure 3.7a) then the linearity of the polarization curve is extended. On the other hand, when low values are selected (such as $\beta_a = - \beta_c = 0.030$ V, in b, then the linearity is limited. Moreover, when Tafel constants are unequal (Figure 3.7c), the linearity is even more limited and the polarization curve does not present symmetry [Jones, 1995]. However, in any case, **the slope of the curve, and consequently the polarization resistance, remains the same.**

In order to **convert the polarization resistance into the corrosion rate** the Tafel parameters must be known in advance. To face this problem, several numerical methods have been proposed to obtain both Tafel parameters and corrosion rate from the same polarization measurement in the vicinity of the corrosion rate. Nevertheless, the success is limited since the determined Tafel parameters will not be very accurate, which may compromise the non-destructive nature of the LPR technique. However, this fact does not have to be assumed as a disadvantage of this technique, since polarization resistance is known and it is widely used as a unit to express corrosion rates, it is not necessary to calculate the corrosion rate in mils per year (mpy).

(a)   *(b)*   *(c)*
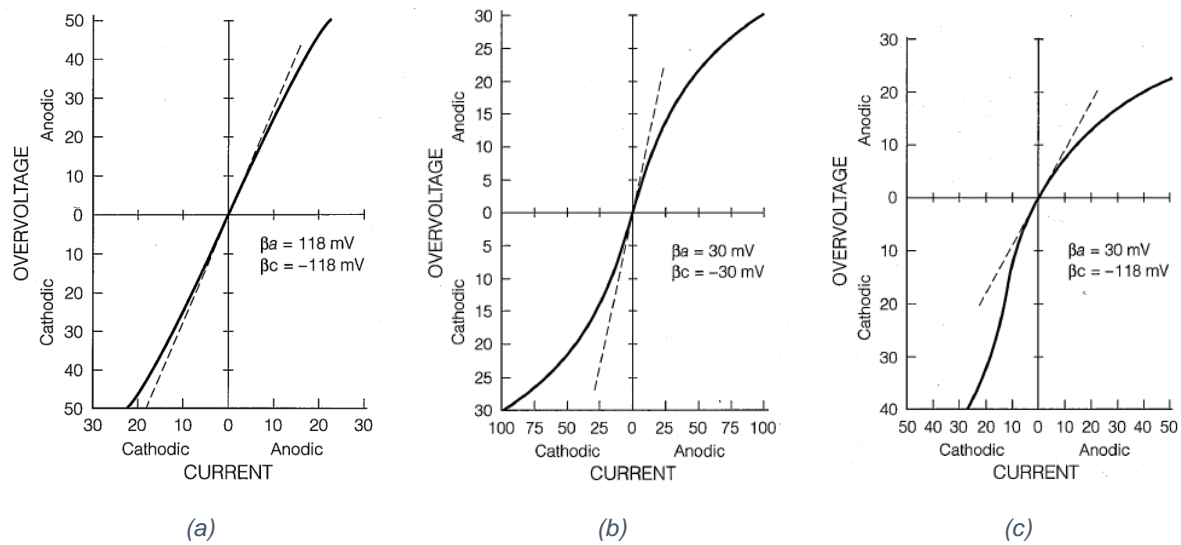
Figure 3.7: Hypothetical polarization curve plotted on linear coordinates using indicated Tafel constants, βa and βc [Jones, 1995].

A drawback of the LPR method lays in the fact that it will not work properly in low conductive media. Basically, the LPR technique can only be used to determine uniform corrosion rates; it can hardly provide information about localized corrosion.

3.3. Potentiodynamic Polarization - Tafel Extrapolation method

The Tafel extrapolation method is a mathematical technique that estimates the corrosion current, I_{corr}, and potential, E_{corr}, in an electrochemical cell, and by extension, the corrosion rate, CR. Extrapolation involves extending a known sequence of linear values within a Tafel plot to determine these parameters. Extrapolation of the linear portion of the curve to E_{corr} is utilized to gain the corrosion current density. Presuming uniform corrosion, Faraday's law can be utilized to convert the corrosion current density into the rate of penetration or weight loss. Using this technique, it is feasible not only to measure appreciably low corrosion rates, but also to perform continuous monitoring of the system under investigation. Figure 3.8 shows typical experimental polarization curves for steel in an acid solution. The Tafel extrapolation method, along with the corresponding electrochemical kinetic background is presented below.
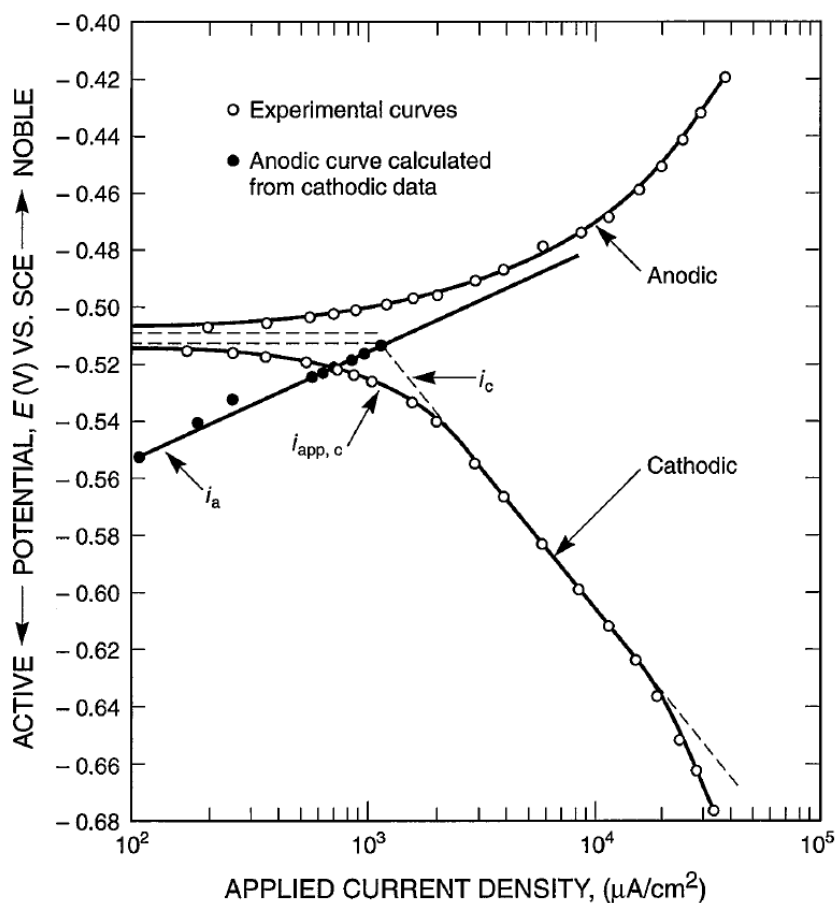
Figure 3.8: Experimental polarization curves for steel in acid solution, with $β_c$=-98mV and $β_a$=38mV (derived from cathodic data). [Bandy and Jones, 1976]

Assume a system in which the following redox reactions take place

anodic reaction:	$M \rightarrow M^{n+} + ne^-$	(3.12)
cathodic reaction:	$2H^+ + 2e^- \rightarrow H_2$	(3.13)

73
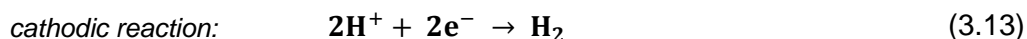
An excess of electron flow is applied to the corroding metal electrode in acid with E_{corr} and i_{corr} defined by Mixed Potential theory (paragraph 2.5.4.). This electron flow corresponds to an applied current density $\mathbf{i_{app,c}}$, as shown in Figure 3.9, and causes the electrode potential to shift negatively from E_{corr} to E. The negative potential shift, $\mathbf{\varepsilon_c = E - E_{corr}}$, is defined as **cathodic** overpotential. The excess of electrons suppresses the rate of the anodic reaction (3.12) from i_{corr} to i_a and similarly increases the cathodic reduction reaction (3.13) from to i_{corr} to i_c. To fulfill the principle of charge conservation, the difference between the increase in the cathodic reduction rate and the decrease in the anodic oxidation rate, prompted by cathodic overpotential, ε_c, must be equal to the applied current:

$$\mathbf{i_{app,c} = i_c - i_a} \tag{3.14}$$
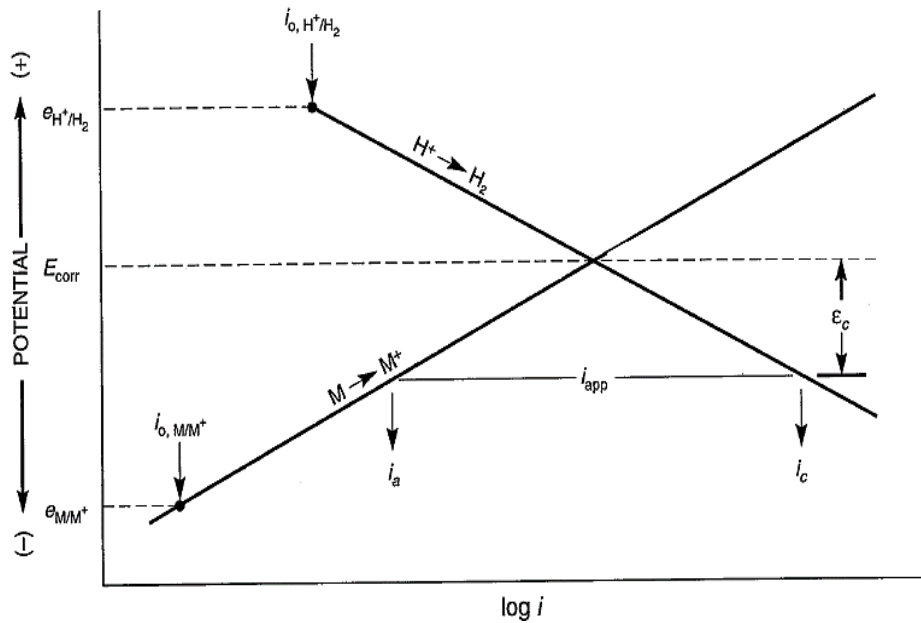
Figure 3.9: Current density, i_{app}, applied to corroding electrode of E_{corr} and i_{corr}, causing cathodic overvoltage of ε_c. [Jones, 1996]

Polarization in the **anodic** (positive) direction is analogous to cathodic polarization. **Electrons are drawn out of the metal**, and the current flows in the opposite direction from cathodic currents above. The deficiency of electrons makes the potential change positive with respect to E_{corr}. The anodic oxidation rate, i_a, is increased, while the cathodic reduction rate, i_c, is decreased, so that the applied anodic current density is

$$\mathbf{i_{app,a} = i_a - i_c} \tag{3.15}$$

Figure 3.10, below, shows $i_{app,c}$ represented by simulated data points (●) for various values of ε_c. At low ε_c, i_c is only slightly higher than i_a, and $i_{app,c}$ is very low. As ε_c increases, i_c increases while i_a decreases, both quite rapidly, until i_a becomes insignificant compared to i_c, and the simulated experimental cathodic polarization curve coincides with the dashed line for the cathodic half-cell overpotential of reaction (3.13). Thus, the simulated cathodic polarization curve of potential versus log (i_{app}), is **curved at low overpotential** but becomes **linear at**

higher overpotential. The linearity on a semilog plot is termed **Tafel behavior**, for the German investigator who first reported it [Tafel, 1904]. Experimental Tafel behavior defines the cathodic branch of the half-cell reduction reaction. Figure 3.10 shows that extrapolation of the region of Tafel behavior gives the corrosion rate, i_{corr}, at E_{corr}. The simulated anodic polarization curve, derived from Figure 3.9 and shown in Figure 3.10 defined by (■), is also linear on the semilog plot, in a manner analogous to the cathodic data.
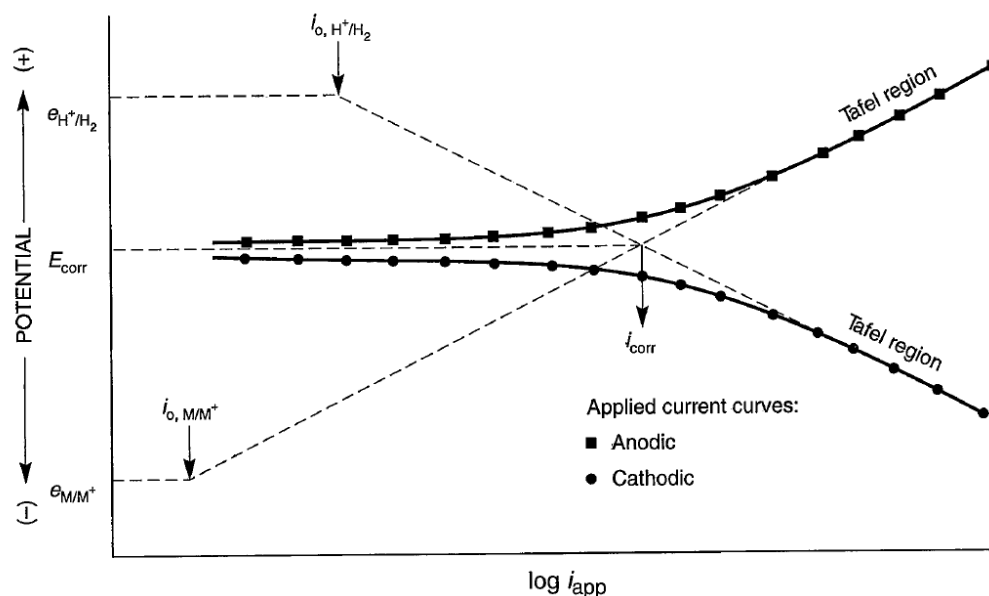
Figure 3.10: Simulated experimental polarization curves derived from Figure 3.9. [Jones, 1996]

An **experimental cathodic** polarization curve for steel in acid solution was presented in Figure 3.8. The linearity, or Tafel behavior, is limited to only about one decade of current density before interferences become apparent at higher current density. These interferences may be caused by near surface **depletion of the oxidizer**, H^+ (concentration polarization), or **ohmic gradients** in the solution. Higher concentration solutions reduce concentration polarization, increase conductivity, and thereby extend Tafel behavior.

The **experimental anodic** polarization curves often do not correspond to the idealization of Figure 3.10. The anodic data of Figure 3.8 are generally **curved** on the semilog plot, and **no sensible linearity or value of β_a can be found**. The reasons for the nonlinearity are not well understood, but some speculations seem reasonable. Anodic dissolution of metal is irreversible in dilute corroding solutions. Rapid anodic dissolution can cause unacceptable solution contamination before the anodic polarization curve is complete. The surface may be roughened or otherwise changed as liberated corrosion products accumulate and precipitate or form oxide/hydroxide films on the surface. In weakly or moderately corrosive solutions, the anodic overpotential is often higher than would be expected from cathodic data, probably due to formation of inhibiting surface films.

Anodic polarization data derived from cathodic data [Stern, 1957] have sometimes provided a reasonable alternative. The anodic current density, can be calculated from equation (3.15) in the potential region near E_{corr}, where $i_{app} \neq i_c$. The extrapolated Tafel line gives i_c, and the

data points give i_{app}. Substituting these values into equation (3.15) gives corresponding values of i_a, at a number of potentials. The solid data points in Figure 3.8 were derived in this way and give reasonable anodic Tafel behavior.

Anodic and cathodic polarization curves are symmetrical about E_{corr} when $|\beta_a|=|\beta_c|$, as assumed in Figure 3.10. However, for a corroding metal $|\beta_a|$ and $|\beta_c|$ are seldom equal for the separate and distinct anodic and cathodic half-cell reactions which constitute the mixed potential E_{corr}. The inequality is demonstrated typically in Figure 3.8, where $\beta_a = 38$ mV and $\beta_c = -98$ mV [Jones, 1996].

The **Butler-Volmer** equation, when corrosion overpotential, η_{corr}, tends to zero, i.e. **$E \approx E_{corr}$**, was examined through LPR method (paragraph 3.2). When the electrode is polarized at sufficiently large potentials, and far away from the corrosion potential, the corrosion overpotential receives large positive or negative values and as already mentioned, both anodic and cathodic polarization curves present linearity on the semilog plot of potential versus current density.

More specifically, examining Butler-Volmer equation (3.9), when corrosion overpotential, η_{corr}, receives large positive values, i.e. **$E \gg E_{corr}$**, then the second term of the equation tends to zero and can be ignored, so

$$\mathbf{i = i_{corr}\ e^{\frac{2.303}{\beta_a}\eta_{corr}}}, \qquad \text{for } \eta_{corr} \gg 0 \tag{3.16}$$

and by solving with respect to η_{corr},

$$\boldsymbol{\eta_{corr} = \beta_a \log i_{corr} + \ \beta_a \log i}, \qquad \text{for } \eta_{corr} \gg 0 \tag{3.17}$$

Similarly, when corrosion overpotential, η_{corr}, receives large negative values, i.e. **$E \ll E_{corr}$**, then the first term of the Butler-Volmer equation tends to zero and can be ignored, so

$$\mathbf{-i = i_{corr} e^{-\frac{2.303}{\beta_c}\eta_{corr}}}, \qquad \text{for } \eta_{corr} \ll 0 \tag{3.18}$$

and by solving with respect to η_{corr},

$$\boldsymbol{\eta_{corr} = \beta_c \log i_{corr} - \beta_c \log|i|}, \qquad \text{for } \eta_{corr} \ll 0 \tag{3.19}$$

Equations (3.17) and (3.19) are called anodic and cathodic **Tafel equations** and βa, βc anodic and cathodic **Tafel coefficients**, respectively. From these two equations it is observed that the dependence of the logarithm of the current density on the overpotential is linear with slope equal to Tafel coefficients.

3.3.1. The effect of oxidant diffusion on corrosion

Up to this point, it was assumed that both anodic and cathodic reactions was under activation polarization, so conditions (3.7) and Butler-Volmer equation were applied. In the case that the concentrations of the oxidizer at the electrode's surface cannot be considered equal to that in the bulk of the solution ($C_{O(x=0)} \neq C_O^*$), then the diffusion of the oxidizer should be taken into account at the dependence of the current density from the potential during corrosion.

Due to the concentration difference between the electrode's surface (x=0) and the bulk of the solution, oxidizer particles diffuse towards the electrode. The electrode acts as a cathode where oxidizer's reduction occurs. The flux of the oxidizer, in x direction, due to diffusion is given by First Fick's Law,

$$j_{Diff,O(x=0)} = -D_O \left. \frac{\partial C_O}{\partial x} \right|_{x=0} \approx -D_O \frac{C_O^* - C_O}{\delta} \tag{3.20}$$

where

- x: distance from electrode's surface,
- δ: thickness of the diffusion layer,
- D_O: diffusivity (or diffusion coefficient) of the oxidizer in the electrolyte,
- C_O: concentration of the oxidizer on the electrode's surface and
- C_O^*: concentration of the oxidizer at the bulk of the solution.

The flow of diffusion has been considered one-dimensional (along the x axis) and that it takes place mainly in a layer δ, within which the gradient of the oxidizer concentration is constant and equal to the true gradient at the electrode-electrolyte interface, as depicted in Figure 3.11. These assumptions constitute the diffusion model of the **Nernst diffusion layer** [Karantonis, 2020], which causes **concentration polarization** of the electrochemical process. Thickness of the Nernst diffusion layer varies within the range 0.1 - 0.001 mm depending on the intensity of convection caused by agitation of the electrodes or electrolyte [Kopeliovich, 2013].
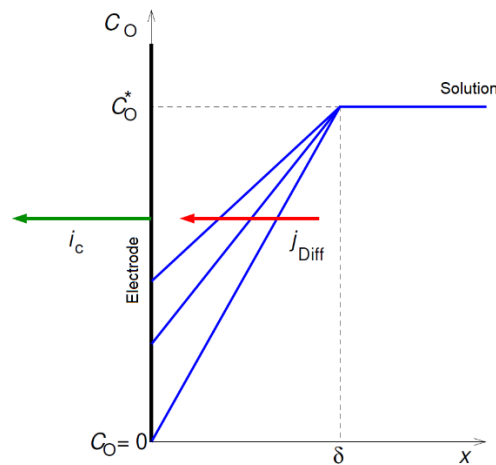
Figure 3.11: Model of the Nernst diffusion layer for the oxidizer diffusion towards to electrode's surface which acts as a cathode. [Karantonis, 2020]

Each ion possesses an electric charge. The density of the electric current formed by the moving ions is

$$i_c = n \, F \, j_{Diff,O(x=0)} = - \, n \, F \, D_O \frac{C_O^* - C_O}{\delta} \tag{3.21}$$

where F is Faraday's constant and n is the number of elementary charges transferred by each ion. The maximum flux of the ions may be achieved when $C_O = 0$ and therefore the cathode current density, i_c, receives maximum (absolute) limit value

$$i_{c,lim} = - \, n \, F \, D_O \frac{C_O^*}{\delta} \tag{3.22}$$

The value of the limiting current density may be increased by increasing the bulk concentration, C_O^*, by increasing the electrolyte temperature, which strongly affects the diffusion coefficient D_O or by agitation resulting in lowering the diffusion layer thickness δ. [Kopeliovich, 2013]

As shown schematically in

Figure 3.12, for the <u>cathodic reaction</u>, it may be assumed from the above, that:

- for $E \approx E_{corr}$, the current density is governed by Butler-Volmer equation (3.18), where in this case, **electron transfer** completely determines the reduction rate (activation polarization of the electrochemical process) and
- for $E \ll E_{corr}$, the current density becomes independent of the overpotential and takes a limit value of $i_{c,lim}$, where in this case, the reduction rate is determined by **diffusion** of oxidizer (concentration polarization of the electrochemical process).

On the other hand, the <u>anodic reaction</u>, i.e. the metal's dissolution, is conducted under **activation polarization** and the anodic current is determined by Butler-Volmer equation (3.16).

At this point, it is worth mentioning that Potentiodynamic Polarization with Tafel extrapolation method is applied and is valid under activation polarization (as well as Tafel regions and Butler-Volmer equation). Although these conditions did not fully apply to the electrochemical experiments of this thesis, the fact that this method was employed and the corresponding diagrams were extracted, **revealed to us the mechanism of corrosion which in this case the phenomenon is controlled by the mechanism of oxidizer diffusion**. This very significant information would not have been easily extracted by any other electrochemical technique.

Therefore, in this study, Tafel extrapolation was used in order to define, first of all, the corrosion potential and the corrosion current on the point of the intersection of the linear extrapolated parts of the experimental anodic and cathodic curves. Moreover, it was possible to determine the corresponding slopes of these linear parts of the curves ($β_a$ and $β_c$). Finally, the corrosion rate is estimated through the following equation:

$$CR = \frac{Icorr \cdot K \cdot EW}{d \cdot A} \qquad (3.23)$$

where K is a constant that defines the units of the corrosion rate, EW is the equivalent weight of the tested metal (which is equal to its molar mass divided by the number of the electrodes involved in the redox reaction), d is the density of the tested metal and A is the sample area.
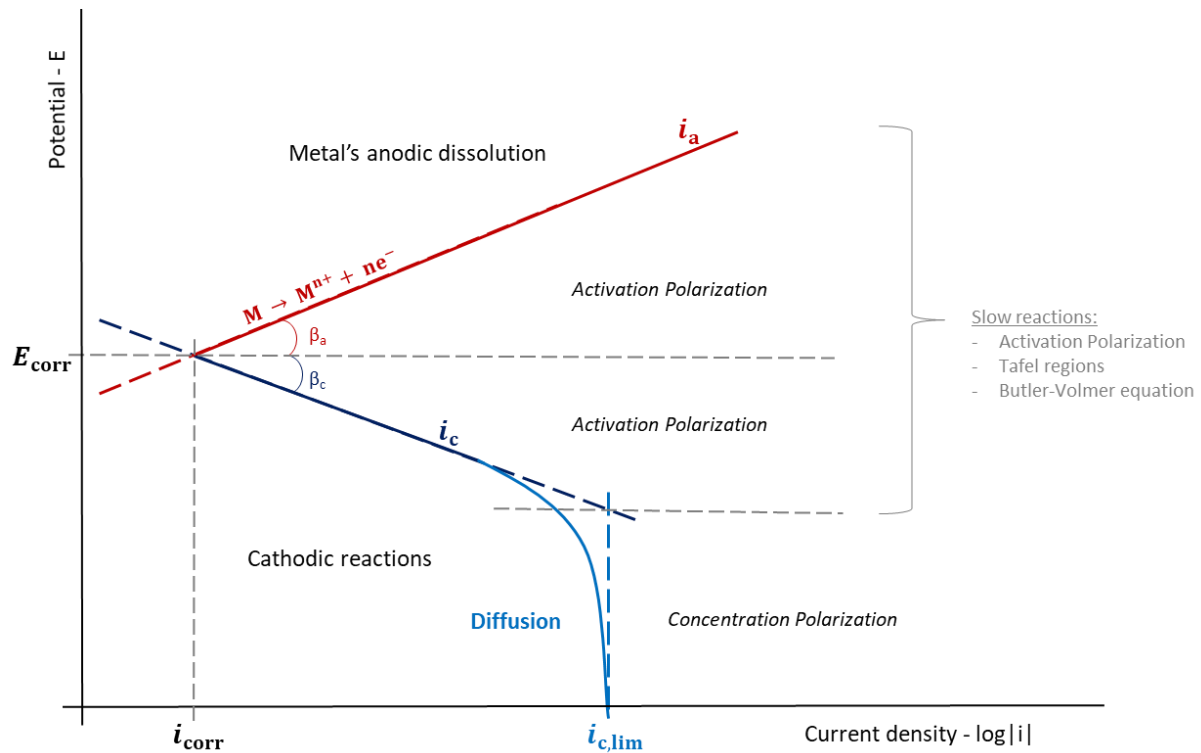
Figure 3.12: Anodic (red) and cathodic (blue) current densities on hypothetical potentiodynamic polarization curves with Tafel extrapolation technique, where the diffusion of the oxidizer causes a limit current density, $i_{c,lim}$, on the cathodic reaction.

In this study, where the specimens were set in a 3.5% NaCl solution for all the Tafel extrapolation experiments, the anodic reaction is the dissolution of Fe:

$$Fe \rightarrow Fe^{2+} + 2e^- \qquad (3.24)$$

whereas, the predominant cathodic half-cell reaction is

$$O_2 + 2H_2O + 4e^- \rightarrow 4OH^- \qquad (3.25)$$

rather than the hydrogen evolution reaction which occurs in acid solutions. As a result of the reduction of oxygen, the cathodic polarization curve displays a limiting diffusion current i_L, while the anodic dissolution of iron obeys Tafel's law, Figure 3.13. Thus, the cathodic process is controlled by concentration polarization rather than activation polarization. Nevertheless, both branches can be extrapolated back to E_{corr} to give i_{corr}, as, at the open-circuit corrosion potential, the net rate of iron dissolution is equal to the net rate of oxyden reduction, i_L.
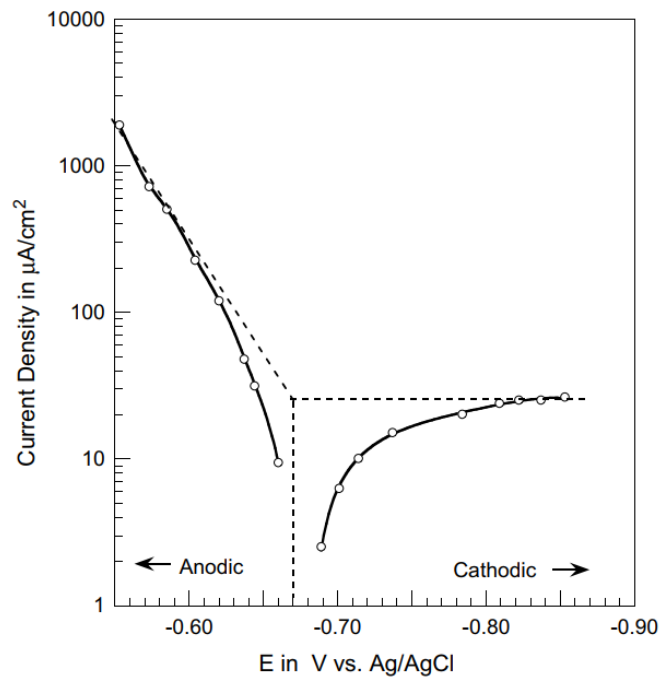
Figure 3.13: Polarization curves for iron in NaCl solution- diffusion display of the cathodic branch [McCafferty, 2005].

3.3.2. Uncertain Tafel Constants

From what has been said above, it follows that there is a possibility that Tafel and corrosion parameters do not provide a satisfying fit, when the redox reaction has not a Tafel behavior but rather a mass transport limited behavior or when passivation occurs. In this cases, it would be better to refer to **βa** and **βc** as **slopes of the extrapolated curves** rather than a Tafel coefficients, since there is no Tafelian region, where the extrapolation is applied.

To obtain i_{corr} accurately from the **Stern - Geary** equation (3.11) one must have reasonably accurate values for βa and βc. However, numerator and denominator of equation (3.11) contain both βa and βc, and as a consequence, i_{corr} is not very sensitive to the values selected for βa and βc. Stem and Weisert suggested that experimental values of:

- **βa** range from **60mV** to about **120mV** and
- **βc** range from **60mV** to **infinity**, the latter corresponding to **diffusion control** by a dissolved oxidizer.

Extreme values correspond to βa=60mV, βc=60mV; and β=120mV, βc = infinity [Jones, 1995].

If we reformulate equation (3.11) in the following form

$$\mathbf{R_P} = \frac{\mathbf{B}}{\mathbf{i_{corr}}} \qquad (3.26)$$

where

$$\mathbf{B} = \frac{\boldsymbol{\beta_a}\,\boldsymbol{\beta_c}}{\mathbf{2.303}\,(\boldsymbol{\beta_a} + \boldsymbol{\beta_c})} \qquad (3.27)$$

and taking the logarithms of equation (3.26), one obtains

$$\log \mathbf{R_P} = \log \mathbf{B} - \log \mathbf{i_{corr}} \qquad (3.28)$$

The values of βa and βc substituted into Equation (3.27) define two lines in Figure 3.14, which differ only in their intercepts on the R_P axis, in agreement with Equation (3.28). Virtually all of the experimental data fall within the error band defined by these two lines oh the graph. Furthermore, the line corresponding to |βa| = |βc| = 0.1 V lies between the two extremes, and the error resulting from using |βa| = |βc| = 0.1 V would not exceed a factor of 2 in any case. Hence, without any detailed knowledge of the system whatever, one can obtain a reasonably good estimate of the corrosion rate from polarization resistance measurements. Any more accurate estimates or measurements of βa and βc will reduce considerably the uncertainty of corrosion rates derived from R_P [Jones, 1995].
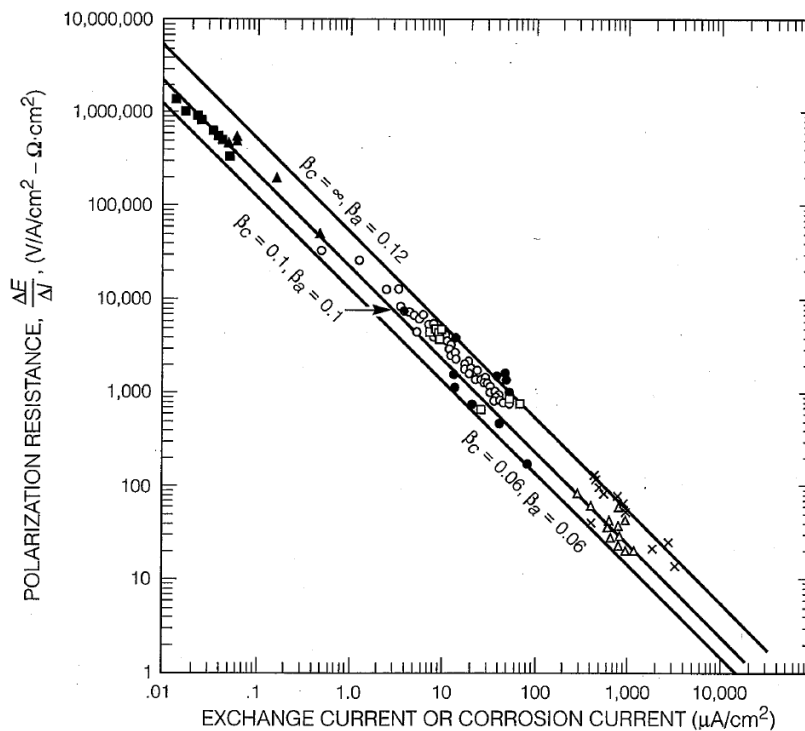
Figure 3.14: Experimental correlation between corrosion rate, i_{corr} and polarization resistance R_P. [Jones, 1995, from H. Stem and E.D. Weisert, Proc. ASTM, Vol.32, p.1280, 1959].

Following what has been said in the corresponding paragraph of LPR method (Uncertain Tafel Constants), one should not confuse an error in corrosion rate with an error in R_P, which can be measured accurately and precisely. Thus, if relative values of corrosion rate are of greater interest than absolute values (which is often the case), the LPR method becomes even more attractive. In the laboratory, the change in i_{corr} with time or the kinetics of the corrosion process may be of more interest than the absolute value of i_{corr}. The same is true industrially. Often, a large change of corro- sion rate in a process stream is far more important than the exact value of corrosion rate, especially if the corrosion rate is known within a factor of 2.

3.3.3. Ohmic Potential Drop (IR Drop)

Another remarkable point characterizes the experimental curves of this electrochemical method and it is noticeable at high current values of the anodic branch of the polarization curves and is called ohmic potential drop or IR drop.

In general, IR drop is a voltage decrease that appears at the resistive component of any impedance and it is defined as the electrical potential difference between the two ends of a conducting phase during a current flow. This voltage drop across any resistance is the product of current (I) passing through resistance and resistance value (R), according to Ohm's Law.

In electrochemistry, IR drop refers to a voltage drop due to solution resistance (R_S). It is the difference in potential required to move ions through the solution. A typical electrochemical experiment (explained furtherly in Chapter 4) is performed using an electrochemical cell (a glass vessel filled with the electrolyte) and three electrodes immersed in this solution: working electrode (WE), reference electrode (RE), and auxiliary electrode or counter electrode (CE). The WE is the conductor substrate where the chemical reaction of interest takes place. Therefore, the **potential applied** to the cell is controlled by **applying current between the CE and WE,** and **measuring the potential between the RE and WE** [Autolab, 2019]. IR drop results from the electric current flow in ionic electrolytes like dilute acids, saltwater, etc., because it is not possible to place the RE tip (**Luggin capillary**) directly on the WE surface, as shown schematically in Figure 3.15, and so it has great influence on electrochemical measurements.

RE

CE

S/WE

Electrochemical cell
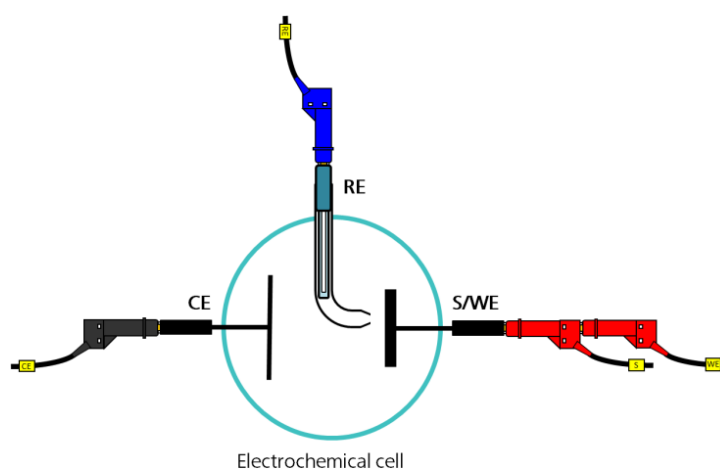
Figure 3.15: Schematic representation of a typical tree-electrode electrochemical experiment. The layout of the reference electrode (RE) with its tip (Luggin capillary) near the working electrode's surface (WE) is shown [Autolab, 2011].

Therefore, its effects should be considered during the interpretation of electrochemical data, since it is an unwanted quantity that must be removed to obtain an accurate potential measurement [CorrosiooPedia, 2019]. For this purpose, assuming that the potential measurement of the potentiostat, according to Ohm's Law, is

$$E_{applied} = IR_{ct} \tag{3.29}$$

where I is the current and R_{ct} is the total resistor which constitutes of the metal's and the solution's resistance, R_P and R_S, respectively, so

$$R_{ct} = R_P + R_S \tag{3.30}$$

then, the measurement of the potential may be written as

$$E_{applied} = I\,(R_P + R_S) = IR_P + IR_S = E_{WE} + IR_S \tag{3.31}$$

and the accurate potential measurement is

$$E_{WE} = E_{applied} - IR_S \tag{3.32}$$

where the minus sign (-) represents the **drop** on the potential. This drop is negligible at low current values but its effects will become more prominent as the scan rate is enhanced following the increase of current.

IR drop depends on the following factors:

- The current and potential distribution in the electrolyte (changing the size or shape of the working electrode will change the shape of the equipotential lines, i.e. regions of the electrode-electrolyte interface where the potential between RE and WE has the same value)
- The position of the reference electrode with respect to the working electrode.
- The conductivity of the electrolyte solution (the lower the conductivity of the electrolyte, the higher the IR drop.)

The following measures will be needed to minimize the IR drop:

- Using a three-electrode system.
- Adding a high concentration of fully dissociated electrolytes to the solution.
- Placing the reference electrode tip within close proximity of the working electrode surface.
- Using low scan rates that will minimize the current.
- Decreasing the electrode surface area.

As earlier mentioned, Tafel plots are generated by plotting both anodic and cathodic data in a semilog diagram as E-logI. From the plot, three values are determined: the anodic curve slope, the cathodic curve slope, and I_{corr} from back-extrapolation of both anodic and cathode curves to E_{corr}. The Tafel extrapolation method presents some limitations when used for determining corrosion rates:

- At least one of the branches of the polarization curves has to be activation controlled.

- Anodic or cathodic parts, which show Tafel behavior, need to exist and be well-defined.

- Large current densities are often required to generate the complete Tafel plots. The use of large current densities can alter the surface conditions of the specimen (e.g., permanent change or surface damage), thereby distorting the results and increasing complications due to mass transport and uncompensated electrolyte resistance.

- The anodic and the cathodic reactions which occur at the corrosion potential are also the only reactions which occur during determination of the polarization curves. This means that changes in electrode potential does not induce additional electrode reactions.

- Corrosion has to be general in nature and localized corrosion in not considered.

- The measurement of current density over a wide potential range may also distort the results, if the adsorption of some species is potential dependent. Since this method applies a large overpotential to the metal surface (e.g., anodic polarization), therefore, the technique is rather destructive and can hardly be used for online corrosion monitoring purposes and in particular in the field.

- The polarization curves are for the steady-state.

3.4. Electrochemical Impedance Spectroscopy method

The electrochemical impedance spectroscopy, EIS, is a technique for the analysis of the response of corroding electrodes to small-amplitude alternating potential signals of widely varying frequency. The EIS technique uses a typical three-electrode cell system controlled by a potentiostat, similar to that used in the LPR technique, but with a Frequency Response Analyzer (FRA). Unlike the previous time-resolved techniques, where the current system response is either the consequence of a large voltage perturbation from the steady-state condition (Tafel extrapolation) or from a smaller perturbation (LPR method), in the EIS approach, by applying a small varying perturbation over a range of frequency, it is possible to probe the full response of the electrochemical system, and not just the resistive components [Bard and Faulkner, 2001].

In that respect, a small AC signal, i.e. alternating potential or voltage **V(ω)** typically a sine wave of amplitude ±10 mV of the corrosion potential, is applied over a wide range of frequency (typically from 10^5 down to 10^{-2} Hz) at a number of discrete frequencies (typically 5–10 frequencies per decade), and the alternating current response, **I(ω)**, is measured at each angular frequency, **ω** (where $\omega = 2\pi f$, with **f** the frequency in Hertz)

When a sinusoidal alternating potential signal **V(t)** is applied to an electrode surface, the time-dependent current response **I(t)** is expressed through an angular dependent impedance **Z(ω)** [Jones, 1995]. **Ohm's Law** connects these three parameters:

$$Z(\omega) = \frac{V(t)}{I(t)} \tag{3.33}$$

where:

$$V(t) = V_0 \sin(\omega t) \tag{3.34}$$

$$I(t) = I_0 \sin(\omega t + \theta) \tag{3.35}$$

where **t** is the time [in second], **θ** is the phase angle [in degree] between V(t) and I(t) and **ω**=2πf is the angular frequency, with **f** the frequency [in Hertz or s^{-1}].

Several processes on the electrode surface absorb electric energy in different frequencies. As effect, they create a time lag between excitation and response. These process is simulated by Resistive (R) –Capacitive (C) electric circuit connected in parallel (Figure 3.16a).

In Chapter 2 (paragraph 2.4.5.3. , Figure 2.12), the equivalent circuit model for the metal/solution interface, was discussed. This equivalent circuit, shown again in Figure 3.16b, contains a double-layer capacitance, C_{dl}, in parallel with the polarization resistance R_P. This parallel component is in series with the solution resistance, R_S, which exists between the electrical double layer (edl) and the Luggin capillary (tip of the reference electrode, Figure 3.15). This model of the equivalent circuit explains the time lag between excitation and response in Figure 3.16a.
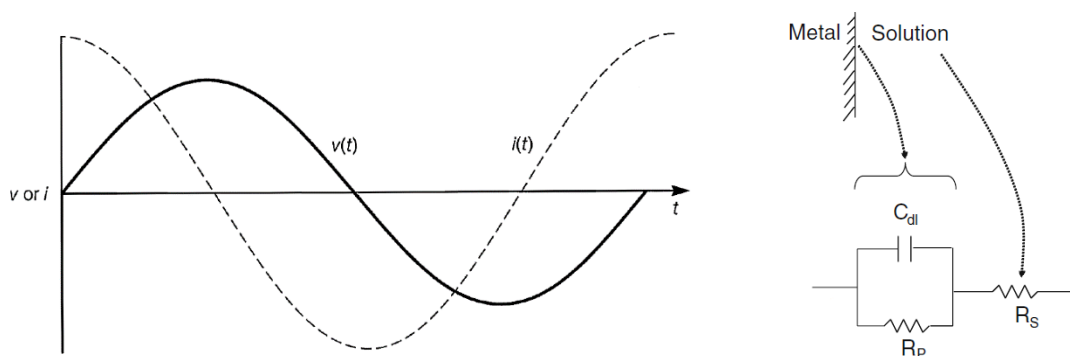
Figure 3.16: (a) Current response, I, to a sinusoidal potential signal, V, for a capacitor. (b) Equivalent circuit for an electrical double layer (edl). C_{dl} is the capacitance of the edl, R_P is the polarization resistance, and R_S is the solution resistance [McCafferty, 2010].

The impedance $Z(\omega)$ may be expressed in terms of **real** and **imaginary** components and by obviating the dependency on the frequency, ω, that is:

$$\mathbf{Z} = \mathbf{Re(Z)} + \mathbf{Im(Z)} \tag{3.36}$$

where Re(Z) and Im(Z) are the real and the imaginary components, respectively, of the impedance Z, expressed in Ohm. The impedance behavior of an electrode may be expressed in Nyquist plots of the -Im(Z) as a function of the Re(Z), or in Bode plots of log|Z| or/and -Phase(Z) vs the frequency, f, in logarithmic scale.

Nyquist plot (Figure 3.22) shows a semicircle, with increasing frequency in a counterclockwise direction. At very high frequency (ω), the imaginary component disappears, leaving only the solution resistance, R_S. At very low frequency, the imaginary part disappears again, leaving the sum of R_S and the polarization resistance, R_P.
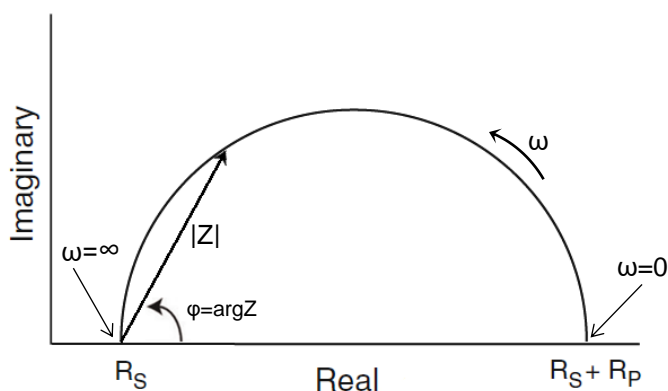
Figure 3.17: EIS Nyquist plot [McCafferty, 2010].

Bode plot (Figure 3.18) gives analogous results. At intermediate frequencies (ω), the log|Z| curve (continuous line) is linear with a slope of -1, while the Phase(Z) curve (dashed line) receives maximum value.
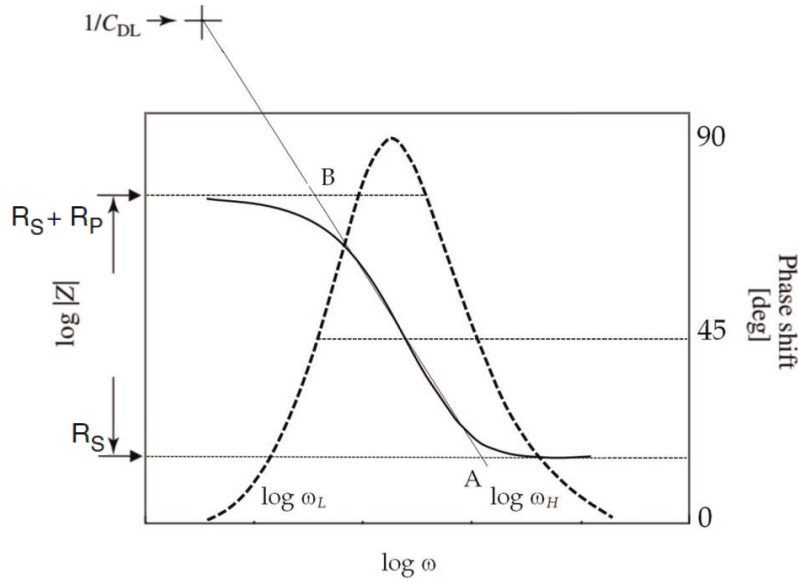
Figure 3.18: EIS Bode plot - log|Z| curve (continuous line), Phase(Z) curve (dashed line) [Berradja, 2019].

The polarization resistance (R_P) is inversely proportional to the corrosion rate. It is evident from Figure 3.22 that the R_S measured at high frequency can be subtracted from the sum of R_P+R_S at low frequency to give a compensated value of R_P free of ohmic interferences [Jones, 1995].

However, the **Capacitor** (**C**) is a common electrical element representing an ideal capacitor. The equivalent electrical circuit component that models more precisely the behavior of an electrical double layer (edl), is the **Constant Phase Element** (**CPE** or **Q**), which is an imperfect capacitor and is also frequency dependent. CPE is an imperfect capacitor and is commonly used in equivalent circuit modelling and data fitting of electrochemical impedance spectroscopy data, as it simulates with great accuracy the metal electrode surface due to surface disorder, porosity or inhomogeneity of surface of electrode materials, [Kochowski and Nitsch, 2002] [Lacey]. The Nyquist plot of such an element (Figure 3.19) corresponds to a straight line in the imaginary positive part (-Im(Z)>0) with an angle with the real axis equal to $-\alpha^{\pi}/_2$, where α is related to the frequency dispersion with range from 0 to 1 (for α=1 → angle= –π/2 → Q=C). The faradaic impedance of the CPE decreases when the frequency increases.
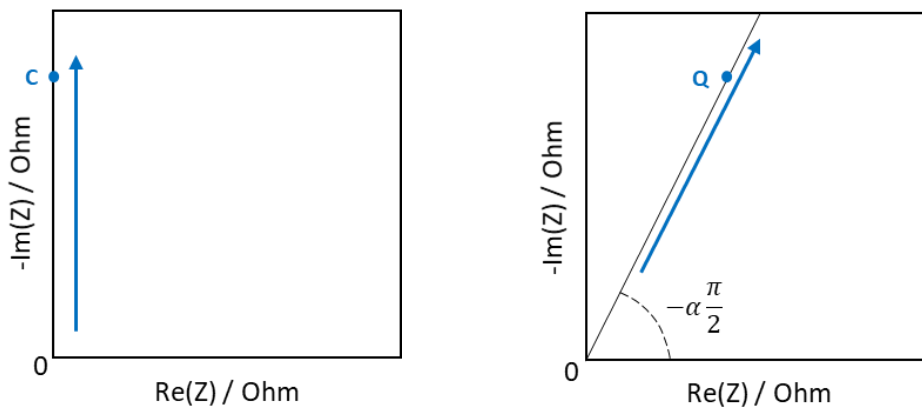
Figure 3.19: The Nyquist plot of a Capacitor, C (left), and a Constant Phase Element, CPE or Q (right).

87

The total impedance of such electrochemical systems are simulated by an equivalent circuit as shown in Figure 3.20, where R_S is the solution resistance, R_P is the Faradaic charge transfer resistor (or polarization resistor) and CPE represent the Constant Phase Element. CPE is also associated with the case of a working electrode having a surface film (e.g., AISI 304 stainless steel immersed in a 0.5 M H_2SO_4 electrolyte), in which case the capacity of the equivalent circuit can be associated with the capacity of the passive oxide surface film and the resistor in parallel with the CPE is considered as the charge transfer resistance, R_{CT} (or the polarization resistance, R_P, under *EIS*-free corrosion conditions), while the ohmic resistance in solution, R_S, between the working electrode and the reference electrode is in series with the parallel resistor and the CPE.
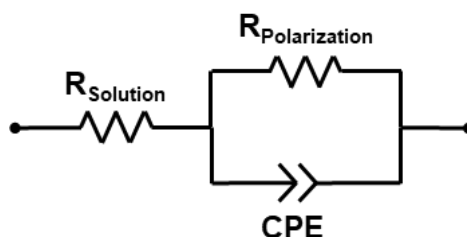
Figure 3.20: The ohmic resistance in solution, R_S, between the working electrode and the reference electrode is in series with the parallel resistor (R_P) and the CPE.

It is important to mention that Electrochemistry Impedance Spectroscopy cannot produce valid results for polarization resistance, R_P, when the exchange current density applied to the system is very large. These experimental conditions approach simple direct-current electric circuit and more complex instruments are needed so that valid measurements are obtained. However, this method is really useful as it offers unambiguous results for polarization resistance and corrosion rate, corrected for ohmic interferences due to solution resistance. Moreover, it can reveal important information about reaction mechanism through frequency response of the corroding electrode.

3.5. Cyclic Potentiodynamic Polarization method

Corrosion is generally considered as uniform pattern in most of the cases. However, many times it cannot be prevented due to passivity. Passivity is defined as a condition of corrosion resistance due to formation of thin surface films under oxidizing conditions with high anodic polarization (e.g. stainless steel). However, localized corrosion (pitting corrosion, crevice corrosion and stress corrosion cracking) can occur by breakdown of the passive film in the presence of aggressive ions. Electrochemical study of passivity is used to evaluate the materials' resistance to localized corrosion. Thus, Cyclic Potentiodynamic Polarization (CPP) method is a suitable way for investigation of the beginning of passivity, breakdown of oxide film, susceptibility to repassivation and calculation of the rate of pitting corrosion due to the vast range of scanning potential [Esmailzadeh, Aliofkhazraei, Sarlak, 2017].

The electrochemical basis for passivity is found in the anodic polarization curve illustrated in Figure 3.21. The shape of this curve is typical of various metals (e.g., iron) which undergo an active–passive transition in acid solutions. After passing through the **region of active corrosion**, where the corrosion rate can be determined as usual by the Tafel extrapolation method, a **critical current** density is achieved. At this current, the potential is called primary passivation potential, E_{PP}, or **Flade potential**. Further increases in potential cause a decrease in the anodic current density. This is because a passive film is being formed on the metal surface, and the metal is said to be undergoing an active/passive transition. The current is observed to drop precipitously as the passive oxide is formed and as the metal enters the **passive region** of the anodic polarization curve. The current density in the passive region is called the **passive current density**. With further increases in anodic potential (**transpassive region)**, the current again increases, due to metallic corrosion (the breakdown of the passive film, the initiation of pitting and occurrence of localized corrosion) or more possibly due to the evolution of oxygen by the breakdown of water in the electrolyte

$$2H_2O \rightarrow O_2 + 4H^+ + 4e^- \qquad (3.37)$$
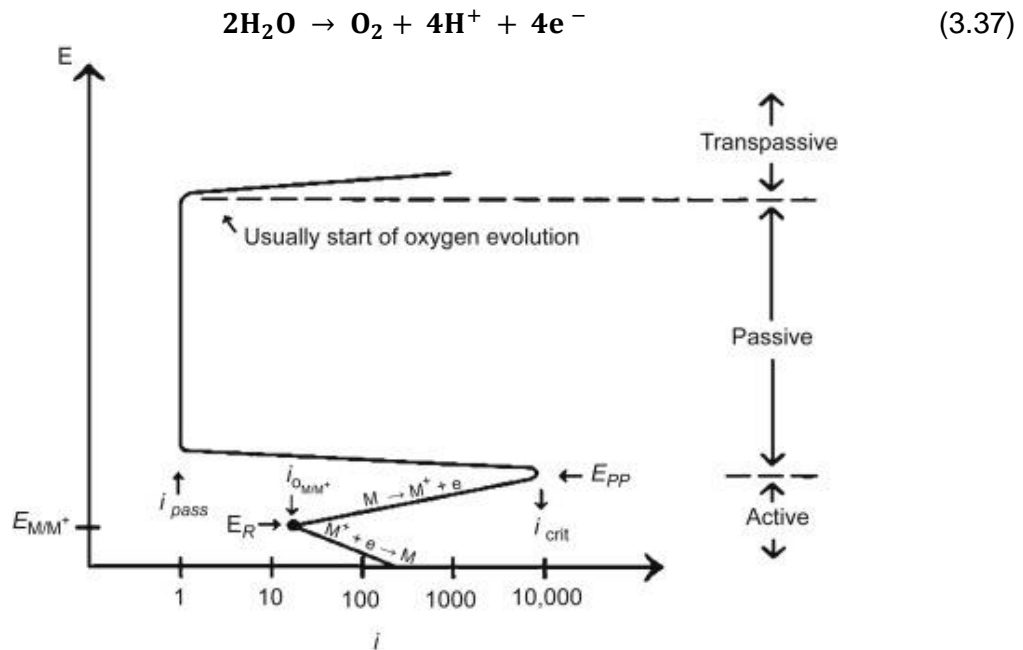
Figure 3.21: Anodic polarization curve (schematic) showing the formation of a passive film after an active/passive transition [Ahmad, 2006].

In order to assess the localized corrosion susceptibility of the materials CPP measurements should be carried out according to the defined ASTM standards (F2129, G61). After stabilizing the specimen at the **rest potential E$_r$** (employing Open Circuit Potential method), the potential scan starts from this potential and moves in the noble direction in a cyclic path with a slow scan rate, between the working electrode and auxiliary electrode and, finally, the scanning potential is reversed to the starting point.

The interpretation of the CPP scan is difficult. The extracted parameters from the cyclic curves are not constant and vary from material to material [Popov, 2015]. They are empirical parameters and change in different experimental conditions. The parameters used to interpret the CPP curves include: pitting potential, repassivation or protection potential, potential of anodic to cathodic transition, hysteresis and active passive transition (anodic nose). In the CPP method, relative position of pitting and repassivation potential with respect to the corrosion potential are the most important parameters for evaluating the pitting corrosion behavior. In the anodic polarization scan, scanning starts from corrosion potential after reaching the steady state. Before reaching the potential of O_2 evolution, a rapid increase in the current density may occur due to either some defects of the surface film or the breakdown of the oxide film and occurrence of the pitting corrosion in the presence of aggressive ions. In that way, the potential at which the current density increases rapidly is called pitting corrosion potential. For some metals, the pitting potential coincides with the corrosion potential, which occurs when there is an oxide film on the material surface prior to the polarization (Figure 3.22a). Due to the intersection of the cathodic branch with the transpassive region of the anodic branch, the value of pitting potential is the same as the corrosion potential.

(a)   *(b)*
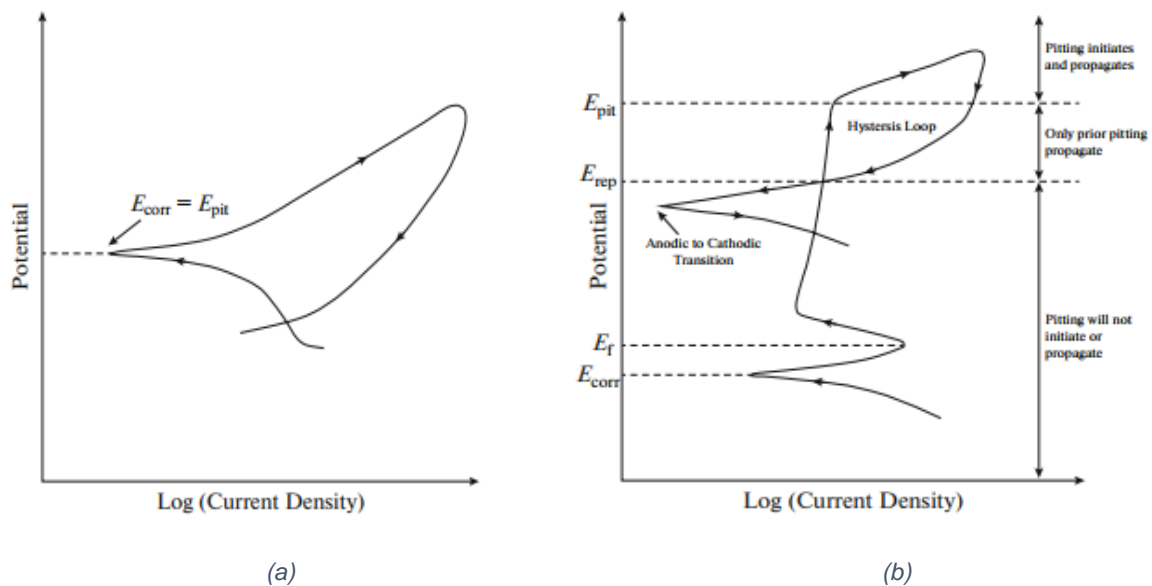
Figure 3.22: Schematic illustration of a) CPP of Al in 3.5 wt % NaCl solution, b) CPP curve and corrosion parameters [Esmailzadeh, Aliofkhazraei, Sarlak, 2017].

In the CPP curve, as shown in Figure 3.22b, after the increase of the current density at pitting corrosion, the scanning direction changes and then, with the potential reduction toward the negative potentials, the current density in the reverse scan may be different than that in the forward scan (**hysteresis**). The scan continues until the reverse curve crosses the forward polarization curve and the intersection point is called **protection potential**.

At potentials between the protection potential and corrosion potential, the passive film is stable and no pits will initiate or grow. This region is called **perfect passivity** (Figure 3.23). At the potentials between the pitting potential and protection potential, only old pits propagate and no new pits are formed (**imperfect passivity region**). Finally, at potentials above the pitting potential, new pits will initiate and develop.
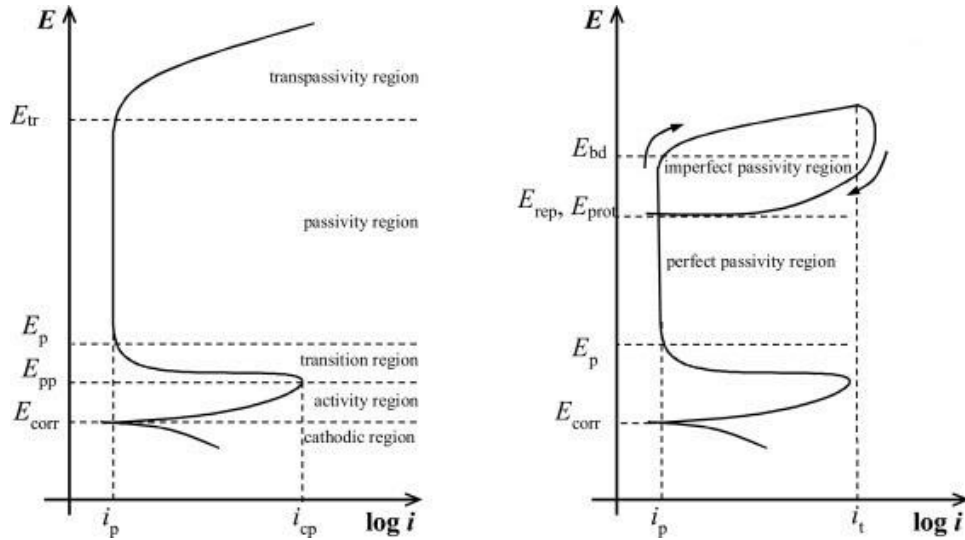
Figure 3.23: Schematic illustration of CPP curves with (from left to right) perfect passivity and imperfect passivity region [Bellezze, Giuliani, Roventi, 2018].

The difference between forward and reverse current densities at the same potential demonstrates **the size of hysteresis**. The bigger size of hysteresis loop means more passive film disruption, following with more difficulty for restoring the damaged passive film. There are two types of hysteresis at the more positive potentials: **positive hysteresis** is related to the decrease of the passivity due to the localized corrosion that causes the increase of the current density in reverse scan, in comparison to the current density in the forward scan, at the same potential, Figure 3.24a. **Negative hysteresis** happens when the degree of surface passivation is greater at more noble potentials, which causes the current densities in the reverse scan to be lower than those in the same potentials of the forward scan, Figure 3.24b.

(a)   *(b)*
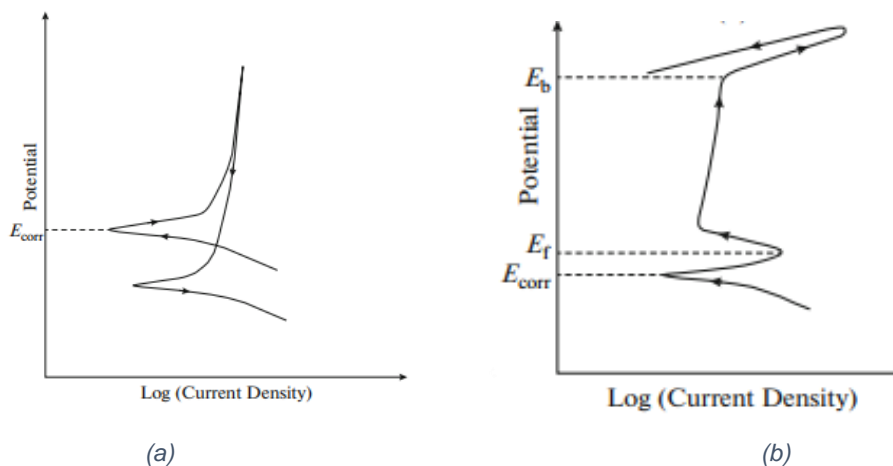
Figure 3.24: a) Schematic illustration of CPP curve with negative hysteresis, b) schematic illustration of CPP curve of Al alloy without hysteresis loop [Esmailzadeh, Aliofkhazraei, Sarlak, 2017].

The absence of hysteresis loop during the potential scan (the forward curve coincides with the reverse curve) means that the localized corrosion does not occur, but it could be a sign of an active surface and general corrosion. The difference between the pitting potential and the protection potential, and also the area of the hysteresis loop, indicate the probability of pitting corrosion. The higher the difference between E_{pit} and E_{rep} and the larger area of positive loop demonstrate the probability of low pitting corrosion resistance [Wang, 2016].

The anodic to cathodic transition potential is the potential at which the anodic current density varies to the cathodic current density. At the reverse curve, the decrease of the corrosion current density at a potential called **active-passive transition potential** (anodic nose) that is more noble than E_{corr} occurs for alloys that are susceptible to passivity and restore the damaged oxide film, Figure 3.24b, or the alloys that are not susceptible to pitting corrosion, Figure 3.24a. For these two groups of alloys, the difference between the anodic to cathodic transition potential and E_{corr} are used to determine the persistence of the passive film. According to the place of anodic to cathodic transition potential relative to the E_{corr}, the passive layer stability is evaluated. If in the reverse scan, the anodic to cathodic transition potential is more noble than E_{corr}, the passive layer will not be stable at E_{corr}, Figure 3.24a, while the passivity will persist, if E_{corr} gets more noble than the anodic to cathodic transition potential.

As already mentioned, a Cyclic Potentiodynamic Polarization curve is presented in plot of working electrode's potential as a function of current density (Ewe/V vs log[|I/mA|]), similarly to that of the Tafel Extrapolation method but with the difference of being employed for a very wider range in the anodic scan. Finally, there are a lot of critical parameters which affect the CPP curve. Those are the solution resistivity, the scan rate, the point of scan reversal, the effect of aggressive ions, the effect of corrosion inhibitor and the effect of some metallurgical variables, such as heterogeneity at grain boundaries, disorder in the passive film by impurity atoms or inclusions. Some additional parameters that may affect the CPP curve are the temperature and the pH values, the dissolved gases in the electrolyte, the immersion duration, the fluid velocity and the surface roughness [Jones, 1995]. Thus, it is very important to take under consideration a lot of different factors in order to study the behavior of the CPP curve of a specimen.

References – Chapter 3

[1] **Ahmad Z.**, (2006), <u>Principles of Corrosion Engineering and Corrosion Control - Types of Corrosion: Repassivation</u>, Science Direct.

[2] **Autolab,** (2011), <u>Basic overview of the working principle of a potentiostat / galvanostat (PGSTAT) – Electrochemical cell setup</u>, Autolab Application Note EC08, Metrohm – Autolab B.V.

[3] **Autolab,** (2019), <u>Ohmic Drop: Part 1 – Basic Principles</u>, Autolab Application Area: Fundamental AN-EC-003, Metrohm – Autolab.

[4] **Bard A.J., Faulkner L.R.**, (2001), <u>Electrochemical Methods: Fundamentals and applications</u>, Second edition, John Wiley & Sons.

[5] **Bellezze T., Giuliani G., Roventi G.**, (2018), <u>Study of stainless steels corrosion in a strong acid mixture. Part 1: cyclic potentiodynamic polarization curves examined by means of an analytical method</u>, Corrosion Science Vol. 130, Elsevier, Italy.

[6] **Berradja A.,** (2019), <u>Electrochemical Techniques for Corrosion and Tribocorrosion Monitoring: Methods for the Assessment of Corrosion Rates</u>, IntechOpen.

[7] **CorrosionPedia** (2019), <u>IR Drop</u> (website: https://www.corrosionpedia.com/definition/2203/ir-drop

[8] **Esmailzadeh S., Aliofkhazraei M., Sarlak H.,** (2017), <u>Interpretation of Cyclic Potentiodynamic Polarization Test Results for Study Behavior of Metals: A Review</u>, Pleiades Publishing.

[9] **Jones A. D.** (1995), <u>Principles and Prevention of Corrosion</u>, 2nd ed., Prentice Hall Publishing, University of Nevada, Reno, Nevada.

[10] **Karantonis A.**, (2015), <u>Basic Principles of Electrochemistry</u>, (in Greek:Βασικές Αρχές Ηλεκτροχημείας, Ελληνικά Ακαδημαϊκά Ηλεκτρονικά Συγγράμματα και Βοηθήματα), Athens.

[11] **Karantonis A.**, (2020), Electrochemical Principles of Corrosion of Metals, (in Greek: Ηλεκτροχημικές Αρχές της Διάβρωσης των Μετάλλων), NTUA, Athens.

[12] **Kissinger P., Heineman W. R.**, (1996), <u>Laboratory Techniques in Electroanalytical Chemistry</u>, 2nd ed. Marcel Dekker, New York.

[13] **Kochowski S., Nitsch K**., (2002), <u>Description of the frequency behavior of metal-SiO2-GaAs structure characteristics by electrical equivalent circuit with constant phase element</u>, Thin Solid Films. 415 (1–2): 133–137, Retrieved 22 October 2012.

[14] **Kopeliovich D.**, (2013), <u>Diffusion layer</u> (website: https://www.substech.com/dokuwiki/doku.php?id=diffusion_layer)

[15] **Lacey M**., Battery Science and Electrochemistry – Electrochemical Impedance Spectroscopy: Constant Phase Element (website:<u>http://lacey.se/science/eis/constant-phase-element/</u>)

[16]   **Langhus D. L**., (2002), Fundamentals of Electroanalytical Chemistry, J. Chem. Educ.

[17]   **McCafferty E.,** (2005), Validation of corrosion rates measured by the Tafel extrapolation method, Corrosion Science 47, Elsevier, Washington.

[18]   **McCafferty E.,** (2010), Introduction to Corrosion Science, Springer, Washington, DC.

[19]   **Pantelis D.I., Chrysoulakis G.**, (2008), Materials Science and Technology, (in Greek: Επιστήμη και Τεχνολογία των Μεταλλικών Υλικών), Second Edition, Papasotiriou, Athens.

[20]   **Popov B.N**., (2015), Basics of Corrosion Measurements, Corrosion Engineering, Elsevier.

[21]   **Ribeiro D.V., Souza C.A.C., Abrantes J.C.C.,** (2015), Use of Electrochemical Impedance Spectroscopy (EIS) to monitoring the corrosion of reinforced concrete, IBRACON Structures and Materials Journal

[22]   **Roberge R.R**, (2000), Handbook of Corrosion Engineering, McGraw-Hill.

[23]   **Robert G. Kelly G.R., Scully R.J., Shoesmith W.D., Buchheit G.R.,** (2003), Electrochemical Techniques in Corrosion Science and Engineering, Marcel Dekker, New York.

[24]   **Silverman D.C**., (2011), Practical Corrosion Prediction Using Electrochemical Techniques, Argentum Solutions.

[25]   **Wang J.**, (2006), Analytical Electrochemistry, 3rd ed., John Wiley & Sons, Hoboken, NJ.

[26]   **Wang S.**, (2016), Corrosion Resistance and Electrocatalytic Properties of Metallic Glasses, IntechOpen.

[27]   https://corrosion-doctors.org/Electrochem/LPR.htm

[28]   https://pineresearch.com/shop/kb/software/methods-and-techniques/basic-methods/open-circuit-potential-ocp/

Experimental Procedure

Introduction

The aim of the present thesis is the study of the susceptibility to corrosion of S560 and S700 steels and the study of their microstructures.

As previously mentioned, corrosion rates for metals undergoing uniform corrosion can be determined by various methods. However, electrochemical techniques have the capability to provide insights into the underlying mechanism of corrosion and, in addition, offer the possibility of mitigating corrosion by controlling the electrode potential. For this purpose, five electrochemical techniques, Open Circuit Potential (OC), Linear Polarization Resistance (LPR), Potentiodynamic Polarization – Tafel Extrapolation, Electrochemical Impedance Spectroscopy (EIS) and Cyclic Potentiodynamic Polarization (CPP), were used for conducting corrosion experiments on the metallic specimens.

In order to study the microstructure and for the electrochemical techniques to be applied, some procedures had to be carried out for the preparation of the specimens. Finally, for the complete study of the corroded area of the specimens, some additional techniques were required.

In the following paragraphs, the precise sequence of steps followed are presented, along with the basic characteristics of the instruments employed. It is, therefore, appropriate to make a schematic distinction of the experimental process in order to be more comprehensible. This separation includes:

1. preparation of specimens and the metal surface,
2. observation and study of the metal alloy,
3. application of electrochemical methods and observation of the corroded surface.

In Figure 4.1 the experimental process in details is schematically presented.
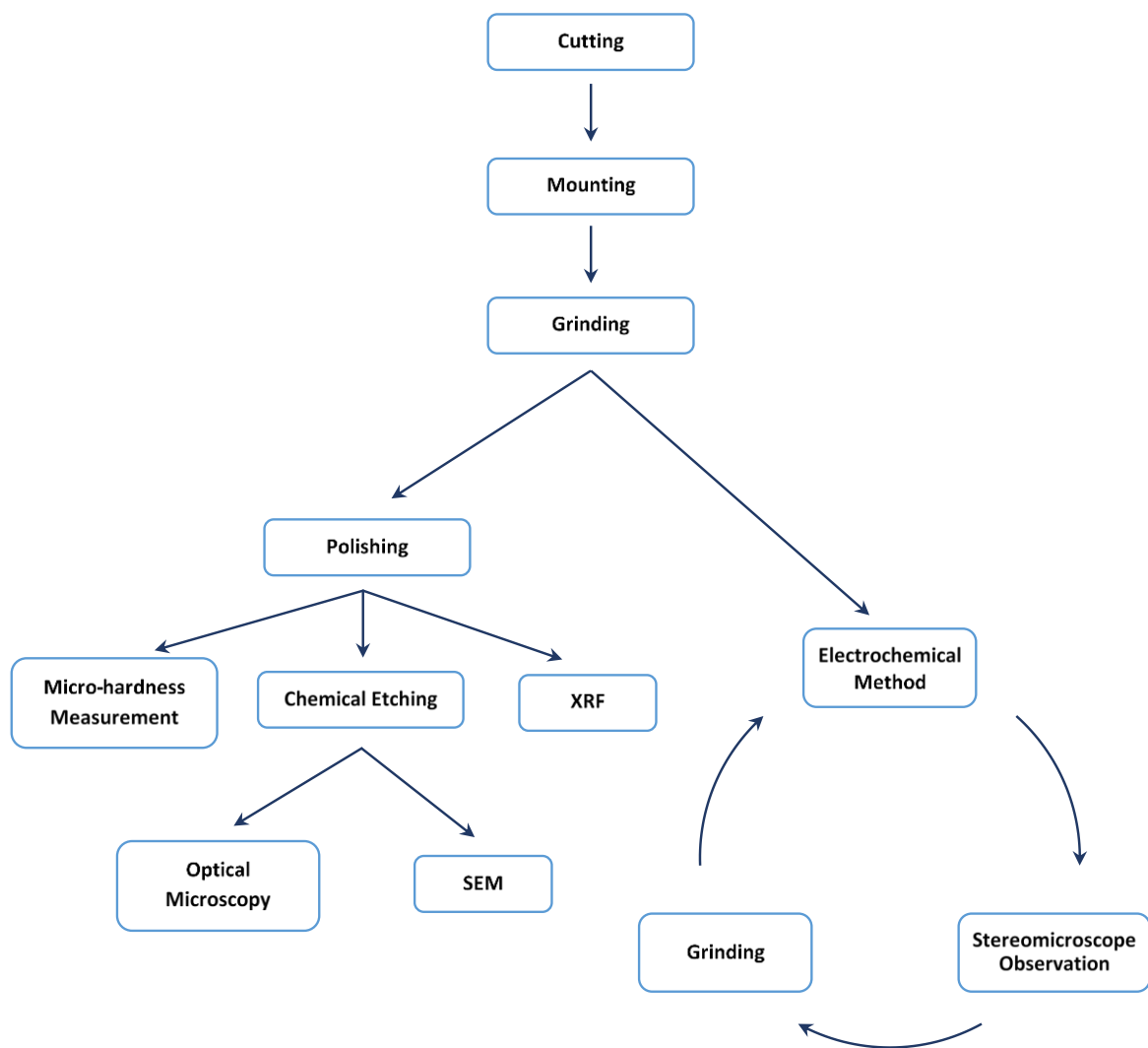
Figure 4.1: Experimental process schematically presented.

4.1. Preparation of Specimens

Both specimens, S560 and S700, were provided by FINCANTIERI Shipbuilding Company, in Italy, and sent in large dimensions (Figure 4.2 and Figure 4.3) to Shipbuilding Technology Laboratory (STL).

Thus, the first step was to **cut** the metal plates firstly with a band saw and consequently with a discotom (Figure 4.4) in sizes that would fit in the mounting molds (Figure 4.5).
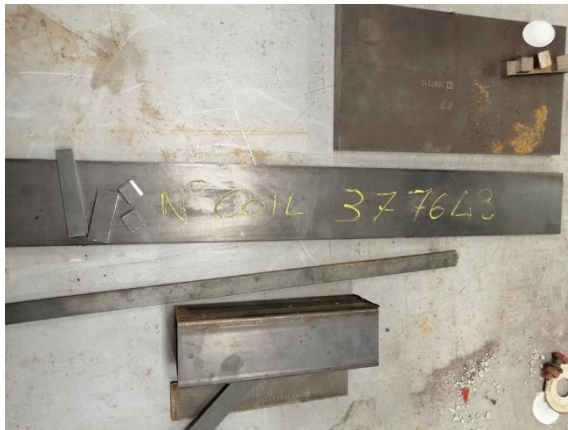
Figure 4.2: S560 (long sample).

Figure 4.3: S700 after cutting with band saw.

Figure 4.4: Struers discotom of STL [www.struers.com].

Figure 4.5: S700 after cutting with discotom.

Afterwards, specimens were cold **mounted** in epoxy resin. So, after lubricating the mold with Struers Silicon Oil, the piece of metal was placed inside it and then the resin mixture was poured. The mixing ratio was 25 parts Struers Epofix resin and 3 parts Epofix hardener by weight (Figure 4.6 and Figure 4.7a). Specimens were mounted in a way that only the tested surface would be kept free from resin (after grinding the excess resin from the top). The purpose of mounting was to produce specimens with uniform size in order to facilitate their handling during grinding process and application of electrochemical methods. Struers technical data sheet recommended curing for 12h. In Figure 4.7b a specimen after removing the mold is shown.

a)   *b)*   *c)*

Figure 4.6: a) Mounting mold, b) Lubricating oil, c) Epoxy resin, hardener and mixing cup [www.struers.com].

a)   *b)*
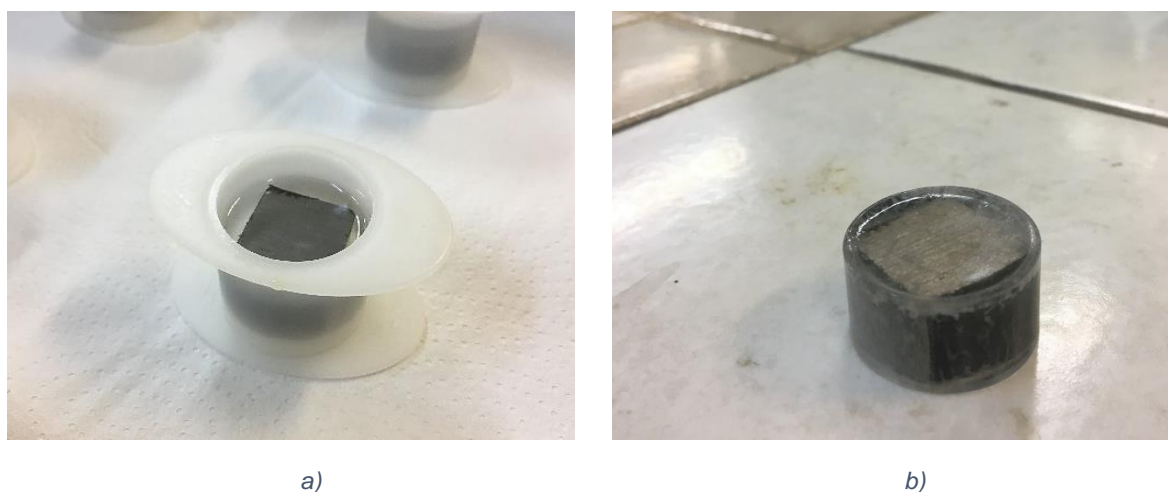
Figure 4.7: a) Specimen while curing, b) Specimen after removing the mold [personal photos].

The next step was **grinding** both surfaces of the metal specimens in order to be electrically permeable (necessary for the application of electrochemical methods) and to eliminate the geometric irregularities of the surface. During wet grinding, Silicon Carbide (SiC) Grinding Papers of grit (FEPA P) #80, #120, #180, #220, #320, #500, #800, #1000, #1200, #2000, #4000 were used, for 4 minutes each. The instrument employed was Struers Labopol5 (Figure 4.8), with running water for the removal of all debris but also for cooling purposes.

a)   b)
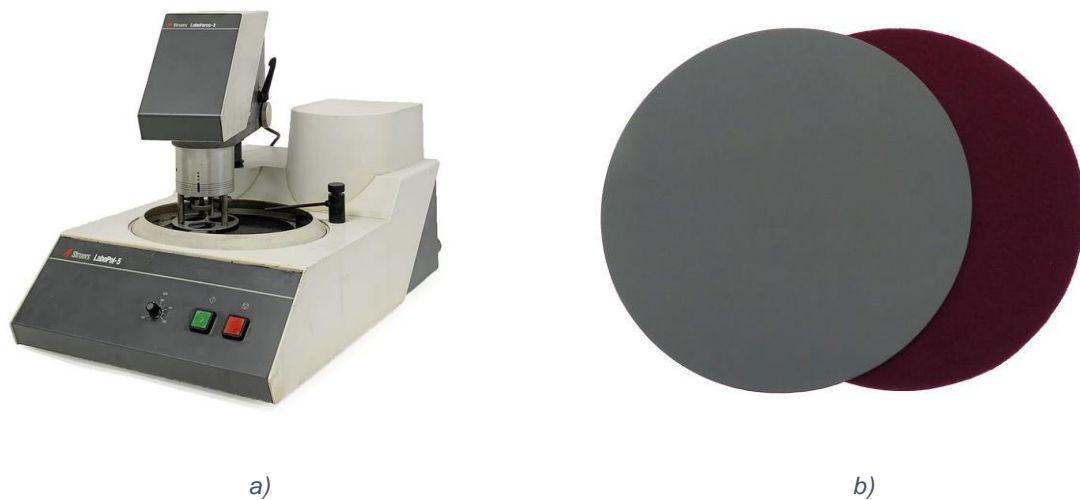
Figure 4.8: a) The metallurgical grinder and polisher Struers Labopol-5, b) Examples of grinding paper (left) and polishing cloth (right) [www.struers.com].

Then, **polishing** was followed using the same instrument. For this purpose, 3-5 grams of 1 μm and 0.1 μm agglomerated Al_2O_3 (alumina) ointments (Struers AP-A Suspension) were applied, on a velvet polishing cloth disc, for 8 minutes one after another, while keeping the cloth moist with distilled water. After cleaning the specimen and the polishing cloth with distilled water, 2-3 ml of water based diamond suspension of 1μm (Struers DiaPro) was used. Finally, all specimens were cleaned by distilled water and were degreased in pure ethanol.

It is worth mentioning that grinding and polishing were repeated before every experimental procedure of optical observation, micro-hardness measurements, X-Ray Fluorescent spectroscopy (XRF) and Scanning Electron Microscope (SEM). For the application of electrochemical techniques only grinding (from #80 to #4000 grid) was needed.

4.2. Observation and Study of the Metal Alloy

In the following section, the procedure followed and the equipment employed in this thesis are presented, along with a summary of the relevant theory. Optical Microscope (OM) and Scanning Electron Microscope (SEM) were both used for the study of the microstructure of the specimens. Moreover, a stereo microscope was used for the observation of their surface topography after each electrochemical technique. Last but not least, the micro-hardness of the steel and the chemical composition of the surface of the specimens were also measured using a micro-hardness tester and X-ray Fluorescent (XRF) spectroscopy, respectively.

4.2.1. Optical Observation

Optical Microscopy (OM)

Microscopes are effectively just tubes packed with lenses, curved pieces of glass that bend (or refract) light rays passing through them. The simplest microscope of all is a magnifying glass made from a single convex lens, which typically magnifies by about 5–10 times. There's a lens above the object (called the objective lens) and another lens near your eye (called the eyepiece or ocular lens). Each of these may, in fact, be made up of a series of different lenses. Most compound microscopes can magnify by 10, 20, 40, or 100 times, though professional ones can magnify by 1000 times or more. For greater magnification than this, scientists generally use electron microscopes.

In this thesis, a Leica DM ILM optical microscope was used for the observation of the specimens' microstructure, Figure 4.9. The parts of a microscope are the light source, the lenses that guide the light beam, the diaphragm, the magnifiers, the semi - reflective mirror, the objective lens, the table on which the specimen is placed for observation and allows its movement and the eyepiece. The main parts of an optical microscope as well as its function are shown schematically in Figure 4.10.

Figure 4.9: Microscope Leica DM ILM [www.leica-microsystems.com].
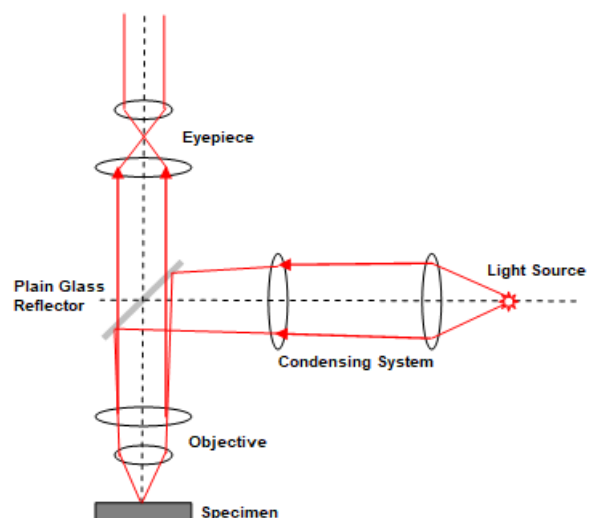
Figure 4.10: Schematic representation of the optical microscope function [www.substech.com].

In order for the microstructure of specimens to be visible with the optical microscope, their **chemical etching** is required. This is the most usual technique revealing the features of the structure and is based on 'selective' corrosion of grain boundaries. Also, the atoms which belong to different crystal lattices (i.e. in different phases) are dissolved at different rates, creating contrast in the surface. Thus, the appearance and the display of the microstructural characteristics, when they are observed by the optical microscope, are more visible.

The etching was done by immersing the polished metal surface in an appropriate chemical reagent. For this purpose, a solution of nitric acid 3% v/v and ethanol 97% v/v (Nital 3%) was made. Specimens' surface were immersed in the solution for 8 to 15 seconds and they cleaned directly by distilled water and ethanol. Afterwards, the specimens were examined in different areas of their surface through the microscope, using LAS Software for image editing.

Scanning Electron Microscopy (SEM)

The Scanning Electron Microscope (SEM) is used to observe and characterize surface features over large (or small) surface of the specimen. The primary electron beam interacts with the specimen surface to produce secondary electrons, backscattered electrons and X-rays. With detectors mounted just above the specimen, these electrons and X-rays can be collected and analyzed to provide important information about the specimen surface. Subsequently, we look at each interaction. In Figure 4.11, the basic operating principles of a Scanning Electron Microscope are presented, along with a sketch showing some of the different types of electrons and x-rays, generated by the interaction of the primary incident electron beam, which will be explained in detail below.
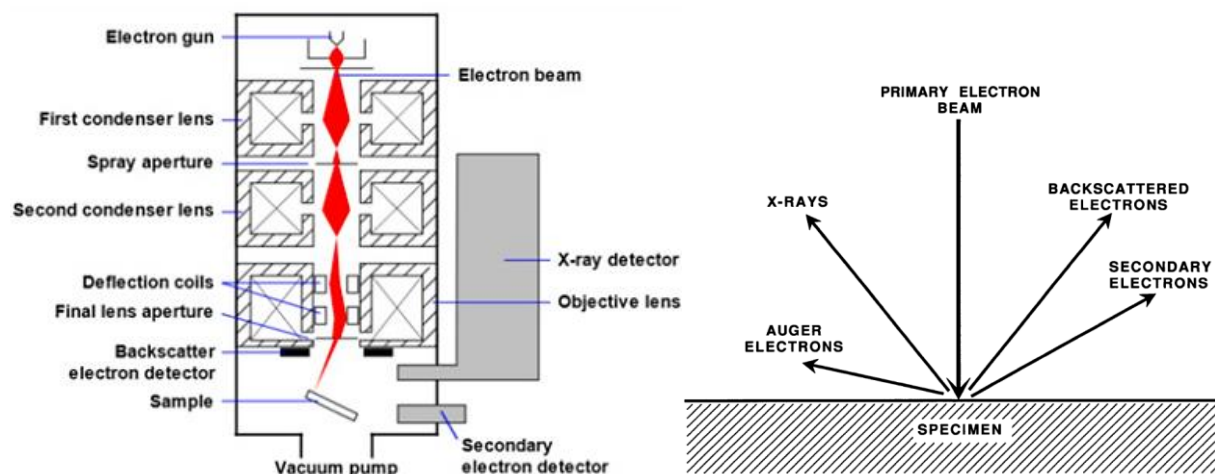
Figure 4.11: From left to right: Schematic representation of a Scanning Electron Microscope [NanoScience Instruments], a sketch showing some of the different types of electrons and x-rays generated by the interaction of the primary incident electron beam with the specimen in the electron microscope [Bramfitt and Benscoter, 2002].

The backscattered electrons are those electrons that are scattered from the specimen surface and can be collected as the primary beam scans the specimen surface. The collected backscattered electron image of the specimen surface is displayed on a cathode ray tube

(CRT) and can be photographed. The higher the atomic number of the elements in the sample, the greater the degree of backscattering (less energy loss). This means that elements with higher atomic numbers (e.g. Fe, with an atomic number of 26) will appear brighter on the backscattered electron image on the CRT than elements with lower atomic numbers (e.g. O_2, with an atomic number of 8).

Secondary electrons, on the other hand, are the result of the interaction of primary beam electrons with the electrons contained within the atoms in the sample. The primary electrons can actually knock the loosely held orbital electrons from atoms, which are called secondary electrons and have much lower energy than the backscattered electrons. Thus, the secondary electrons can only be detected from the surface and near-surface regions of the specimen because those from deeper regions are easily absorbed by the sample. As a result, the secondary electrons yield a secondary electron image on the CRT that reveals surface topography and produces an image with enhanced depth of field, which makes the SEM one of the most useful microscopes.

X-rays are also emitted from the sample, because of the interaction of the primary and backscattered electrons with the inner shell electrons of atoms in the sample. The primary/backscattered electrons have sufficient energy to knock inner shell electrons out of orbit. Where an electron is knocked out of a particular inner electron shell, an X-ray is emitted when an electron moves into space. The X-rays have a characteristic energy and wavelength for the particular atomic species present. Because of this, they are called characteristic X-rays, which means that every X-ray that is collected has an energy and wavelength that is unique to the particular element present in the sample. The importance of collecting these X-rays is that compositional information can be obtained. Generally, in a SEM, only the X-ray energy is analyzed.

In this study, the JEOL JSM-6390 Scanning Electron Microscope was used, Figure 4.12, in order to study in detail the metal microstructure. In order for this method of observation to be applied, the specimen's surface was **chemical etched**, following the same procedure as with the previous method of OM.

Figure 4.12: JEOL JSM-6390 Scanning Electron Microscope [Ziakas, 2020].

Stereo Microscopy

The stereo microscope is an optical microscope for low magnification observation of a sample using incident light illumination. The two objectives and two eyepieces provide the eyes with slightly different viewing angles. In essence, the left and right eye are seeing the same object but in a different way. Thus, it produces a three-dimensional visualization of the specimen.

Stereomicroscopy overlaps macro photography for recording and examining solid samples with complex surface topography where a three-dimensional view is essential for analyzing the detail. The stereo microscope is often used to study the surface of solid specimens or to carry out close work.

In this study, a Leica MZ6 stereo microscope was used for the observation of the specimens' surface, Figure 4.13, after the application of each electrochemical technique. LAS Software was used for the image editing.

Figure 4.13: Stereomicroscope Leica MZ [www.leica-microsystems.com].

4.2.2. Micro-hardness Measurement

Microhardness Tester

A hardness testing for the two samples was conducted at STL, using Wolpert Wilson Instruments 402 MVD, Figure 4.14. This is actually a pressure testing, with a penetrator of known geometry and mechanical properties, and with application of a small load to the specimen. Vickers micro-hardness testing method was used. In this method the penetrator is a diamond in the form of a square-based pyramid, with face angles of $136°$.

Figure 4.14: Wolpert Wilson Instruments 402 MVD.
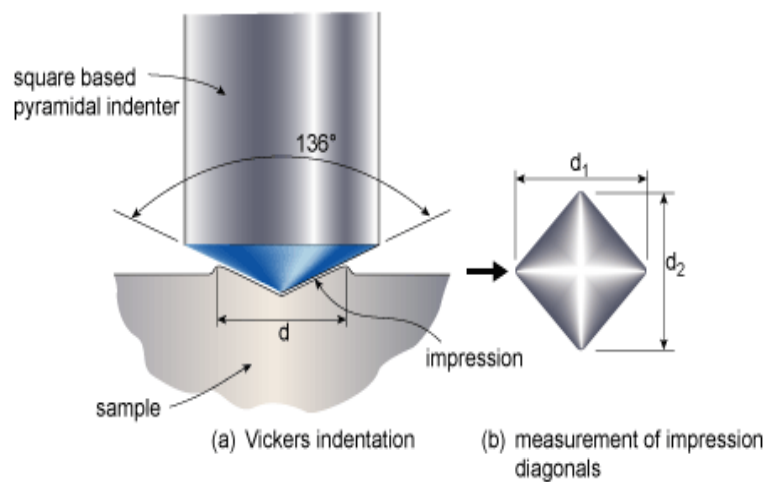
Figure 4.15: Vickers testing mechanism.

The applied load was 0.3 kilopond (= 300 p = 300 gr or 2.9420 N) and the loading time was 10 seconds (according to standard ASTM E 384). After testing, a diamond-shaped indent appears on the surface of the specimens, as shown schematically in Figure 4.15. The lengths of the two diagonals d_1 and d_2 of the resulting square indent are measured by the micro hardness tester and their average value d is used in order for the HV to be calculated, as:

$$HV = \frac{1854.4 \ \times P}{d^2}$$

(4.1)

where P is the applied force in gr and d is the mean diagonal length in mm. Ten (10) measurements were taken for each specimen, in different area of their surface every time.

4.2.3. Chemical Composition Measurement

X-Ray Fluorescent Spectroscopy (XRF) – Carbon Equivalent

X-ray Fluorescence (XRF) spectroscopy was used to calculate the chemical and elemental composition of the materials. It is the measurement and analysis of samples excited by incident radiation. The two primary components of an XRF spectrometer are an X-ray output and a sensitive detector capable of determining fluorescent X-rays from the incident light. XRF spectrometer works because if a sample is illuminated by an intense X-ray beam, known as the incident beam, some of the energy is scattered whilst some is absorbed within the sample in a manner that depends on its chemistry. When this primary X-ray beam illuminates the sample, it is said to be excited. The excited sample in turn emits X-rays along a spectrum of wavelengths characteristic of the types of atoms present in the sample.
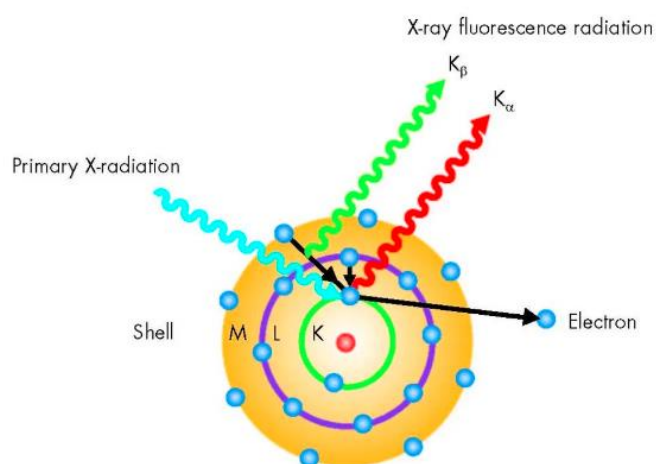
Figure 4.16: The principle of X-ray fluorescent spectroscopy [FISCHER].

Figure 4.17: XRF S1 Turbo Bruker [www.bruker.com].

The atoms in the sample absorb X-ray energy by ionizing, ejecting electrons from the lower energy levels (Figure 4.16). The ejected electrons are replaced by electrons from an outer, higher energy orbital. When this happens, energy is released due to the decreased binding energy of the inner electron orbital compared with an outer one. This energy release is in the form of emission of characteristic X-rays indicating the type of atom present.

For the purposes of this study, an XRF S1 Turbo Bruker portable device (Figure 4.17) was employed for the analysis of the elemental composition of the specimens. Three measurements were taken for each specimen. It has to be mentioned that XRF instrument has a specially designed software that recognizes only metallic elements (i.e. will not present values for carbon) and records those with content greater than 0.01%.

Thus, knowing the chemical composition, **Carbon Equivalent**, for each specimen, was calculated. Carbon Equivalent (CE) is an empirical value in weight percent, relating the combined effects of different alloying elements used in the manufacturing of carbon steels to an equivalent amount of carbon.

This value can be calculated using a mathematical equation. These kind of relationships originate from about 1940 when Dearden and O'Neill proposed a carbon equivalent formula to predict steel strength, hardenability and HAZ hardness. In 1967, the International Institute for Welding (IIW) adopted a somewhat simplified form of Dearden and O'Neill's formula for hardenability which became a generally accepted measure of steel weldability:

$$CE_{IIW} = C + \frac{Mn}{6} + \frac{Cr + Mo + V}{5} + \frac{Ni + Cu}{15} \qquad (4.2)$$

where C, Mn, Cr, Mo, V, Ni, Cu are the content of carbon, manganese, chromium, molybdenum, vanadium, nickel and copper, respectively, of the alloy steel. The CE_{IIW} formula is based on seven elements although carbon is considered to have more significance than the others. Since its adoption by IIW, the equation has been incorporated into a number of material standards and codes, including EN 1011-2:2001.

Carbon equivalent formula were originally developed to give a numerical value for a steel composition which would give an indication of a carbon content that contributes to an equivalent level of hardenability for that steel. They are also used as compositional characterising parameters for other properties that may be linked to hardness, such as toughness and strength. By varying the amount of carbon and other alloying elements in the steel, the desired strength levels can be achieved by proper heat treatment. A better weldability and low temperature notch toughness can also be obtained. In terms of welding, the Carbon Equivalent governs the hardenability of the parent metal. These formulas were later extended to represent the contribution of the composition to the hydrogen cracking susceptibility of steel.

4.3. Corrosion Study

A simplified way of visualizing an electrochemistry experiment consists of imagining a system that responds to a given perturbation. When a given excitation function (e.g. a potential step) is applied to the electrochemical cell, a response function to that perturbation is recorded (e.g. the produced current variation as a function of time), keeping all other system variables constant. Thus, the main goal of an electrochemistry experiment is to obtain information (thermodynamic, kinetic, analytic, etc.) from the observation of perturbation and response processes, which may contribute to the construction of appropriate models, and the comprehension of the fundamentals aspects of the investigated system. This allows a better control of the variables influencing the electrochemical behavior.

For this purpose, the procedure of the corrosion study includes the forced imposition of corrosion of the specimens, employing an appropriate laboratory setup, the extraction of data from it and their processing and of course the observation of the corroded specimens' surface with a stereo microscope. The aforementioned actions are described thoroughly in the next paragraphs.

4.3.1. Experimental Setup

Electrochemical corrosion tests are performed using an experimental setup, consisting of a potentiostat, equipped with a data logger, and an electrochemical cell. Moreover, a computer with the corresponding software is employed to import the appropriate parameters and record data. This layout is schematically shown at Figure 4.18.
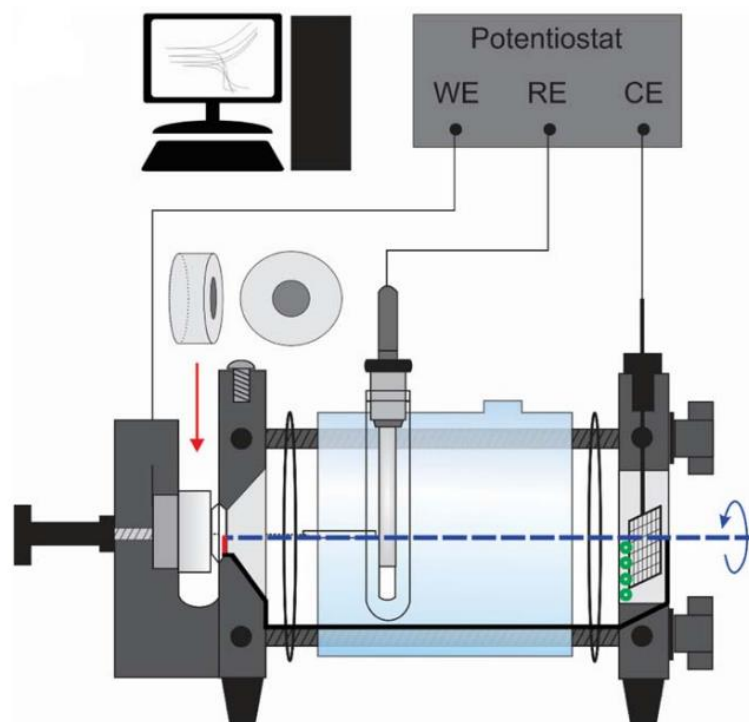
Figure 4.18: Simulation of the experimental setup for the application of the electrochemical techniques. WE: Working Electrode, RE: Reference Electrode, CE: Counter Electrode or Auxiliary Electrode [Perry, 2019].

In electrochemical experiments, a typical **electrochemical cell** is formed by a vessel commonly made of glass where the electrolyte is inserted. The electrodes are then immersed in this solution. The cell can be covered by an external and isolated glass wall jacket connected to a thermostatic bath to maintain the electrolyte temperature constant. Other ways of developing the cell and controlling the electrolyte temperature during the process can also be employed. Generally, three types of electrodes are used in this type of experiment: working electrode (**WE**), reference electrode (**RE**), and auxiliary electrode or counter electrode (**CE**). The **working electrode** is the conductor substrate where the chemical reaction of interest takes place. The working electrode potential is measured in relation to the **reference electrode**, which must present a known constant potential with respect to the standard hydrogen electrode within the potential window analyzed. An **auxiliary** or **counter electrode** is necessary for the flow of electric and ionic current, it closes the electrical circuit of the system and allows for the passing of a current through the external system. A magnetic stirrer can also be used to keep constant the transport process of species at the electrode/electrolyte interface. A bubbler for N_2 input and a saturator can also be employed for removal of the oxygen dissolved in the electrolyte, and the maintenance of an inert gaseous phase inside the cell. This type of cell configuration is commonly used in electrodeposition reactions, which are reactions where the ions present in the electrolyte are deposited over the substrate surface by means of a reduction reaction. A typical cell used in these types of reactions is shown in Figure 4.20.

More specifically, the **potentiostat** system used for this study is VersaSTAT 4 Potentiostat Galvanostat (Figure 4.19) along with its software, VersaStudio. The potentiostat comes with four cables:

1. **CE**: Counter Electrode or Auxiliary Electrode
2. **RE**: Reference Electrode,
3. **WE**: Working Electrode and
4. **GND**: Ground connection,

the first three of which are getting connected to the electrochemical cell, as mentioned above.

It is also worth mentioning that the **reference electrode** employed for the experiments of this thesis was Saturated Calomel Electrode (SCE) in saturated Potassium Chloride (KCl) solution. This electrode's potential, according to the Standard Hydrogen Electrode (SHE) at 25∘C, is E = + 0.242 V. The **auxiliary electrode** was a Platinum (Pt) Mesh Electrode. Finally, for each experiment, **working electrode** was the specimen studied, which was clamped to the cell, exposing 1.0 cm^2 of the specimen surface to the electrolyte.

Figure 4.19: The potentiostat VersaStat 4 [www.ameteksi.com] and its connection cables [Autolab, 2011].
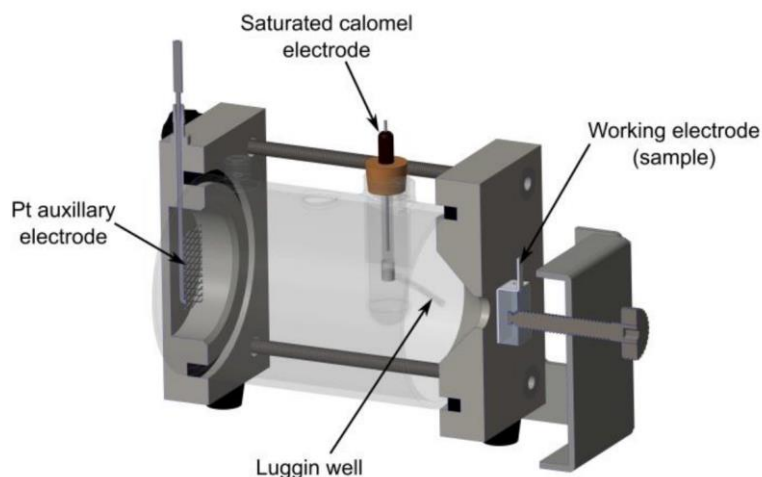
Figure 4.20: Side view of longitudinal section of the three – electrode electrochemical cell [Bailey and Sun, 2017].

The **electrolyte** used for all tests was aerated 3.5% w/v (0.6 M) NaCl solution, which was prepared from analytical grade Sodium Chloride and distilled water, and it has been considered to simulate sea water according to Standard ASTM G44. To be specific, the existence of salts raises the conductivity of the solution, which permits lower polarization with higher corrosion currents between adjacent anodes and cathodes [Jones D. A., 1996]. Figure 4.21 shows that the maximal relative corrosion rate occurs when concentration of NaCl reaches about 3% w/v. The relative corrosion rate decreases when concentration of NaCl increases beyond this percentage, as still higher dissolved salt decreases the solubility of dissolved oxygen. However, seawater has a NaCl concentration of about 3.5% weight percentage, which is very close to the critical NaCl concentration where highest corrosion rate occurs. Therefore, seawater would have a high tendency to cause corrosion [Zhang and Dzombak,2010]. Inter alia, all tests were conducted at standard room temperature open to the air (aerated solution).

Finally, after each corrosion experiment, the specimens were cleaned again with distilled water and ethanol and were observed via modular stereomicroscope (see Appendix A).
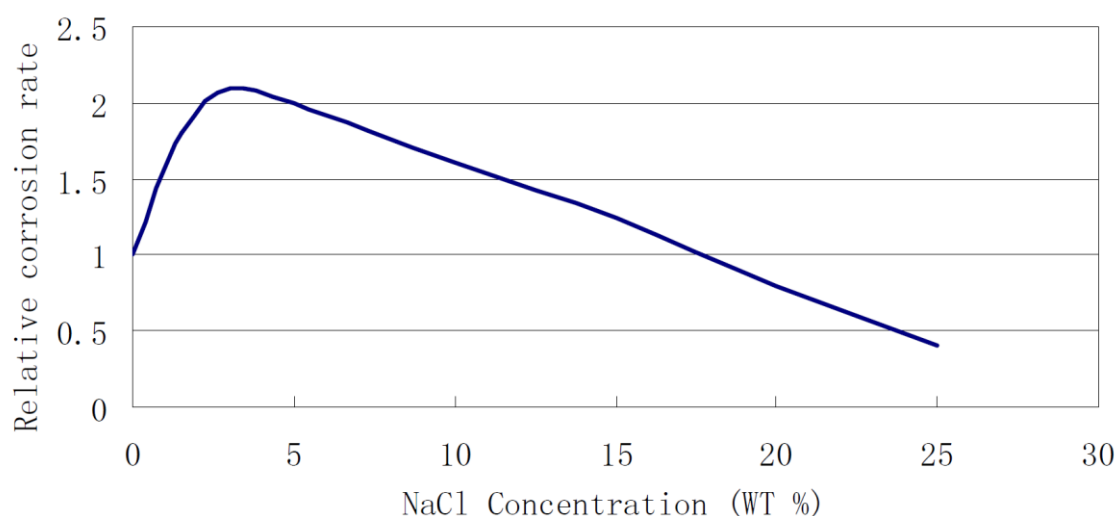
Figure 4.21: Dependence of relative iron corrosion rate with NaCl concentration in water (Reproduced from Jones D. A., 1996), [Zhang and Dzombak,2010].

4.3.2. Application of Electrochemical Techniques (VersaStudio)

For the evaluation of the corrosion resistance of the specimens, **five (5) electrochemical techniques** were employed; Open Circuit Potential (OC), Linear Polarization Resistance (LPR), Potentiodynamic Polarization - Tafel Extrapolation, Electrochemical Impedance Spectroscopy (EIS) and Cyclic Potentiodynamic Polarization (CPP).

As mentioned in paragraph 4.3.1. the software used is **VersaStudio** and in Figure 4.22 there is a listing from the program's environment of the available "technique actions".
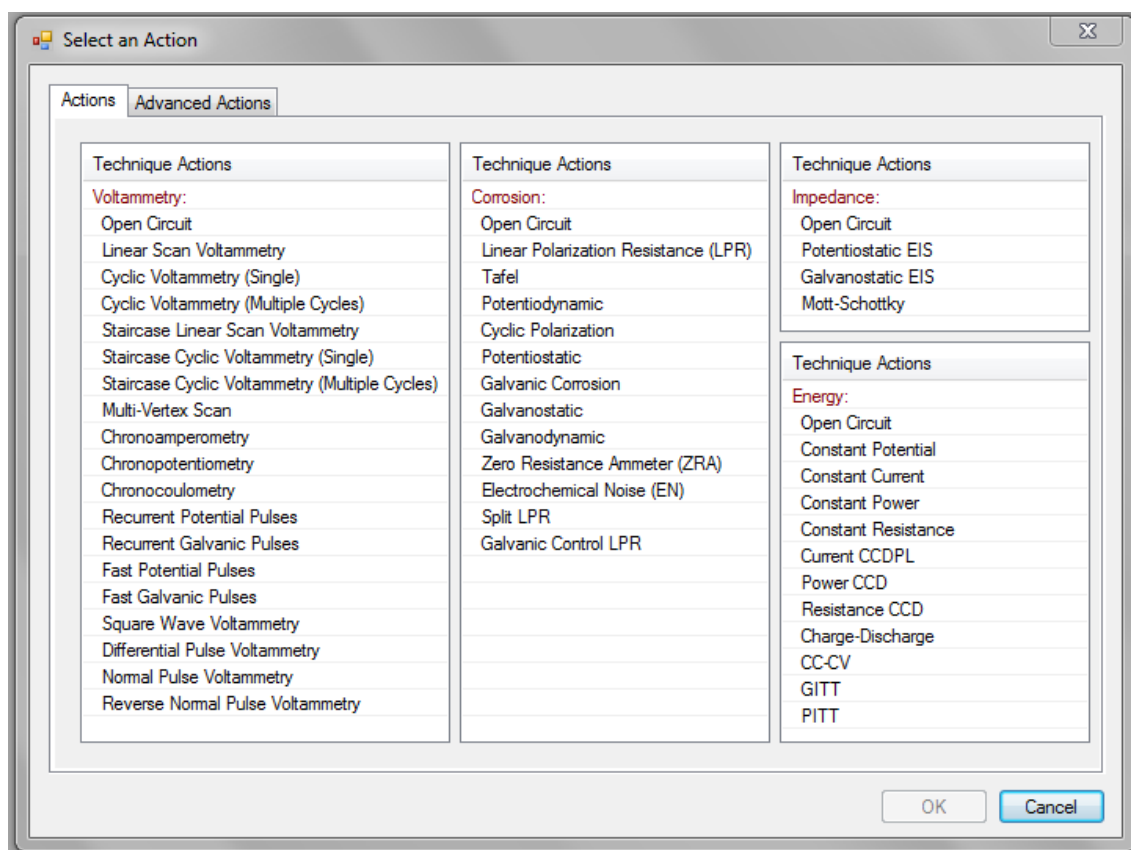
Figure 4.22: Available technique actions at VersaStudio menu box [VersaStudio Software Manual].

A single action or multi-action (sequence or loop) experiment can be performed. A brief description of the actions used for this thesis is cited below [VersaStudio Software Manual], along with a schematic categorization in Figure 4.23.

Open Circuit: Corrosion technique that does not apply any Voltage or Current (Cell OFF), and simply measures the Voltage difference between the Working-Sense and Reference electrodes. The data is acquired for either a set Period of time (here this method used), or preferably to a minimum Drift Rate. The current readings that are shown are the resolution limits for the Current Range on which the data was collected; these Current magnitudes are artifacts and should not be considered actual Currents for the **OC** actions.

Linear Polarization: Corrosion technique that uses a single voltage scan or ramp programmed from an Initial Potential to a Final Potential (range generally limited to +/- 20 mV

vs. Open Circuit at Ecorr) that progresses at a defined Step Height per Step Time. Technique also referred to as **LPR** (Linear Polarization Resistance) and provides the capability to calculate corrosion rate.

Tafel: Corrosion technique that uses a single voltage scan or ramp programmed from an Initial Potential to a Final Potential (range generally limited to +/- 250 mV vs. Open Circuit at Ecorr) that progresses at a defined Step Height per Step Time. Provides capability to calculate Tafel constants and corrosion rates.

Potentiostatic EIS: Electrochemical impedance spectroscopy (**EIS**) measures impedance (Z) by applying a sinusoidal (AC) voltage across a cell and measuring the resulting ac current along with phase shifts between the ac voltage and ac current. In this technique, a sequence of impedance measurements is carried out starting at an initial frequency and stopping at a final frequency. The DC potential within the EIS action can be applied as a step for a constant voltage relative to open circuit or reference, or the DC voltage can be applied as a ramp up to the final voltage which is then held constant for the entire EIS experiment.

Cyclic Polarization: Corrosion technique utilizing a two-step voltage scan or ramp programmed from an Initial Potential to a Vertex Potential, and from the Vertex to a Final Potential, at a defined Step Height per Step Time. The Vertex Potential may also be defined by a specific current (Threshold Current) that limits the forward scan to the potential at which that current is reached. Technique also referred to as a **CP** or a "pitting scan," as it is used to determine the tendency of a material to undergo surface pitting or crevice corrosion.
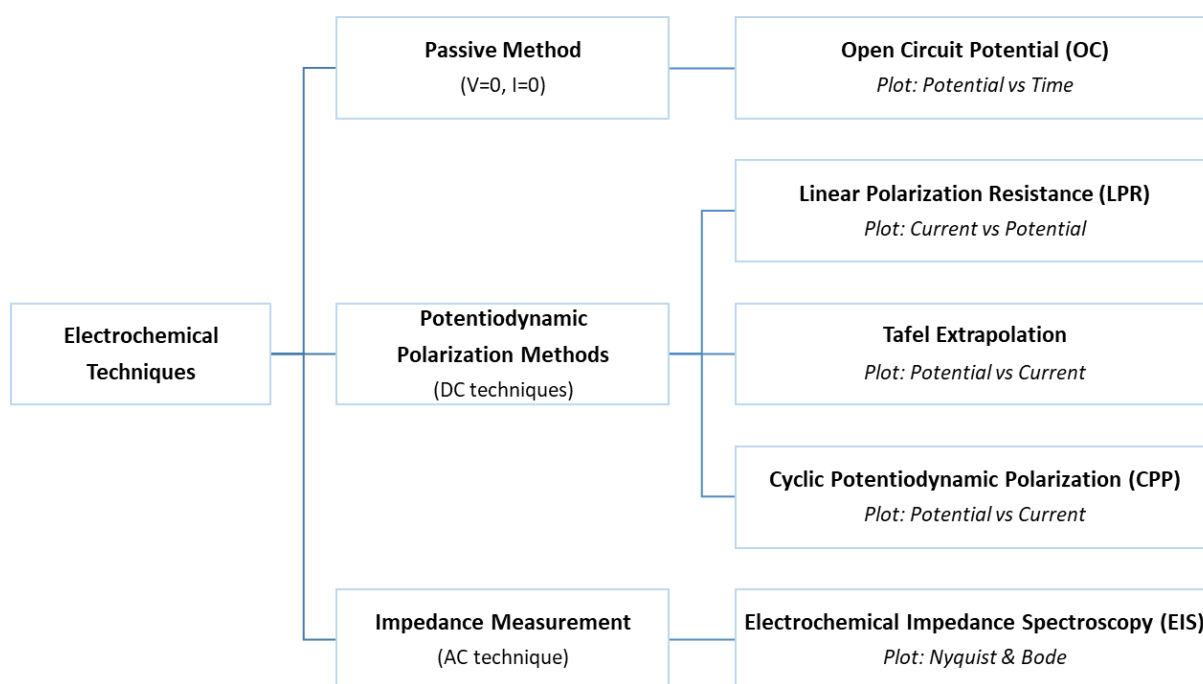
Figure 4.23: Categories of electrochemical techniques employed in the present thesis. The plot which depicts the results of each technique is also mentioned.

In order to apply each electrochemical technique, certain **parameters** were set at VersaStudio <u>Experiment Properties window</u>. At this window there is, also, the **Common action**

for every single-Action or multi-action experiment built, where Reference Electrode type, Working Electrode Type, and Working Electrode Area are set. These settings are mentioned in Table 4.1.

Table 4.1: Electrochemical techniques' parameters – VersaStudio.

Method	Parameters		Value
LPR	Step Properties	Initial potential:	-0.02 V vs OC
		Final potential:	0.02 V vs OC
	Scan Properties	Step height:	0.2 mV
		Step time:	0.2 sec
Tafel	Endpoint Properties	Initial potential:	-0.25 V vs OC
		Final potential:	0.25 V vs OC
	Scan Properties	Step height:	0.5 mV
		Step time:	3 sec
EIS	AC Properties	Start frequency:	10000 Hz
		End frequency:	0.01 Hz
		Amplitude:	10 mV RMS
	Scan Properties	Point spacing:	Logarithmic
		Number of points:	30
		Points per decade:	10
		Data quality:	1
		Measurement delay:	0 sec
CP	Endpoint Properties	Initial potential:	-0.1 V vs OC
		Vertex potential:	1.2V vs ref.
		Final potential:	0 V vs OC
	Scan Properties	Step height:	1 mV
		Step time:	1 sec

Properties for Common	
Reference Electrode:	SCE Saturated Calomel – st'd KCl
Working Electrode Type:	Solid Electrode
Working Electrode Area:	1 cm^2

For both samples, six (6) different sequences of electrochemical techniques were performed:

1. **24h OC:** Open Circuit Polarization (OC) was applied with duration of 24 hours.

2. **48h OC:** Open Circuit Polarization (OC) was applied with duration of 48 hours.

3. **OC – 2 consecutive LPR – TAFEL** (3 repetitions)**:** Firstly, a single Open Circuit Polarization (OC) of 30 minutes duration was applied. Afterwards, two (2) single-action Linear Polarization Resistance (LPR) were applied, each one with final potential of 0.02 Volt versus the previous OC. Lastly, Potentiodynamic Polarization

(Tafel Extrapolation) was applied with final potential of 0.25 Volt versus the OC. This routine was repeated for three (3) times.

4. **OC – 3 consecutive EIS:** Firstly, a single Open Circuit Polarization (OC) of 30 minutes duration was applied. Afterwards, three (3) single-action Electrochemical Impedance Spectroscopy (EIS) were applied, each one with end frequency of 0.01 Hertz.

5. **24h 6loop OC–EIS:** Six (6) loops of Open Circuit Polarization (OC) and Electrochemical Impedance Spectroscopy (EIS) were applied with total duration of about 24 hours. Firstly, a single OC of 30 minutes duration was applied. Afterwards, the EIS method was imposed at specific time and ended when reached at frequency of 0.01 Hertz. In the meantime, OC method was running.

6. **OC – CP** (2 repetitions)**:** Firstly, a single Open Circuit Polarization (OC) of 30 minutes duration was applied. Afterwards, Cyclic Potentiodynamic Polarization (CP) was applied with final potential of 0 Volt versus the previous OC. This routine was repeated for two (2) times.

The aforementioned experimental procedures applied are summarized in the Table 4.2 below:

Table 4.2: Schedule of electrochemical experiments for each specimen.

Schedule													

Experiment	Techniques Applied												
24h OC	OC												
48h OC	OC												

	1st Run			2nd Run			3rd Run		
OC – LPR – TAFEL	OC	LPR_1 LPR_2	TAFEL	OC	LPR_1 LPR_2	TAFEL	OC	LPR_1 LPR_2	TAFEL

OC – EIS	OC	EIS_1	EIS_2	EIS_3

	t = 0h		t = 2h		t = 4h		t = 8h		t = 16h		t = 24h	
24h OC – EIS	OC_1	EIS_1	OC_2	EIS_2	OC_3	EIS_3	OC_4	EIS_4	OC_5	EIS_5	OC_6	EIS_6

	1st Run		2nd Run	
OC – CP	OC	CPP	OC	CPP

4.3.3. Elaboration of Experimental Data (EC-Lab)

For the elaboration and the plotting of the experimental data obtained from Versa Studio software, **EC Lab software** was used. The procedure used for the analysis and its mathematical background are described below and are derived from the EC-Lab Software Manual.

For several of the applied techniques, such as Linear Polarization Resistance (LPR), Potentiodynamic Polarization with Tafel Extrapolation and Potentiostatic EIS, a different fitting process for the experimental curves is available and it is used to characterize the corrosion behavior of the materials. These measurements are used to determine the characteristic parameters such as:

- The corrosion potential, E_{corr}.
- The corrosion current, I_{corr}.
- The Tafel constants β_a (anodic coefficient) and β_c (cathodic coefficient) for the anodic and cathodic reactions, respectively, defined as positive numbers. The Tafel constants can be given as b_a and b_c where $b_a = \ln10/\beta_a$ and $b_c = \ln10/\beta_c$.
- The polarization resistance R_P.

These techniques are built upon the assumption that the electrochemical systems are **Tafelian** i.e. that the current flowing in the electrode is only limited <u>by the electron transfer</u> and <u>not by mass transport</u>. In this case the potential-current relationship is described by the **Stern or Wagner-Traud equation**

$$\mathbf{I} = \mathbf{I_{corr}} \cdot \mathbf{exp} \frac{\mathbf{ln10(E - E_{corr})}}{\boldsymbol{\beta_a}} - \mathbf{I_{corr}} \cdot \mathbf{exp} \frac{\mathbf{-ln10(E - E_{corr})}}{\boldsymbol{\beta_c}} \qquad (4.3)$$

It is, also, worth mentioning that all the techniques are valid for a negligible ohmic drop.

The corrosion analysis menu contains tools such as **R_p Fit,** for the analysis of the data of LPR experiments**,** and **Tafel Fit**, for the extrapolation of the experimental data of the Potentiodynamic Polarization technique, to determine current and coefficients of corrosion.

4.3.3.1. Tafel Fit

The Stern equation predicts that for $E \gg E_{corr}$ the **anodic** reaction predominates and that for $E \ll E_{corr}$ the **cathodic** reaction predominates. This is known as the Tafel approximation:

$$\mathbf{I} \approx \mathbf{I_{corr}} \cdot \mathbf{exp} \frac{\mathbf{ln10(E - E_{corr})}}{\boldsymbol{\beta_a}}, \qquad \text{for } E \gg E_{corr}$$

$$\mathbf{I} \approx -\mathbf{I_{corr}} \cdot \mathbf{exp} \frac{\mathbf{-ln10(E - E_{corr})}}{\boldsymbol{\beta_c}}, \quad \text{for } E \ll E_{corr} \qquad (4.4)$$

This can be written:

$$I \approx I_{corr} 10^{\frac{(E-E_{corr})}{\beta_a}}, \qquad \text{for } E \gg E_{corr}$$

$$I \approx -I_{corr} 10^{\frac{-(E-E_{corr})}{\beta_c}}, \quad \text{for } E \ll E_{corr}$$

(4.5)

So, in a **log|I| vs. E** representation, one should see two linear parts, one for $E \gg E_{corr}$ (the anodic) and one for $E \ll E_{corr}$ (the cathodic):

$$\log|I| \approx \frac{E - E_{corr}}{\beta_a} + \log I_{corr}, \qquad \text{for } E \gg E_{corr}$$

$$\log|I| \approx \frac{E_{corr} - E}{\beta_c} + \log I_{corr}, \quad \text{for } E \ll E_{corr}$$

(4.6)

A typical Potentiodynamic Polarization experimental curve (the potential, E, in Volts as a function of absolute micro Amperes of the current, I, in logarithmic scale) is presented in Figure 4.24 with blue trace. The Tafel Extrapolation (Tafel fit) is shown with red color, where the linear parts of the curves allows the user to find the Tafel coefficients. The black linear curves are the representation of the equations (4.6). E_{corr} is also visible with a black horizontal line.
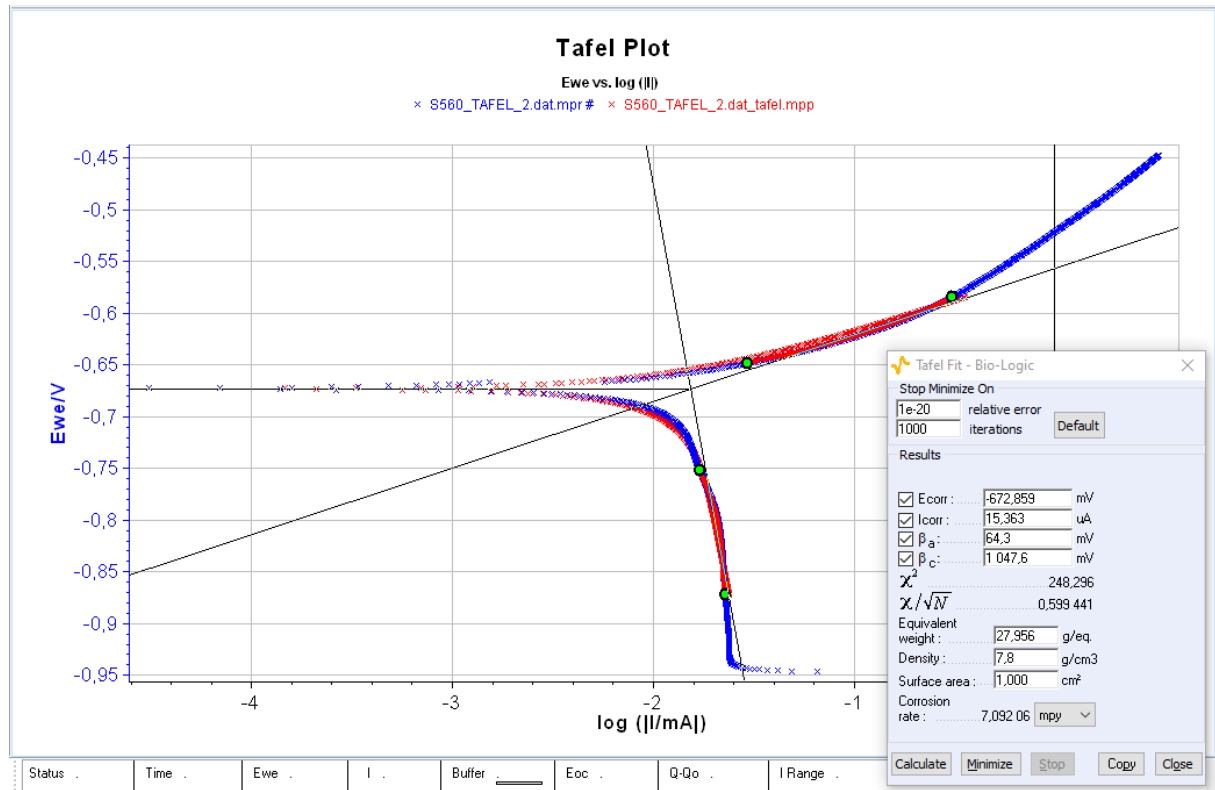
Figure 4.24: Potentiodynamic Polarization curve with Tafel Extrapolation (Tafel fit) analysis.

Firstly, two linear regressions are automatically made using the least square method. Each linear fit (the anodic and the cathodic) is limited with two circle markers that can be moved.

The results of the Tafel Fit are recalculated whenever a marker is moved. The default positions of the markers are ± 80 mV and ± 200 mV around E_{corr}. Thanks to the intersection of the linear regressions, the software calculates:

- the corrosion potential E_{corr},
- the corrosion current I_{corr} and
- the Tafel coefficients, β_a and β_c.

Finally the corrosion rate, CR, is in milli-meter per year [mmpy] or milli-inches per year [mpy], is calculated according to the following equation:

$$CR = \frac{I_{corr} \cdot K \cdot EW}{d \cdot A}$$

(4.7)

where:

- I_{corr}: corrosion current [A],
- K: constant that defines the units of the corrosion rate,
- EW: equivalent weight [g/equivalent], is defined as the molar mass of the oxidized metal divided by the number of electrons involved in the dissolution reaction,
- d: density [g/cm^3] and
- A: sample area [cm^2].

The fit can be minimized with a Simplex method and the fit accuracy can be estimated with the χ^2 or the $\chi/\sqrt{N}$. More specifically, in some cases the calculation of the Tafel parameters and corrosion parameters may not yield a satisfying fit because for instance within the default potential ranges chosen, the material does not exhibit a "Stern" behavior but more a mass transport limited behavior or a passivation. In these cases, it is possible to numerically find satisfying parameters and reduce the error between the model Icalc,i and the measured data Imeas,i by minimizing the following value:

$$\chi^2 = \frac{1}{N} \sqrt{\frac{\sum_{i=1}^{n}\left(I_{meas,i} - I_{calc,i}\right)^2}{I_{meas,i} + 10^{-9}}}$$

(4.8)

4.3.3.2. Rp Fit

For $E \approx E_{corr}$, it is possible to simplify the Stern equation using near-field approximation, so that:

$$I = I_{corr}(E - E_{corr})\frac{\beta_a + \beta_c}{\beta_a \beta_c} \ln 10, \qquad for\ E \approx E_{corr} \tag{4.9}$$

This equation is commonly presented with E as function of I:

$$E = \frac{I \cdot \beta_a \beta_c}{I_{corr}(\beta_a + \beta_c) \ln 10} + E_{corr} \tag{4.10}$$

When expressed this way, it is easy to see that $E = E_{corr}$ for $I = 0$. The **slope** of this equation dE/dI is named the **polarization resistance** because it has the unit of a resistance (if the current is used) and is commonly abbreviated R_P:

$$\left(\frac{dE}{dI}\right)_{E_{corr}} = R_{P,E_{corr}} = \frac{\beta_a \, \beta_c}{I_{corr}\,(\beta_a + \beta_c) \ln 10} \tag{4.11}$$

This relationship is commonly named the Stern-Geary (or Wagner-Traud) relationship.

A typical Linear Polarization experimental curve (the current I, in micro Amperes, as a function of the potential, E, in Volts) is presented in Figure 4.25 with blue trace. The selected fitted data points are shown with red color. The black linear curve represents the slope of the curve, i.e. the polarization resistance R_P.
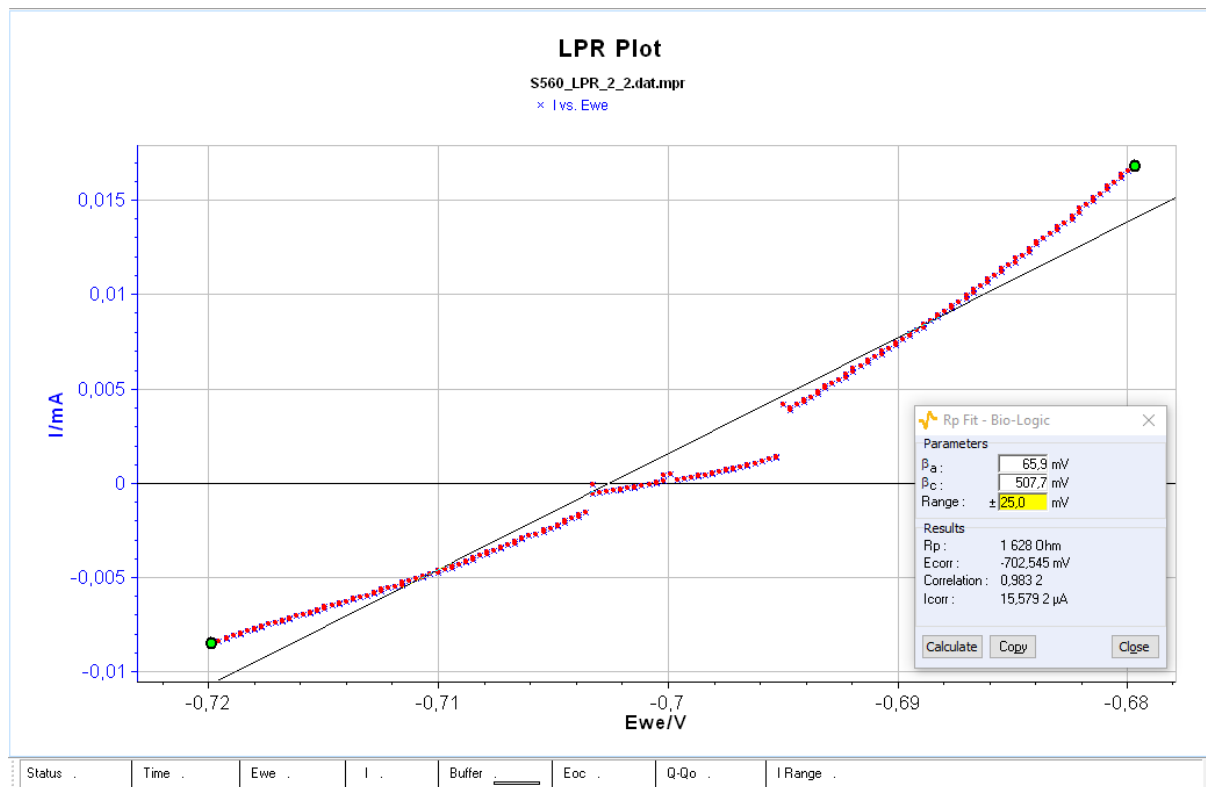
Figure 4.25: Linear Polarization curve and fitted curve representing the Polarization Resistance R_P. Right down the Rp Fit window is shown.

For the Rp Fit, the user has to select the experimental data points and the software will automatically find a potential value E_1 on the curve for I = 0. Then, the Tafel coefficients, β_a and β_c, determined previously by the Tafel fit, are inserted along with a range of potential (here ± 25 mV). Two circle markers are set in the potential range selected around E_1, which define the area that is qoing to be fitted. The fit can be adjusted by the user by moving the markers. The Rp Fit calculates:

- the polarization resistance, R_P,
- the open circuit potential E_{corr},
- the correlation coefficient, which shows the accuracy of the linear regression, and
- the corrosion current I_{corr}.

4.3.3.3. Electrochemical Impedance Spectroscopy (Z fit)

Impedance analysis is a powerful tool to determine the mechanism involved in an electrochemical reaction and the values of the kinetic parameters of this mechanism. Electrochemical impedance data analysis allows the user to propose an electrochemical reaction mechanism to define the system. The expression of the faradaic impedance of a certain type of reaction can be represented by an equivalent circuit of resistors, capacitors, inductors and diffusion elements with specific values. Knowing these values and the type of equivalent circuit help interpreting the impedance data.

As already mentioned in Chapter 3, the EIS technique normally uses a typical three-electrode cell system controlled by a potentiostat. By applying a small varying perturbation over a range of frequency, it is possible to probe the full response of the electrochemical system, and not just the resistive components. When a sinusoidal alternating potential signal V(t) is applied to an electrode surface, the time-dependent current response I(t) is expressed through an angular dependent impedance Z(ω). **Ohm's Law** connects these three parameters:

$$Z(\omega) = \frac{V(t)}{I(t)} \tag{4.12}$$

where:

$$V(t) = V_0 \sin(\omega t) \tag{4.13}$$

$$I(t) = I_0 \sin(\omega t + \theta) \tag{4.14}$$

where **t** is the time [in second], **θ** is the phase angle [in degree] between V(t) and I(t) and **ω**=2πf is the angular frequency, with **f** the frequency [in Hertz or s^{-1}]. Several processes on the electrode surface absorb electric energy in different frequencies. As effect, they create a time lag between excitation and response. These process is simulated by Resistive (R) – Capacitive (C) electric circuit connected in parallel.

The impedance Z(ω) may be expressed in terms of real and imaginary components and by obviating the dependency on the frequency, ω, that is

$$Z = Re(Z) + Im(Z) \tag{4.15}$$

where Re(Z) and Im(Z) are the real and the imaginary components, respectively, of the impedance Z, expressed in Ohm.

The impedance behavior of an electrode may be expressed in **Nyquist plots** of the -Im(Z) as a function of the Re(Z), or in **Bode plots** of log|Z| or/and -Phase(Z) as a function of the logarithmic scale of the frequency f.

The Impedance analysis tool is called **Z Fit** and the fitting process is done in the Nyquist plot of the experimental data. will be available only if impedance data are already opened. The first thing to be defined by the user is the cycle for which the minimization is performed (either one single minimization performed on the current cycle displayed on the graph or successive

minimizations made on all the cycles of the experiment). Then, an equivalent circuit of the experiment conducted should be selected. The Z Fit selection window enables the user to Edit and create an equivalent circuit. The impedance analysis tool contains currently 13 different electric components, some of which are resistors (R), self/inductors (L), capacitors (C), Constant Phase Elements – CPE (Q), Warburg elements simulating the semi-infinite diffusion (W), etc. The elements used for the representation of our electrochemical systems are presented below.

The **Resistor** (**R**) is defined as a passive component with a constant value when frequency varies. The resistor element is characterized by a constant value that can be measured in the Nyquist plot (Figure 4.29) by the real part – ohmic impedance (Re(Z)>0). The imaginary part – faradic impedance equals to zero (- Im(Z)=0). Thus, the resistor's impedance is given by the equation (4.16) and its unit is **Ohm**.

$$Z(f) = R \qquad\qquad (4.16)$$
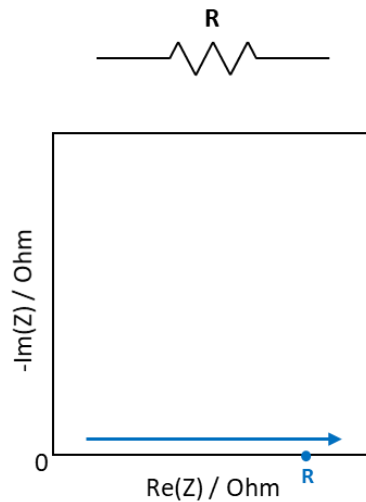
Figure 4.26: Circuit element symbol and domain of resistor's (R) impedance in Nyquist plot.

The **Capacitor** (**C**) is a common electrical element representing an ideal capacitor. Its impedance is frequency dependent. The Nyquist plot (Figure 4.30) of such an element corresponds to a vertical straight line in the imaginary positive part: (-Im(Z)>0 or phase = -π/2). The faradaic impedance decreases when the frequency increases. Thus, the capacitor's impedance is given by the equation (4.17) and its unit is **Ohm·s⁻¹= Farad** (F).

$$Z(f) = \frac{1}{C\, j2\pi f} \qquad\qquad (4.17)$$
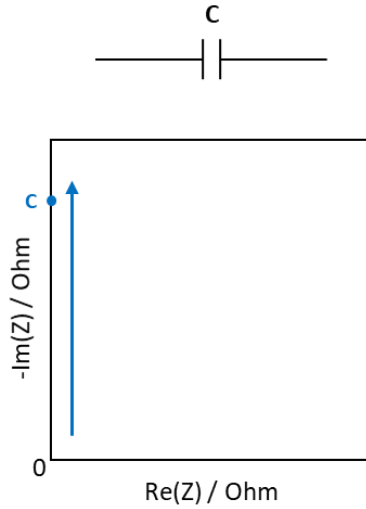
Figure 4.27: Circuit element symbol and domain of capacitor's (C) impedance in Nyquist plot.

The **Constant Phase Element** (**CPE** or **Q**) impedance is also frequency dependent. CPE is an equivalent electrical circuit component that models the behavior of an electrical double layer (edl) which is an imperfect capacitor, due to surface disorder, porosity or inhomogeneity of surface of electrode materials [Kochowski and Nitsch, 2002] [Lacey]. It is commonly used in equivalent circuit modelling and data fitting of electrochemical impedance spectroscopy data. The Nyquist plot (Figure 4.28) of such an element corresponds to a straight line in the imaginary positive part (-Im(Z)>0) with an angle with the real axis equal to $-\alpha\,{}^{\pi}/_{2}$, where α is related to the frequency dispersion with range from 0 to 1 (for α=1 → angle= −π/2 → Q=C). The faradaic impedance of the CPE decreases when the frequency increases. Thus, the CPE's impedance is given by the equation (4.18) and its unit is Ohm·s$^\alpha$ = **F·s$^{(\alpha-1)}$**.

$$\mathbf{Z(f)} = \frac{\mathbf{1}}{\mathbf{Q\,(j2\pi f)^\alpha}} \tag{4.18}$$
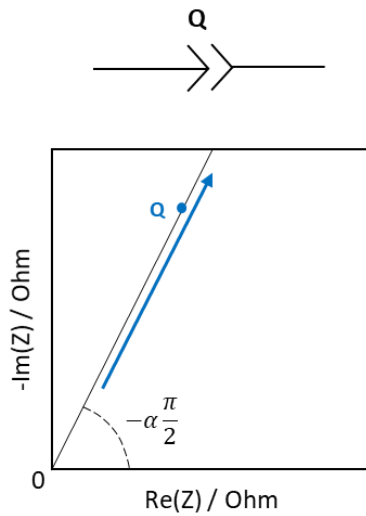
Figure 4.28: Circuit element symbol and domain of CPE's (Q) impedance in Nyquist plot.

121

As mentioned earlier, the lag between potential and current is simulated by an electrical circuit of. However, the behavior of the working electrode in the present thesis, due to the electrical double layer created on the interface between the electrode and the electrolyte (which was explained in chapter 2) is simulated by a resistor ($R_{Polarization}$ or R_P) in parallel with a constant phase element (**CPE** or **Q**). In addition to these elements, the electrolyte solution of the electrochemical cell also contributes as a resistor ($R_{Solution}$ or R_S) connected in series with the electrode's circuit. Thus, the equivalent impedance of the electrochemical systems of the experiments conducted is simulated as shown in Figure 4.29 and by the equation (4.19) below:
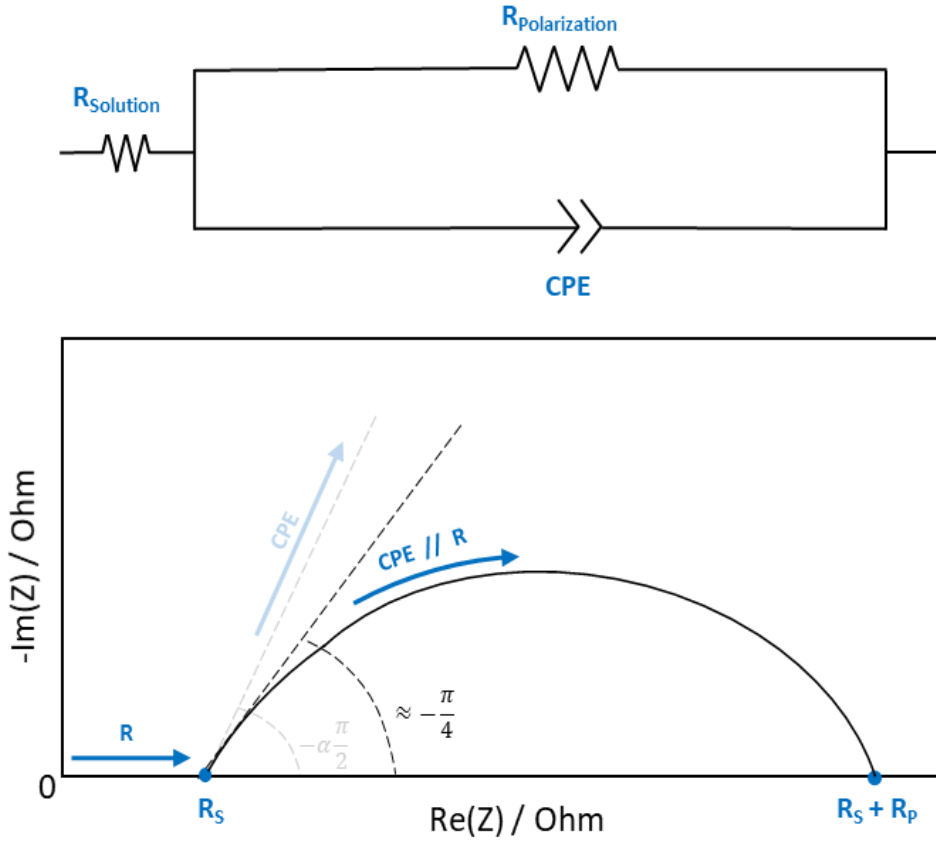
Figure 4.29: Equivalent electrical circuit of the conducted EIS experiments and Nyquist plot representation of the equivalent impedance.

while, from Kirchhoff's laws, the equation for the calculation of the value of the equivalent impedance is:

$$Z(f) = R_S + \frac{R_P}{R_P Q (j2\pi f)^\alpha + 1} \tag{4.19}$$

Thus, after the selection of the appropriate equivalent circuit, the calculation of the fitted curve is started. A typical EIS experimental curve in Nyquist plot is presented in Figure 4.30 with blue trace. The Fitted curve (Z fit) is shown with red dots. The Nyquist plot is a representation of the negative value of Im(Z) as a function of Re(Z) and shows a semicircle, with increasing frequency in a counterclockwise direction.
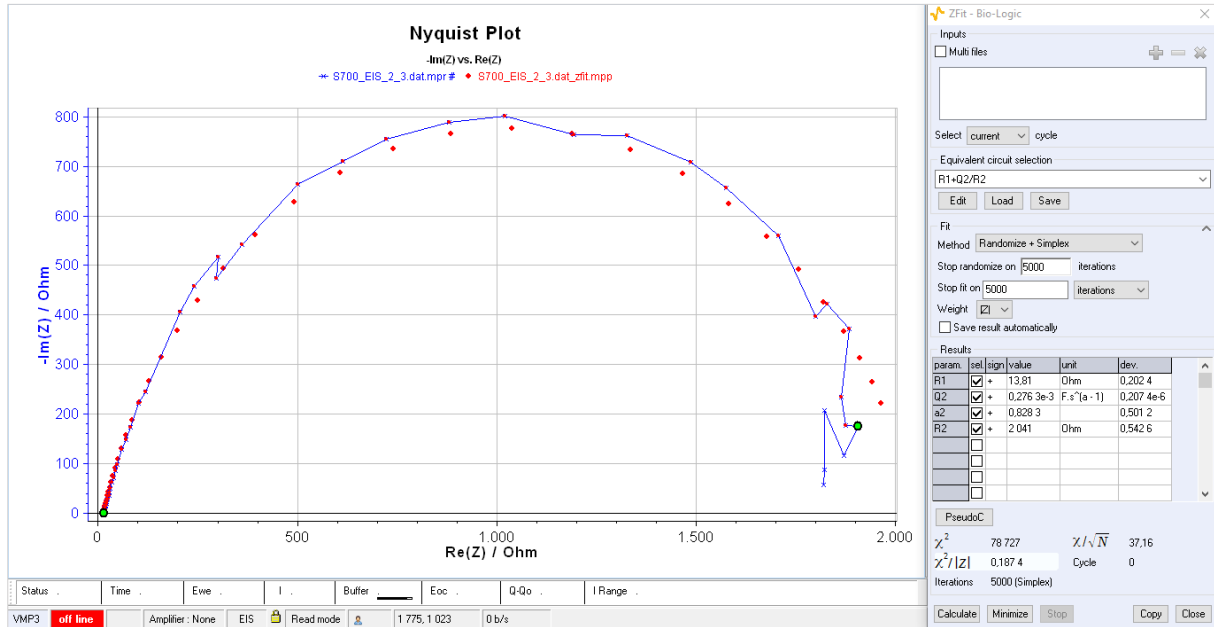
Figure 4.30: Nyquist plot of EIS experiment with Z Fit window. The experimental curve is presented in blue color and the fitted curve in red color.

The fit can be adjusted by the user by moving the markers (shown in green color in Figure 4.30). The Z Fit calculates:

- the electrolyte's resistance, R_S (or R1 on EC-Lab),
- the constant phase element, CPE (or Q2 on EC-Lab),
- the angle of CPE with the real axis, α, and
- the polarization resistance, R_P (or R2 on EC-Lab).

The **pseudo-capacitance** (**PseudoC**) associated with a CPE, can also be calculated. This value can be estimated only for an equivalent circuit of the form R'+(R/Q). This calculation corresponds to the determination of a capacitance value C at a frequency f_0 corresponding to the maximum imaginary part on the Nyquist circle obtained by fitting with the equivalent circuit R'+(R/Q). This value is the solution of the following equation

$$\frac{1}{2\pi(RQ)^{1/\alpha}} = \frac{1}{2\pi RC} \tag{4.20}$$

where α and Q the CPE parameters.

The fit error can be minimized and the fit accuracy can be estimated with the calculation of the values: χ^2, $\chi^2/|Z|$ or $\chi/\sqrt{N}$.

More specifically, default values are set for every parameter but they rarely fit the real experimental values. Before fitting, in order to help the algorithm to find the best values, it is necessary to use initial values as close as possible to the real ones. A randomization is added before the fitting to select the most suitable set of parameter values.

The most suitable set of parameter values are the values that yield the **lower χ^2 value**, **which** gives an estimation of the distance between the real data and the simulated data. Its expression is:

$$\chi^2 = \sum_{i=1}^{n} \frac{|Z_{meas}(i) - Z_{simul}(f_i, param)|^2}{\sigma_i^2} \qquad (4.21)$$

where

- $\triangleright$ $Z_{meas}(i)$ the measured impedance at the fi frequency
- $\triangleright$ $Z_{simul}(f_i, param)$ is a function of the chosen model
- $\triangleright$ f_i is the frequency i
- $\triangleright$ param is the model parameters (ex: R1, R2, C1, Q1, …)
- $\triangleright$ σ_i is the standard deviation.

Considering that for each frequency the impedance has the same standard deviation then σ_i is equal to σ. In this case, minimizing χ^2 is the same as minimizing χ^2/σ. Hence, when no weighing is chosen or weight equals to unit, the expression of the χ^2 criterion as it is used in Z Fit is:

$$\chi^2 = \sum_{i=1}^{n} |Z_{meas}(i) - Z_{simul}(f_i, param)|^2 \qquad (4.22)$$

In this case the unit of χ^2 is **Ohm^2**.

If the user chooses to weigh the data points with **|Z|** the impedance modulus, then the parameter that is being minimized is $\chi^2/|Z|$ in **Ohm** and its expression is:

$$\chi^2\big/_{|Z|} = \sum_{i=1}^{n} \frac{|Z_{meas}(i) - Z_{simul}(f_i, param)|^2}{|Z_{meas}(i)|} \qquad (4.23)$$

The values of χ^2 and $\chi^2/|Z|$ were defined above and are the criterions that are minimized during fitting depending on weighing or not. The lower it is, the better the fit is. One more value is calculated, $\chi/\sqrt{N}$, with N the number of points, which is a normalized expression of χ^2, whose

value is independent on the number of points. It is equivalent to an <u>error</u> and is expressed in **Ohm**. Its expression is the following:

$$\chi\big/{\sqrt{N}} = \frac{1}{\sqrt{N}}\sqrt{\sum_{i=1}^{n}|Z_{meas}(i) - Z_{simul}(f_i, param)|^2} \tag{4.24}$$

During the fitting process, the iteration number as well as the cycle number are displayed at the bottom of the window. <u>Minimize</u> is used to calculate the value of the impedance for each data point and minimize the distance between the calculated value and the experimental value. The <u>Calculate</u> button will calculate and plot the data points for the parameter values set in the table without performing any minimization.

References – Chapter 4

[1] **Autolab B.V**., (2011), <u>Basic overview of the working principle of a potentiostat/galvanostat (PGSTAT) – Electrochemical cell setup</u>, Autolab Application Note EC08, Metrohm – Autolab.

[2] **Bailey R., Sun Y**., (2017), <u>Corrosion and Tribocorrosion Performance of pack carburized Commercially Pure Titanium with Limited Oxygen diffusion in a 0.9% NaCl Solution</u>, School of Engineering and Sustainable Development, Faculty of Technology, Journal of Bio- and Tribo-Corrosion, Springer, UK.

[3] **BioLogic – Science Instruments**, (2018), <u>BT-Lab & EC-Lab, Software Analysis and Data Process</u>, Manual.

[4] **Bramfitt L.B., Benscoter O.A.**, (2002), <u>Metallographer's Guide: Practices and Procedures for Irons and Steels</u>, ASM International, The Materials Information Society, United States of America.

[5] **Dearden J., Neill O.H.**, (1940), <u>A guide to the selection and welding of low alloy structural steel</u>, Transactions of the Institute of Welding, Vol.3, 1940, pp203-214.

[6] **EN 1011-2**, 'Welding - Recommendations for welding of metallic materials - Part 2: Arc welding of ferritic steels', British Standards Institution, March 2001 AMD A1 Dec 2003.

[7] **FISCHER**, X-Ray Fluorescence Measuring Systems.

[8] **Jones A. D.** (1995), <u>Principles and Prevention of Corrosion</u>, 2nd ed., Prentice Hall Publishing, University of Nevada, Reno, Nevada.

[9] **Kochowski S., Nitsch K**., (2002), <u>Description of the frequency behavior of metal-SiO2-GaAs structure characteristics by electrical equivalent circuit with constant phase element</u>, Thin Solid Films. 415 (1–2): 133–137, Retrieved 22 October 2012.

[10] **Krinis I.,** (2020), <u>Corrosion Susceptibility of AH36 and S690 Steel Weldments</u>, (Thesis), School of Naval Architecture and Marine Engineering, National Technical University of Athens.

[11] **Lacey M**., Battery Science and Electrochemistry – Electrochemical Impedance Spectroscopy: Constant Phase Element (website:<u>http://lacey.se/science/eis/constant-phase-element/</u>)

[12] **NanoScience Instruments**, Scanning Electron Microscopy.

[13] **Pantelis D.I., Chrysoulakis G.**, (2008), <u>Materials Science and Technology</u>, (in Greek: Επιστήμη και Τεχνολογία των Μεταλλικών Υλικών), Second Edition, Papasotiriou, Athens.

[14] **Perry S. C., Gateman S. M., Stephens L. I., Lacasse R., Schulz R., Mauzeroll J.**, (2019), <u>Pourbaix Diagrams as a Simple Route to First Principles Corrosion Simulation</u>, Journal of The Electrochemical Society, Canada.

[15]   **VersaStudio Software Manual** (P/N 224181 Rev. C), Priceton Applied Research, AMETEK.

[16]   **Zhang L., Dzombak A.D**., (2010), <u>Challenges and strategies for the use of saline water as cooling water in power plant cooling systems</u>, Technical report at ResearchGate, Carnegie Mellon University - NETL, Pennsylvania.

[17]   **Ziakas A.,** (2020), <u>Corrosion Behavior of AH36 and S460 Steel Weldments</u>, (Thesis), School of Naval Architecture and Marine Engineering, National Technical University of Athens.

[18]   <u>www.ameteksi.com/products/potentiostats/single-channel/versastat-series/versastat-4</u>

[19]   <u>www.bruker.com</u>

[20]   <u>www.leica-microsystems.com</u>

[21]   <u>www.struers.com</u>

[22]   <u>www.substech.com/dokuwiki/doku.php?id=metallurgical_microscope</u>

Experimental Results

Introduction

The objective of the present diploma thesis is to study the possible introduction of the HSLA steels in marine industry in order to reduce the ship weight, one of the most challenging topic of the research in the marine field in the last years. In fact this is the factor that mainly affects the fuel consumption and the payload capacity of the ship.

Although the use of the HSLA steels can potentially achieve this objective of weight savings due to the better mechanical performances, compared with conventional steels, technical properties like corrosion as well as economic and regulatory issues must be investigated carefully before reaching an extensive use of these steels in the marine industry. Compared to conventional steel, the HSLA steels can guarantee better static performances being their yielding point greater, but also their long term behavior is better having generally better fatigue and corrosive performances.

European shipbuilding industries like FINCANTIERI, are strongly interested in using specific HSLA steels, in addition to the commonly used AH36. FINCANTIERI is investigating the replacement AH36 with these steels in areas or parts of the metal structure that undergo high fatigue loads. These specific steels have the peculiarity of having higher fatigue resistance than AH36 and they are also called FCA – Fatigue Crack Arresters, as they are able to delay crack propagation, resulting from cyclic loadings.

The aim of the present thesis is the study of the susceptibility to corrosion of S560 and S700 steels and the examination of their microstructures. S560 and S700 offer a much higher yield and tensile strength, compared to AH36, good weldability, and hardenability. So, they could potentially be used in these critical areas of the metal structure. Moreover, S560's ductility is similar to that of AH36, so, it could be used even in larger areas of the structure.

The corrosion study, which is the most extensive and significant part of this thesis, was accomplished by employing electrochemical techniques applying AC and DC excitation techniques. For the interpretation of the results obtained and the completion of this thesis, detailed study of the microstructure (Optical Microscopy, Micro-hardness, XRF analysis) was also performed.

In the following paragraphs the results of the study of the microstructure, micro-hardness and chemical composition of S560 and S700 specimens are presented (paragraphs 5.1 and 5.2, respectively), complemented with data from the literature where necessary, as well as, the results of the electrochemical techniques employed. In paragraph 5.3 comparison of the results of the two different steels is cited, while, in paragraph 5.4 the general conclusions of the study are presented, along with suggestions for future research.

5.1. S560 steel

As mentioned in Chapter 1, S560 is a high-strength low-alloy (HSLA) steel, produced by thermomechanically controlled process (TMPC) with a minimum yield strength of 560 MPa. The study of the metal alloy and its behavior to corrosion is presented in the next paragraphs.

5.1.1. Study of metal alloy - S560

5.1.1.1. Chemical composition of S560

In order to define the precise values of the main alloying elements X-Ray Fluorescence method was applied. In Table 5.1 the chemical composition of S560 is cited, showing the values of each element, as presented in its technical data sheet certificate (provided by SSAB) and as it was calculated via XRF. It has to be mentioned that XRF method does not present values for carbon (C) and for elements with content lower than 0.01%. S560 steel presents low carbon content assuring good machinability and high weldability.

Table 5.1: S560 chemical composition.

Chemical Composition of S560		
	XRF	**Certificate**
C		0.063
Si		0.010
Mn	1.390	1.360
P	0.010	0.010
S		0.003
Al$_{tot}$		0.038
Nb	0.043	0.041
V		0.010
Ti	0.027	0.000
Cr	0.017	0.020
Cu	0.020	0.010
Ni	0.040	0.040
Mo	0.000	0.000
B		0.0001
N		0.004
Carbon Equivalent	**0.302**	**0.299**

With the chemical composition provided from the **XRF** method, the following were calculated:

- **Carbon Equivalent,** by the equation (4.2) in chapter 4, taking also into account the carbon content from the certificate:

$$CE_{IIW} = C + \frac{Mn}{6} + \frac{Cr + Mo + V}{5} + \frac{Ni + Cu}{15} = \mathbf{0.302}$$

- **Total Number of Equivalents** and **Equivalent Weight**, by the equations (2.34) and (2.35), respectively, in chapter 2:

$$N_{EQ} = \sum \left(\frac{f_i}{\alpha_i / n_i} \right) = \sum \left(\frac{f_i \cdot n_i}{\alpha_i} \right) = \mathbf{0.03577}$$

$$EW = N_{EQ}^{-1} = \mathbf{27.96}$$

The chemical analysis of the steel specimen by XRF is in <u>agreement</u> with the data sheet certificate of S560.

5.1.1.2. Micro-hardness of S560

The micro-hardness of the specimen has been studied employing Vickers' hardness test method. Ten (10) different micro-hardness measurements were applied, as shown in Table 5.1 and Figure 5.1, with a load of 0.3kp (2.942 N) for dwell time 10secs, on distinct spots on the specimen. The values obtained range from 189.2 HV0.3 to 194.6 HV0.3, with average value of **193.9** HV0.3 and standard deviation of 4.9 $HV_{0.3}$. The values of the micro-hardness obtained is are in agreements with the literature for this type of steels.

Table 5.2: Micro-hardness of S560

Micro-Hardness of S560

Measurements	1	2	3	4	5	6	7	8	9	10	AVG	SD
HV 0.3	194.1	192.2	194.7	204.7	187.6	194.7	194.6	189.7	189.2	197.5	**193.9**	**4.9**
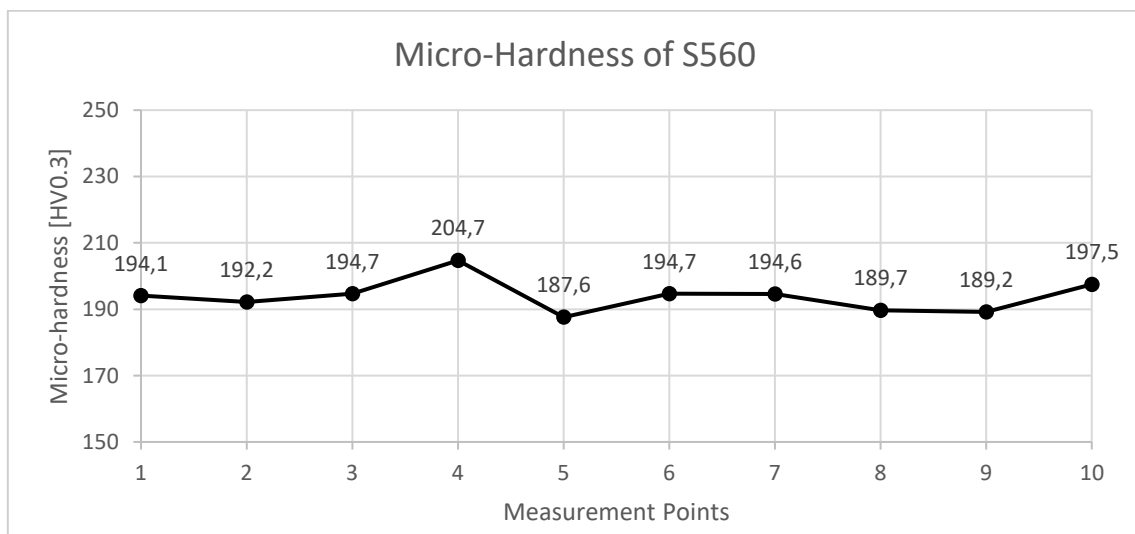
Figure 5.1: Diagrams of the micro-hardness measurements on S560.

5.1.1.3. Microstructure

The microstructure of the specimen (metallography) has been studied employing Optical Microscopy – OM (Figure 5.2) and Scanning Electron Microscopy – SEM (Figure 5.3). The results are presented below.

S560 steel is a High Strength Low Alloy steel (HSLA). During the production of S560, thermomechanical rolling together with accelerated cooling is applied. Optical observation resulted that the microstructure of the S560 steel presents ferritic pearlitic microstructure, which is also justified due to strictly controlled hot rolling. S560 TMCP steel is **fine gained** consisted of distinct **ferritic** and **pearlitic** grains.

(a)

(b)

(c)
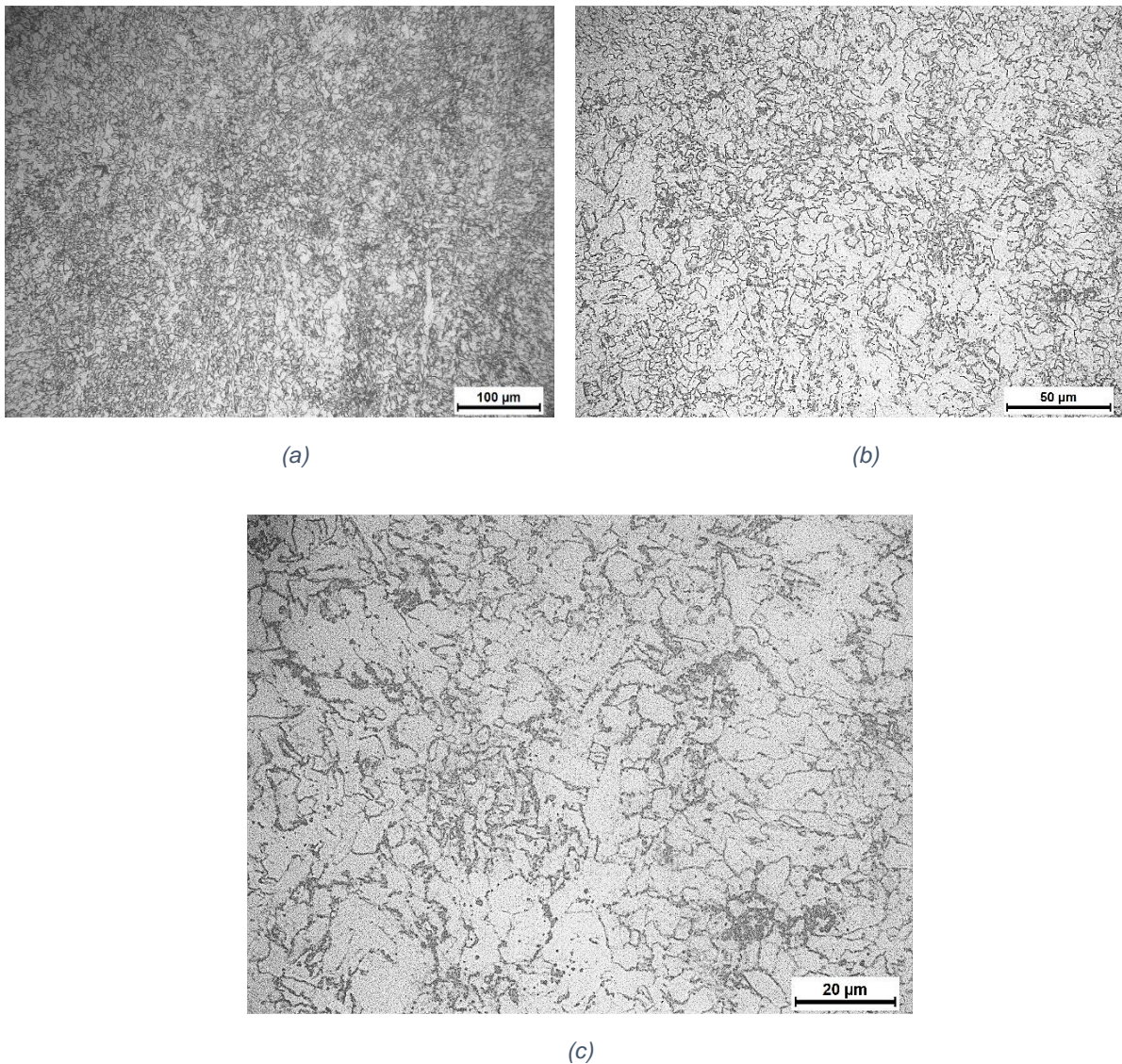
Figure 5.2: Optical observation of S560 employing Optical Microscopy (OM). Magnification of the instrument at (a) x200, (b) x500, (c) x1000.

(a)

(b)

(c)
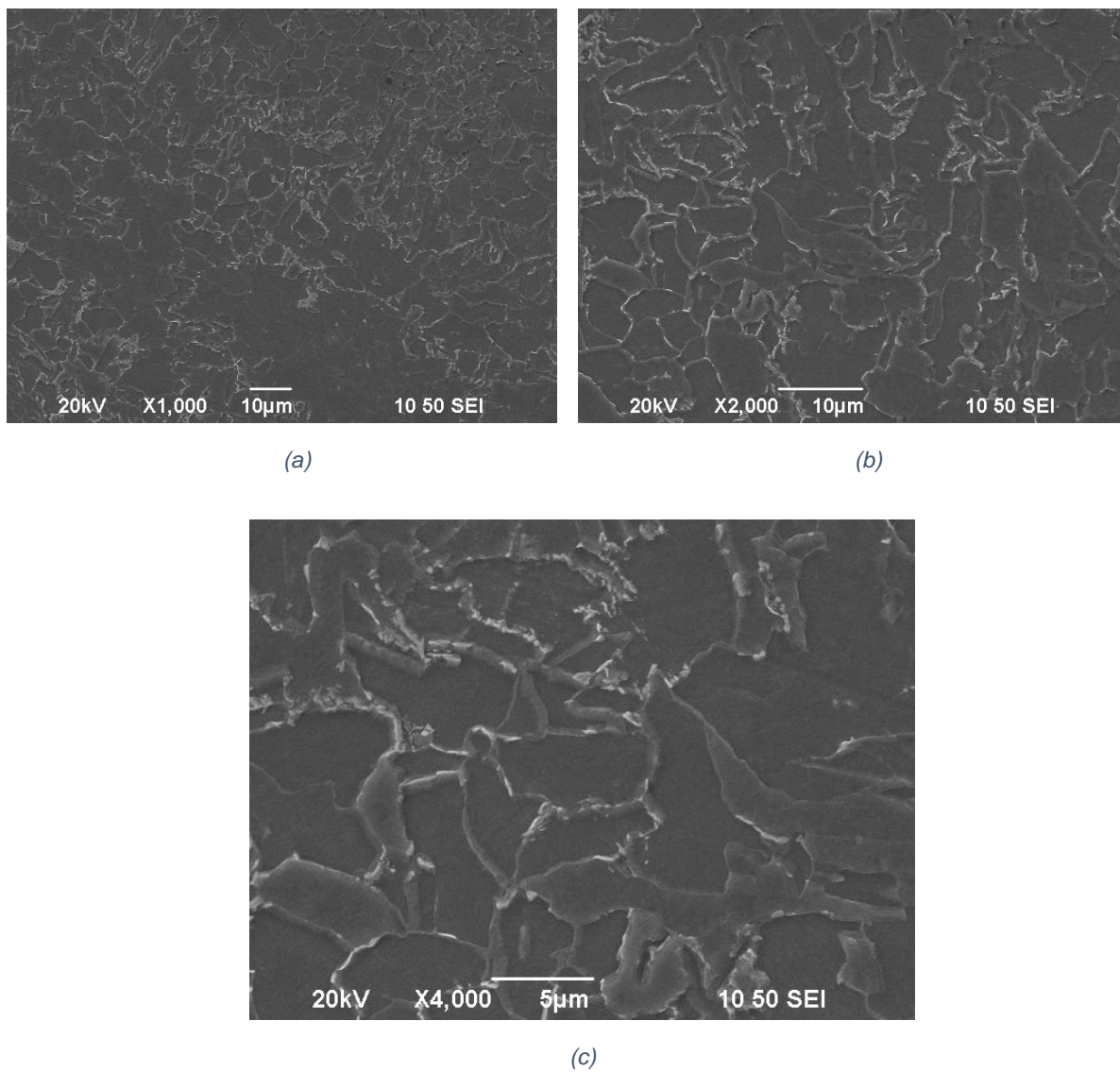
Figure 5.3: Optical observation of S560 employing Scanning Electron Microscopy (SEM). Magnification of the instrument at (a) x1000, (b) x2000, (c) x4000.

5.1.2. Study of corrosion – S560

In the following paragraphs, the results of the electrochemical techniques for S560 are presented. As mentioned in Chapter 4, EC-Lab Software was employed for the analysis of the data obtained from the electrochemical measurements through Versa Studio Software.

5.1.2.1. Open Circuit Potential (OC)

Open Circuit (OC) experimental curves show the evolution of the potential of the working electrode Ewe (in Volt) as a function of the elapsed time t (in second) of S560 are presented. OC measurements were recorded for a period of 24hour OC, and of 48hour (Figure 5.4). The potential versus time showed that after 1700sec a drop in the potential is observed, while after 40000 secs (≈11hrs) a rather stable value of **-752mV** is observed. Similar behavior is observed for the 48h recording, where the stable potential is obtained after 40000 secs (≈11hrs) in the value of **-733mV**. The stabilization of potential proves that equilibrium has been attained for the corrosion phenomena in the system and, taking into account the Potentiodynamic Polarization Curves, it can be assumed that the equations are the dissolution of Fe:

$$Fe \leftrightharpoons Fe^{2+} + 2e^-$$

and the oxygen's reduction:

$$O_2 + 2H_2O + 4e^- \leftrightharpoons 4OH^-$$
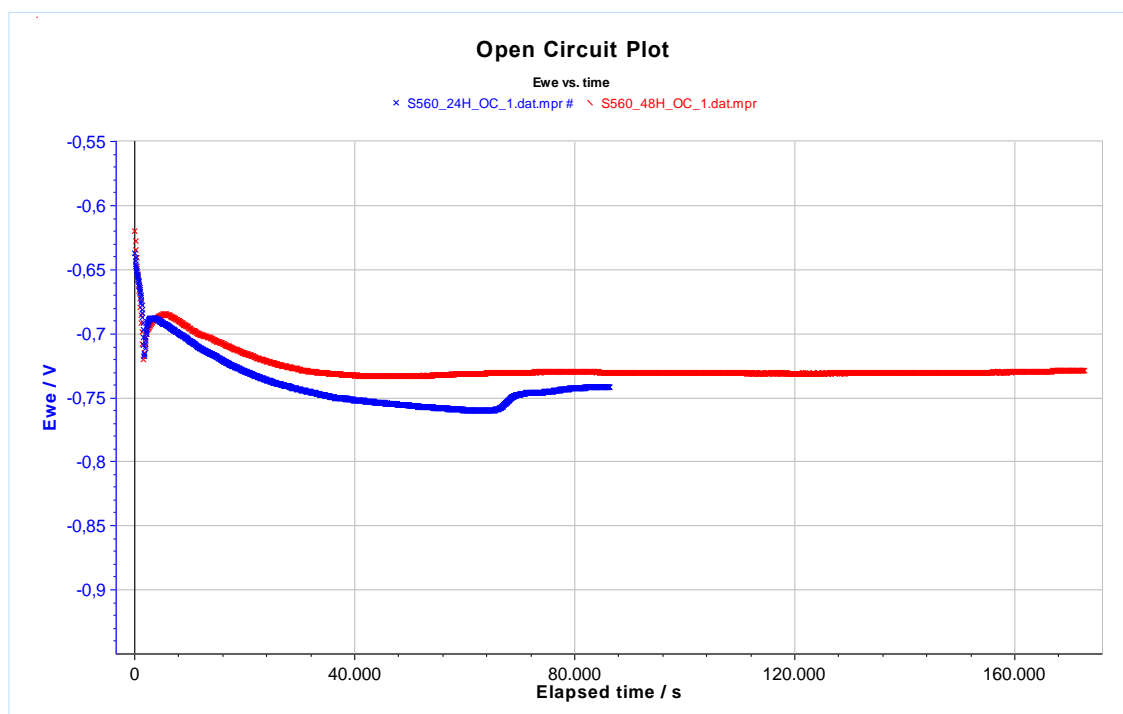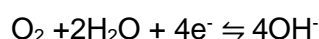
Figure 5.4: Summary of experiments on OC method of S560,
*specifically: **Blue:** 24hour experiment VS **Red:** 48hour experiment.*

134

In Figure 5.5 the recorded Open Circuit measurements during the 24h (6 loop) OC-EIS experiment (between every EIS perturbation) are presented. The curve of the serial 24hour Open Circuit experiments is also presented for comparison. It is obvious that the measurements obtained are consistent for both experiments, so it can be assumed that the results are credible.
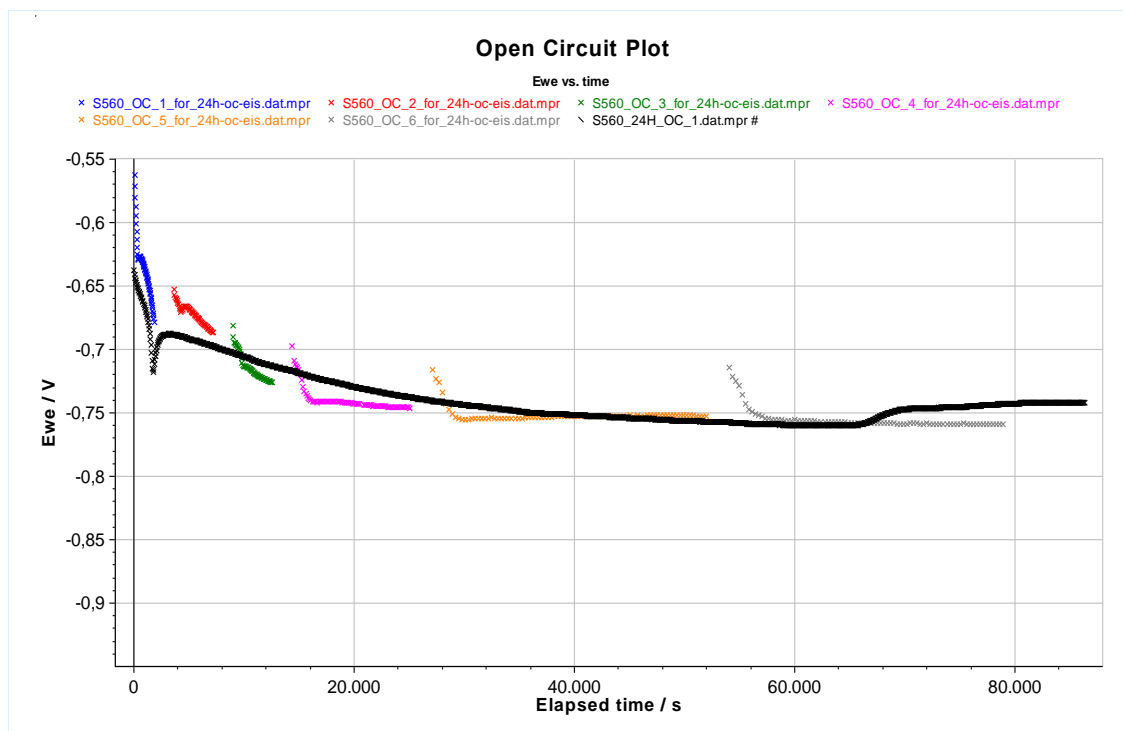
Figure 5.5: Summary of experiments on OC method of S560, specifically:
Black: *24hours experiment VS* **Colored:** *six cycles of OC for the 24hour experiment OC-EIS.*

5.1.2.2. Linear Polarization Resistance (LPR)

Three (3) individual experiments took place employing the Linear Polarization method; each one consisted of two (2) consecutive runs, six experimental curves obtained in total. In Figure 5.6 the experimental curves of the current I (in milli-Ampere) as a function of the potential of the working electrode Ewe (in Volt) S560 are presented.
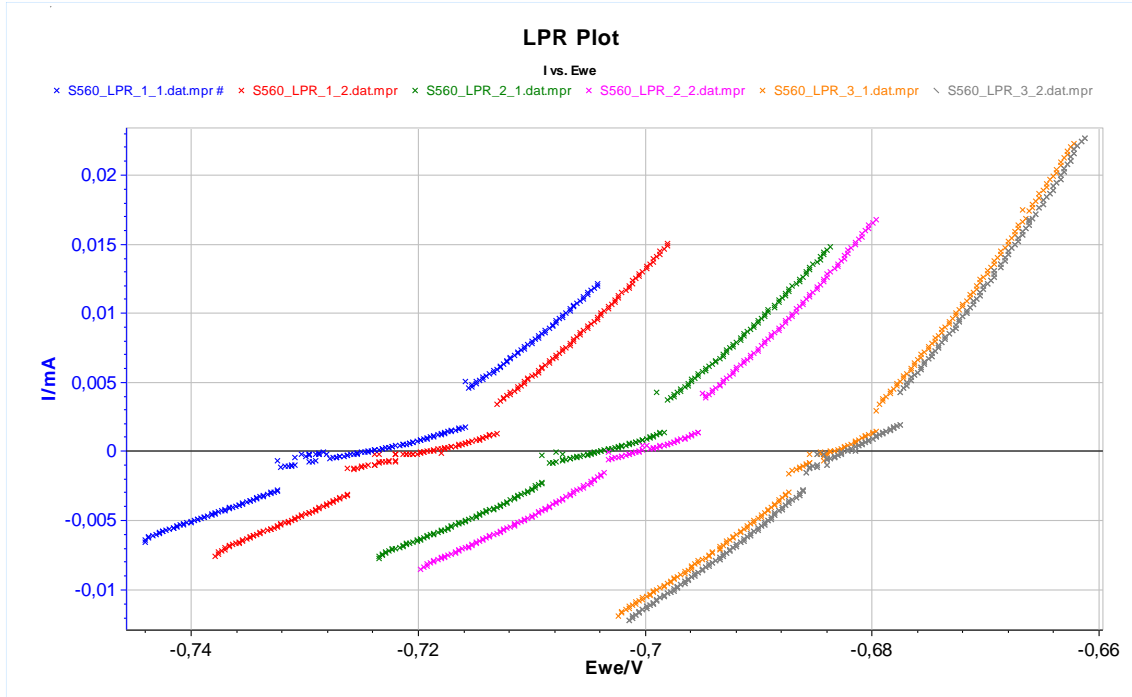
Figure 5.6: Summary of experiments on LPR method of S560, specifically:
Blue: exp.1_1, **Red**: exp.1_2, **Green**: exp.2_1, **Magenta**: exp.2_2, **Orange**: exp.3_1, **Grey**: exp.3_2.

The measurements obtained were elaborated employing the open source EC Lab software. As already mentioned in paragraph 4.3.3.2. in order to apply Rp fit, for $E \approx E_{corr}$, we can simplify the Stern equation using near-field approximation, so that:

$$I = I_{corr}(E - E_{corr})\frac{\beta_a + \beta_c}{\beta_a\beta_c}\ln 10, \quad \text{for } E \approx E_{corr} \tag{4.9}$$

This equation is commonly presented with E as function of I:

$$E = \frac{I \cdot \beta_a\beta_c}{I_{corr}(\beta_a + \beta_c)\ln 10} + E_{corr} \tag{4.10}$$

Thus, for **E=E_{corr}, I=0**. The **slope** of this equation **dE/dI** is the **polarization resistance R_P**, it has the unit of a resistance (Ohms) and is calculated by the Stern-Geary equation:

$$\left(\frac{dE}{dI}\right)_{E_{corr}} = R_{P,E_{corr}} = \frac{\beta_a\,\beta_c}{I_{corr}\,(\beta_a + \beta_c)\ln 10} \tag{4.11}$$

136

For I=0, the value of **E$_{corr}$** is calculated and by a linear regression (all the data points are used) around E$_{corr}$, on I vs. E plot, as well as the **R$_P$** as the slope of the linear regression. For the **I$_{corr}$** determination β$_a$ and β$_c$ values need to be known. The usually applied values for β$_a$ and β$_c$, in the literature, are equal to ±120mV.

However, in the present thesis two different approaches were performed for I$_{corr}$ determination:

i.   The values of β$_a$ and β$_c$ were taken as β$_a$ = 120mV and β$_c$ = -120mV (Table 5.3), according to the literature.

Table 5.3: Corrosion and LPR parameters for each experiment of S560 (for β$_a$ = β$_c$ = 120mV).

S560 – Linear Polarization Resistance

Parameters									
βa	*[mV]*				120				
βc	*[mV]*				120				
Range	*[mV]*				+/- 25.0				
Results									
Specimen:		**1**		**2**		**3**			
Experiment:		**1_1**	**1_2**	**2_1**	**2_2**	**3_1**	**3_2**	**AVG**	**SD**
R$_P$	*[Ohm]*	2337	1874	1839	1628	1198	1176	**1675**	444
E$_{CORR}$	*[mV]*	-726.7	-721.3	-706.2	-702.5	-685.1	-684.1	**-704.3**	17.7
Correlation		0.9694	0.9806	0.9815	0.9832	0.9894	0.9881	**0.9820**	0.0071
I$_{CORR}$	*[µA]*	11.16	13.92	14.19	16.03	21.77	22.18	**16.54**	4.49

ii.   The values of β$_a$ and β$_c$ were calculated from equation (4.11) by using experimental data from the employed electrochemical techniques of Potentiodynamic Polarization (PP) and Electrochemical Impedance Spectroscopy (EIS). In particular, employing **PP with Tafel extrapolation** method (paragraph 5.1.2.3.) an average of **β$_a$ = 65.9mV** was calculated for the anodic part, which is Tafelian (activation polarization). However, due to the fact that the cathodic curve is not Tafelian (concentration polarization controls the cathodic half-cell reaction), it would be invalid to use the slope of this curve as a Tafel coefficient β$_c$. When the behavior is not Tafelian, β$_c$, i.e. the slope of the cathodic branch tends to infinity. Then, by employing **EIS** (paragraph 5.1.2.4. - three consecutive runs experiment), the **R$_P$ = 1646 Ohm** was calculated. So, by **equation (4.11)** it is possible to calculate β$_c$ which found equal to **β$_c$ = 507.7 mV**. For β$_a$ = 65.9mV and β$_c$ = -507.7mV, the LPR results are shown in *Table 5.4*.

Table 5.4: Corrosion and LPR parameters for each experiment of S560 (for β_a =65.9mV and βc = 507.7mV).

S560 – Linear Polarization Resistance

Parameters								
βa	*[mV]*	65.9						
βc	*[mV]*	507.7						
Range	*[mV]*	+/- 25.0						
Results								
Specimen:		**1**		**2**		**3**		
Experiment:		**1_1**	**1_2**	**2_1**	**2_2**	**3_1**	**3_2**	**AVG**	**SD**
R_P	*[Ohm]*	2337	1874	1839	1628	1198	1176	**1675**	444
E_CORR	*[mV]*	-726.7	-721.3	-706.2	-702.5	-685.1	-684.1	**-704.3**	17.7
Correlation		0.9694	0.9806	0.9815	0.9832	0.9894	0.9881	**0.9820**	0.0071
I_CORR	*[μA]*	10.85	13.53	13.79	15.58	21.17	21.56	**16.08**	4.36

In Table 5.3 and Table 5.4 both approaches are presented. It is observed that the difference in I_{corr} is insignificant, while the rest of the values remain equal in both approaches. The values of R_P represent the ability of the electrons to pass through the steel specimen. Thus the higher the R_P values the better the corrosion resistance of the steel.

The polarization curves in Figure 5.6 and the results in Table 5.3 and Table 5.4 show that specimens 1 and 3 present significant differences ranging from 2000Ohms to 1200 Ohms, resulting also in relevant differences in I_{corr} values, 10μA/cm^2 up to 20μA/cm^2. This difference can be attributed to the variations in the microstructure of the specimens, which might affects the corrosion behavior.

However, both values can be assigned to good corrosion behavior for steel specimen according to Figure 2.14 [McCafferty, 2010] indicating a "good" corrosion rate for iron with corrosion current density between 11 and 43μA/cm^2 and "excellent" below 11μA/cm^2.

Concerning the E_{corr}, its values are close to E_{corr} = -700mV, which is representative for this type of steel and consistent with the literature, with low standard deviation. It is also worth-mentioned that the correlation of the values is close to unit, proving the accuracy of the linear regression.

5.1.2.3. Potentiodynamic Polarization - Tafel Extrapolation

Three (3) individual experiments took place employing the Potentiodynamic Polarization (PP) method. In Figure 5.7 three (3) experimental curves of the potential of the working electrode Ewe (in Volt) as a function of the current I (in milli-Ampere) expressed in logarithmic scale of S560 are presented.
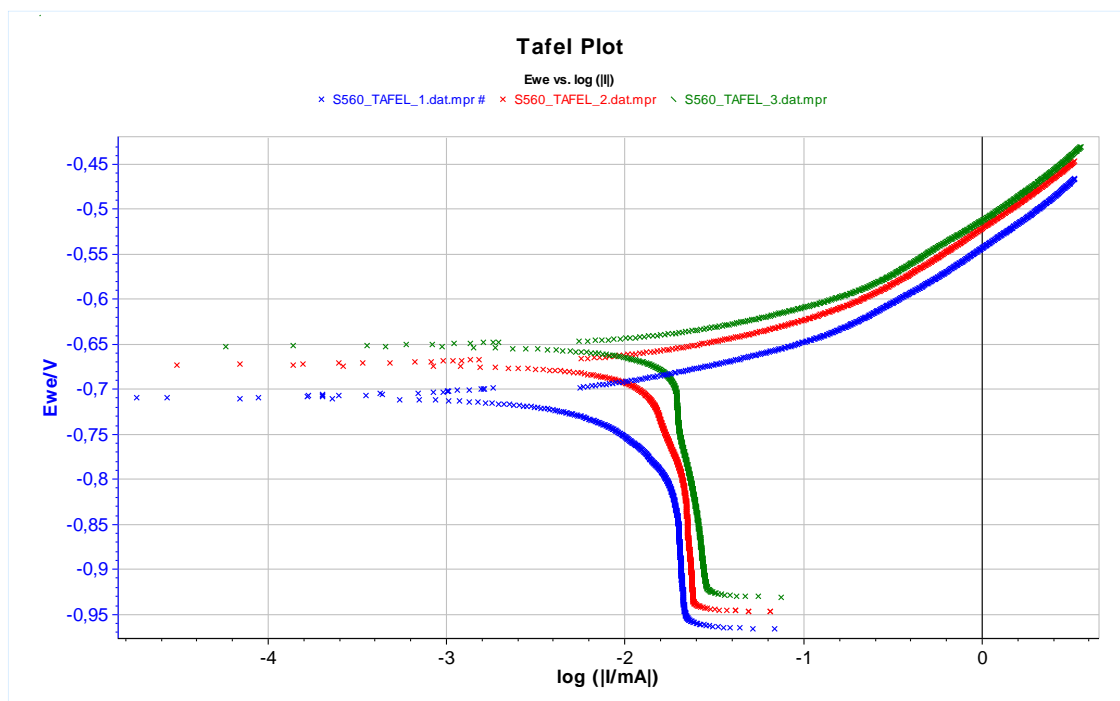
Figure 5.7: Summary of experiments on Potentiodynamic Polarization method of S560, specifically: **Blue**: exp.1, **Red**: exp.2, **Green**: exp.3.

The polarization curves in Figure 5.7 present the anodic branch, whose shape proves that S700 presents continuous anodic dissolution, without evidence of passive behavior (for this range of polarization), according to the reaction:

$$Fe \rightarrow Fe^{2+} + 2e^-$$

Possibly, other alloying elements' present anodic reactions, however these are of minor importance.

The shape of the cathodic branch shows that cathodic behavior is dominated by the O_2 diffusion in the electrolyte solution, by the reaction of:

$$O_2 + 2H_2O + 4e^- \rightarrow 4OH^-$$

and in the last part of the cathodic reaction one can recognize the reduction of hydrogen:

$$2H^+ + 2e^- \rightarrow H_2$$

As already mentioned in paragraph 3.3, according to Tafel extrapolation method, the crossing point of the tangent to the linear part of the anodic branch, the tangent to the linear part of the cathodic branch and the line through the E_{corr} parallel to the x-axis defines the I_{corr} value on x-axis. The anodic reaction (metal's dissolution) is **activation polarization controlled**, presents Tafelian behavior, so β_a represents the Tafel coefficient. However, in **diffusion controlled** cathodic curves, β_c values cannot be defined and the calculated values in Table 5.5, only represent the slopes of the cathodic branches which tend to infinity.

Figure 5.7 shows all the experiments, which present the aforementioned behavior, which evidence very good repeatability. Corrosion potential E_{corr} has mean value of **-677mV** while I_{corr} has an average of **15.4μA/cm²** and corrosion rate is equal to **7.1mpy** (calculated according to equation (4.7)). Anodic Tafel constant β_a is 65.9mV/decade, while cathodic slope β_c tends to infinity due to O_2 diffusion.

Table 5.5: Corrosion and Tafel parameters for each experiment of S560.

S560 – PP with Tafel Extrapolation

Parameters						
equivalent weight	[g/eq.]	27.956				
density	[g/cm3]	7.8				
surface area	[cm²]	1.000				
Results						
Experiment:		**1st**	**2nd**	**3rd**	**AVG**	**SD**
E_CORR	[mV]	-709.3	-670.1	-650.6	**-676.6**	29.9
I_CORR	[μA]	14.55	15.27	16.40	**15.40**	0.93
I_LIM	[μA]	21.73	23.82	26.18	**23.91**	2.23
βc	[mV]	1144.3	1047.6	991.3	**1061.1**	77.4
βa	[mV]	79.9	62.1	55.6	**65.9**	12.6
corrosion rate	[mmpy]	0.1706	0.1791	0.1923	**0.1806**	0.0109
corrosion rate	[mpy]	6.714	7.049	7.569	**7.111**	0.431

Ohmic Potential Drop (IR drop)

Another remarkable phenomenon characterizes the experimental curves of this method and it is noticeable at high current values of the anodic branch and is called Ohmic Potential Drop or IR drop, as already discussed in paragraph 3.3.3. Experimentally, the potential applied to the electrochemical cell is controlled by applying current between the Counter Electrode (CE) and Working Electrode (WE), and measuring the potential between the Reference Electrode (RE) and WE. IR drop results from the electric current flow in ionic electrolytes because it is not possible to place the RE tip (Luggin capillary) directly onto the WE surface. To obtain an accurate potential measurement of the WE, we assume that the potential measurement of the potentiostat, according to Ohm's Law, is

$$E_{applied} = IR_{ct} \qquad (3.29)$$

where I is the current and R_{ct} is the total resistor which constitutes of the metal's and the solution's resistance, R_P and R_S, respectively, so

$$R_{ct} = R_P + R_S \qquad (3.30)$$

then, the measurement of the potential may be written as

$$E_{applied} = I\,(R_P + R_s) = IR_P + IR_S = E_{WE} + IR_S \qquad (3.31)$$

and the accurate potential measurement on the WE (specimen) is

$$E_{WE} = E_{applied} - IR_S \qquad (3.32)$$

where the factor IR_S represents the **potential drop**.

The corrected curve, taken into account the potential drop (Equation (3.32)), is presented graphically in Figure 5.8 in red color versus to the experimental data curve in blue. This drop become more prominent as the scan rate is enhanced following the increase of current, but its effects are negligible at low current values, i.e. around I_{corr}. Due to this fact, in these experiments of Potentiodynamic Polarization it does not affects either the values of E_{corr} and I_{corr} or those of β_a and β_c, as the extrapolation of the potentiodynamic anodic and cathodic curves for all the experiments was performed at their linear part close to E_{corr}.
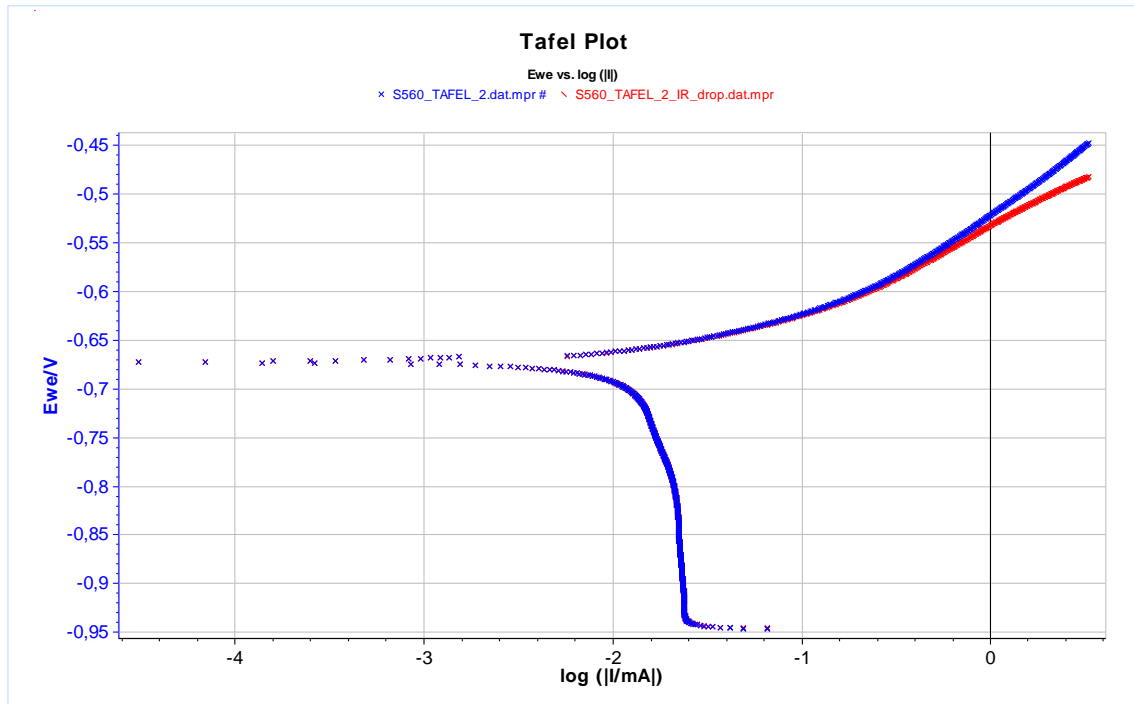
*Figure 5.8: Experiment on Potentiodynamic Polarization method of S560, specifically: **Blue**: Potential V, **Red**: Ohmic Potential Drop $E_{WE} = E_{ap} - IR_S$.*

5.1.2.4. Electrochemical Impedance Spectroscopy (EIS)

Two (2) individual experiments took place employing the Electrochemical Impedance Spectroscopy (EIS) method:

- the first one consisted of <u>three (3) consecutive runs</u> and
- the second one was <u>a 24hour experiment with 6 loops of an OC followed by an EIS, as an attempt to study the corrosion evolution in 24 hour period</u>.

The impedance behavior of the electrode is expressed in **Nyquist plots** of –Im(Z) (in Ohm) as a function of Re(Z) (in Ohm) or in **Bode plots** of log|Z| (Z in Ohm) and –Phase(Z) (in degrees) as a function of log|frequency| (frequency in Hertz). Three figures for each experiment are presented below, one Nyquist and two Bode plots (Figures: Figure 5.9, Figure 5.10, Figure 5.11 /Figure 5.12, Figure 5.13, Figure 5.14), respectively. In this chapter are presented only the summary diagrams of each specimen along with the common diagrams for both metals. The rest of the diagrams are presented in the Annex B.

Three consecutive EIS experiment
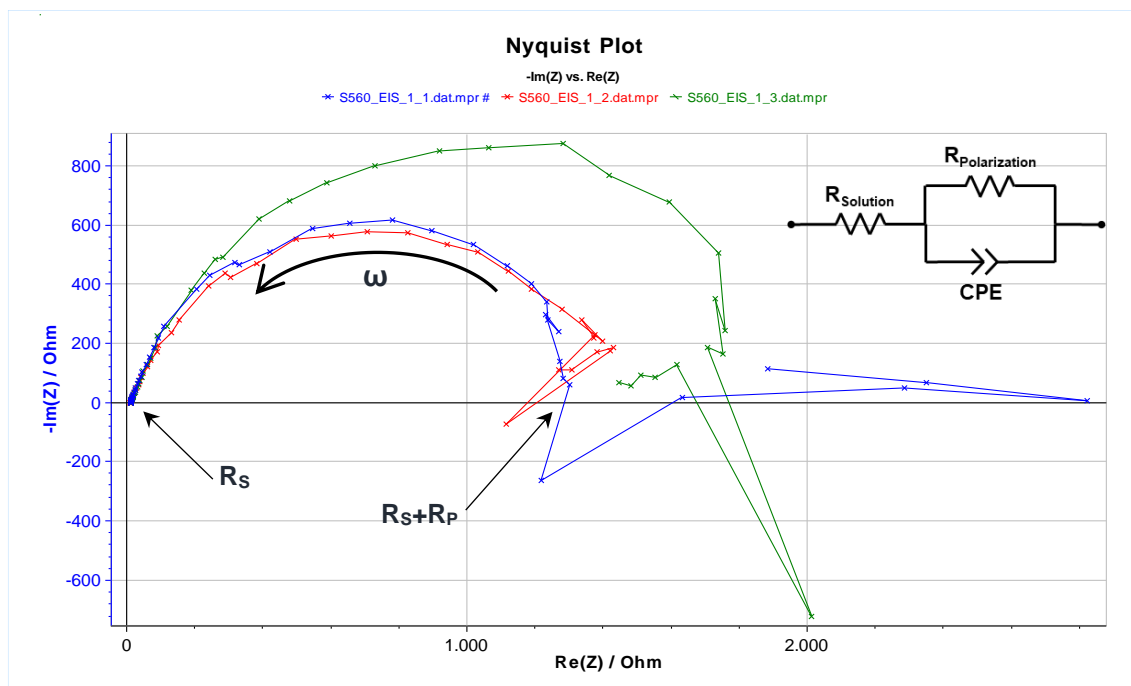
*Figure 5.9: Nyquist summary plot of 3 consecutive experiments on EIS method of S560, specifically: **Blue**: 1st EIS, **Red**: 2nd EIS, **Green**: 3rd EIS.*

In the three (3) consecutive EIS experiments of same duration were conducted, after a 30-minutes Open Circuit (OC) corrosion experiment. In both Nyquist and Bode plot, the Z of high frequency implies solution resistance, whereas the Z of low frequency is the total resistance R_{CT}, including the solution R_S and the polarization resistance R_P.

The interpretation of EIS plots provides information of surface/electrolyte solution interface. The shape of the Nyquist plot for S560 displays only one capacitive semicircle. This type of curve is interpreted as a mechanism of charge transfer on an inhomogeneous surface.

The diameter of the capacitive semi-circle is almost the same for the two first experiments and presents larger diameter for the third experiment. Deviations at the low frequency end of the semi-circle are due to changes in impedance during the long times required to conduct measurements at low frequencies. Moreover, no indication of Warburg impedance line is indicated (Figure 5.9). Similarly, the Bode plots of the S560 steel show only one time constant as in Figure 5.10 and Figure 5.11.

To describe the impedance response of the corrosion behavior of S560 in chloride environment, the equivalent circuit analysis was performed employing EC Lab software. The equivalent circuit model from the literature was applied on the EIS results (Figure 5.9). In the circuits, R_S and R_P indicate solution resistance and charge transfer resistance of the electrolyte–substrate interface, respectively. For perfect semi-circles the element Q is well represented by the capacitor C associated with the double layer capacitance. This type of circuit is named Randles cell.

However, in S560, the shape of the Nyquist curve is not a perfect semicircle centered on the Z' axis at the (R/2, 0) point. It presents deviation from the Resistance Capacitor behavior and there is a deformation and broadening of the semicircle. For this reason, in the equivalent modelled circuit the capacitor C is substituted by the Constant Phase Element CPE, still parallel with the resistor R_P. This deformation is attributed to the roughness of the electrode-electrolyte interfaces or to inhomogeneities in the local distribution of defects in the vicinity of grain boundaries.

In the Table 5.6, the electrical elements of the impedance fitting via EC Lab are presented. In general, R_P, is inversely proportional to the corrosion rate of a given metal. For S560 the average value of R_P is 1646 Ohms, with SD of 381Ohms, while R_S is stable at 10.6 Ohms. CPE, Constant Phase Element presents an average value of 3.06E-04 F.s^(a - 1). The element a is a fluid element which for corrosion systems ranges from 0.5 to 1. If the electrolyte – electrode interface was a perfect capacitor it would be equal to average value of 2.68E-04 F.

Table 5.6: Equivalent circuit parameters of S560, on 3 consecutive EIS experiment.

S560 – Electrochemical Impedance Spectroscopy					
Results					
Experiment:	**1_1**	**1_2**	**1_3**	**AVG**	**SD**
R_S	*[Ohm]*	10.66	10.56	10.6	**10.61**	0.05
CPE	*[F.s^(a - 1)]*	2.45E-04	3.49E-04	3.25E-04	**3.06E-04**	5.42E-05
a		0.8515	0.8199	0.8248	**0.8321**	0.0170
R_P	*[Ohm]*	1409	1443	2085	**1646**	**381**
PseudoC					
R_S	*[Ohm]*	10.66	10.56	10.6	**10.61**	0.05
C	*[F]*	2.04E-04	3.00E-04	2.99E-04	**2.68E-04**	5.53E-05
R_P	*[Ohm]*	1409	1443	2085	**1646**	381
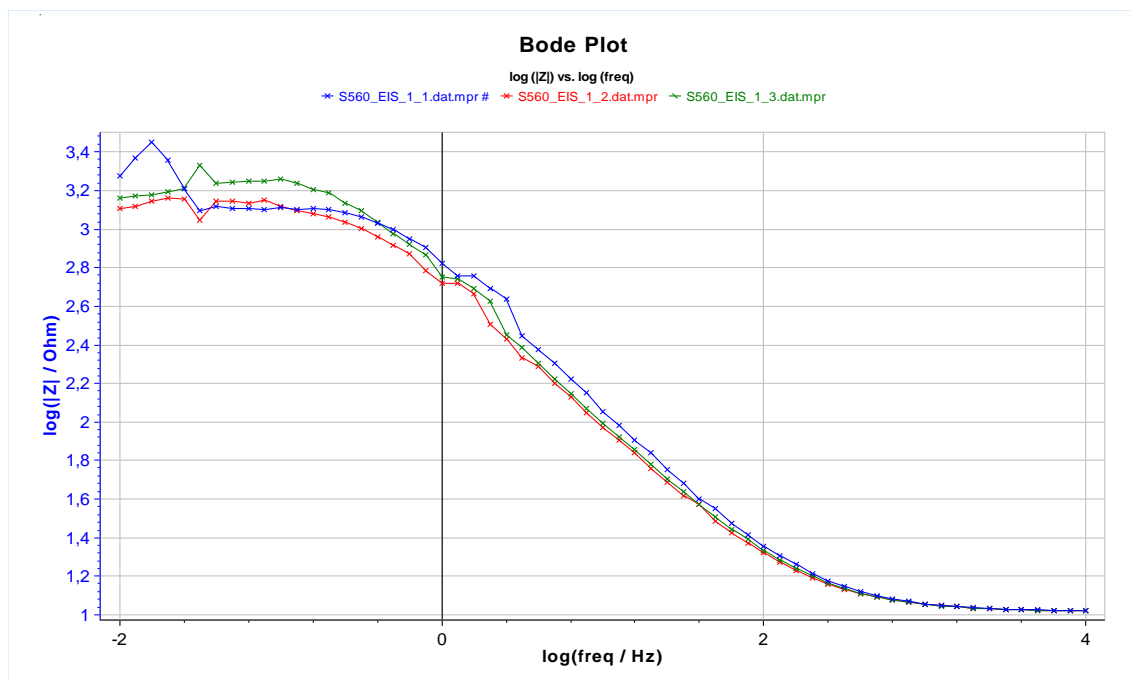
Figure 5.10: Bode (log|Z|) summary plot of 3 consecutive experiments on EIS method of S560, specifically: **Blue**: 1st EIS, **Red**: 2nd EIS, **Green**: 3rd EIS.
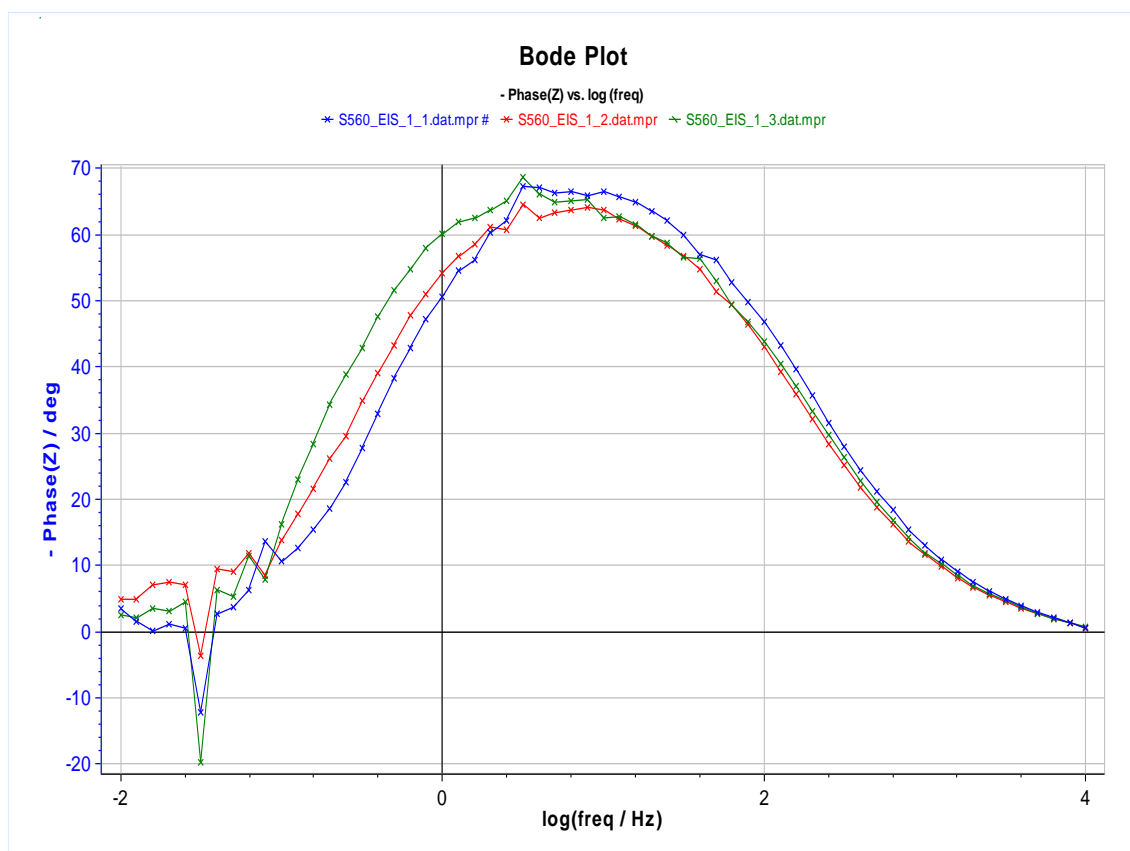
Figure 5.11: Bode (-Phase(Z)) summary plot of 3 consecutive experiments on EIS method of S560, specifically: **Blue**: 1st EIS, **Red**: 2nd EIS, **Green**: 3rd EIS.

144

24 hour experiment

For the 24-hours experiments, the summary diagram, Figure 5.12 is presented, along with the parameters in Table 5.7.
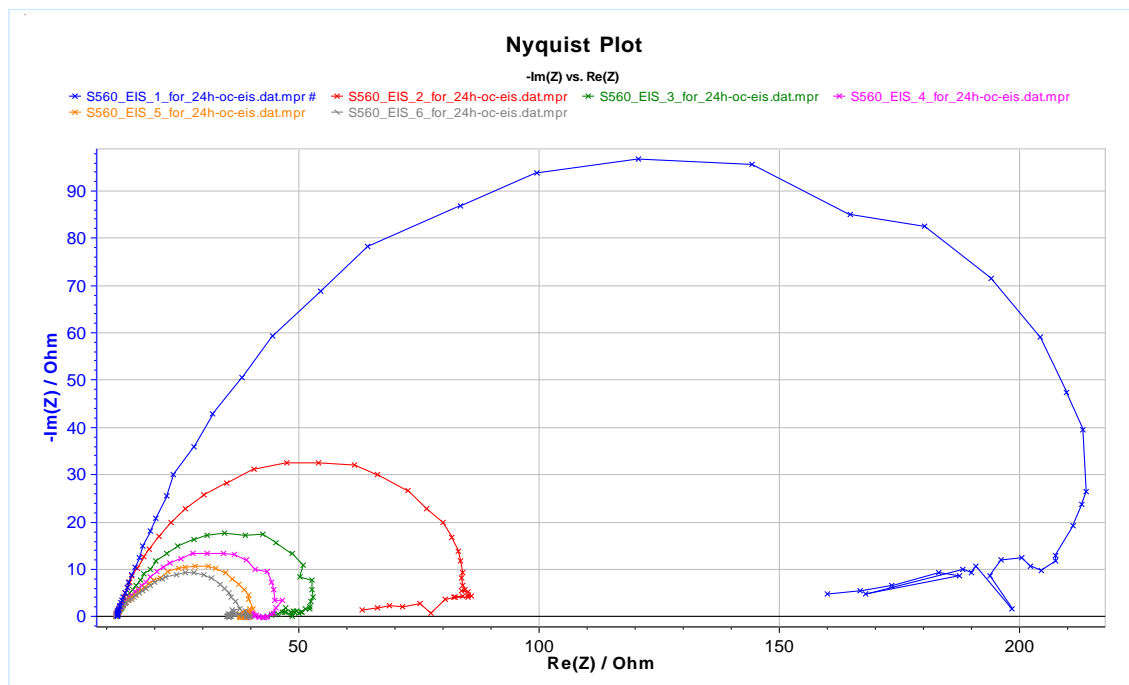
Figure 5.12: Nyquist summary plot of 24h experiment on EIS method of S560, specifically:
***Blue**: t=0h, **Red**: t=2h, **Green**: t=4h, **Magenta**: t=8h, **Orange**: t=16h, **Grey**: t=24h.*

The Nyquist plots for the 24h experiments present smaller diameters for longer exposure periods of the specimen to the solution. Thus after 2 hours the diameter is smaller than the half comparing to the initial one at t=0. It proves that R_P is diminishing, showing that the anodic dissolution of the specimen is continuing. The same behavior is apparent for the 4 hours curve. The 8 hours, the 16 hours and the 24 hours curve are very close implying that some corrosion products are formed on the surface halting further dissolution of the specimen. (Figure 5.12).

To describe the impedance response of the corrosion behavior vs time for S560 in chloride environment, the equivalent circuit model of Randles cell was employed also for these experiments. (Figure 5.12), where the capacitor C has been replaced by the Constant Phase Element CPE, due to the deformation and broadening of the semicircle. As already mentioned, this deformation is attributed to the roughness of the electrode-electrolyte interfaces or to inhomogeneities in the local distribution of defects in the vicinity of grain boundaries.

The values of the electric elements in Table 5.7 show that the resistance of the solution is stable R_S and R_P is diminishing over time.

Table 5.7: Equivalent circuit parameters of S560, on 24h EIS experiment.

S560 – Electrochemical Impedance Spectroscopy (24h)

	Results						
	Experiment:	**0 h**	**2 h**	**4 h**	**8 h**	**16 h**	**24 h**
R_S	*[Ohm]*	12.45	12.31	12.39	12.07	11.99	11.96
CPE	*[F.s^(a - 1)]*	2.47E-04	6.09E-04	6.32E-04	6.23E-04	8.05E-04	1.02E-03
a		0.8579	0.8595	0.8137	0.7389	0.7083	0.6889
R_P	*[Ohm]*	228.8	78.69	45.26	38.76	32.05	28.79
	PseudoC						
R_S	*[Ohm]*	12.45	12.31	12.39	12.07	11.99	11.96
C	*[F]*	1.53E-04	3.71E-04	2.80E-04	1.67E-04	1.79E-04	2.08E-04
R_P	*[Ohm]*	228.8	78.69	45.26	38.76	32.05	28.79
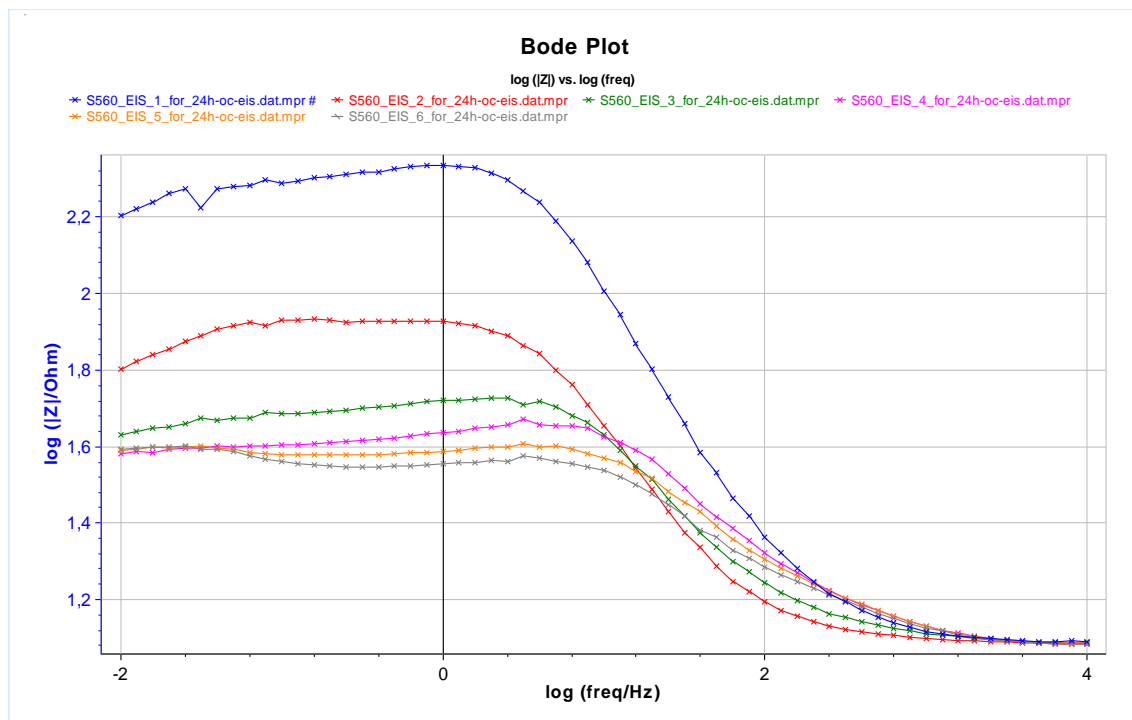
Figure 5.13: Bode (log|Z|) summary plot of 24h experiment on EIS method of S560, specifically:
***Blue**: t=0h, **Red**: t=2h, **Green**: t=4h, **Magenta**: t=8h, **Orange**: t=16h, **Grey**: t=24h.*
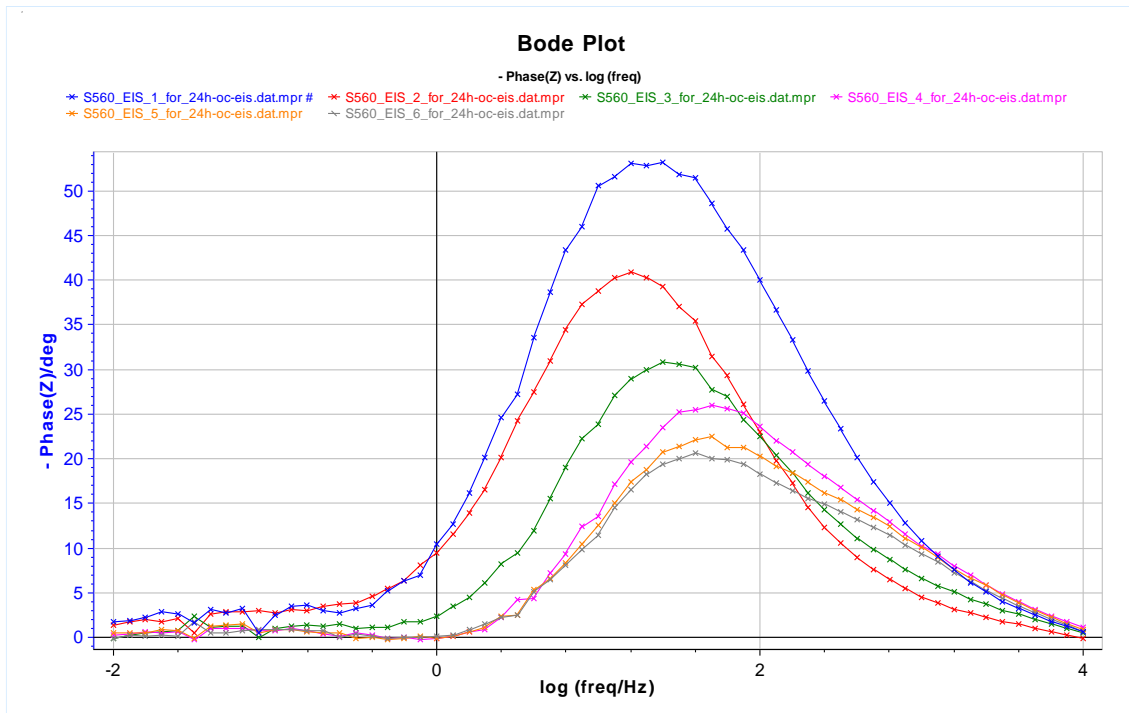
Figure 5.14: Bode (-Phase(Z)) summary plot of 24h experiment on EIS method of S560, specifically:
***Blue**: t=0 h, **Red**: t=2 h, **Green**: t=4 h, **Magenta**: t=8 h, **Orange**: t=16 h, **Grey**: t=24 h.*

5.1.2.6. Cyclic Potentiodynamic Polarization (CPP)

Two (2) individual experiments took place employing the Cyclic Potentiodynamic Polarization (CPP) method. In Figure 5.15 the experimental curves of the potential of the working electrode Ewe (in Volt) as a function of the current I (in milli-Ampere) expressed in logarithmic term of S560 are presented.

Cyclic polarization curves of S560 shows that, in the anodic polarization scan, scanning starts from corrosion potential after reaching the steady state. The anodic polarization curve presents a continuous increase in the anodic dissolution, implying that the oxide film formed is not stable with defects and that these defects enhance the dissolution. Only after 200mV a passive region starts to appear. Considering the hysteresis loop, no significant increase in the current density is observed, implying no significant pitting corrosion. This small loop shows that very limited pitting corrosion might developed. It has to be mentioned that the aforementioned IR drop phenomenon might affect the shape of the Cyclic Polarization Curves. However, the experiments could not be repeated taking into account the IR drop, due to COVID pandemic.
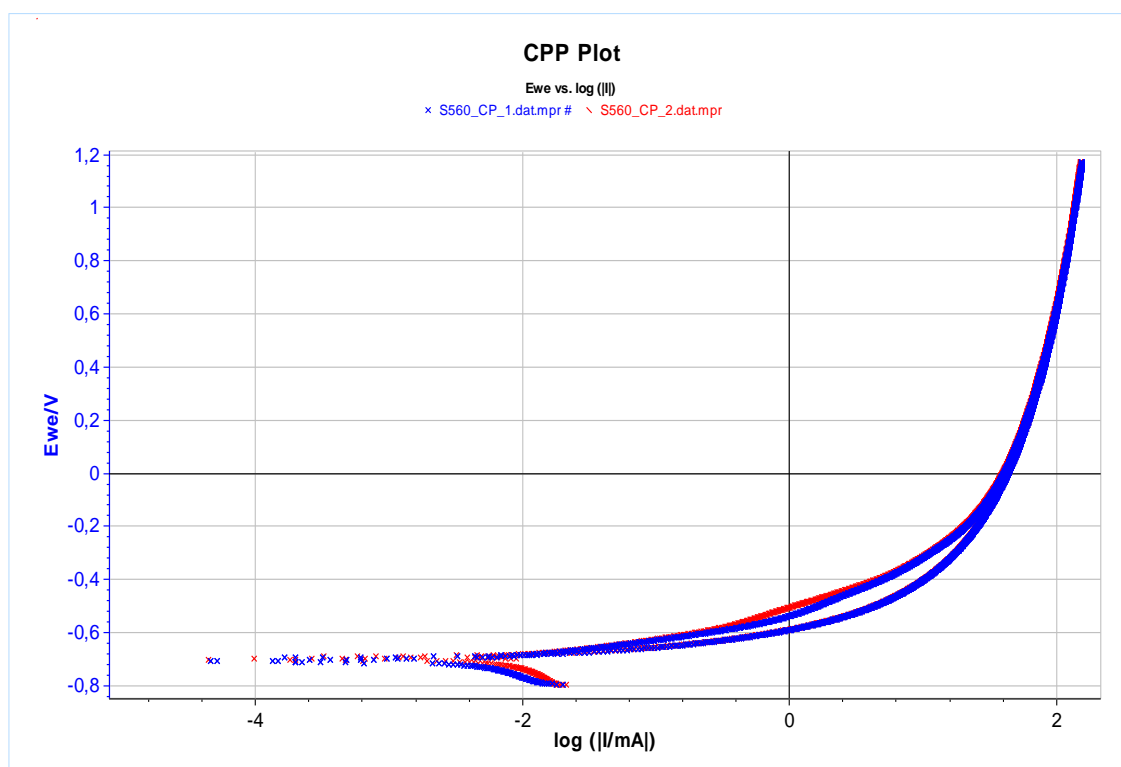
Figure 5.15: Experiments on CPP method of S560,
*specifically: **Blue**: 1st experiment, **Red**: 2nd experiment.*

5.2. S700 steel

As mentioned in Chapter 1, S700 is a high-strength low-alloy (HSLA) steel, produced by Quenching & Tempering (QT) with a minimum yield strength of 650-700 MPa. The study of the metal alloy and its behavior to corrosion is presented in the next paragraphs.

5.2.1. Study of metal alloy – S700

5.2.1.1. Chemical composition of S700

In order to define the precise values of the main alloying elements X-Ray Fluorescence method was employed. In Table 5.8 the chemical composition of S700 is cited, showing the values of each element, as presented in its technical data sheet certificate (provided by SSAB) and as it was calculated via XRF. It has to be mentioned that XRF method does not present values for carbon (C) and for elements with content lower than 0.01%. S700 steel presents low carbon content assuring good machinability and high weldability.

Table 5.8: S700 chemical composition.

Chemical Composition of S700		
	XRF	**Certificate**
C		0.140
Si	0.253	0.300
Mn	1.180	1.150
P	0.013	0.012
S		0.001
Al$_{tot}$		0.035
Nb		0.001
V	0.040	0.013
Ti		0.009
Cr	0.300	0.295
Cu	0.020	0.010
Ni	0.053	0.065
Mo	0.163	0.172
B		0.001
N		0.002
Zr		0.002
Carbon Equivalent	**0.442**	**0.433**

With the knowledge of the chemical composition from the **XRF** method, the following were calculated:

- ▪ **Carbon Equivalent,** by the equation (4.2) in chapter 4, taking also into account the carbon content from the certificate:

$$CE_{IIW} = C + \frac{Mn}{6} + \frac{Cr + Mo + V}{5} + \frac{Ni + Cu}{15} = \mathbf{0.442}$$

- **Total Number of Equivalents** and **Equivalent Weight**, by the equations (2.34) and (2.35), respectively, in chapter 2:

$$N_{EQ} = \sum \left(\frac{f_i}{\alpha_i/n_i} \right) = \sum \left(\frac{f_i \cdot n_i}{\alpha_i} \right) = \mathbf{0.03533}$$

$$EW = N_{EQ}^{-1} = \mathbf{28.14}$$

The chemical analysis of the steel specimen by XRF is in <u>agreement</u> with the data sheet certificate of S700.

5.2.1.2. Micro-hardness of S700

The micro-hardness of the specimen has been studied employing Vickers' hardness test method. Ten (10) different micro-hardness measurements were applied, as shown in Table 5.9 and Figure 5.16, with a load of 0.3kp (2.942 N) for dwell time 10secs on distinct spots on the specimen. The values obtained range from 240.0 $HV_{0.3}$ to 267.3 $HV_{0.3}$, with average value of **256.1** $HV_{0.3}$ and standard deviation of 9.9 $HV_{0.3}$. The value of the micro-hardness is in agreement with the literature for this type of steels.

Table 5.9: Micro-hardness of S700.

Micro-Hardness of S700

Measurements	1	2	3	4	5	6	7	8	9	10	AVG	SD
HV 0.3	240.0	259.1	261.1	244.1	244.6	263.8	266.8	260.1	254.2	267.3	**256.1**	9.9
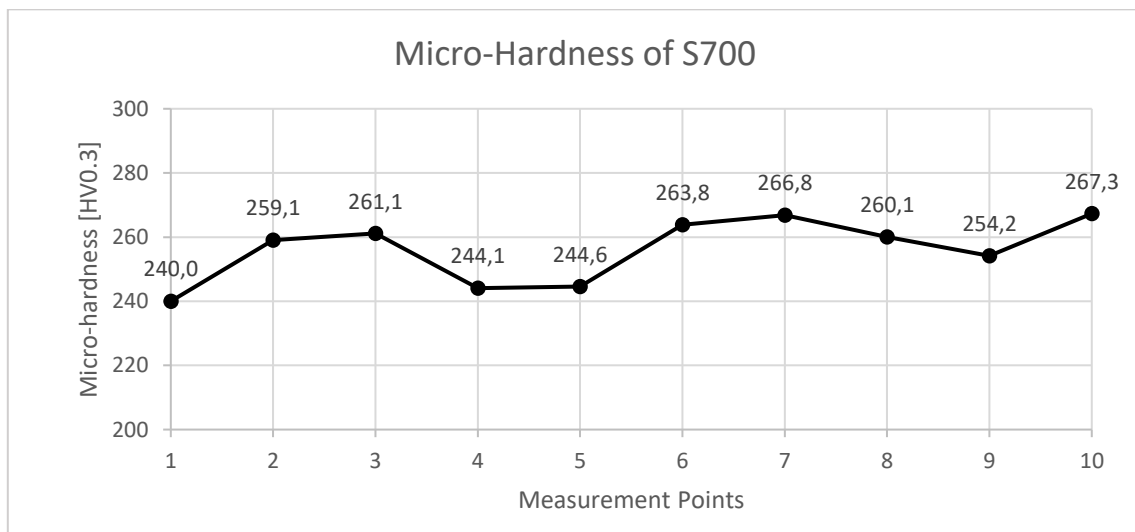
Figure 5.16: Diagrams of the micro-hardness measurements on S700.

5.2.1.3. Microstructure

The microstructure of the specimen (metallography) has been studied employing Optical Microscopy – OM (*Figure 5.17*) and Scanning Electron Microscopy – SEM (Figure 5.18). The results are presented below.

S700 steel is a High Strength Low Alloy steel (HSLA). During the production of S700, quenching and tempering (QT) is applied. So, the microstructure of the S700 consists of a homogeneous mixture of tempered martensite and bainite, along with ferrite. The volume fraction of tempered martensite (bright-colour areas) is usually higher than the one of bainite. No grain orientation appears in S700, as a result of its heat treatment. In this case, the S700 QT, exhibits a fine elongated ferrite - bainite microstructure.

(a)

(b)

(c)
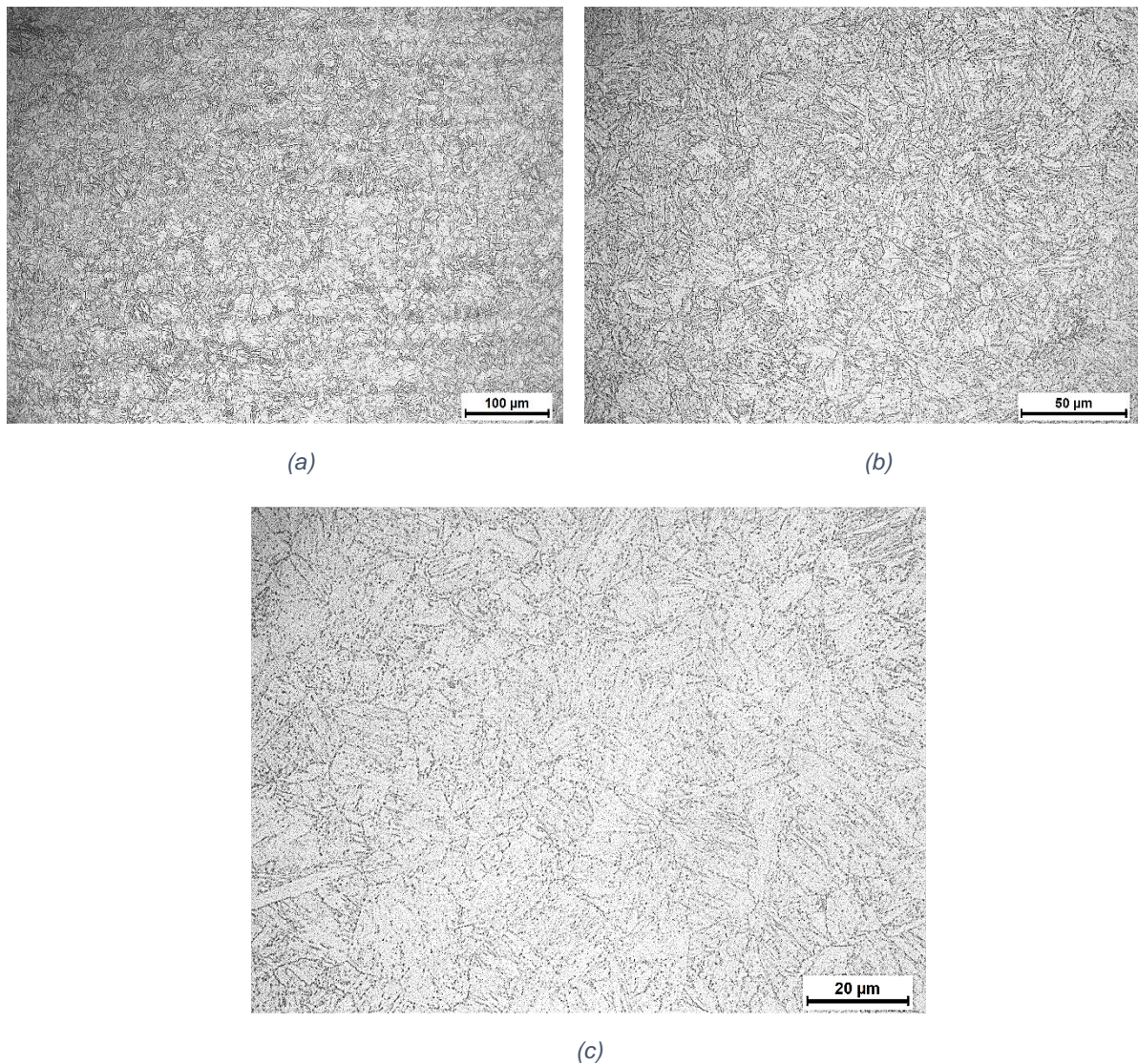
Figure 5.17: Optical observation of S700 employing Optical Microscopy (OM). Magnification of the instrument at (a) x200, (b) x500, (c) x1000.

(a)

(b)

(c)
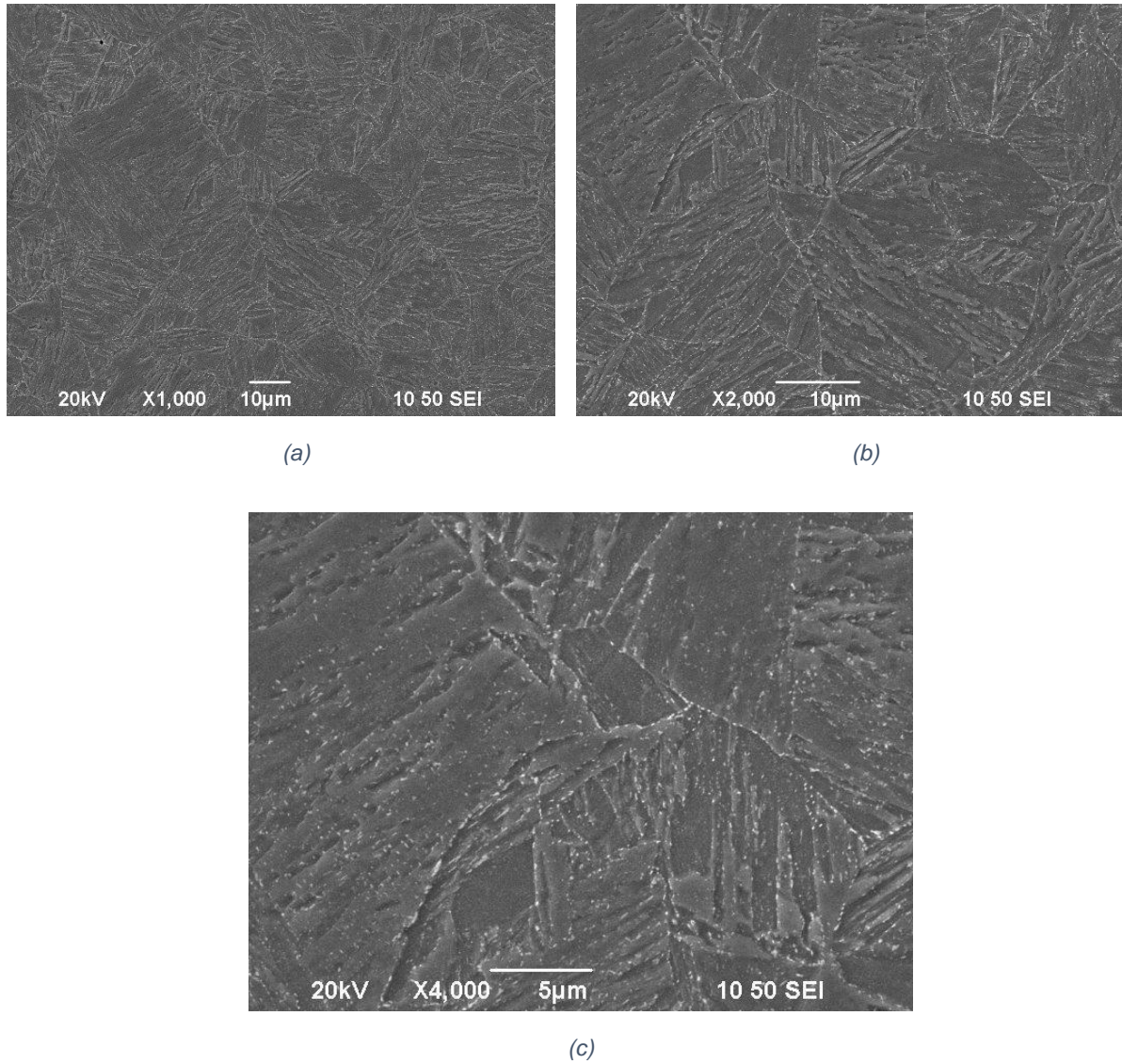
Figure 5.18: Optical observation of S700 employing Scanning Electron Microscopy (SEM). Magnification of the instrument at (a) x1000, (b) x2000, (c) x4000.

152

5.2.2. Study of corrosion – S700

In the following paragraphs, the results of the electrochemical techniques for S700 are presented. As mentioned in Chapter 4, EC-Lab Software was employed for the analysis of the data obtained from the electrochemical measurements through Versa Studio Software.

5.2.2.1. Open Circuit Potential (OC)

Open Circuit (OC) experimental curves show the evolution of the potential of the working electrode Ewe (in Volt) as a function of the elapsed time t (in second) of S700 are presented. OC measurements were recorded for a period of 24hour OC, and of 48hour (Figure 5.19). The potential versus time showed that after 7000sec a drop in the potential is observed, while after 5600 secs (≈15.5hrs) a rather stable value of **-721mV** is recorded. Similar behavior is observed for the 48h recording, where the stable potential is obtained after 40000 secs (≈11hrs) in the value of **-785mV**. The stabilization of potential proves that equilibrium has been attained for the corrosion phenomena in the system and it can be assumed, taking into account the Potentiodynamic Polarization Curves, that the equations are the dissolution of Fe:

$$Fe \leftrightharpoons Fe^{2+} + 2e^-$$

and the oxygen's reduction:

$$O_2 + 2H_2O + 4e^- \leftrightharpoons 4OH^-$$
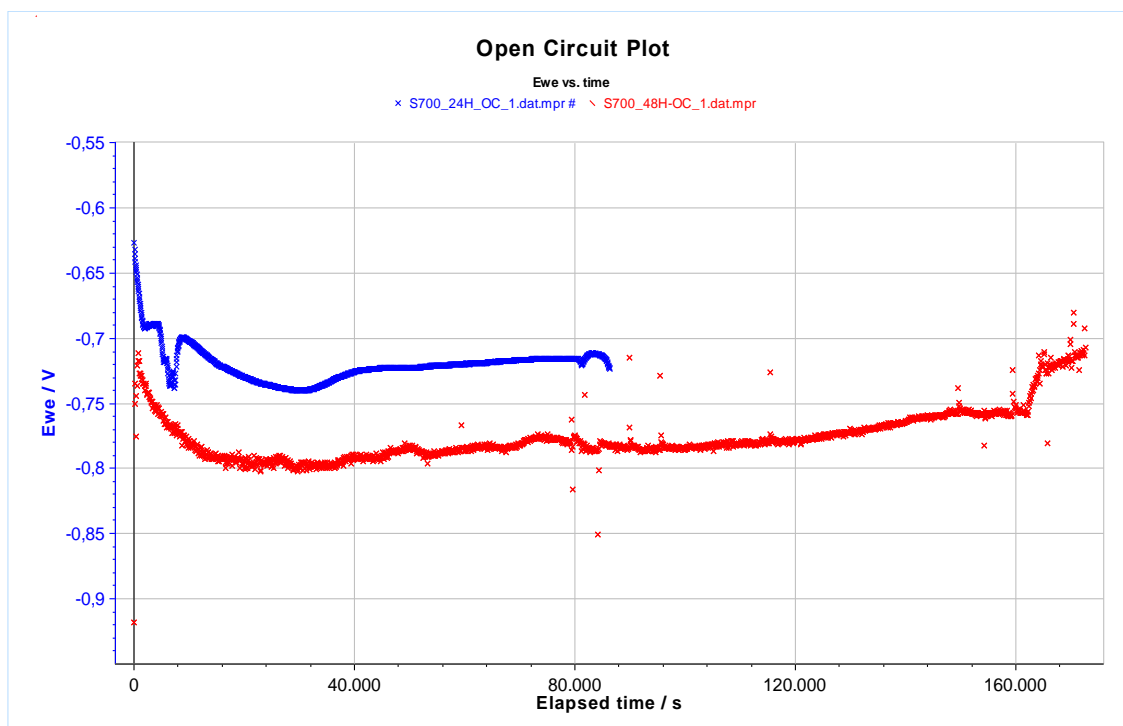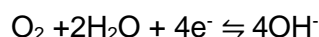
Figure 5.19: Summary of experiments on OC method of S700, specifically:
Blue: 24hour experiment VS **Red:** 48hour experiment.

153

In Figure 5.20 the recorded Open Circuit measurements during the 24h (6 loop) OC-EIS experiment (between every EIS perturbation) are presented. The curve of the serial 24hour Open Circuit experiments is also presented for comparison. It is obvious that the measurements obtained are consistent for both experiments, so it can be assumed that the results are credible.
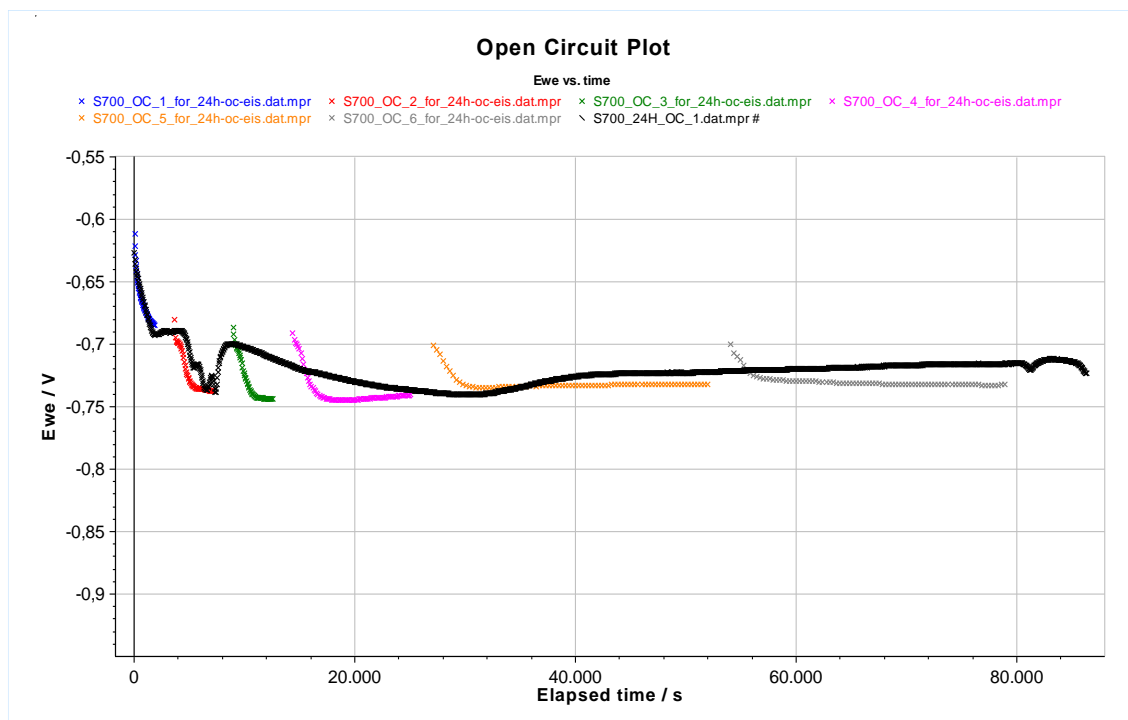
Figure 5.20: Summary of experiments on OC method of S700, specifically:
Black: *24hours experiment VS* **Colored:** *six cycles of OC for the 24hour experiment OC-EIS.*

5.2.2.2. Linear Polarization Resistance (LPR)

Three (3) individual experiments took place employing the Linear Polarization method, each one consisted of two (2) consecutive runs, six experimental curves obtained in total. In *Figure 5.21* the experimental curves of the current I (in milli-Ampere) as a function of the potential of the working electrode Ewe (in Volt) S700 are presented.
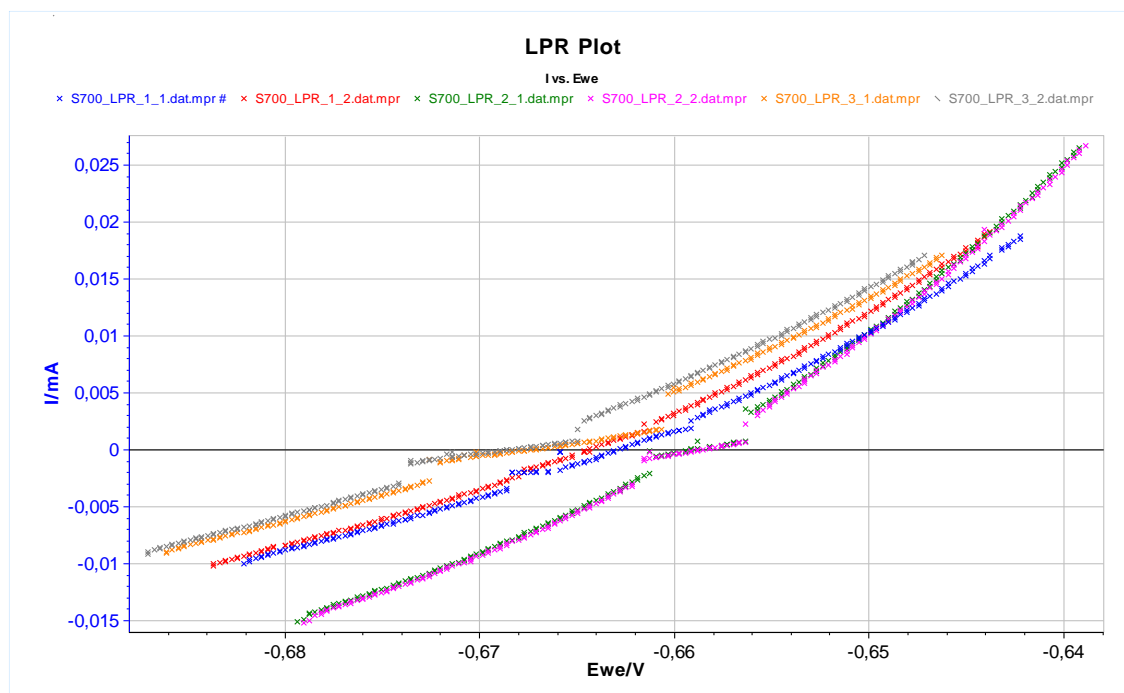
Figure 5.21: Summary of experiments on LPR method of S700, specifically:
Blue*: exp.1_1,* **Red***: exp.1_2,* **Green***: exp.2_1,* **Magenta***: exp.2_2,* **Orange***: exp.3_1,* **Grey***: exp.3_2.*

As it can be observed in Figure 5.21, the curves are very similar, showing rather stable behavior.

The measurements obtained by this method were elaborated employing EC-Lab software, as already mentioned in paragraph 5.1.2.2. For the I_{corr} determination, literature's values of β_a and β_c (=120mV) were used. The results are presented in Table 5.10. In this method it was not possible to calculate I_{corr} values employing the second approach, as in S560 steel, because the β_c value obtained was considered invalid and out of the range of the values accepted by literature. In any case, as proved for S560, similar values of I_{corr} result from both approaches, while the rest of the values do not alter.

Table 5.10: Corrosion and LPR parameters for each experiment of S700.

S700 – Linear Polarization Resistance

		Parameters						
βa	*[mV]*	120						
βc	*[mV]*	120						
Range	*[mV]*	+/- 25.0						
		Results						
Specimen:		**1**		**2**		**3**		
Experiment:		**1_1**	**1_2**	**2_1**	**2_2**	**3_1**	**3_2**	**AVG**	**SD**
R$_P$	*[Ohm]*	1444	1405	989	984	1592	1581	**1332**	277
E$_{CORR}$	*[mV]*	-664.9	-666.3	-661.1	-660.9	-669.1	-670.4	**-665.4**	4.0
Correlation		0.9885	0.9885	0.9873	0.9877	0.9830	0.9902	**0.9875**	0.0024
I$_{CORR}$	*[µA]*	18.07	18.57	26.37	26.52	16.39	16.50	**20.40**	4.76

The values of R$_P$ represent the ability of the electrons to pass through the steel specimen. Thus the higher the R$_P$ values the better the corrosion resistance of the steel.

The polarization curves in Figure 5.21 and the results in Table 5.10 show that the S700 specimens present good repeatability with **R$_P$** average value is **1322Ohms**, while the standard deviation is 277Ohms. The **I$_{corr}$** average value is **20.40µA** with standard deviation of 4.76µA.

Slight differences (on specimen 2 compared with sp.1 or sp.3) can be attributed to the variations in the microstructure of the specimens, which might affects the corrosion behavior. However, all the obtained values of I$_{corr}$ can be assigned to good corrosion behavior for steel specimen according to Figure 2.14 [McCafferty, 2010] indicating a "good" corrosion rate for iron with corrosion current density between 11 and 43µA/cm^2 and "excellent" below 11µA/cm^2.

Concerning the **E$_{corr}$**, its average value is **-665mV**, which is representative for this type of steel and consistent with the literature, with low standard deviation. It is also worth-mentioned that the correlation of the values is close to unit, proving the accuracy of the linear regression.

5.2.2.3. Potentiodynamic Polarization - Tafel Extrapolation

Three (3) individual experiments took place employing the Potentiodynamic Polarization (PP) method. In Figure 5.22 three (3) experimental curves of the potential of the working electrode Ewe (in Volt) as a function of the current I (in milli-Ampere) expressed in logarithmic scale of S700 are presented.
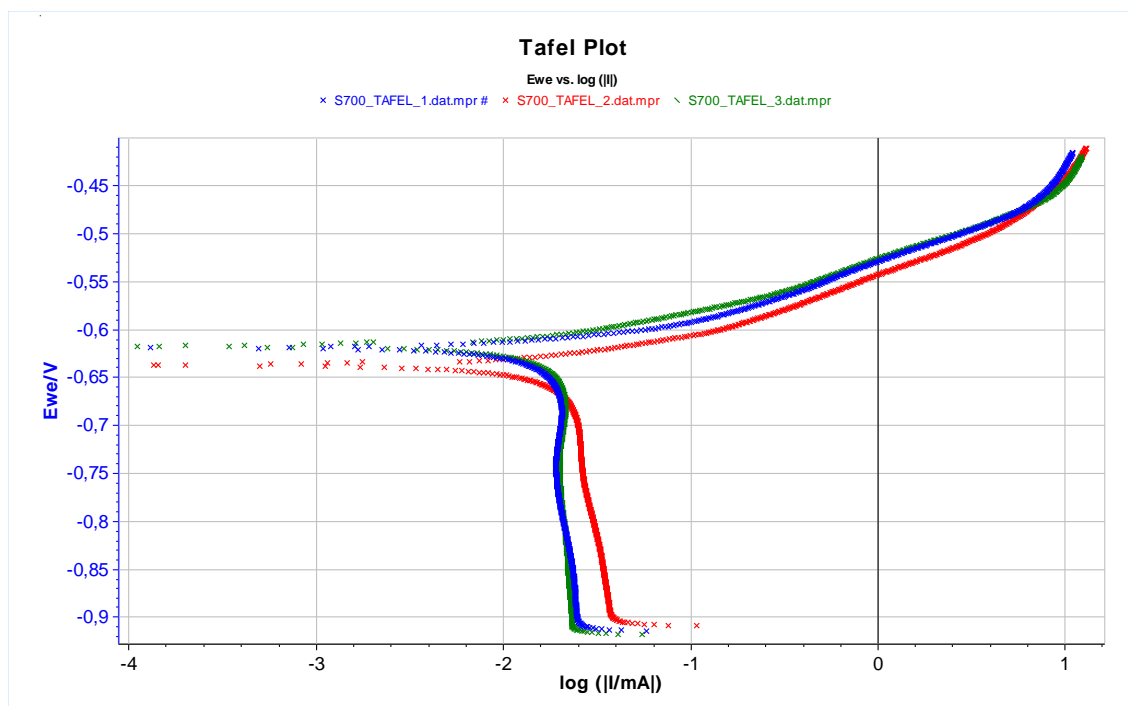
*Figure 5.22: Summary of experiments on Potentiodynamic Polarization method of S700, specifically: **Blue**: exp.1, **Red**: exp.2, **Green**: exp.3.*

The polarization curves in Figure 5.22 presents the anodic branch, whose shape proves that S700 presents continuous anodic dissolution, without evidence of passive behavior, according to the reaction of:

$$Fe \rightarrow Fe^{2+} + 2e^-$$

Possibly, other alloying elements' present anodic reactions, however these are of minor importance.

The shape of the cathodic branch shows that cathodic behavior is dominated by the O_2 diffusion in the electrolyte solution, by the reaction of:

$$O_2 + 2H_2O + 4e^- \rightarrow 4OH^-$$

and the last part of the cathodic reaction one can recognize the reduction of hydrogen:
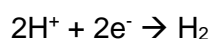
$$2H^+ + 2e^- \rightarrow H_2$$

157

As already mentioned in paragraph 3.3, according to Tafel extrapolation method, the crossing point of the tangent to the linear part of the anodic branch, the tangent to the linear part of the cathodic branch and the line through the E_{corr} parallel to the x-axis defines the I_{corr} value on x-axis. The anodic reaction (metal's dissolution) is **activation polarization controlled**, presents Tafelian behavior, so β_a represents the Tafel coefficient. However, in **diffusion controlled** cathodic curves, β_c values cannot be defined and the calculated values in Table 5.11, only represent the slopes of the cathodic branches which tend to infinity.

Figure 5.22 shows all the experiments, which present the aforementioned behavior and evidence very good repeatability. Corrosion potential E_{corr} has mean value of -625mV while I_{corr} has an average of 19.9μA/cm^2 and corrosion rate is equal to 9.2mpy (calculated according to equation (4.7)). Anodic Tafel constant β_a is 46.7mV/decade, while cathodic slope β_c is very high due to O_2 diffusion.

Table 5.11: Corrosion and Tafel parameters for each experiment of S700.

S700 – PP with Tafel Extrapolation

Parameters					
equivalent weight	*[g/eq.]*	28.143			
density	*[g/cm3]*	7.8			
surface area	*[cm²]*	1.000			
Results					
Experiment:		**1st**	**2nd**	**3rd**	**AVG**	**SD**
E_{CORR}	*[mV]*	-621.1	-634.6	-618.2	**-624.7**	8.8
I_{CORR}	*[μA]*	18.82	21.40	19.57	**19.93**	1.32
I_{LIM}	*[μA]*	20.74	31.54	20.60	**24.29**	6.28
βc	*[mV]*	4189.9	1127.5	7075.7	**4131.0**	2974.5
βa	*[mV]*	43.8	46	50.4	**46.7**	3.4
corrosion rate	*[mmpy]*	0.2222	0.2526	0.2310	**0.2353**	0.0156
corrosion rate	*[mpy]*	8.747	9.943	9.094	**9.261**	0.615

Ohmic Potential Drop (IR Drop)

As shown in Figure 5.23 the IR drop phenomenon (red curve) is not noticeable around Icorr, so, it does not affect either the values of E_{corr} and I_{corr} or those of β_a and β_c, as the extrapolation of the potentiodynamic anodic and cathodic curves for all the experiments was done at their linear part close to E_{corr}.
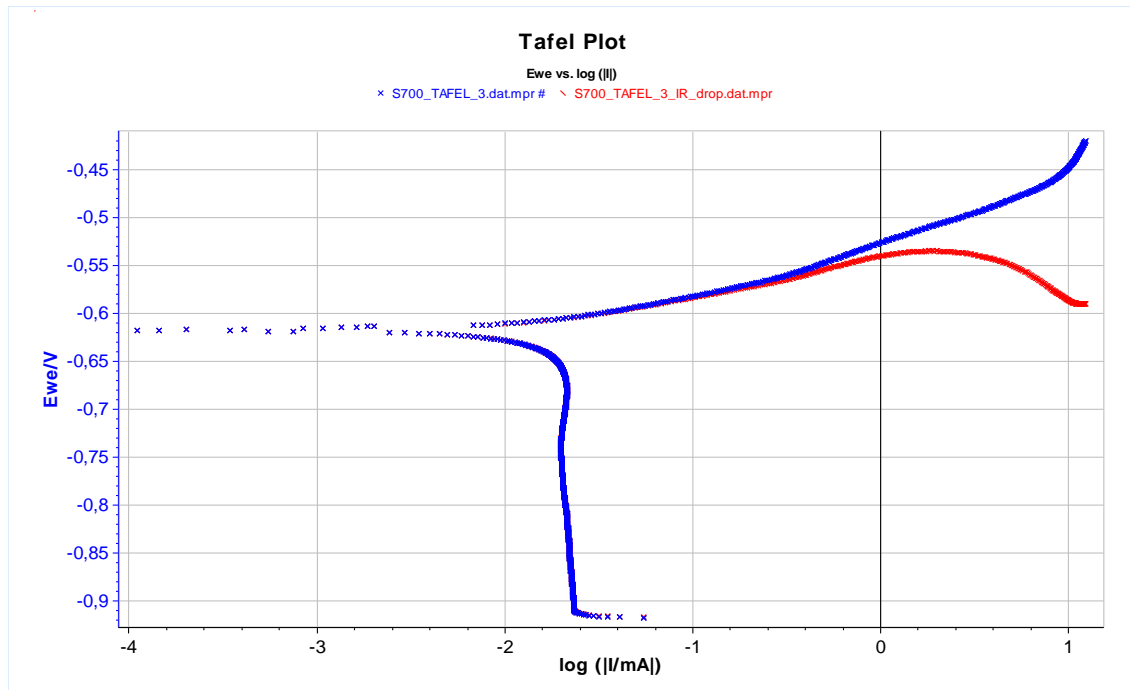
Figure 5.23: Experiment on Potentiodynamic Polarization method of S700, specifically: **Blue***: Potential V,* **Red***: Ohmic Potential Drop $E_{WE} = E_{ap} - IR_S$.*

5.2.2.4. Electrochemical Impedance Spectroscopy (EIS)

Two individual experiments took place employing the Electrochemical Impedance Spectroscopy (EIS) method, one of which consisted of <u>three consecutive runs</u> and the other one was <u>a 24hour experiment with 6 loops of an OC followed by an EIS</u>. The impedance behavior of the electrode is expressed in Nyquist plots of –Im(Z) (in Ohm) as a function of Re(Z) (in Ohm) or in Bode plots of log|Z| (Z in Ohm) and –Phase(Z) (in degrees) as a function of log|frequency| (frequency in Hertz). Three figures for each experiment are presented below, one Nyquist and two Bode plots (Figures: Figure 5.24, Figure 5.25, Figure 5.26 / Figure 5.27, Figure 5.28, Figure 5.29), respectively.

Three consecutive EIS experiment
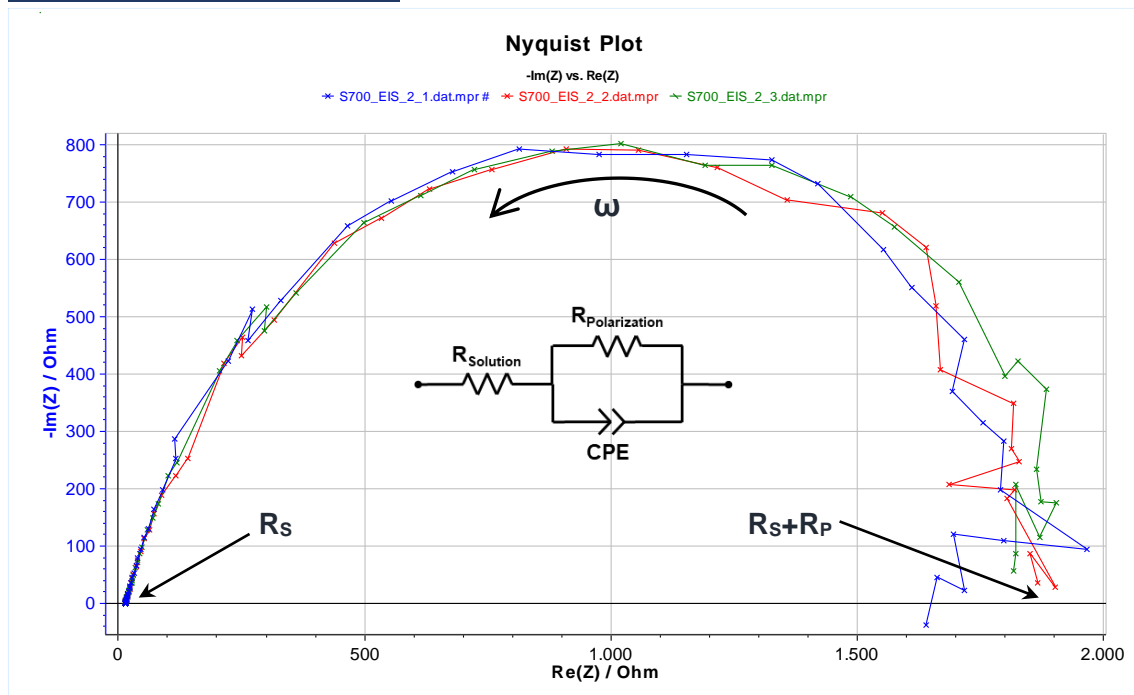
*Figure 5.24: Nyquist summary plot of 3 consecutive experiments on EIS method of S700, specifically: **Blue**: 1st EIS, **Red**: 2nd EIS, **Green**: 3rd EIS.*

The three (3) consecutive EIS experiments of same duration were conducted, after a 30-minutes Open Circuit (OC) corrosion experiment. In both Nyquist and Bode plot, the Z of high frequency implies solution resistance, whereas the Z of low frequency is the total resistance R_{CT}, including the solution R_S and the polarization resistance R_P.

The interpretation of EIS plots provides information of surface/electrolyte solution interface. The shape of the Nyquist plot for S700 displays only one capacitive semicircle. This type of curve is interpreted as a mechanism of charge transfer on an inhomogeneous surface.

The diameter of the capacitive semi-circle is almost the same for all the experiments. Minor deviations at the low frequency end of the semi-circle are due to changes in impedance during the long times required to conduct measurements at low frequencies. Moreover, no indication of Warburg impedance line is indicated (Figure 5.24). Similarly, the Bode plots of the S700 steel show only one time constant as in Figure 5.25 and Figure 5.26.

160

To describe the impedance response of the corrosion behavior of S700 in chloride environment, the equivalent circuit analysis was performed employing EC Lab software. The equivalent circuit model from the literature was applied on the EIS results (Figure 5.24). In the circuits, R_S and R_P indicate solution resistance and charge transfer resistance of the electrolyte–substrate interface, respectively. For perfect semi-circles the element Q is well represented by the capacitor C associated with the double layer capacitance. This type of circuit is named Randles cell.

However, in S700, the shape of the Nyquist curve is not a perfect semicircle centered on the Z' axis at the (R/2, 0) point. It presents deviation from the Resistance- Capacitor behavior and there is a deformation of the semicircle. For this reason, in the equivalent modelled circuit the capacitor C is substituted by the Constant Phase Element CPE, still parallel with the resistor R_P. This deformation is attributed to the roughness of the electrode-electrolyte interfaces or to inhomogeneities in the local distribution of defects in the vicinity of grain boundaries.

In the Table 5.12, the electrical elements of the impedance fitting via EC Lab are presented. In general, R_P, is inversely proportional to the corrosion rate of a given metal. For S700 the average value of R_P is 200 Ohms, with very low SD of 33 Ohms, while R_S is stable at 13 Ohms. CPE, Constant Phase Element presents an average value of 2.6E-04 F.s^(a - 1). If the electrolyte – electrode interface was a perfect capacitor it would be equal to average value of 2.29E-04 F.

Table 5.12: Equivalent circuit parameters of S700, on 3 consecutive EIS experiment.

S700 – Electrochemical Impedance Spectroscopy

Results						
	Experiment:	**1_1**	**1_2**	**1_3**	**AVG**	**SD**
R_S	*[Ohm]*	14.02	13.84	13.81	**13.89**	0.11
CPE	*[F.s^(a - 1)]*	2.42E-04	2.65E-04	2.76E-04	**2.61E-04**	1.77E-05
a		0.839	0.8272	0.8283	**0.8315**	0.0065
R_P	*[Ohm]*	1976	2009	2041	**2009**	**33**
PseudoC						
R_S	*[Ohm]*	14.02	13.84	13.81	**13.89**	0.11
C	*[F]*	2.10E-04	2.32E-04	2.45E-04	**2.29E-04**	1.81E-05
R_P	*[Ohm]*	1976	2009	2041	**2009**	32.5013
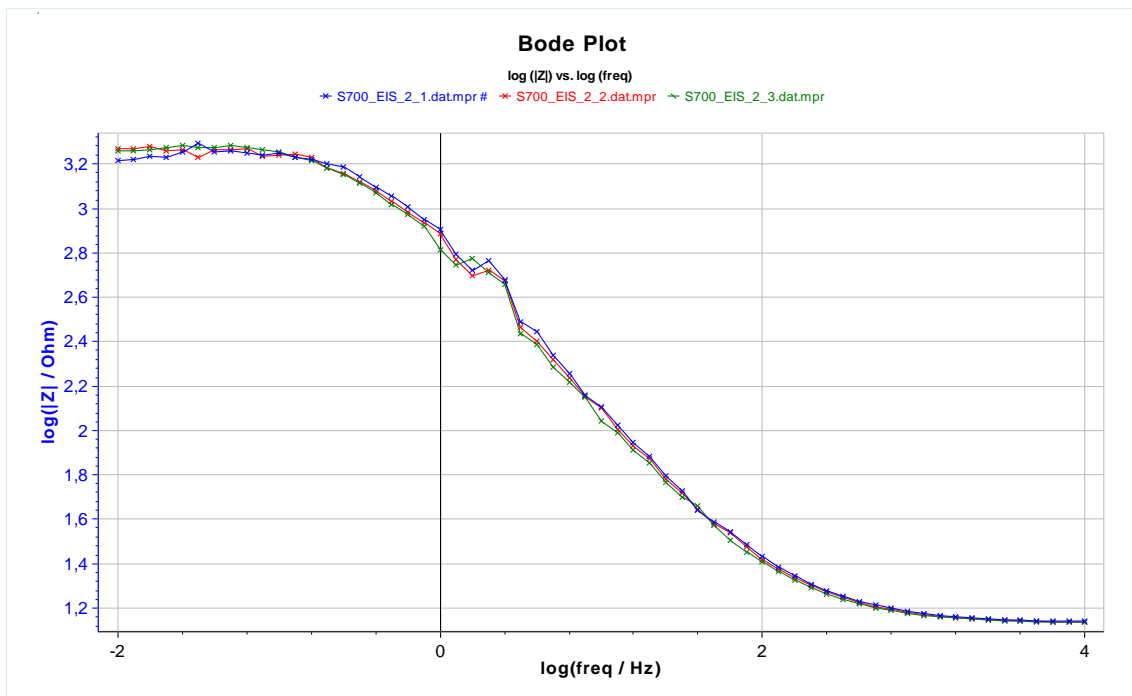
Figure 5.25: Bode (log|Z|) summary plot of 3 consecutive experiments on EIS method of S700, specifically: **Blue**: 1ˢᵗ EIS, **Red**: 2ⁿᵈ EIS, **Green**: 3ʳᵈ EIS.
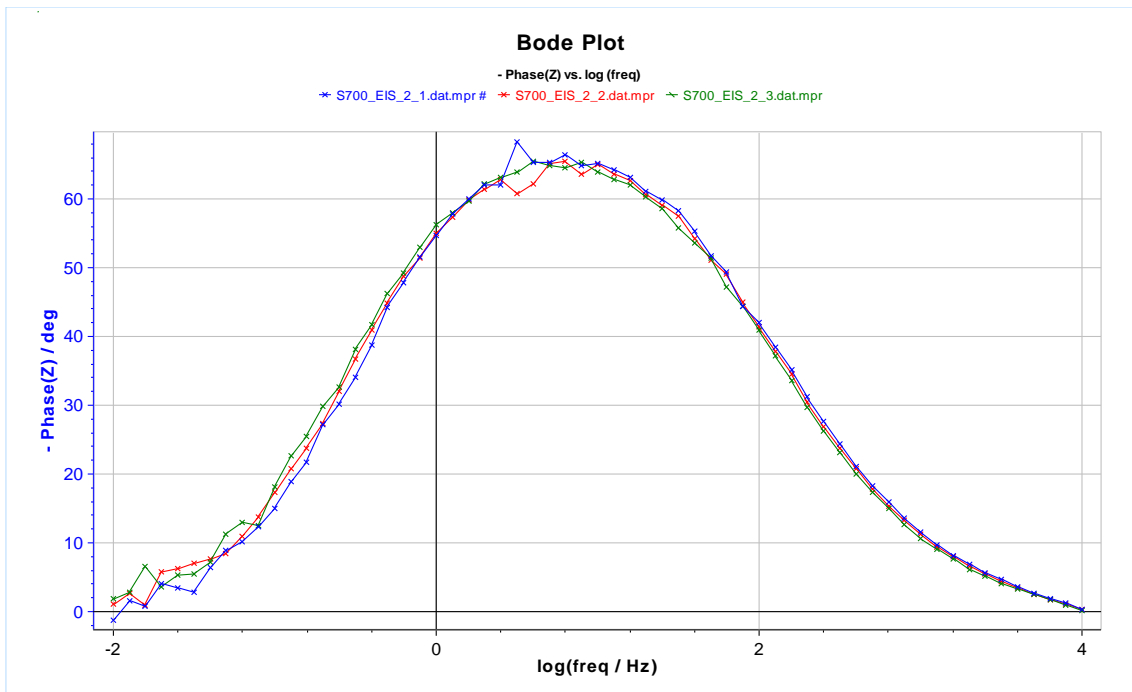
Figure 5.26: Bode (-Phase(Z)) summary plot of 3 consecutive experiments on EIS method of S700, specifically: **Blue**: 1ˢᵗ EIS, **Red**: 2ⁿᵈ EIS, **Green**: 3ʳᵈ EIS.

24 hour experiment

For the 24-hours experiments, the summary diagram, Figure 5.27 is presented, along with the parameters in Table 5.13.
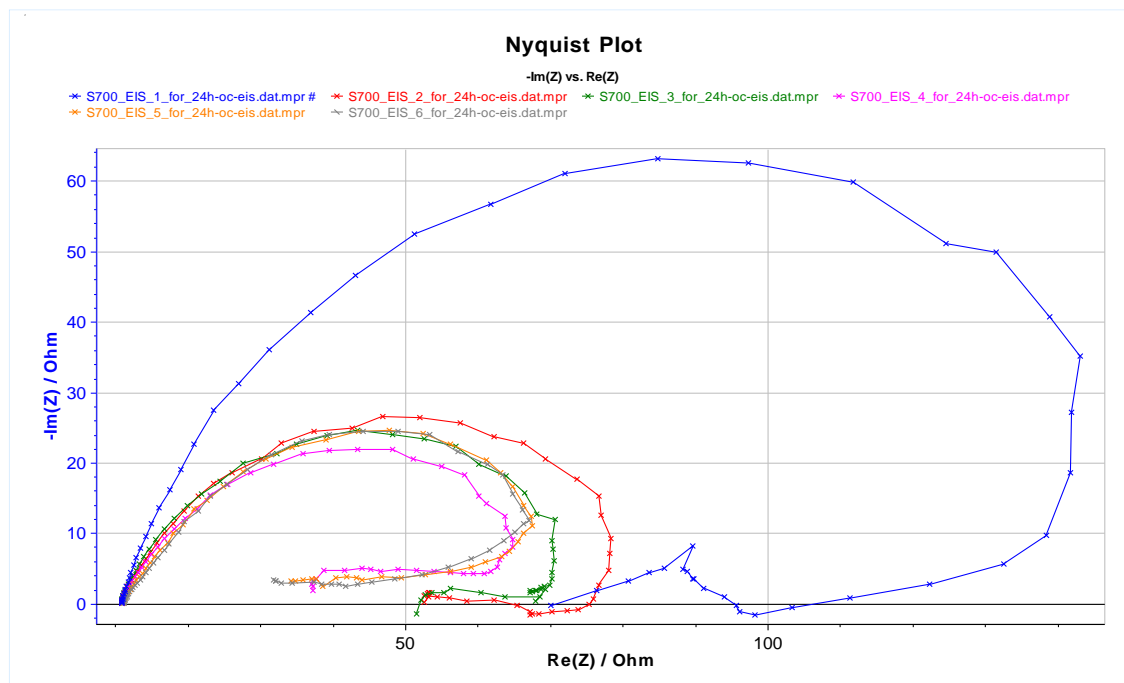
Figure 5.27: Nyquist summary plot of 24h experiment on EIS method of S700, specifically:
***Blue**: t=0 h, **Red**: t=2 h, **Green**: t=4 h, **Magenta**: t=8 h, **Orange**: t=16 h, **Grey**: t=24 h.*

The Nyquist plots for the 24h experiments present smaller diameters for longer exposure periods of the specimen to the solution. Thus after 2 hours the diameter is almost half comparing to the initial one at t=0. It proves that R_P is diminishing, showing that the anodic dissolution of the specimen is continuing. The same behavior is observed also at the 8hour curve. However the 16h and the 24h curve a slight increase is observed and the two curves are rather similar. This could imply that the corrosion rate is rather stabilized, maybe due to corrosion products formation on the surface. (Figure 5.27, Figure 5.28, Figure 5.29).

To describe the impedance response of the corrosion behavior vs time for S700 in chloride environment, the equivalent circuit model of Randles cell was employed also for these experiments, where the capacitor C has been replaced by the Constant Phase Element CPE, due to the deformation and broadening of the semicircle. As already mentioned, this deformation is attributed to the roughness of the electrode-electrolyte interfaces or to inhomogeneities in the local distribution of defects in the vicinity of grain boundaries.

The values of the electric elements in Table 5.13 show that the resistance of the solution is stable R_S and R_P is diminishing for period of 4hours and afterwards is rather stable.

Table 5.13: Equivalent circuit parameters of S700, on 24h EIS experiment.

S700 – Electrochemical Impedance Spectroscopy (24h)

Results							
	Experiment:	**0 h**	**2 h**	**4 h**	**8 h**	**16 h**	**24 h**
R$_S$	[Ohm]	10.82	10.74	10.69	10.76	11.05	11.26
CPE	[F.s^(a - 1)]	3.10E-04	4.08E-04	3.31E-04	5.65E-04	9.38E-04	1.12E-03
a		0.8352	0.764	0.7879	0.7481	0.7275	0.7204
R$_P$	[Ohm]	156.4	74.82	65.94	62.21	69.99	71.05
PseudoC							
R$_S$	[Ohm]	10.82	10.74	10.69	10.76	11.05	11.26
C	[F]	1.71E-04	1.39E-04	1.18E-04	1.83E-04	3.38E-04	4.19E-04
R$_P$	[Ohm]	156.4	74.82	65.94	62.21	69.99	71.05
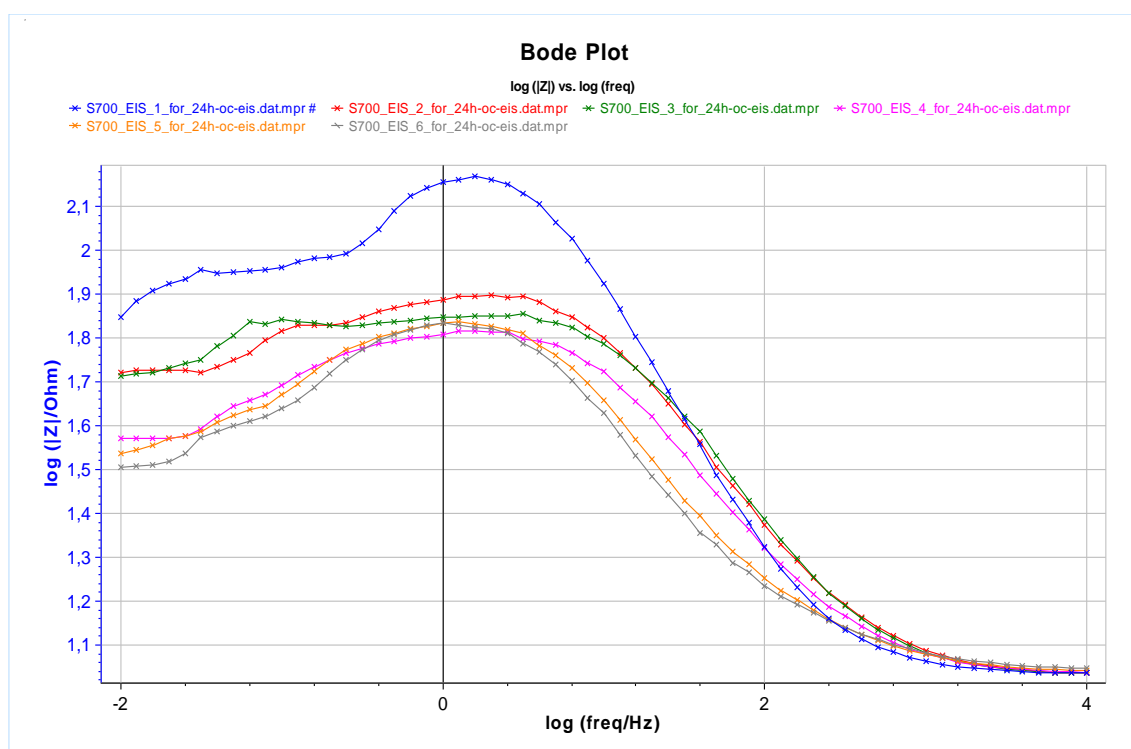
Figure 5.28: Bode (log|Z|) summary plot of 24h experiment on EIS method of S700, specifically:
***Blue**: t=0 h, **Red**: t=2 h, **Green**: t=4 h, **Magenta**: t=8 h, **Orange**: t=16 h, **Grey**: t=24 h.*
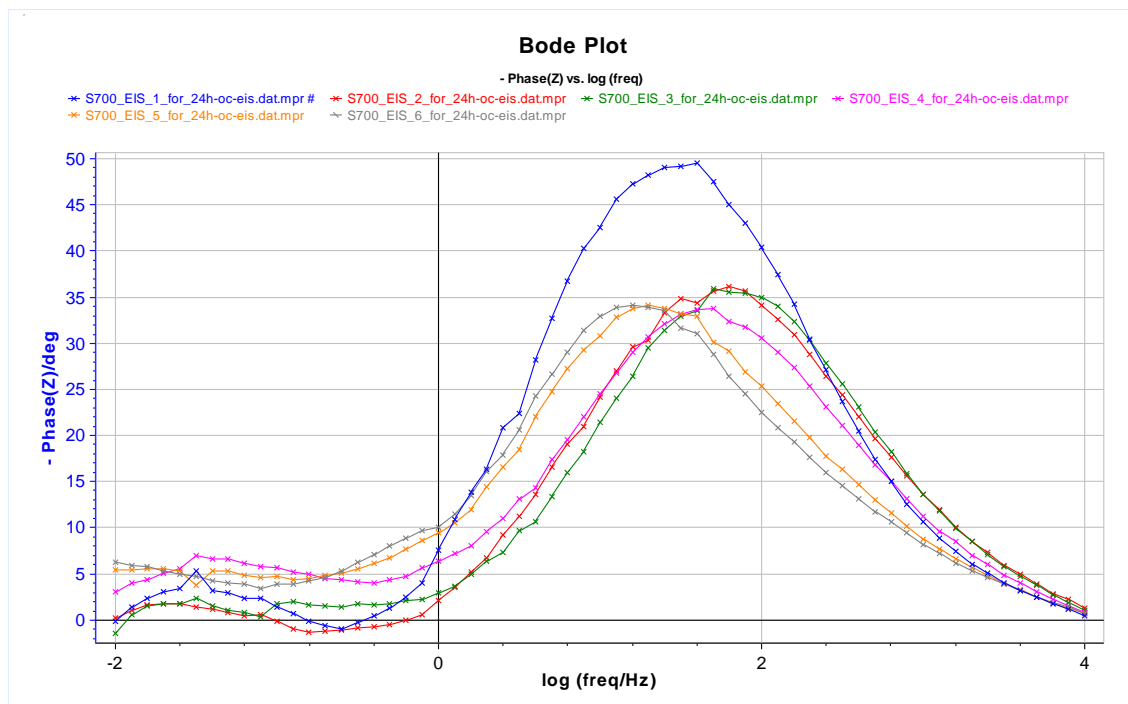
Figure 5.29: Bode (-Phase(Z)) summary plot of 24h experiment on EIS method of S700, specifically:
***Blue**: t=0 h, **Red**: t=2 h, **Green**: t=4 h, **Magenta**: t=8 h, **Orange**: t=16 h, **Grey**: t=24 h.*

5.2.2.5. Cyclic Potentiodynamic Polarization (CPP)

Two individual experiments took place employing the Cyclic Potentiodynamic Polarization (CPP) method. In Figure 5.30 the experimental curves of the potential of the working electrode Ewe (in Volt) as a function of the current I (in milli-Ampere) expressed in logarithmic term of S700 are presented.

Cyclic polarization curves of S700 shows that, in the anodic polarization scan, scanning starts from corrosion potential after reaching the steady state. The anodic polarization curve presents a continuous increase in the anodic dissolution, implying that the oxide film formed is not stable with defects and that these defects enhance the dissolution. Only after 200mV a passive region starts to appear. Considering the hysteresis loop, no significant increase in the current density is observed, implying no significant pitting corrosion. This small loop shows that some pitting corrosion is developed.

It has to be mentioned that the aforementioned IR drop phenomenon might affect the shape of the Cyclic Polarization Curves. However, the experiments could not be repeated taking into account the IR drop, due to COVID pandemic.
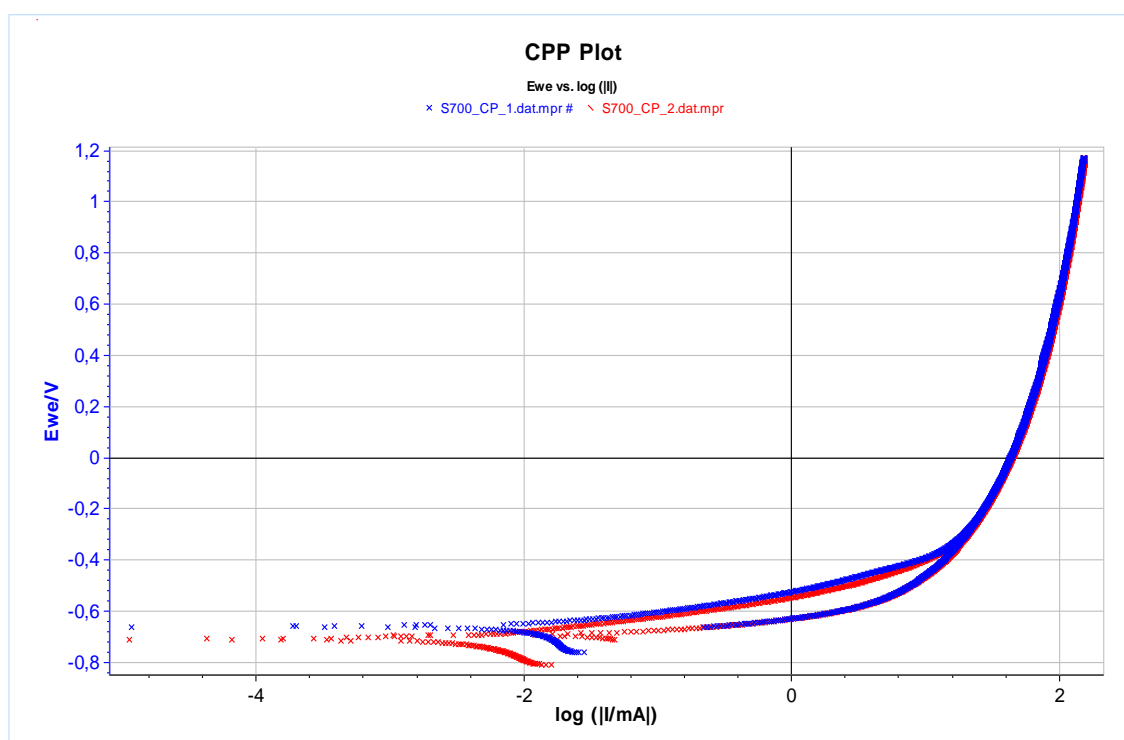
*Figure 5.30: Experiments on CPP method of S700, specifically: **Blue**: 1st experiment, **Red**: 2nd experiment.*

5.3. Comparison

In the following paragraphs, comparison of the two specimens, S560 and S700, is cited. Summary results from the individual experiments employed are included, concerning their microstructure study and their behavior to corrosion from the electrochemical techniques.

5.3.1. Comparison of metal alloys

5.3.1.1. Chemical composition comparison

In Figure 5.31 the chemical composition of S560 and S700 are cited, showing the values of each alloy element. For S560 carbon is equal to **0.06** and its Carbon Equivalent (CE) is **0.30**, while S700, carbon equals to **1.4** and CE is **0.44**. For both steels the content of Mn more than 1% provides high fracture toughness. Cr content is higher for S700 and it must be noted this alloy element contributes to higher yield stress and higher tensile stress. Mo also contributes to better mechanical properties.
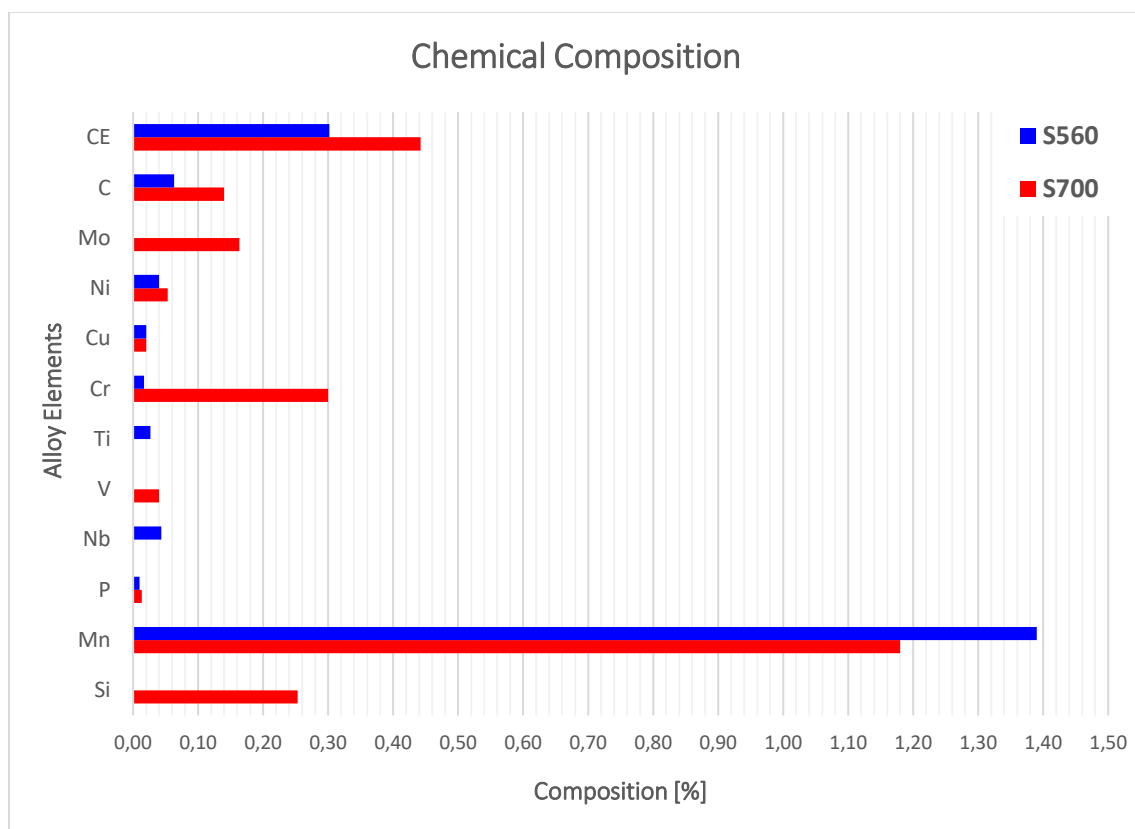
*Figure 5.31: Bar graph of the percent composition of the alloy elements and carbon equivalent of **S560** (in **Blue**) and **S700** (in **Red**).*

5.3.1.2. Micro-hardness comparison

The micro-hardness of the specimens, employed by Vickers' hardness test method, resulted an average value of **194HV$_{0.3}$** for S560 and **256HV$_{0.3}$** for S700. The ten different micro-hardness measurements applied are presented in Figure 5.32. The higher micro-hardness values for S700 are attributed to the process of quenching and tempering and the microstructure of martensite and bainite.
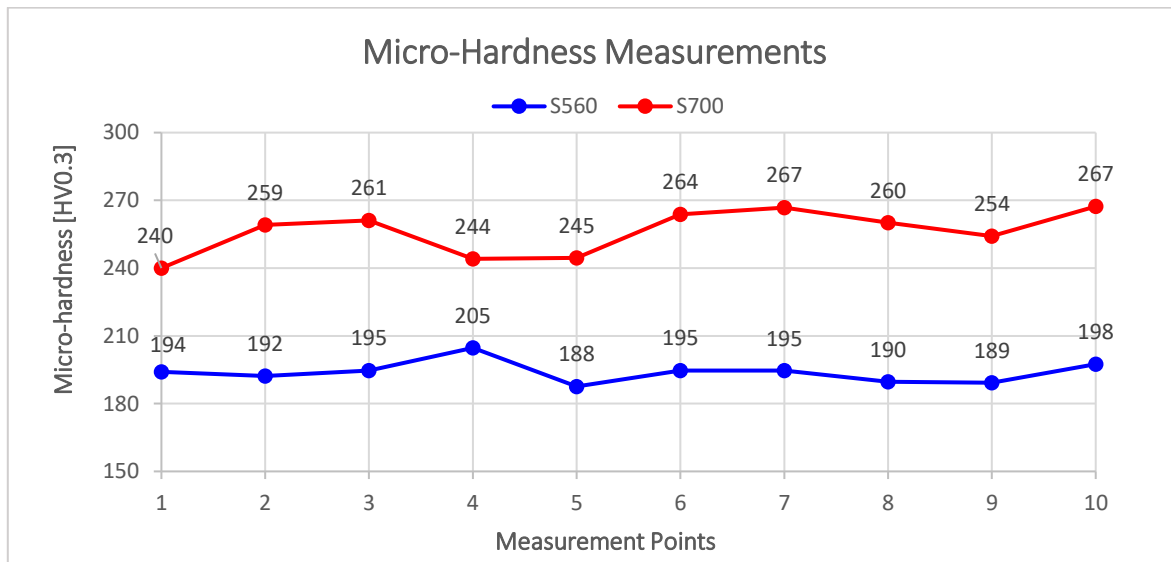
*Figure 5.32: Micro-hardness measurements of **S560** (in **Blue**) and **S700** (in **Red**).*

5.3.1.3. Microstructure comparison

High strength Low Alloy steel **S560** is **fine gained** consisted of distinct **ferritic** and **pearlitic** grains, due to production process of thermomechanical rolling, while **S700** consists of a homogeneous mixture of **tempered martensite**, along with elongated **bainite – ferrite** microstructure, due to quenching and tempering.
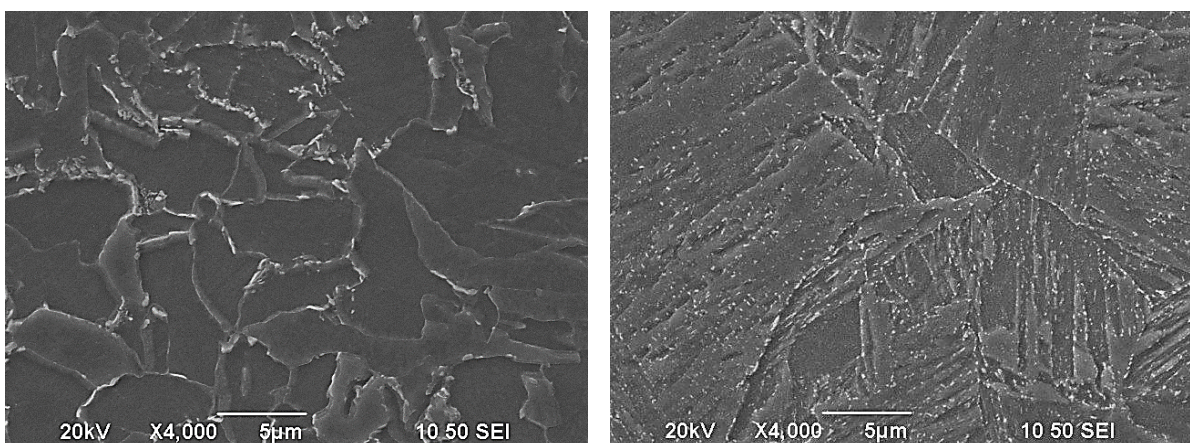
Figure 5.33: Microstructure of S560 (left) and S700 (right) - SEM magnification x4000.

168

5.3.2. Comparison of corrosion behavior

5.3.2.1. Open Circuit Potential (OC)

In Figure 5.34 one representative Open Circuit (OC) experimental curve of S560 (in blue) and one of S700 (in red) are shown. In particular, the OC experiments showed that S560 acquires a rather stable value of **-750mV** after 40000 secs (≈11hrs) is observed. Similarly, for S700 a stable potential of about **-720mV** is obtained after 5600 secs (≈15.5hrs). The stabilization of potential proves that equilibrium has been attained for the corrosion phenomena in both systems and according to the electrochemical experiments it can be assumed that the equations are the dissolution of Fe:

$$Fe \leftrightharpoons Fe^{2+} + 2e^-$$

and the oxygen's reduction:

$$O_2 + 2H_2O + 4e^- \leftrightharpoons 4OH^-$$
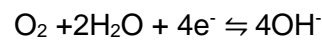
Both steels present similar open circuit potential, thus similar corrosion susceptibility.
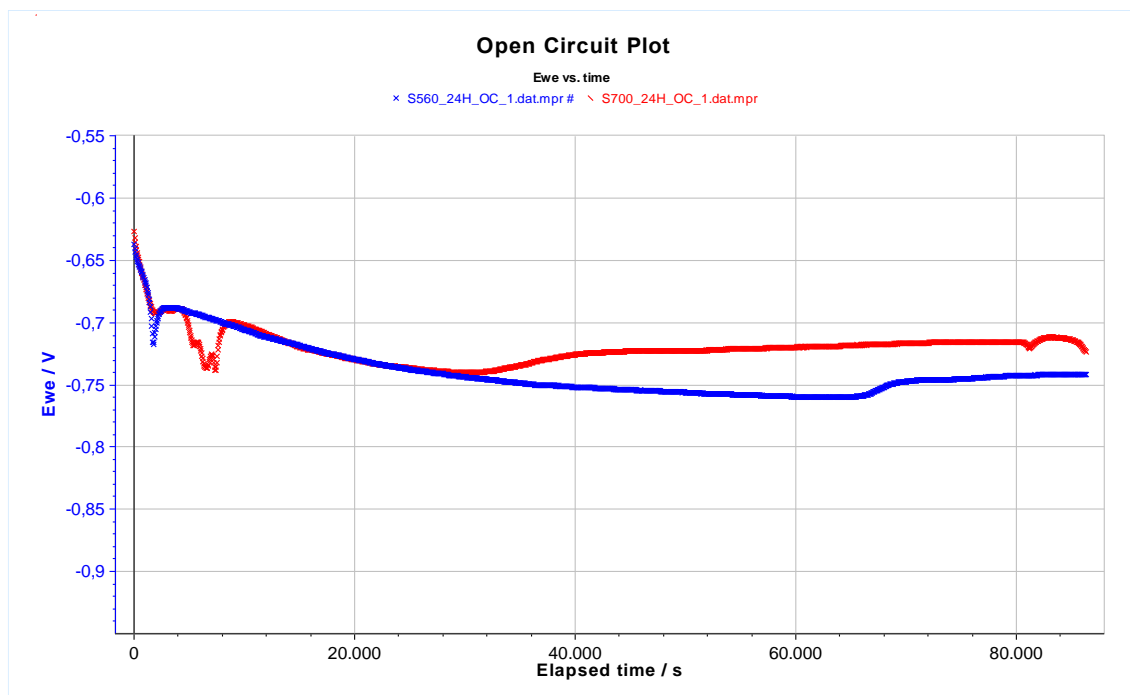
Figure 5.34: 24hour experiments on OC method of **S560** (in **Blue**) and **S700** (in **Red**).

5.3.2.2. Linear Polarization Resistance (LPR)

In Figure 5.35 one representative Linear Polarization experimental curve of S560 (in blue) and one of S700 (in red) are shown.

The **corrosion parameters in** Table 5.14 show that S560 presents a slightly better corrosion behavior that S700. For this method, more valid result considered the polarization resistance (R_P) of the metal. In particular, S560's corrosion resistance is equal to R_P = **1675 Ohm**, while S700's corrosion resistance is equal to R_P = **1333 Ohm**, meaning that S560 present a more resistive behavior to corrosion, but not of great difference (343 Ohm).
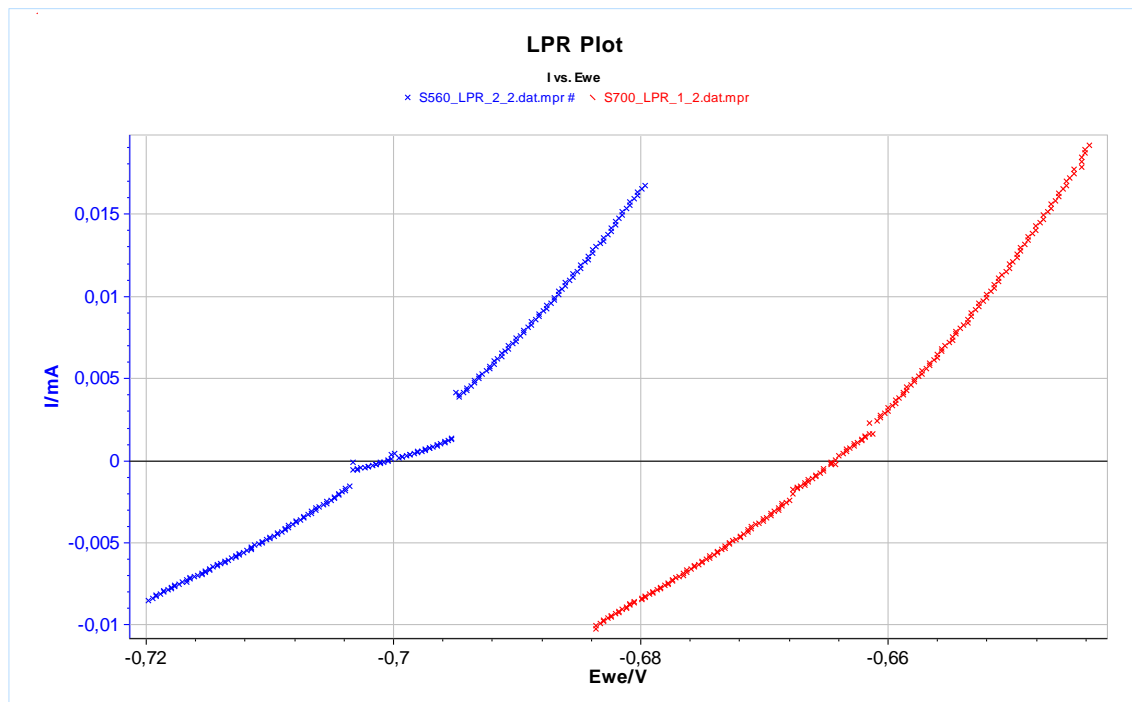
*Figure 5.35: Representative experimental curves of the specimens, **S560** (in **Blue**) and **S700** (in **Red**), on LPR method.*

Table 5.14: Average corrosion and LPR parameters for each experiment of S560 and S700.

Linear Polarization Resistance - Average Results				
Parameters				
βa	*[mV]*	120		
βc	*[mV]*	120		
Range	*[mV]*	+/- 25.0		
Results				
	Specimen:	**S560**	**S700**	**difference**
R_P	*[Ohm]*	1675	1333	**343**
E_{CORR}	*[mV]*	-704.3	-665.4	38.9
Correlation		0.982	0.988	-
I_{CORR}	*[µA]*	16.54	20.40	**3.86**

170

5.3.2.3. Potentiodynamic Polarization - Tafel Extrapolation

In Figure 5.36 one representative Potentiodynamic Polarization (PP) experimental curve of S560 (in blue) and one of S700 (in red) are shown. The **corrosion parameters in** Table 5.15 show that S560 presents slightly better corrosion behavior that S700. In particular, **S560** presents stable repeatable behavior for i_{corr} with average value of **15.4 µA/cm²** (corresponding to corrosion rate of **7.11mpy**) and average i_{LIM} equal to **23.9 µA/cm²**, while **S700** presents stable repeatable behavior for i_{corr} with average value of **20.2 µA/cm²** (corresponding to corrosion rate of **9.26mpy**) and average i_{LIM} equal to **24.3 µA/cm²** . In any case, both steels present similar corrosion behavior, i.e. anodic dissolution, controlled be charge transfer and cathodic behavior defined by oxygen O_2 diffusion.
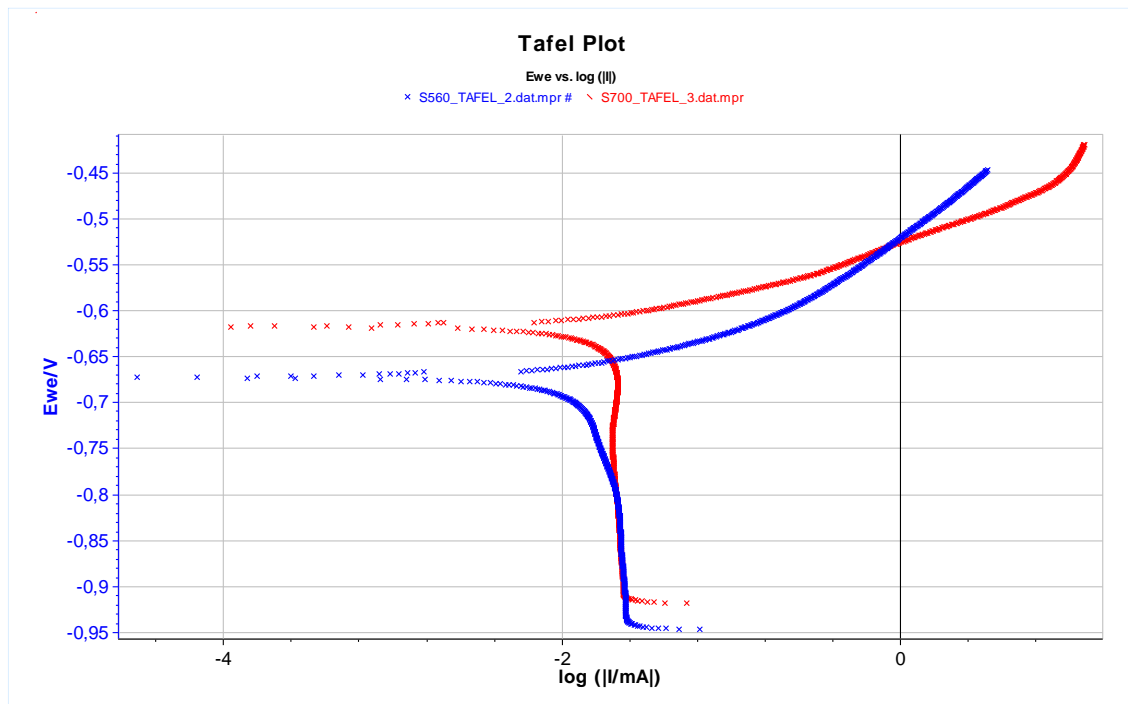
*Figure 5.36: Representative experimental PP curves of the specimens, **S560** (in **Blue**) and **S700** (in **Red**).*

Table 5.15: Average corrosion and Tafel parameters for each experiment of S560 and S700.

PP with Tafel Extrapolation - Average Results

Results				
Specimen:		**S560**	**S700**	**difference**
E_{CORR}	*[mV]*	-677	-623	53
I_{CORR}	*[µA]*	15.40	20.19	4.78
I_{LIM}	*[µA]*	23.91	24.29	0.39
βc	*[mV]*	1061	6663	5602
βa	*[mV]*	65.9	45.3	20.5
corrosion rate	*[mmpy]*	0.1806	0.2383	0.0577
corrosion rate	*[mpy]*	7.111	9.381	2.270
Parameters				
equivalent weight	*[g/eq.]*	27.956	28.143	
density	*[g/cm3]*	7.8	7.8	-
surface area	*[cm²]*	1.000	1.000	-

171

5.3.2.4. Electrochemical Impedance Spectroscopy (EIS)

Consecutive EIS experiments

In Figure 5.35 one representative EIS experiment of S560 (in blue) and one of S700 (in red) are shown. It can be observed that S700 presents more resistant behavior to corrosion compared to S560, due to the higher and longer curve in the Nyquist plot. The fitting of the EIS curves, as of Randles cell, provided the values for the electric elements. The average values of the two experiments shown in Table 5.16. S560's corrosion resistance is equal to **1646 Ohm**, while S700's corrosion resistance is equal to **2009 Ohm**. The higher value of S700 metal's resistance depicts the better (more resistive) corrosion behavior.
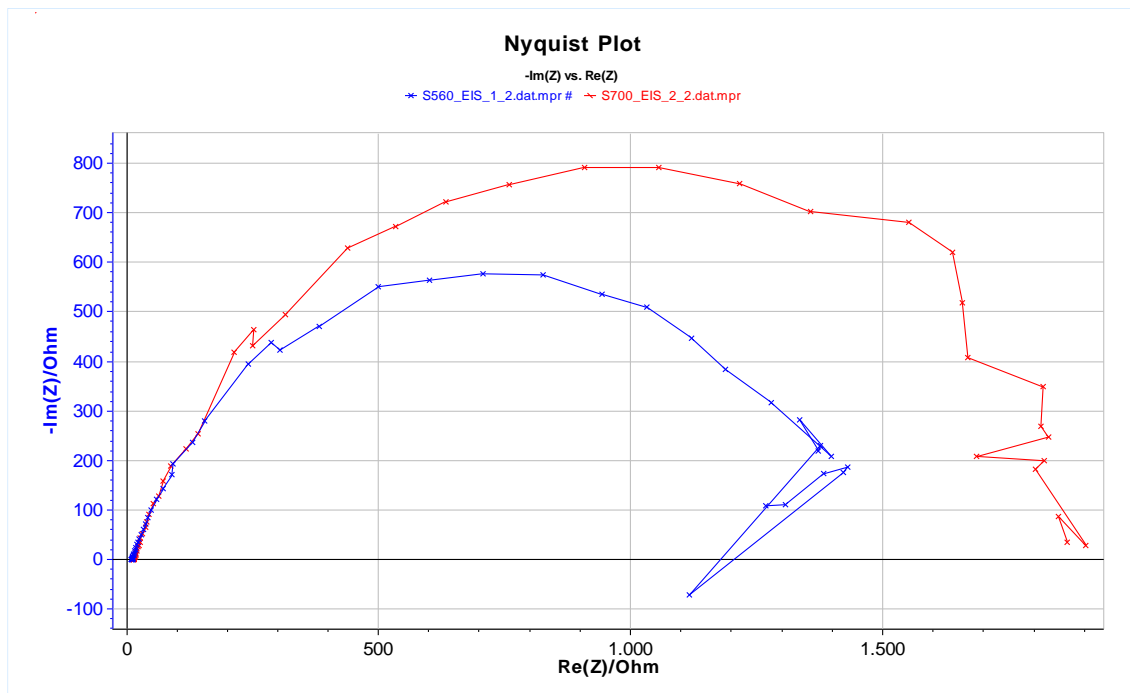
*Figure 5.37: Nyquist plot of one representative curve of each specimen of the experiment "three consecutive EIS". **S560** (in **Blue**) and **S700** (in **Red**).*

Table 5.16: Equivalent circuit parameters of S560 and S700, on 3 consecutive experiments on EIS method.

Electrochemical Impedance Spectroscopy - Average Results

Results				
	Specimen:	**S560**	**S700**	**difference**
R$_S$	*[Ohm]*	10.61	13.89	3.28
CPE	*[F.s^(a - 1)]*	3.06E-04	2.61E-04	4.56E-05
a		0.8321	0.8315	-
R$_P$	*[Ohm]*	1646	2009	363
PseudoC				
R$_S$	*[Ohm]*	10.61	13.89	3.28
C	*[F]*	2.68E-04	2.29E-04	3.88E-05
R$_P$	*[Ohm]*	1646	2009	363

In Figure 5.38 and Figure 5.39 the respective Bode plots are presented.
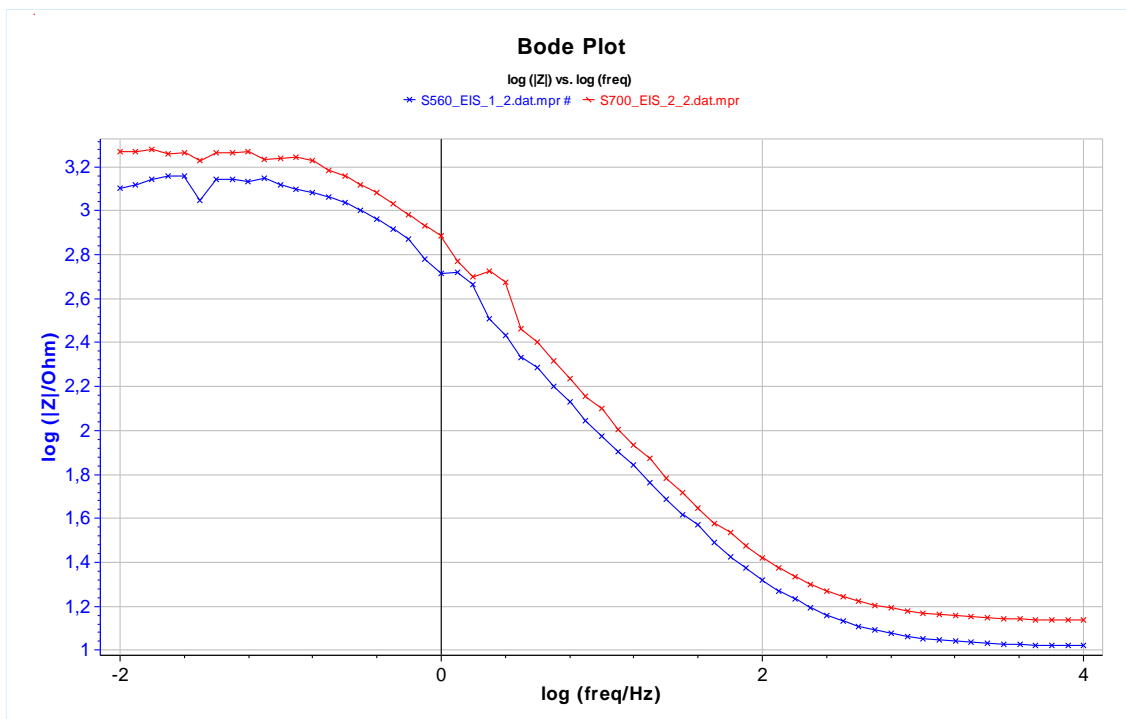
*Figure 5.38: Bode (log|Z|) plot of one representative curve of each specimen of the experiment "three consecutive EIS". **S560** (in **Blue**) and **S700** (in **Red**).*
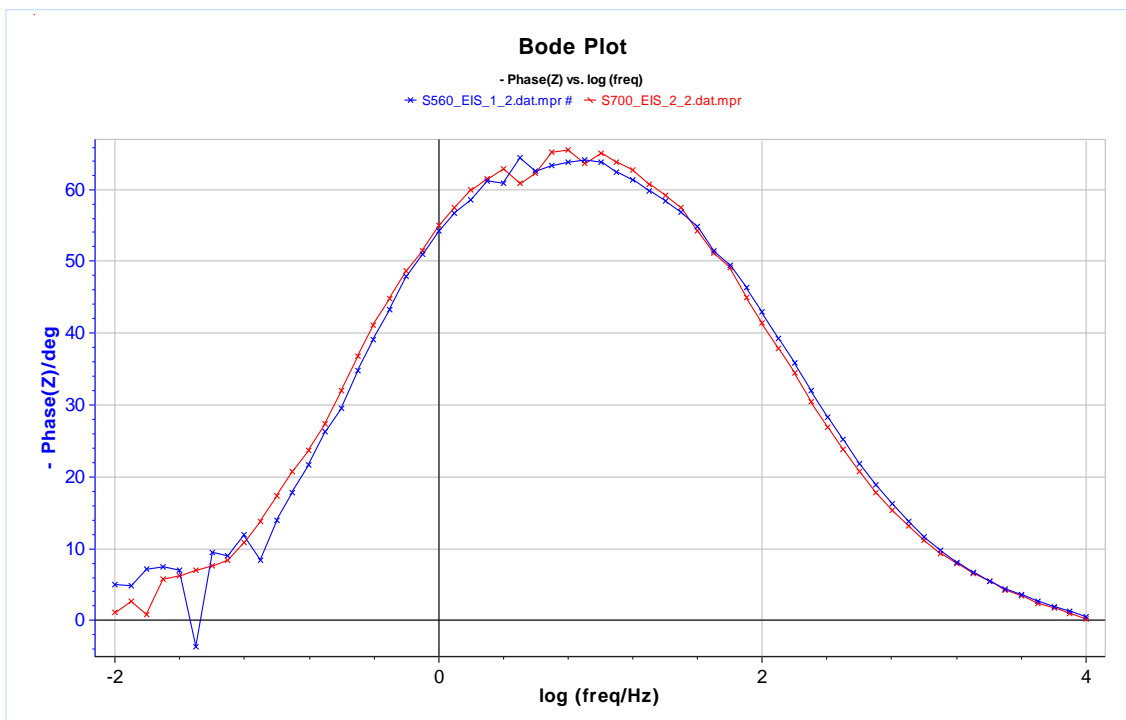
*Figure 5.39: Bode (-Phase(Z)) plot of one representative curve of each specimen of the experiment "three consecutive EIS". **S560** (in **Blue**) and **S700** (in **Red**).*

24h EIS experiments

In Figure 5.40 two EIS curves of the 24hour experiment on this method for each steel are presented. In particular, the imposing time **t=0h** and **t=24h** for S560 (in blue and dark blue, respectively) and for S700 (in red and dark red, respectively) are shown.
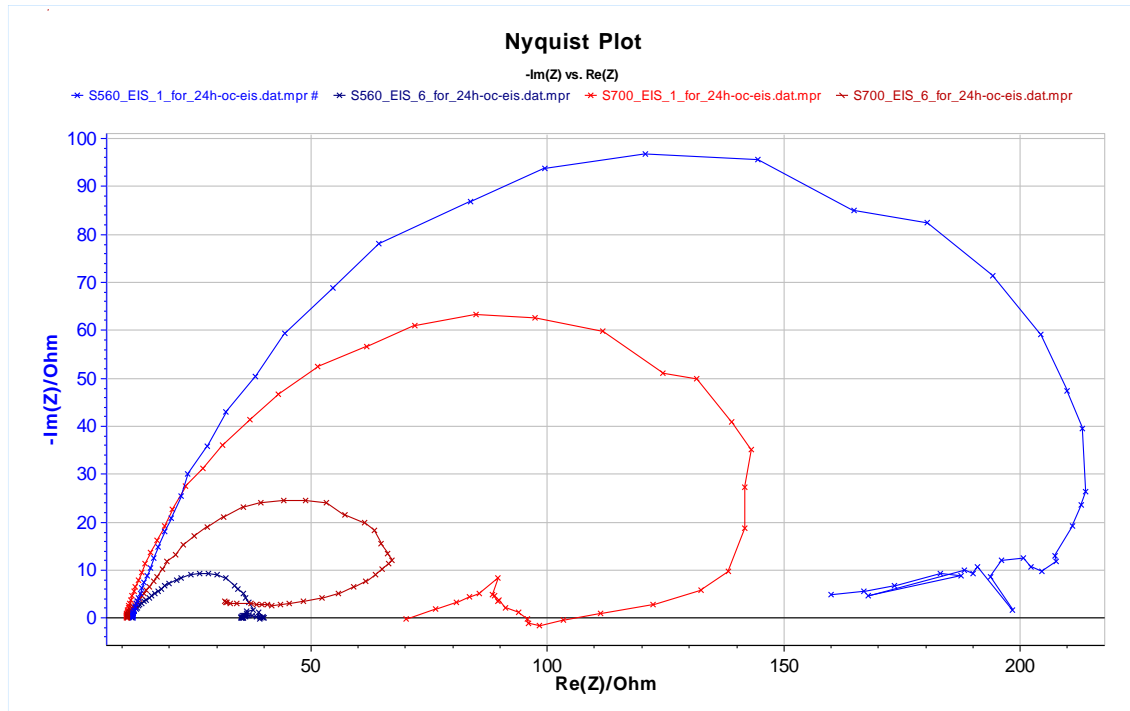
Figure 5.40: Nyquist plot of 24h experiment on EIS method, specifically:
*for S560: **Blue**: t=0 h, **Dark blue**: t=24 h and for S700: **Red**: t=0 h, **Dark red**: t=24 h.*

The experiments versus time proved that for S700 the dissolution continuous until 4 hours (Figure 5.27) and after that corrosion products are formed on the surface limiting the dissolution of the specimen.

For S560 different behavior is observed. Some kind of protection is achieved after 4 hours, however these products are not very stable, thus some kind of dissolution takes place even after 24 hours (Figure 5.12).

The most important observation is that although S560 starts (t=0h, blue curve) with a higher resistance (more external curve) than S700 (t=0h, red curve), S560 ends (t=24h, dark blue curve) with a lower resistance that S700 (t=24h, dark red curve), meaning that S700 maintains a more passive behavior after a few hours, due to the corrosion products formed on its surface, as mentioned above. This change on steels' Resistance (R_P) is presented schematically in Figure 5.41.

This behavior of S560 may also be due to the fact that the corrosion products created on the surface of the metal are not firmly attached to it and thus, they can be easily removed away and the metal keeps on corroding. This was also observed during the experimental procedures; after removing the specimen from the electrochemical cell, the corrosion products were removed easily removed even by distilled water, something that never happened with the

corroded surface of S700. These values prove that S700 present the highest R_P value, thus the better corrosion behavior.
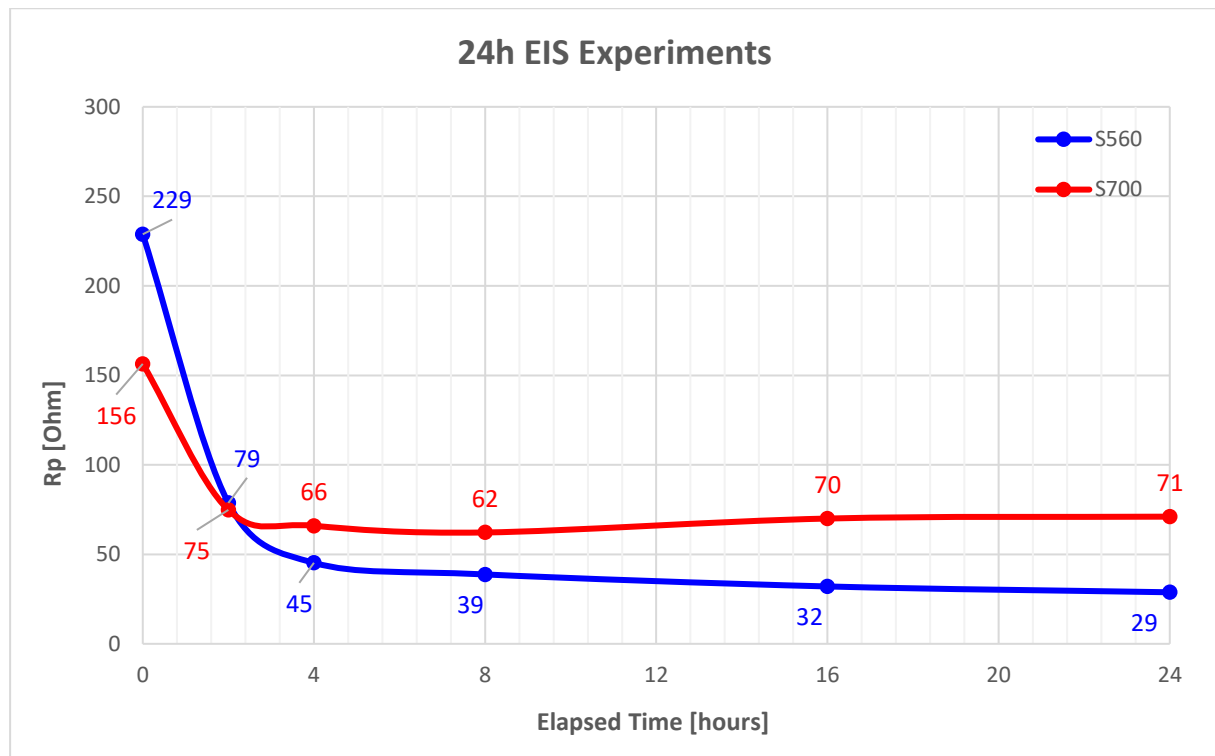
*Figure 5.41: Change on the steels' Resistance (R_P) during their 24hour EIS experiments. **S560** (in **Blue**) and **S700** (in **Red**).*

Table 5.17: Equivalent circuit parameters of S560 and S700, on 24h experiment (imposed EIS at 0h and 24h).

Electrochemical Impedance Spectroscopy (24h)				
Results				
Specimen:	**S560**		**S700**	
EIS imposing time:	**t = 0h**	**t = 24h**	**t = 0h**	**t = 24h**
R$_S$ *[Ohm]*	12.45	11.96	10.82	11.26
CPE *[F.s^(a - 1)]*	2.47E-04	1.02E-03	3.10E-04	1.12E-03
a	0.8579	0.6889	0.8352	0.7204
R$_P$ *[Ohm]*	**229**	**29**	**156**	**71**
PseudoC				
R$_S$ *[Ohm]*	12.45	11.96	10.82	11.26
C *[F]*	1.53E-04	2.08E-04	1.71E-04	4.19E-04
R$_P$ *[Ohm]*	229	29	156	71
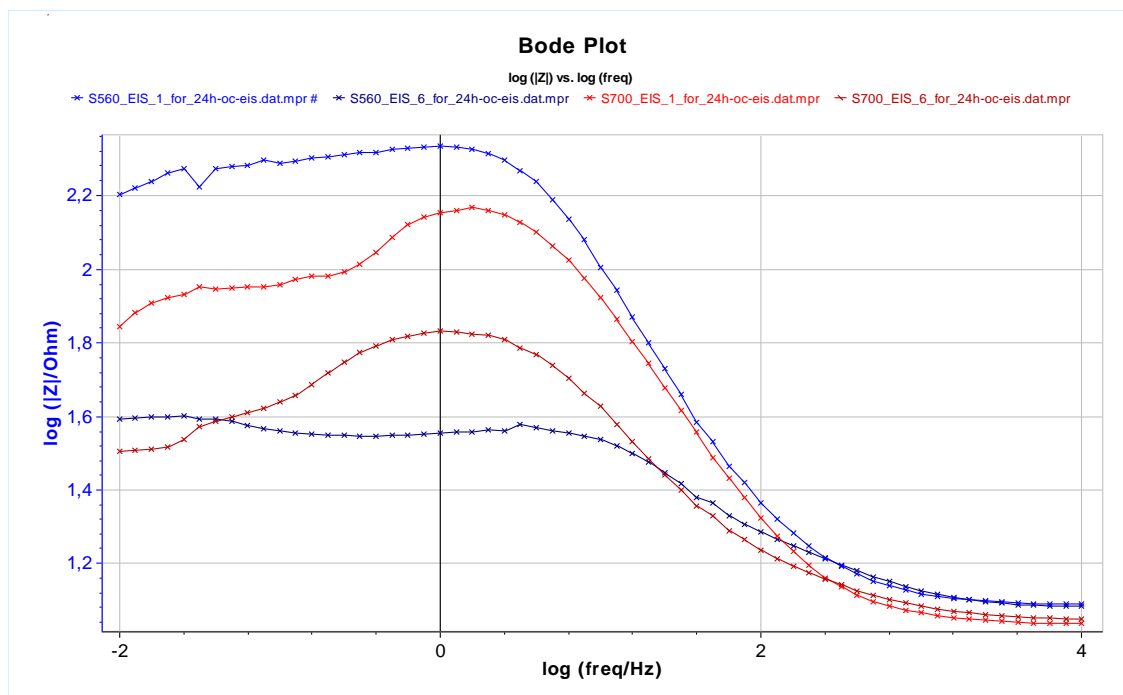
175

Figure 5.42: Bode (log|Z|) plot of 24h experiment on EIS method, specifically:
for S560: **Blue**: t=0 h, **Dark blue**: t=24 h and for S700: **Red**: t=0 h, **Dark red**: t=24 h.
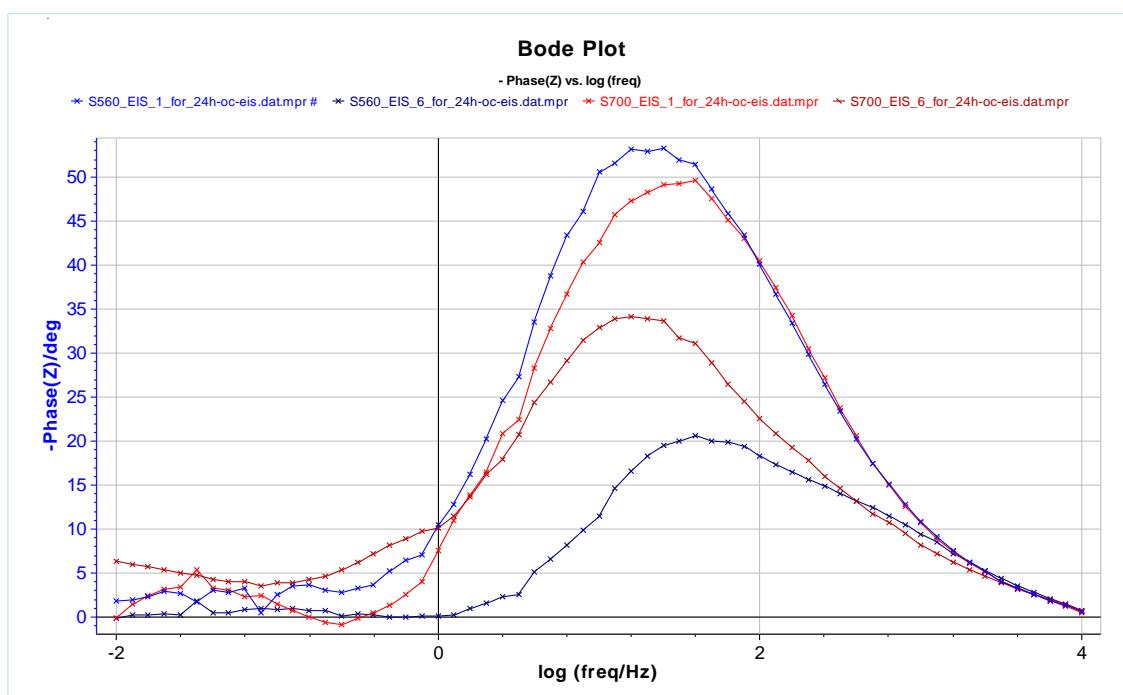
Figure 5.43: Bode (-Phase(Z)) plot of 24h experiment on EIS method, specifically:
for S560: **Blue**: t=0 h, **Dark blue**: t=24 h and for S700: **Red**: t=0 h, **Dark red**: t=24 h.

176

5.3.2.5. Cyclic Potentiodynamic Polarization (CPP)

In Figure 5.44 one representative Cyclic Potentiodynamic Polarization experiment of S560 (in blue) and one of S700 (in red) are shown. Both specimens of S560 and S700 present similar corrosion behavior, without significant differences and all of the curves almost coincide. The continuous increase in the anodic dissolution, implies that the oxide film formed has defects which enhance the dissolution. After 200mV, on both steel's experiments, some passive region starts to appear. Since no significant increase in the current density is observed, no significant pitting corrosion is present both for the S560 and the S700. The very small loop observed denotes possible slight pitting corrosion.
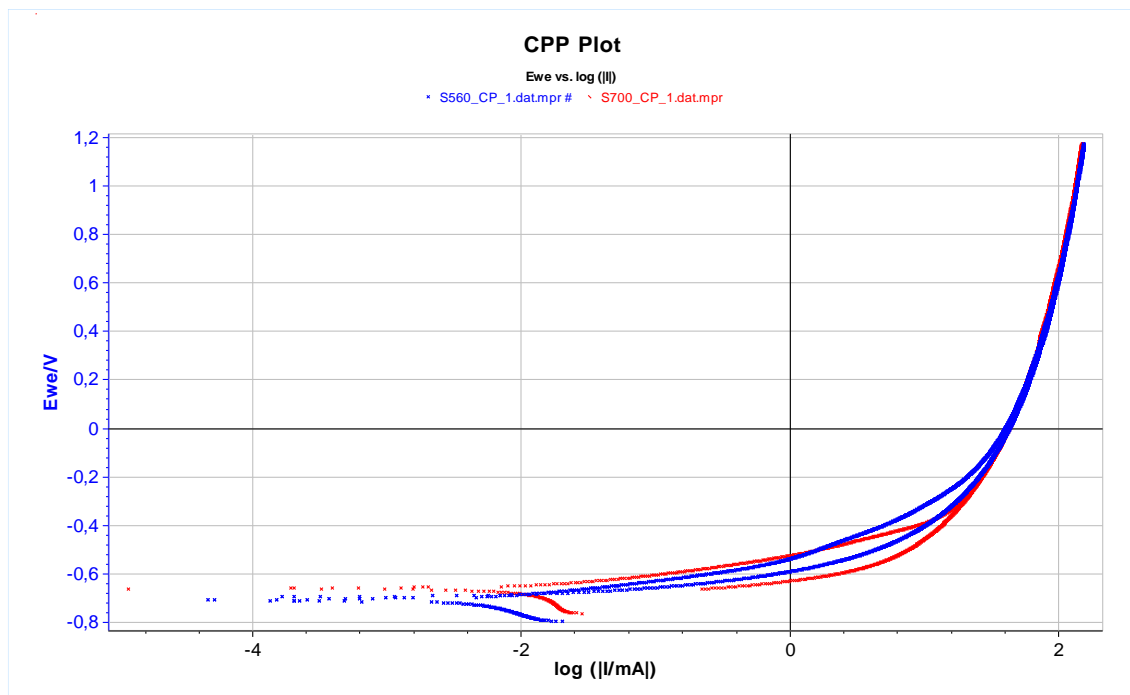
*Figure 5.44: Representative curves of experiments on CPP method of **S560** (in **Blue**) and **S700** (in **Red**).*

5.4. General Conclusion

The objective of the present thesis is to study the corrosion behavior of S560 and S700 HSLA steels. To accomplish it, electrochemical techniques were employed, applying DC and AC perturbation. However, electrochemical techniques are accompanied by study of the micro-structure in order to arrive into sound conclusions. For this reason, study of the microstructure was performed along with the results of micro-hardness and chemical composition analysis. In the following paragraphs conclusions obtained from the individual experiments and general conclusions on the objective of the thesis as well as suggestions for future research are presented.

Due to the fact that this study investigates the corrosion performance of these steels as an alternative to conventional steel AH36 for specific applications on the ship, the inclusion of corresponding results for AH36, according to the literature, was deemed necessary.

5.4.1. Microstructure

The laboratory techniques employed for the study of the microstructure revealed that

- ❖ **S560** is a fine grained HSLA steel consisting of distinct ferritic and pearlitic grains, due to production process of thermomechanical rolling, its Carbon Equivalent is equal to 0.30 and the micro-hardness is $194HV_{0.3}$,

- ❖ **S700** is a HSLA steel consisting of a homogeneous mixture of tempered martensite and fine elongated ferrite – bainite microstructure, due to quenching and tempering, its Carbon Equivalent is equal to 0.44 and the micro-hardness is $256HV_{0.3}$.

- ❖ High strength shipbuilding steel **AH36**, according to the literature, consists of alternate bands of ferrite 75% and pearlite 25% with intense orientation due to production process (hot rolled and normalized), its Carbon Equivalent is equal to 0.48 and the micro-hardness is equal to $153HV_{0.3}$.

5.4.2. Corrosion mechanism – Parameters

The electrochemical techniques employed, revealed valuable information on the mechanism of the corrosion and provided vales on critical parameters, for the metal S560 and S700.

Concerning the **mechanism of corrosion**, the <u>potentiodynamic polarization</u> in the 3.5% NaCl solution, which simulates the seawater environment, showed that both steel S560 and S700 were characterized by an increase of current density while increasing potential in the anodic region, indicating active corrosion behavior. According to this, both steels present similar anodic dissolution determined by charge transfer (activation polarization), i.e. dissolution-corrosion of the material. The cathodic curve shows that the phenomenon is dominated by O_2 diffusion, meaning that the phenomenon is controlled by activation polarization, close to equilibrium and consequently by concentration polarization due to O_2 diffusion, further than equilibrium, attaining limited current value i_{LIM}.

178

The aforementioned behavior is also observed in <u>cyclic polarization</u>. All the specimens present similar corrosion behavior, without significant differences and all of the curves almost coincide. The continuous increase in the anodic dissolution, implies that the oxide film formed has defects which enhance the dissolution. After 200mV some passive region starts to appear. Since no significant increase in the current density is observed, no significant pitting corrosion is present both for the S560 and the S700, proving that the corrosion pattern is general corrosion. A very small loop is although observed denoting a potential pitting corrosion.

The plots provided by <u>Electrochemical Impedance Spectroscopy</u> for all the specimens display only one capacitive semicircle. It is usually interpreted as a mechanism of charge transfer on an inhomogeneous surface. The equivalent circuit chosen, a Randles cell, consists of R_S and R_P and indicates solution resistance and polarization resistance of the electrolyte – edl (electrical double layer) interface, respectively. However, the shape of the Nyquist curve is not a perfect semicircle and it presents a deviation from the Resistance Capacitor behavior with deformation and broadening of the semicircle. For this reason, the capacitor C is substituted by the Constant Phase Element Q, still parallel with the resistor R_P. This deformation is attributed to the roughness of the electrode-electrolyte interfaces or to inhomogeneities in the local distribution of defects in the vicinity of grain boundaries and is better represented by a CPE than a perfect capacitor.

The experiments versus time prove that for S700 the dissolution continuous until 4 hours that the corrosion products formed on the surface limit further dissolution. For S560 it takes less time until some corrosion products are formed on the surface, however the dissolution seems to continue throughout the 24 hours.This behavior implies that the corrosion products formd on the surface of S700 are strongly adhered on the metal surface while the S560 corrosion products can be easily removed away even when washed out. This phenomenon was observed during the experiments.

The **corrosion parameters** show that S560 presents a slightly better corrosion behavior than S700 and AH36, whose metal's dissolution is, also, activation controlled and its cathodic reaction is dominated by O_2 diffusion, considering the same environment. In particular:

❖ **S560** presents stable repeatable behavior for i_{corr} (**15.4 – 16.5 μA/cm^2**) and very similar, for both the AC methods, i.e. Linear Polarization and Potentiodynamic Polarization. These values correspond to corrosion rates equal to **7.11mpy**.

❖ **S700** presents stable repeatable behavior for i_{corr} (**19.9 – 20.4 μA/cm^2**) and very similar, for both the AC methods, i.e. Linear Polarization and Potentiodynamic Polarization. These values correspond to corrosion rates equal to **9.26mpy**.

❖ **AH36**, according to the literature, shows slightly lower values for i_{corr} (**15-18 μA/cm^2**) compared to S700 but with no significant difference when compared with S560. Corrosion rate is equal to **8.20mpy**.

However, all of this values represent a good behavior to corrosion for the steels according to Figure 2.14 [McCafferty, 2010] indicating a "good" corrosion rate for iron with corrosion current density between 11 and 43μA/cm^2 and "excellent" below 11μA/cm^2.

Comparable results are extracted also from the Electrochemical Impedance Spectroscopy method, where

- ❖ S560's corrosion resistance is equal to R_P = **1646 Ohm**
- ❖ S700's corrosion resistance is equal to R_P = **2009 Ohm**
- ❖ AH36, according to the literature, presents lower corrosion resistance (R_P = **1225 Ohm**) than S560 and S700, meaning that both of our steel specimens are more resistant to corrosion than the currently used shipbuilding steel.

Concluding, the corrosion mechanism of S560 and S700 is determined by the oxygen diffusion in 3.5% NaCl. In these specific experimental conditions both metals show actually similar corrosion rates. The same observations stand for all the experimental used electrochemical methods. Only EIS technique indicates that S700 is more resistant to corrosion than both S560 and AH36.

5.4.3. Suggestions for Future Research

The objective of the present thesis was to investigate whether S560 steel and S700 can be used complementary to the usually employed AH36. To this purpose several parameters need to be studied, i.e. mechanical properties mainly fatigue, corrosion etc. This thesis examined the corrosion susceptibility of S560 and S700, while a study for their microstructure was also employed. The electrochemical techniques employed provided sound results, in general.

However, due to the fact that these structural steels are going to be used only in critical areas of high fatigue loads, it is necessary to study the behavior of their homogeneous welded joints and heterogeneous with AH36. Moreover, the electrochemical techniques could be applied in every distinct part of the welds.

It will be, also, very useful to perform experiments under accelerated ageing conditions (salt spray, humidity, drying, etc.) with the intention to identify the pattern of the corrosion (general, pitting). These experiments would provide valuable results for the relief of the surface, useful to the mechanical testing (stress concentration on HAZ).

Furthermore, in depth elaboration of the results from electrochemical tests could provide more thorough results, especially for EIS method.

Taking into account the ship structure, it would be of great interest to perform stress corrosion experiments, or corrosion fatigue experiments to reveal the impact of corrosion on mechanical performance of critical parts. Besides, one could numerically simulate corrosion behavior and mechanical properties to obtain result of the simultaneous action of stress and corrosion.

Finally, although the use of the HSLA steels can potentially achieve this objective of weight savings due to the better mechanical performances compared to the conventional steel AH36, the study of welding procedures/technologies to be used with these high-performance steels must be investigated carefully before reaching a massive use of these steel in the marine industry. Also, the economic impact must be taken into account because the HSLA not only have higher price per tons with respect to the conventional steel, but they could require new welding techniques or to adapt the techniques currently in uses with extra cost.

Optical Observation after Corrosion Experiments

A.1. 24hour Open Circuit Potential experiment

(a)   (b)

Figure A.1: Optical observation of S560 after 24hour experiment on Open Circuit method.
Stereomicroscope's magnification at (a) x1.0, (b) x4.0

(a)   (b)
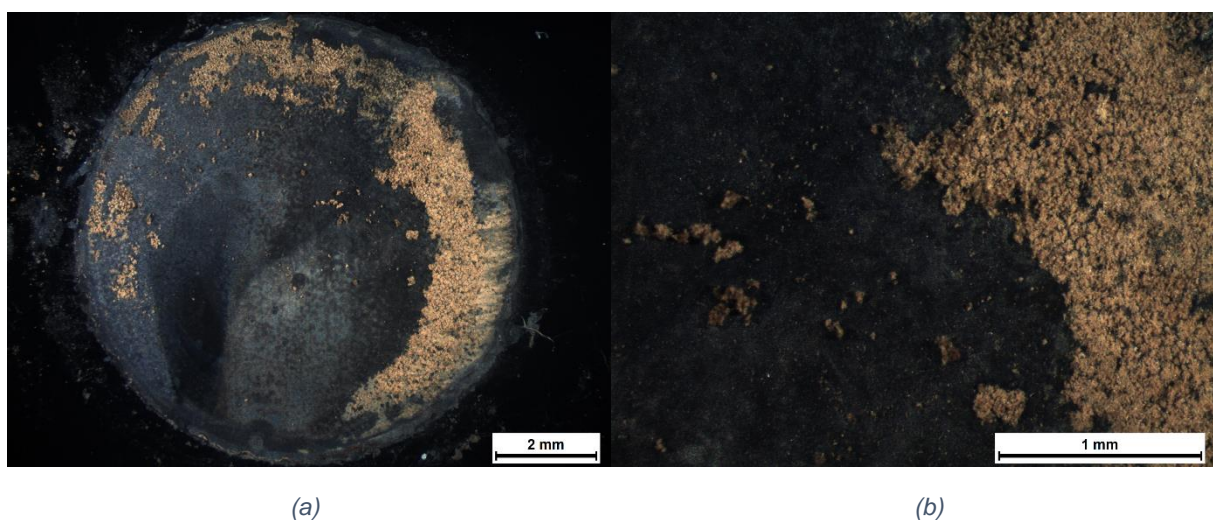
Figure A.2: Optical observation of S700 after 24hour experiment on Open Circuit method.
Stereomicroscope's magnification at (a) x1.0, (b) x4.0

A.2. 48hour Open Circuit Potential experiment

(a)	*(b)*
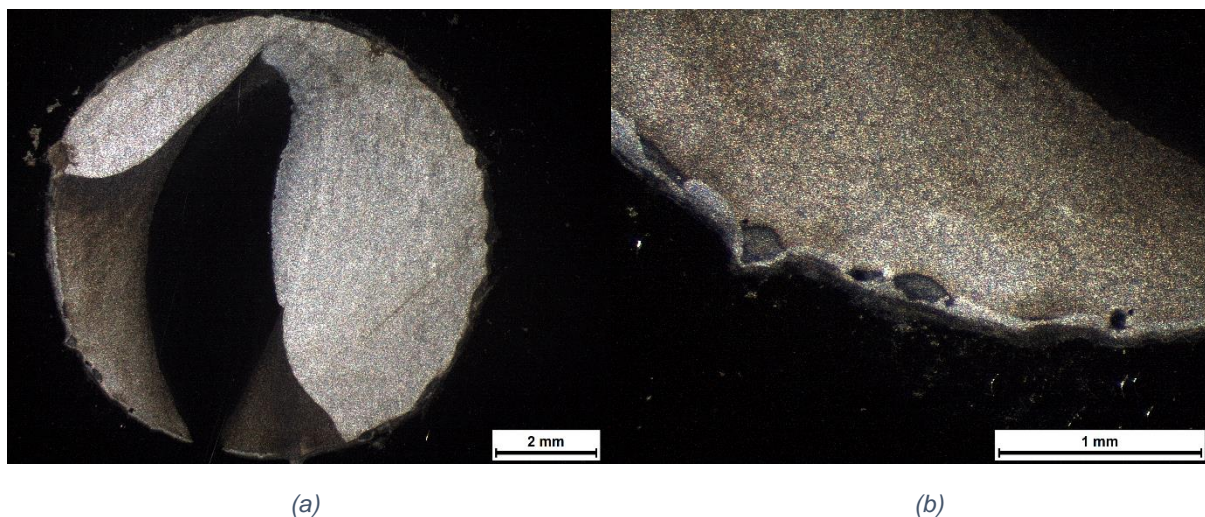
Figure A.3: Optical observation of S560 after 48hour experiment on Open Circuit method. Stereomicroscope's magnification at (a) x1.0, (b) x4.0

(a)	*(b)*
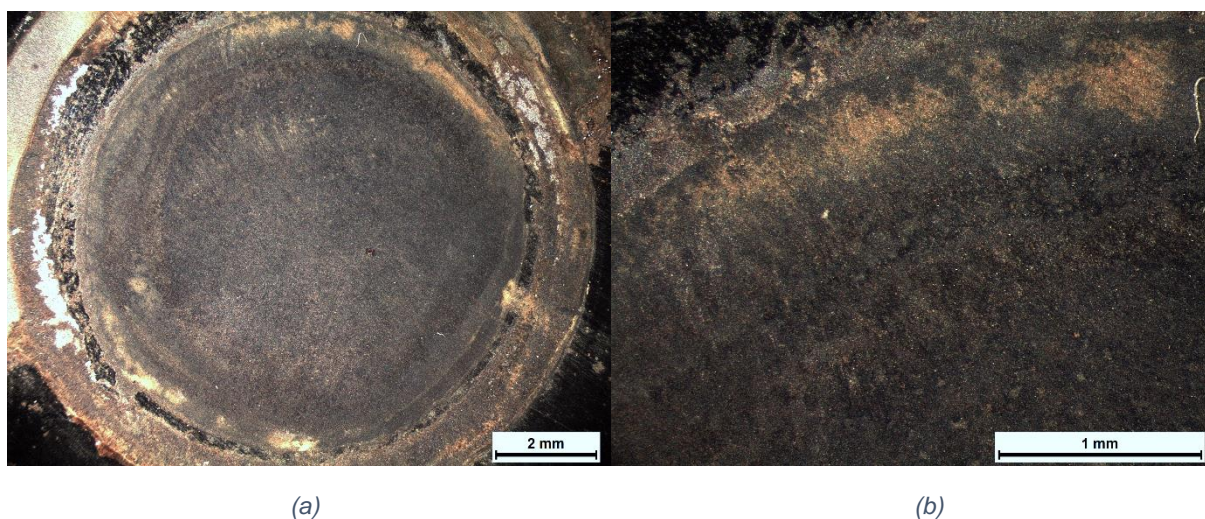
Figure A.4: Optical observation of S700 after 48hour experiment on Open Circuit method. Stereomicroscope's magnification at (a) x1.0, (b) x4.0

A.3. OC – 2 consecutive LPR – TAFEL (3 repetitions)

(a)   *(b)*
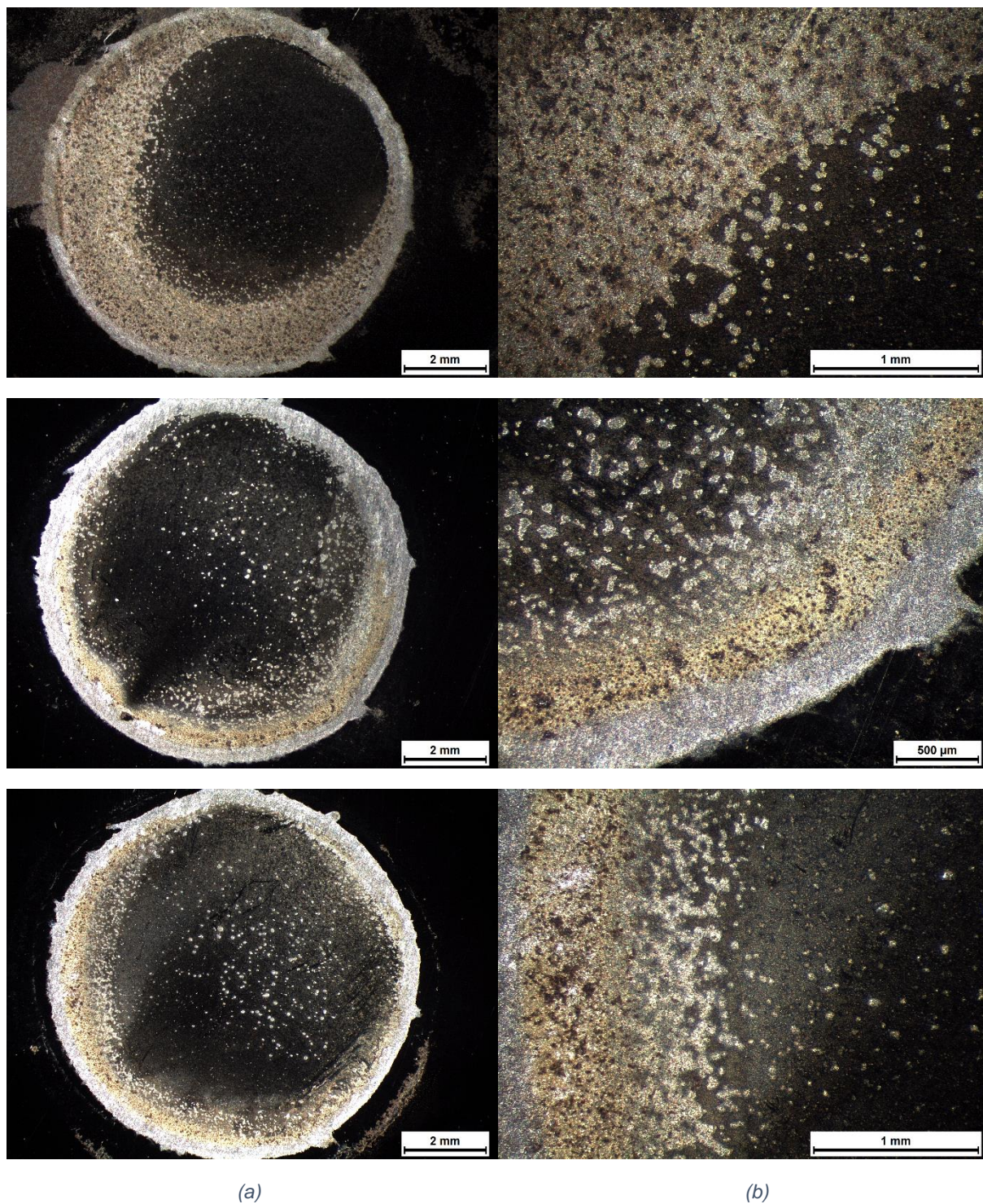
Figure A.5: Optical observation of S560 after potentiodynamic polarization experiment on LPR and Tafel methods. Stereomicroscope's magnification at (a) x1.0, (b) x4.0 – Each row corresponds to a repetition of this experiment.

(a)   (b)
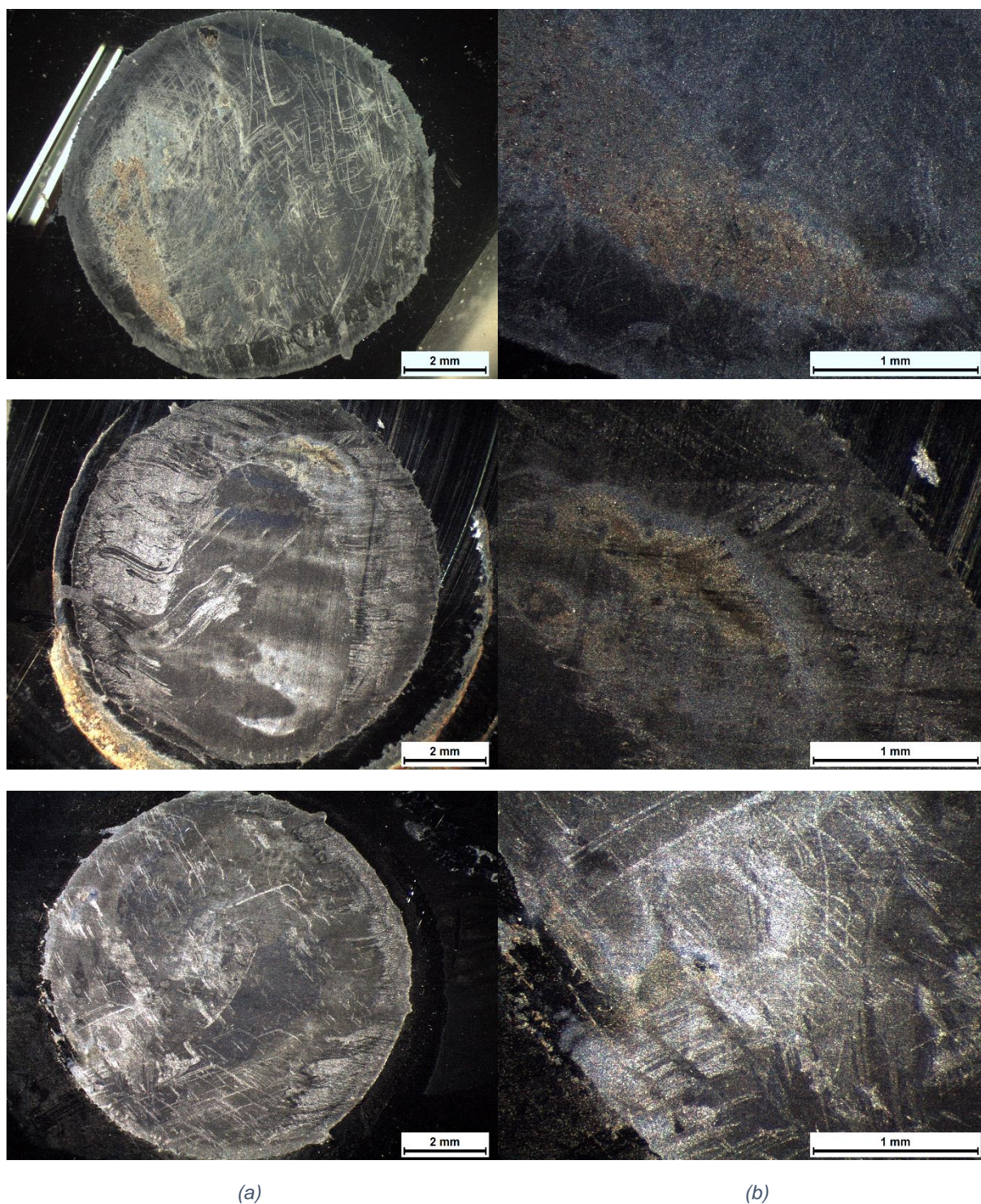
Figure A.6: Optical observation of S700 after potentiodynamic polarization experiment on LPR and Tafel methods. Stereomicroscope's magnification at (a) x1.0, (b) x4.0 – Each row corresponds to a repetition of this experiment.

A.4. OC – 3 consecutive EIS experiment

(a)   (b)
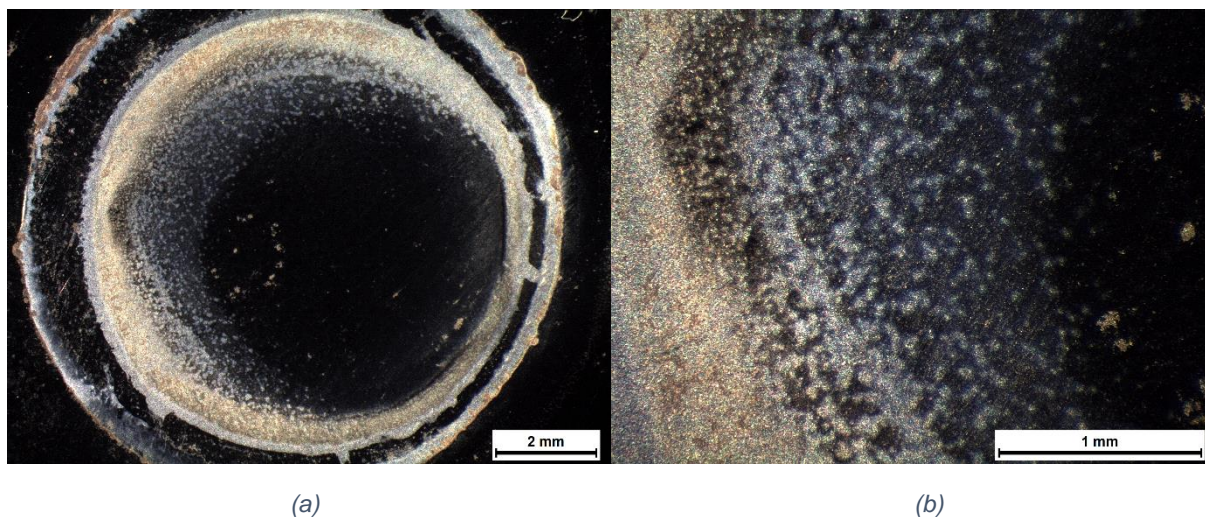
*Figure A.7: Optical observation of S560 after electrochemical experiment on EIS method.
Stereomicroscope's magnification at (a) x1.0, (b) x4.0*

(a)   (b)
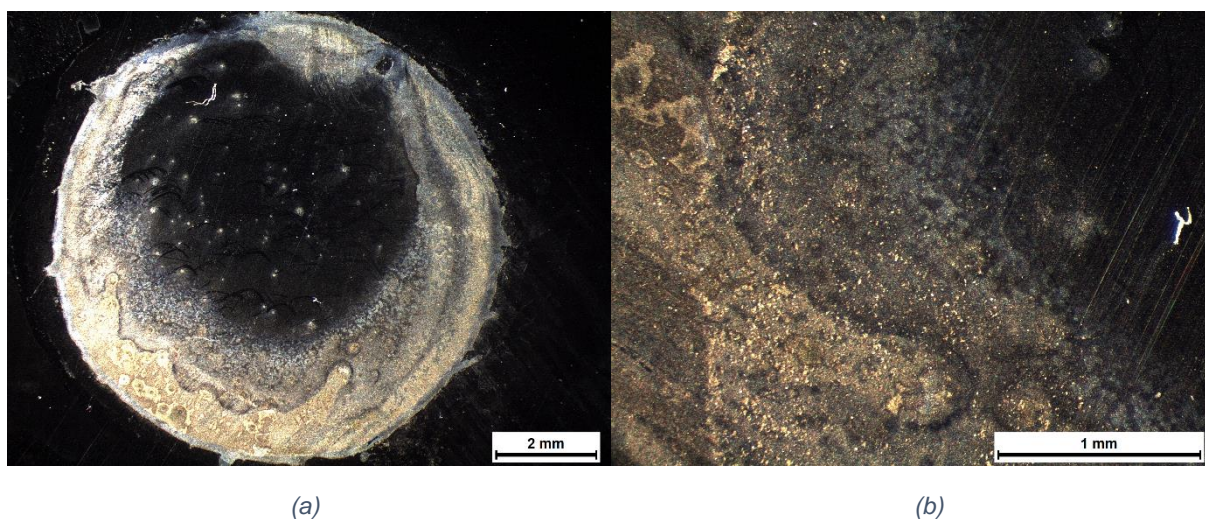
*Figure A.8: Optical observation of S700 after electrochemical experiment on EIS method.
Stereomicroscope's magnification at (a) x1.0, (b) x4.0*

A.5. 24hour 6 loop OC – EIS experiment

(a) *(b)*
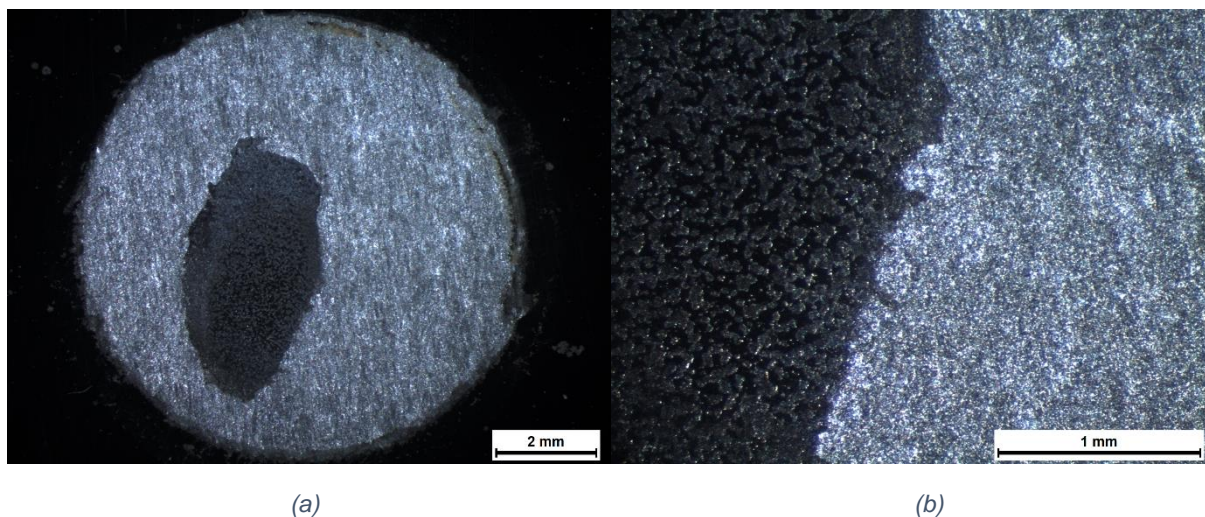
Figure A.9: Optical observation of S560 after 24hour experiment on OC and EIS methods. Stereomicroscope's magnification at (a) x1.0, (b) x4.0

(a) *(b)*
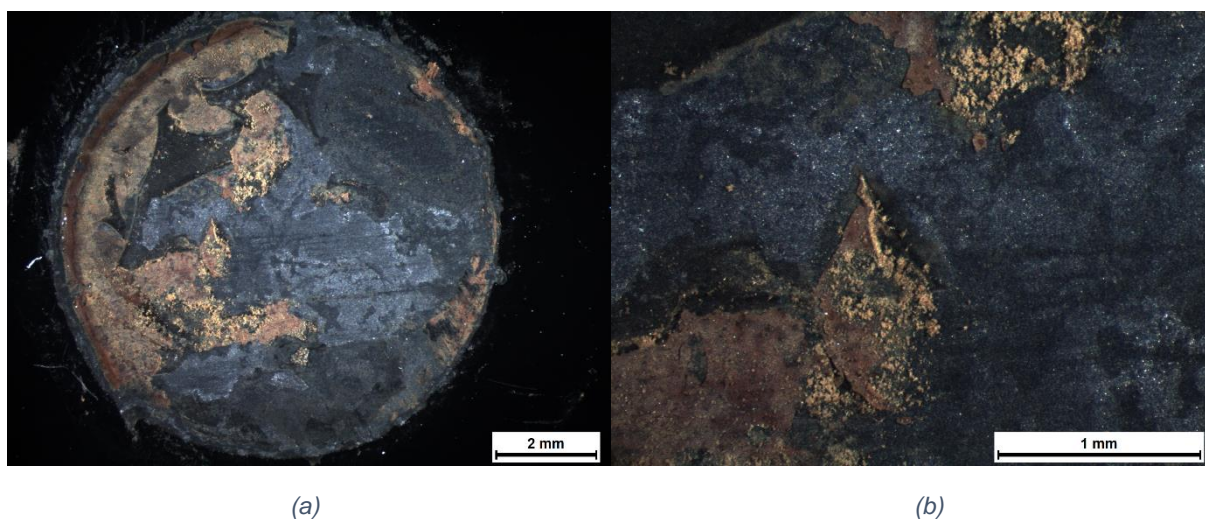
Figure A.10: Optical observation of S560 after 24hour experiment on OC and EIS methods. Stereomicroscope's magnification at (a) x1.0, (b) x4.0

A.6. OC – CP (2 repetitions)

(a)   (b)
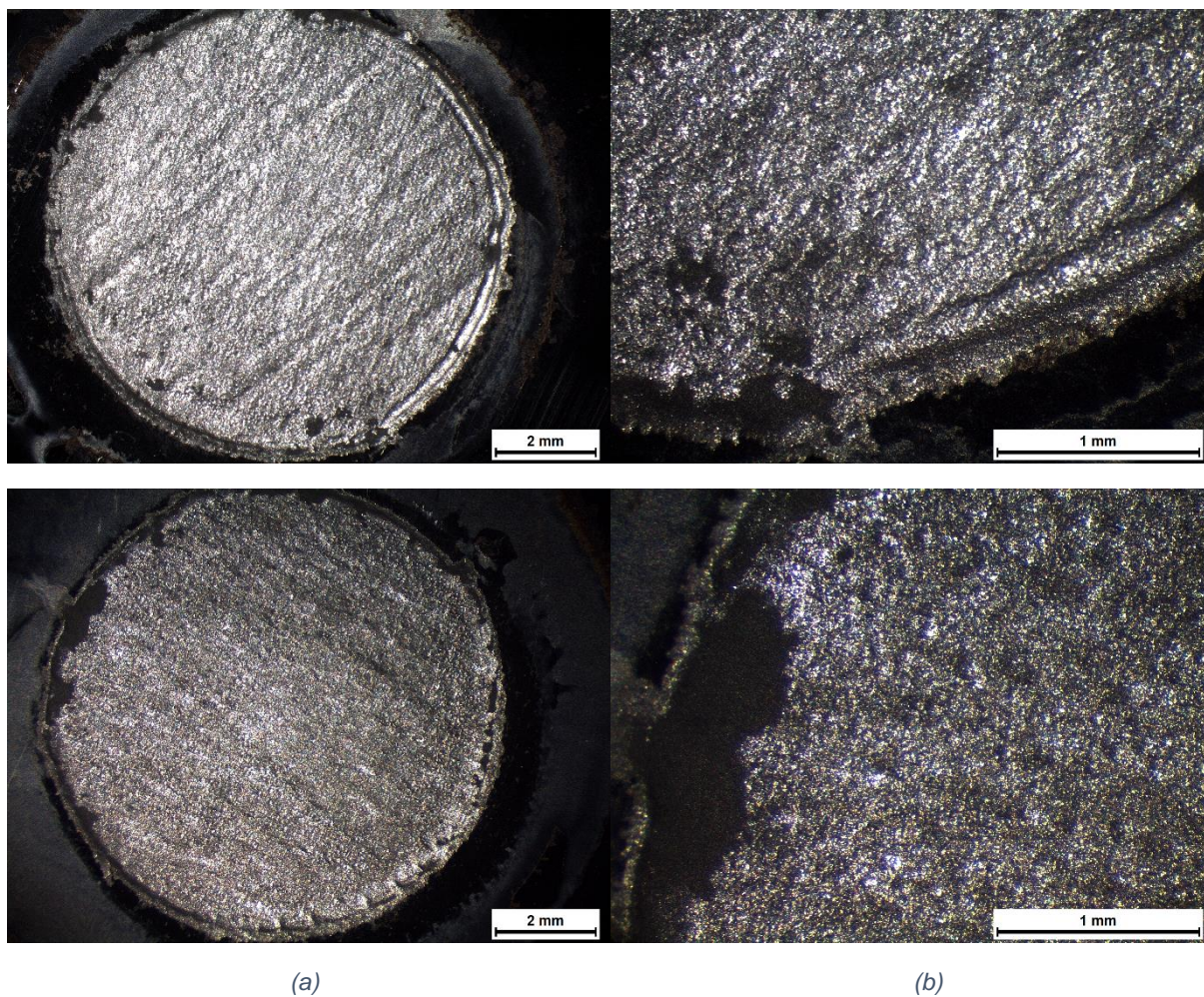
Figure A.11: Optical observation of S560 after potentiodynamic polarization experiments on CPP method. Stereomicroscope's magnification at (a) x1.0, (b) x4.0 – Each row corresponds to a repetition of this experiment.

(a)   *(b)*
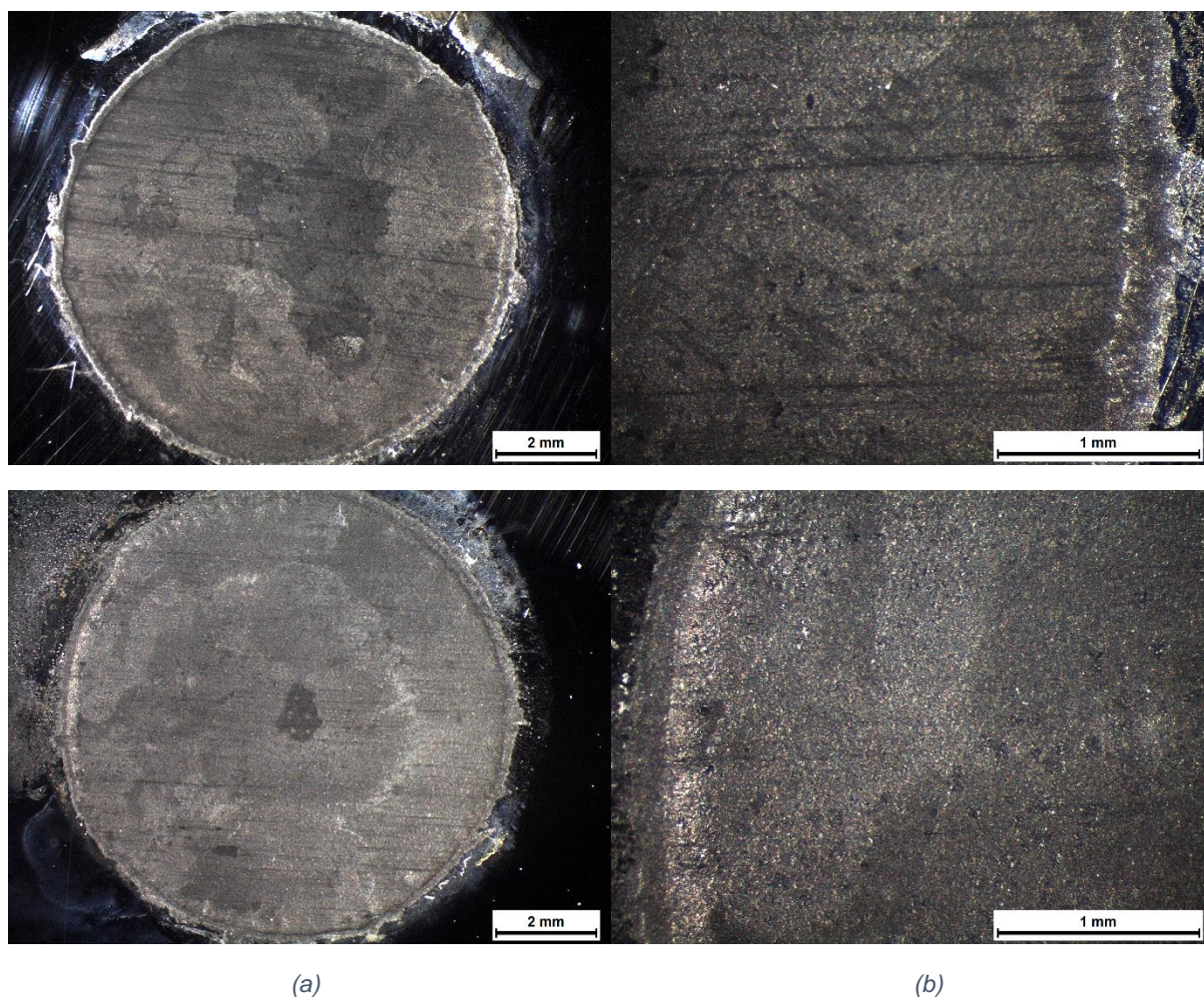
Figure A.12: Optical observation of S700 after potentiodynamic polarization experiments on CPP method. Stereomicroscope's magnification at (a) x1.0, (b) x4.0 – Each row corresponds to a repetition of this experiment.

Supplementary Diagrams

B.1. Open Circuit Potential (OC) experiments
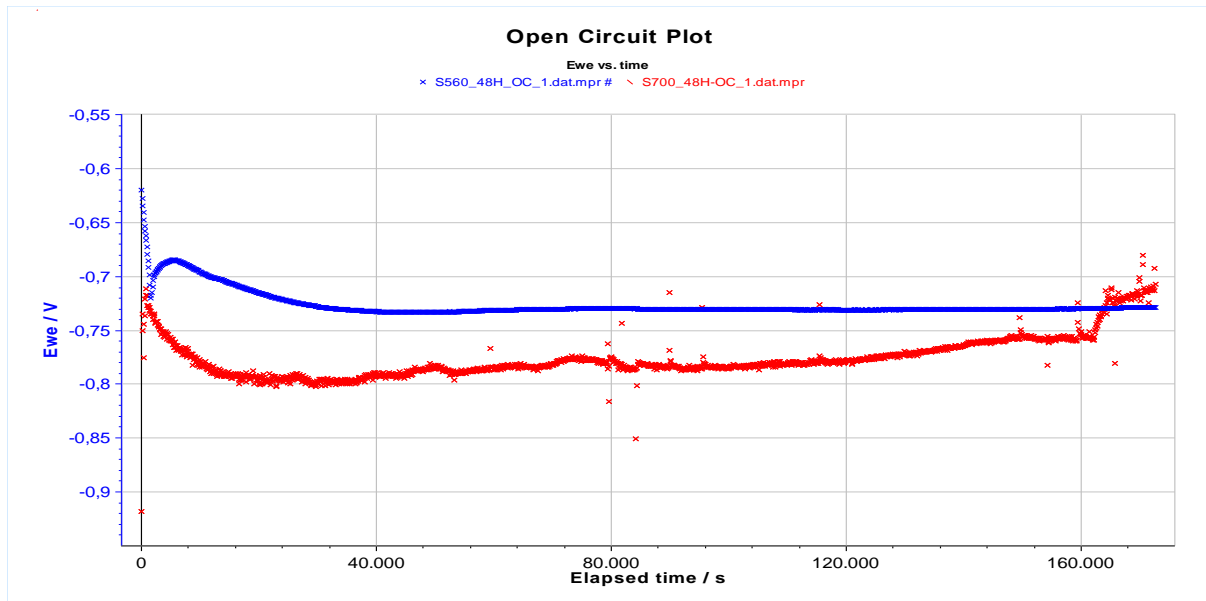
Figure B.1: 48hour experiments on OC method of **S560** (in **Blue**) and **S700** (in **Red**).
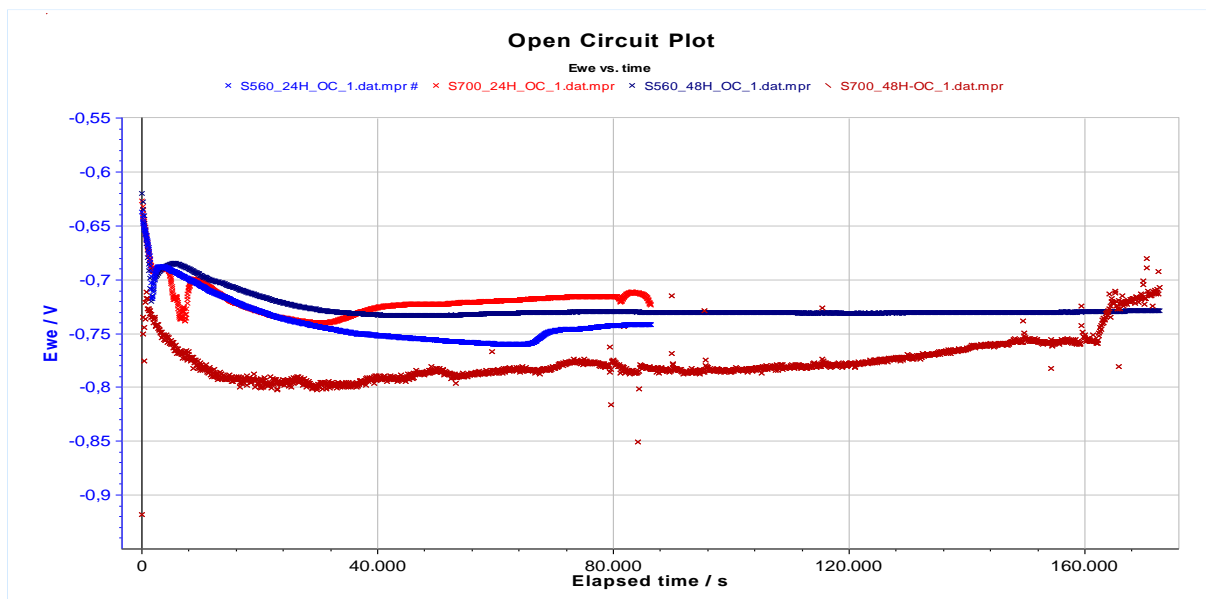
Figure B.2: Experiments on OC method of **S560** (**Blue**: 24hour, **Dark blue**: 48hour) and **S700** (**Red**: 24our and **Dark Red**: 48hour).

B.1.1. 24hour OC experiments
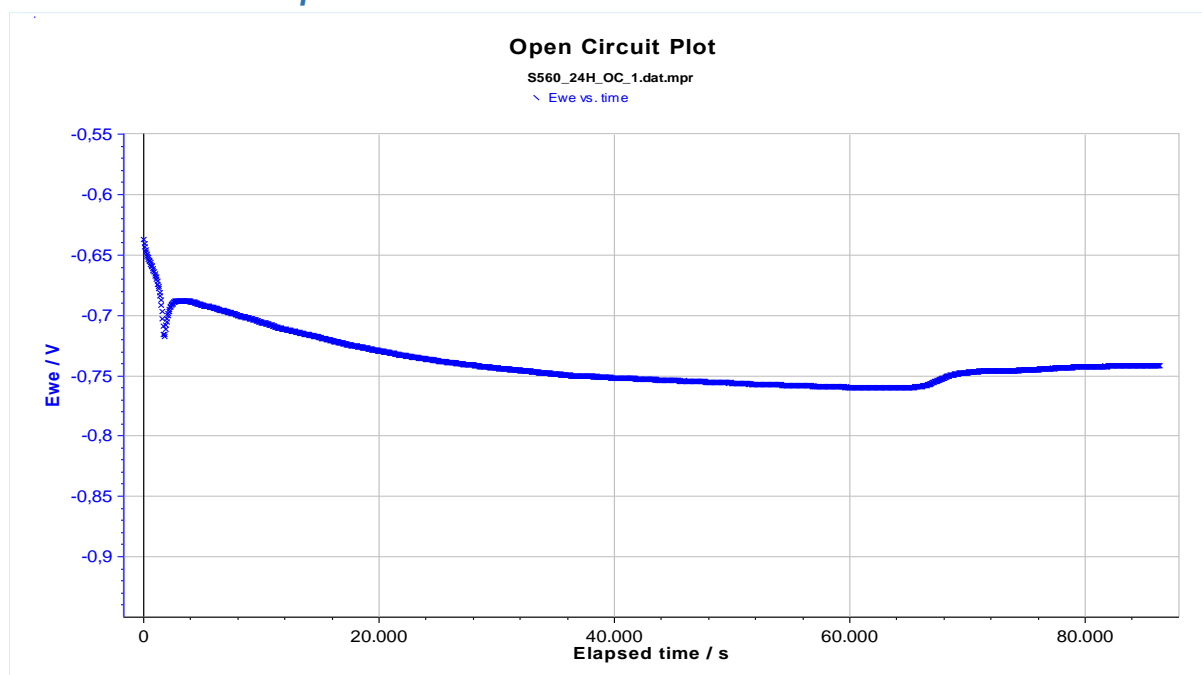
*Figure B.3: **S560** specimen – 24h experiment on Open Circuit electrochemical technique.*
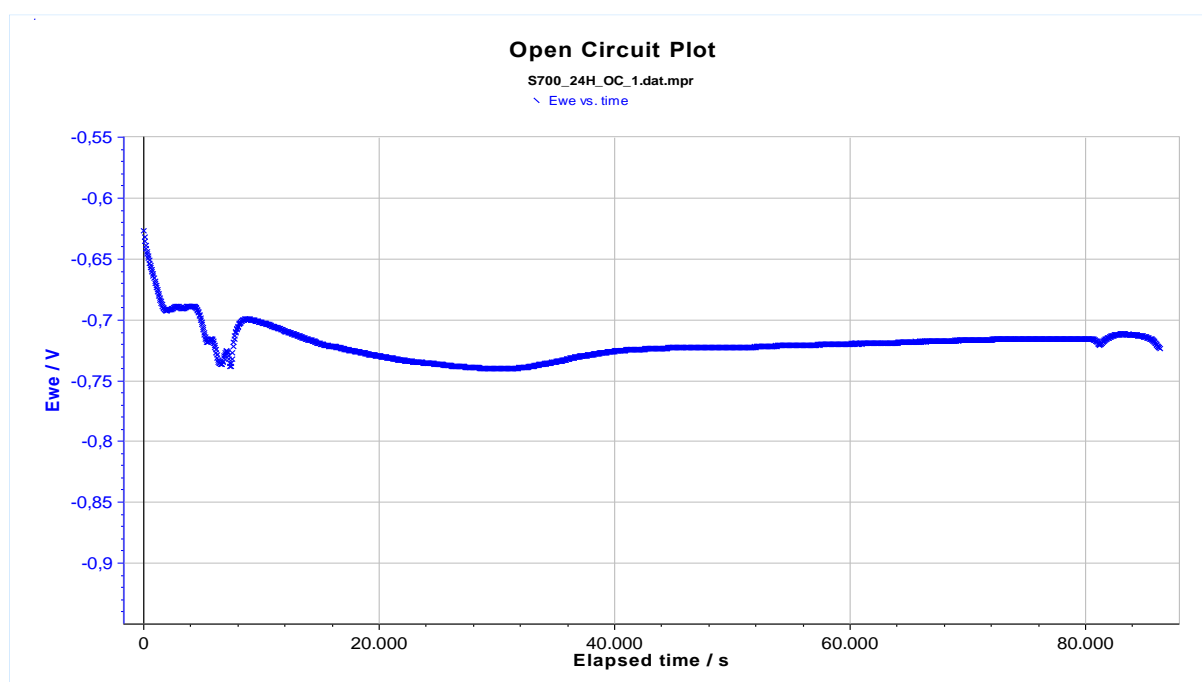
*Figure B.4: **S700** specimen – 24h experiment on Open Circuit electrochemical technique.*

B.1.2. 48hour experiments
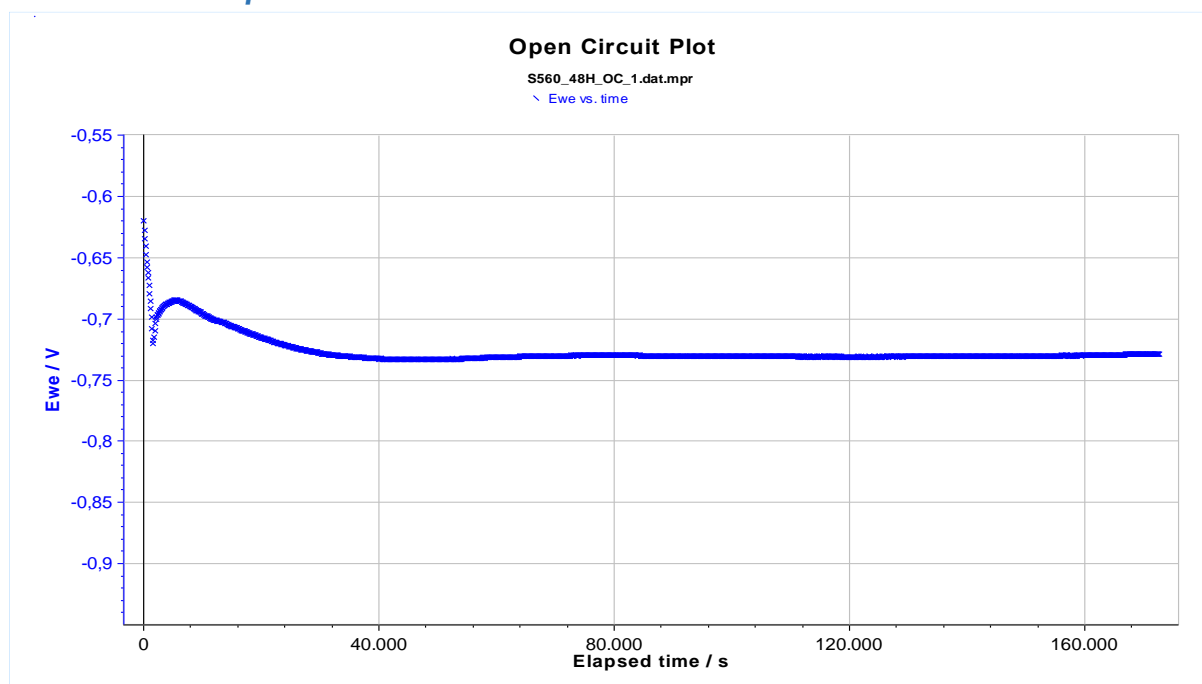
Figure B.5: **S560** specimen – 48h experiment on Open Circuit electrochemical technique.
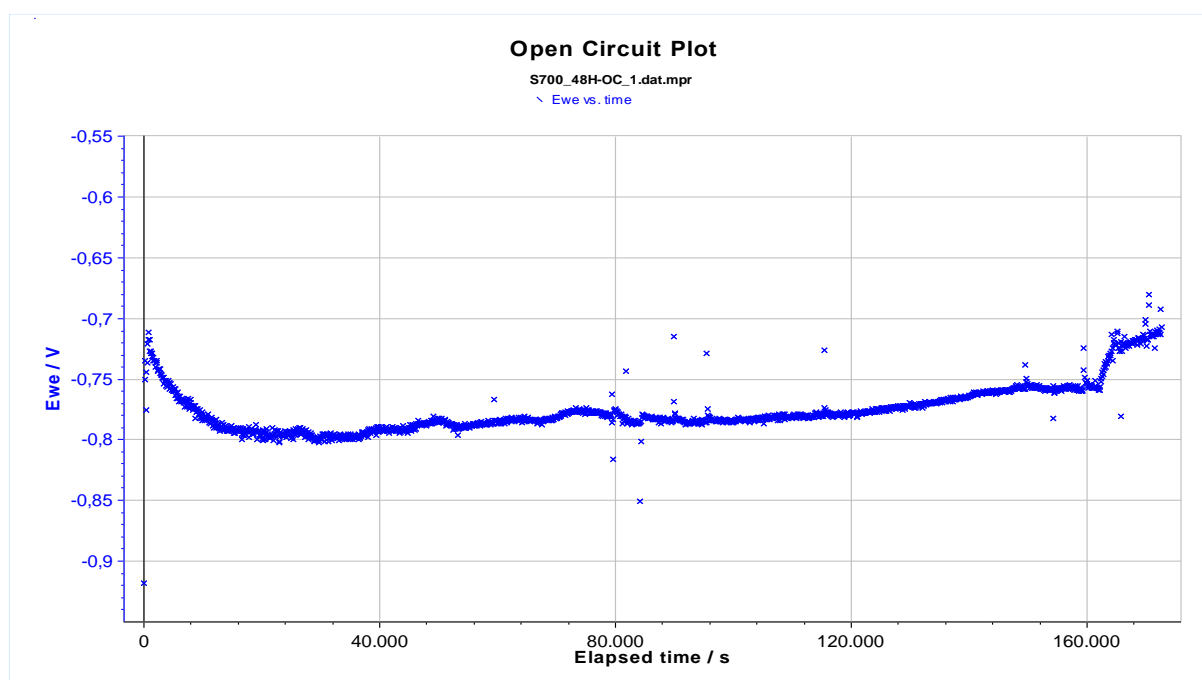
Figure B.6: **S700** specimen – 48h experiment on Open Circuit electrochemical technique.

B.1.3. 24hour OC-EIS experiments
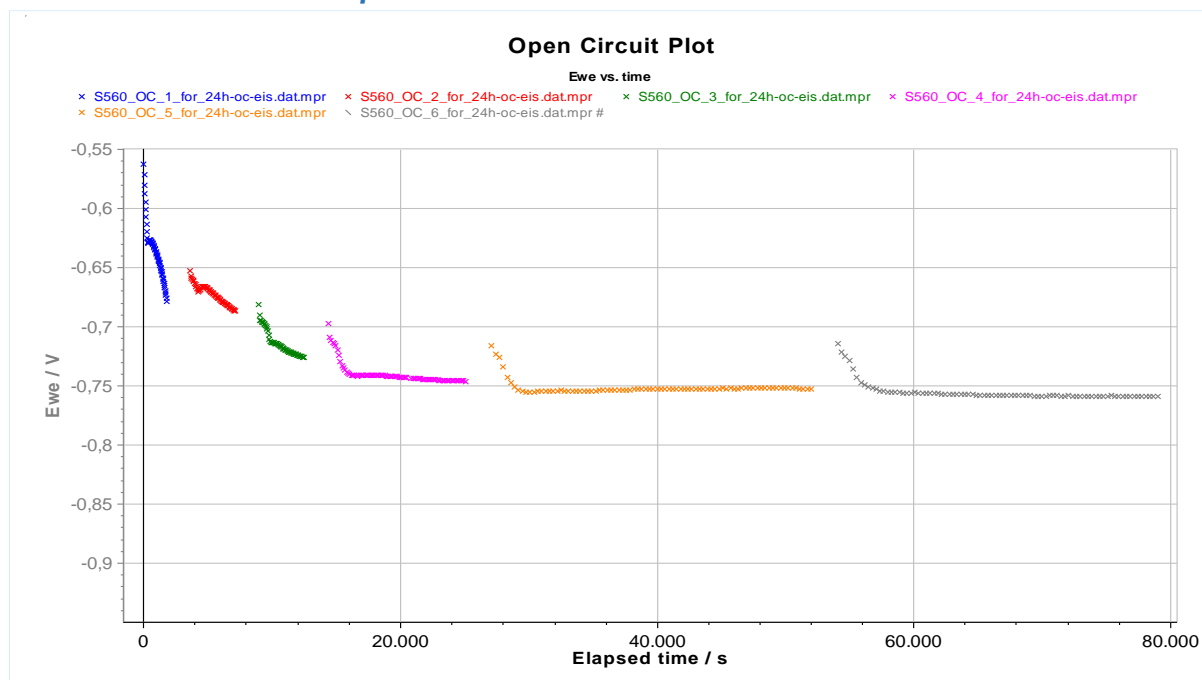
*Figure B.7: **S560** specimen – 24h 6loop OC-EIS experiment. Open Circuit electrochemical technique's results (each color corresponds to each one of the 6 loops).*
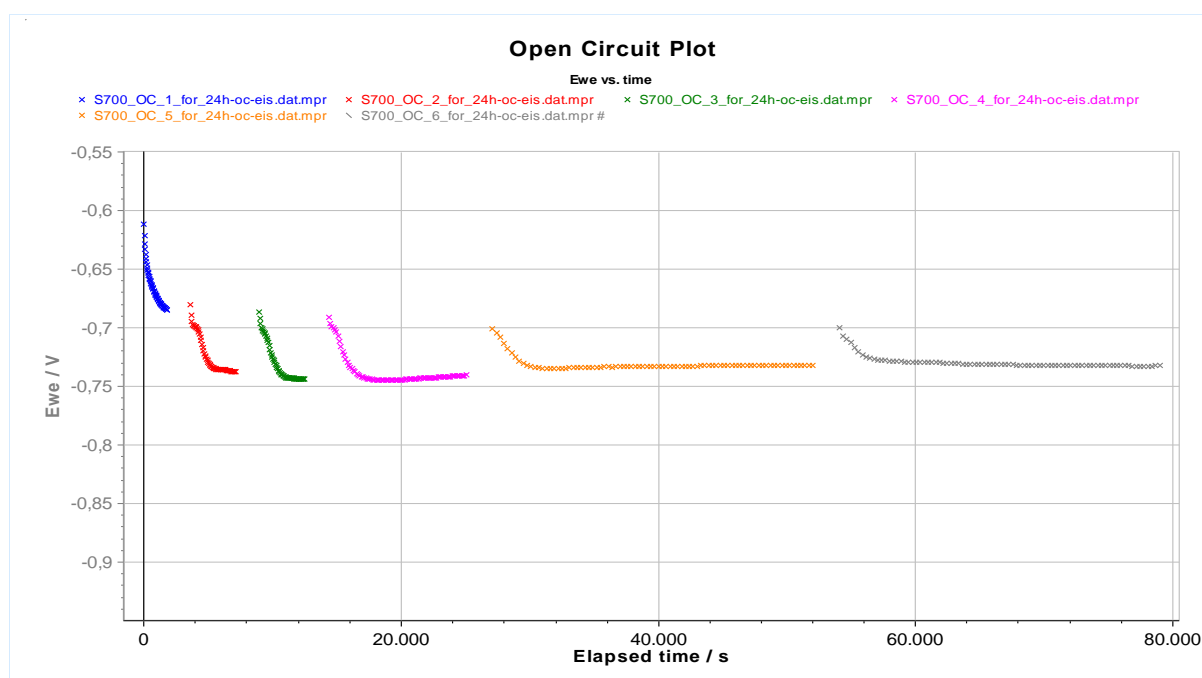
*Figure B.8: **S700** specimen – 24h 6loop OC-EIS experiment. Open Circuit electrochemical technique's results (each color corresponds to each one of the 6 loops).*

B.2. Linear Polarization Resistance (LPR) experiments
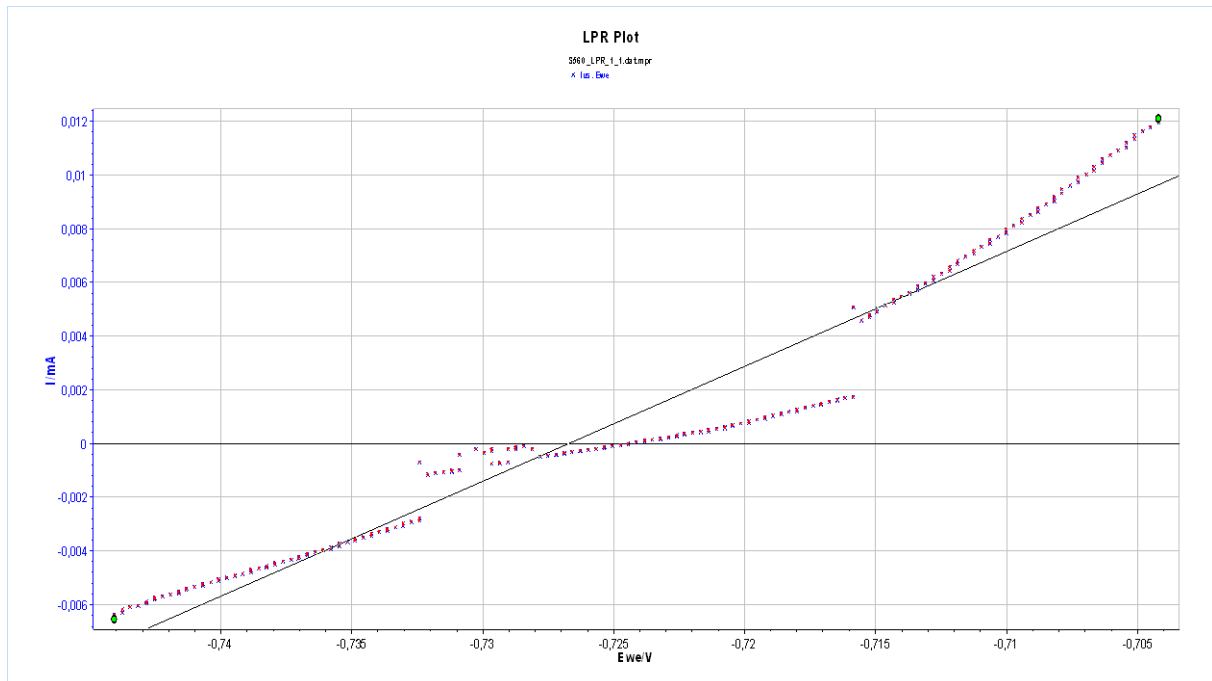
Figure B.9: **S560** *specimen – Potentiodynamic Polarization experiment (#1_1) on LPR method.* **Blue dots**: *experimental points,* **Red dots**: *fitted experimental points,* **Black line**: *fitted linear curve (slope=R_P^{-1}).*
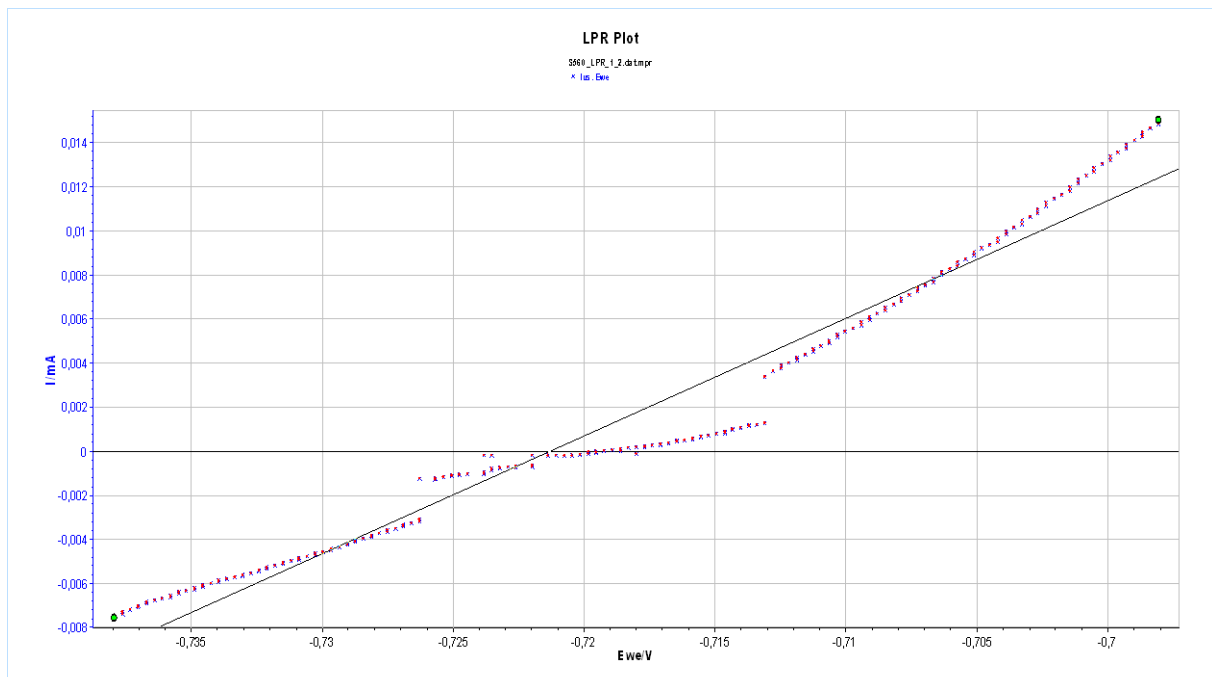
Figure B.10: **S560** *specimen – Potentiodynamic Polarization experiment (#1_2) on LPR method.* **Blue dots**: *experimental points,* **Red dots**: *fitted experimental points,* **Black line**: *fitted linear curve (slope=R_P^{-1}).*
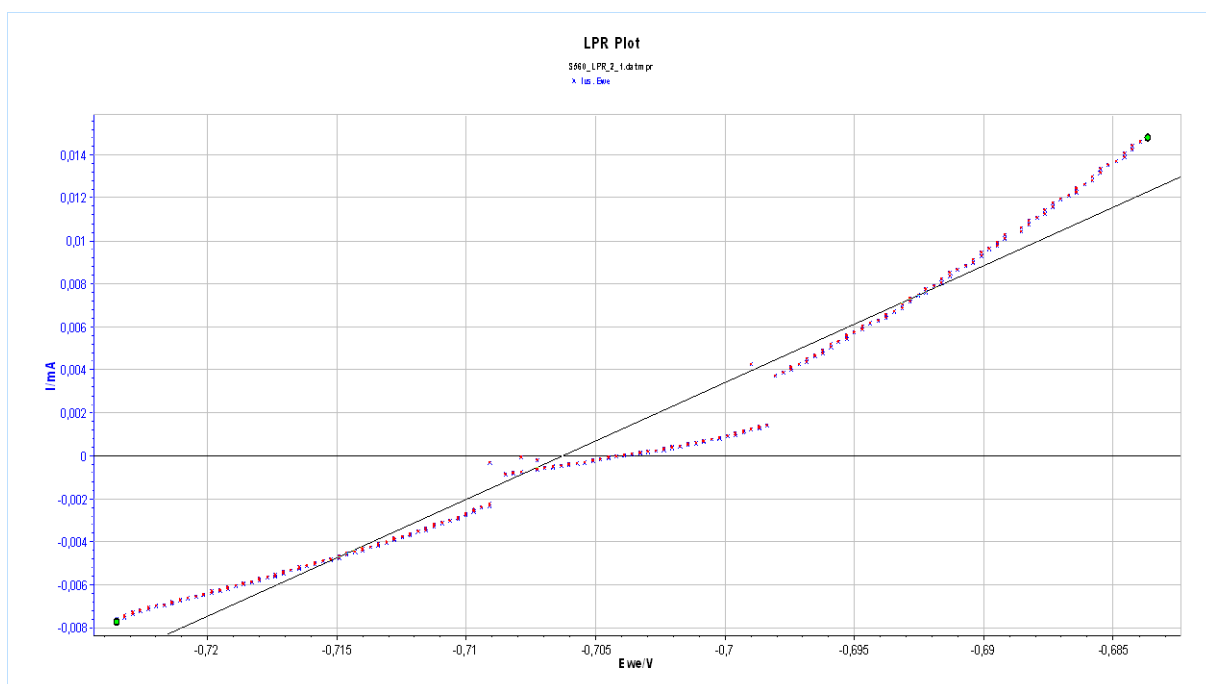
*Figure B.11: **S560** specimen – Potentiodynamic Polarization experiment (#2_1) on LPR method. **Blue dots**: experimental points, **Red dots**: fitted experimental points, **Black line**: fitted linear curve (slope=R_P^{-1}).*
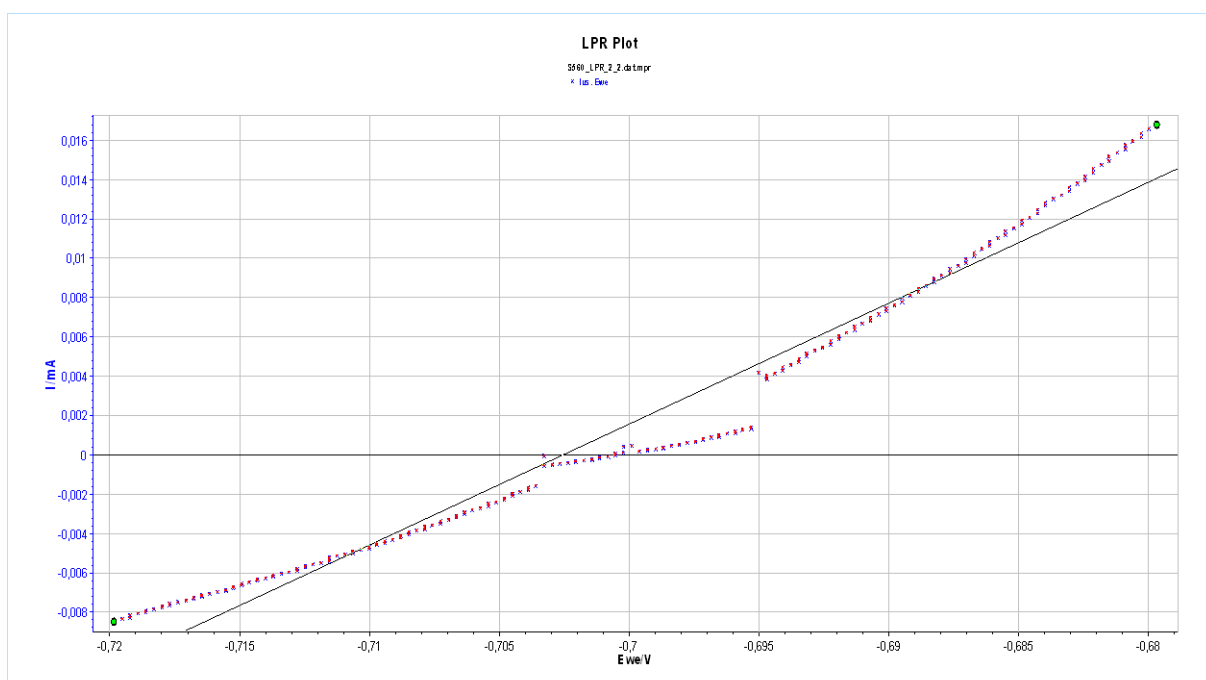
*Figure B.12: **S560** specimen – Potentiodynamic Polarization experiment (#2_2) on LPR method. **Blue dots**: experimental points, **Red dots**: fitted experimental points, **Black line**: fitted linear curve (slope=R_P^{-1}).*
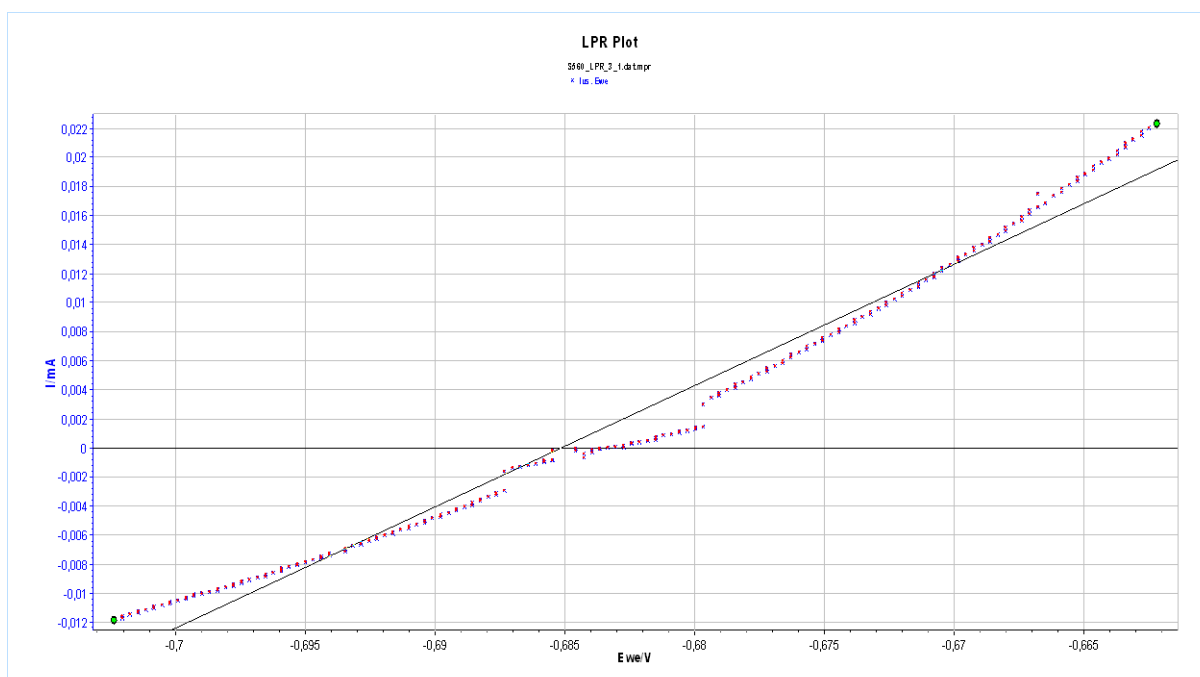
Figure B.13: ***S560*** *specimen – Potentiodynamic Polarization experiment (#3_1) on LPR method.* ***Blue dots****: experimental points,* ***Red dots****: fitted experimental points,* ***Black line****: fitted linear curve (slope=R_P^{-1}).*
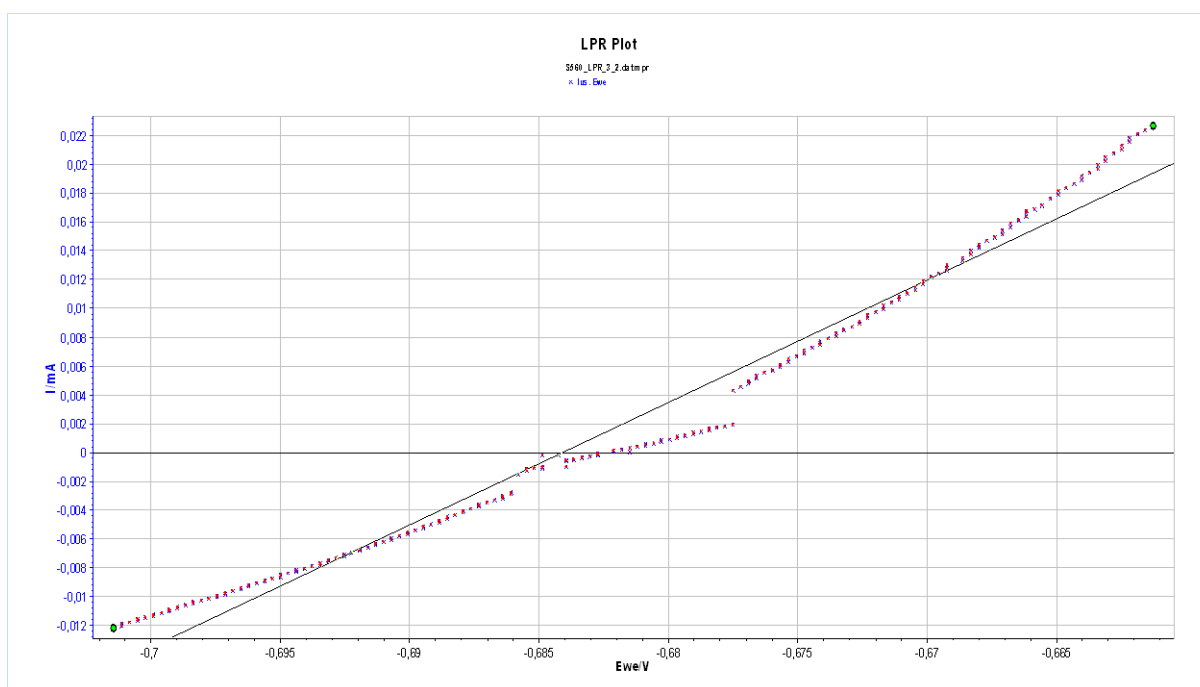
Figure B.14: ***S560*** *specimen – Potentiodynamic Polarization experiment (#3_2) on LPR method.* ***Blue dots****: experimental points,* ***Red dots****: fitted experimental points,* ***Black line****: fitted linear curve (slope=R_P^{-1}).*
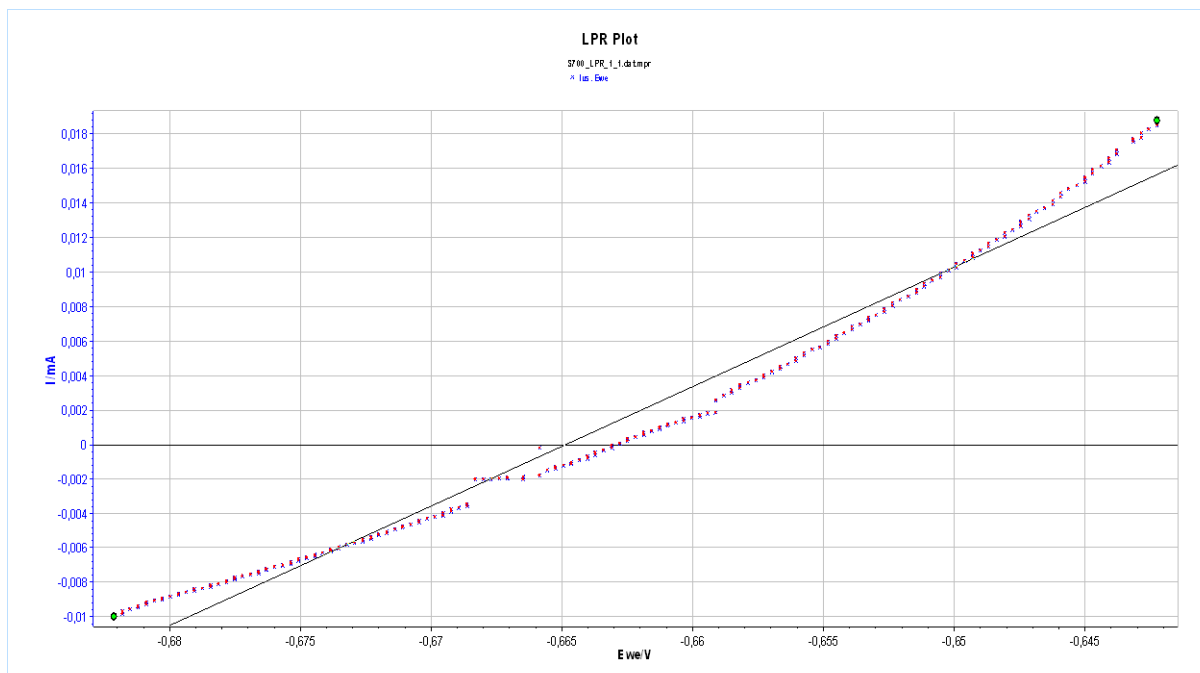
*Figure B.15: **S700** specimen – Potentiodynamic Polarization experiment (#1_1) on LPR method. **Blue dots**: experimental points, **Red dots**: fitted experimental points, **Black line**: fitted linear curve (slope=R_P^{-1}).*
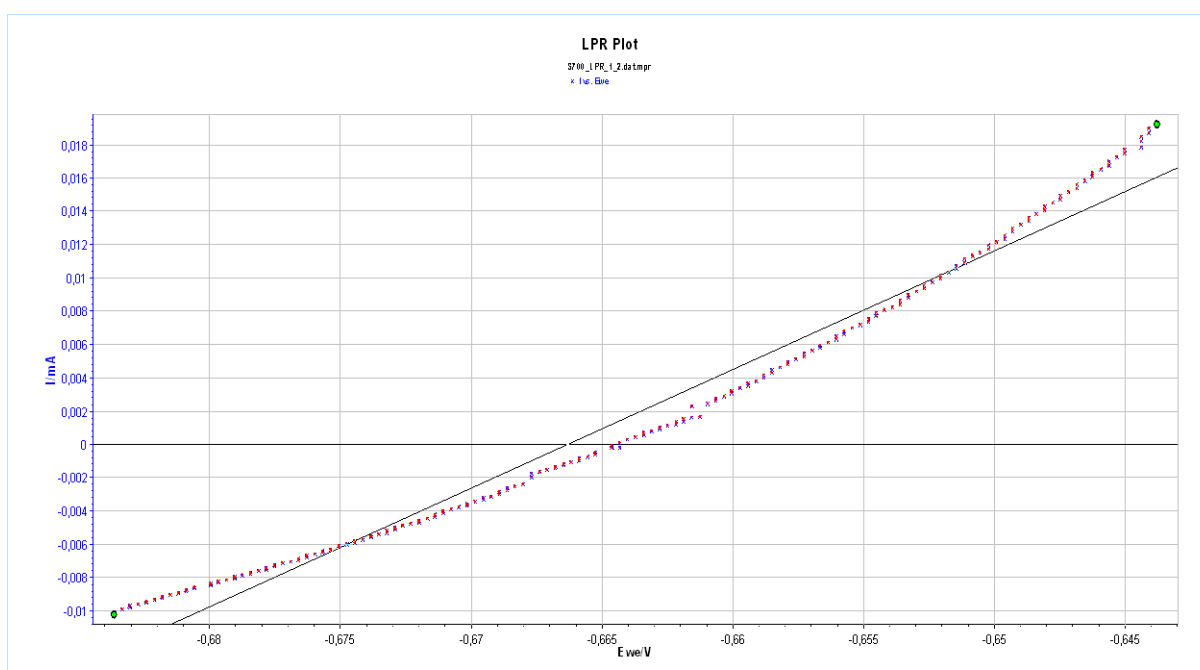
*Figure B.16: **S700** specimen – Potentiodynamic Polarization experiment (#1_2) on LPR method. **Blue dots**: experimental points, **Red dots**: fitted experimental points, **Black line**: fitted linear curve (slope=R_P^{-1}).*
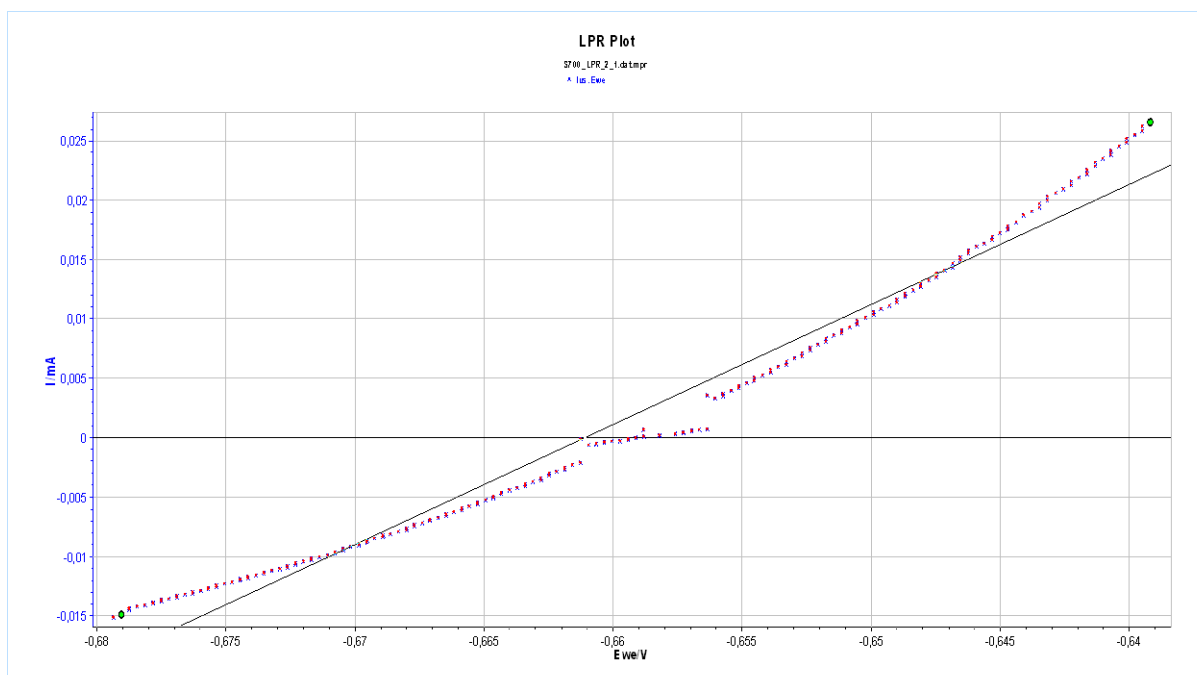
*Figure B.17: **S700** specimen – Potentiodynamic Polarization experiment (#2_1) on LPR method. **Blue dots**: experimental points, **Red dots**: fitted experimental points, **Black line**: fitted linear curve (slope=R_P^{-1}).*
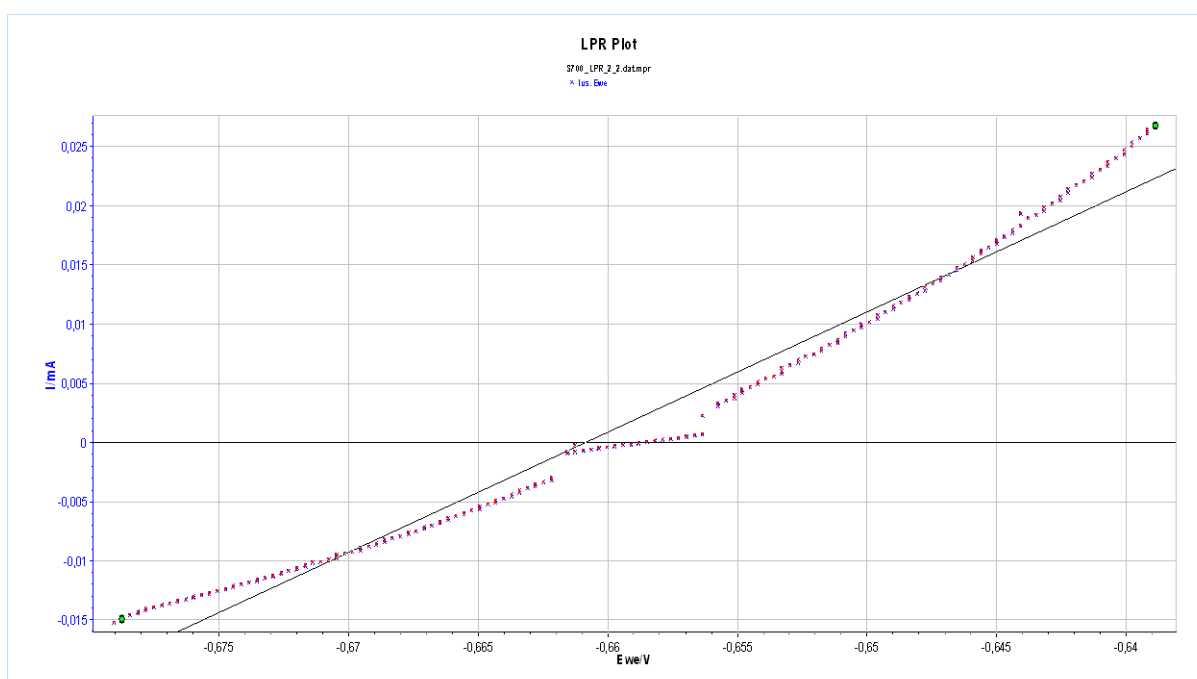
*Figure B.18: **S700** specimen – Potentiodynamic Polarization experiment (#2_2) on LPR method. **Blue dots**: experimental points, **Red dots**: fitted experimental points, **Black line**: fitted linear curve (slope=R_P^{-1}).*
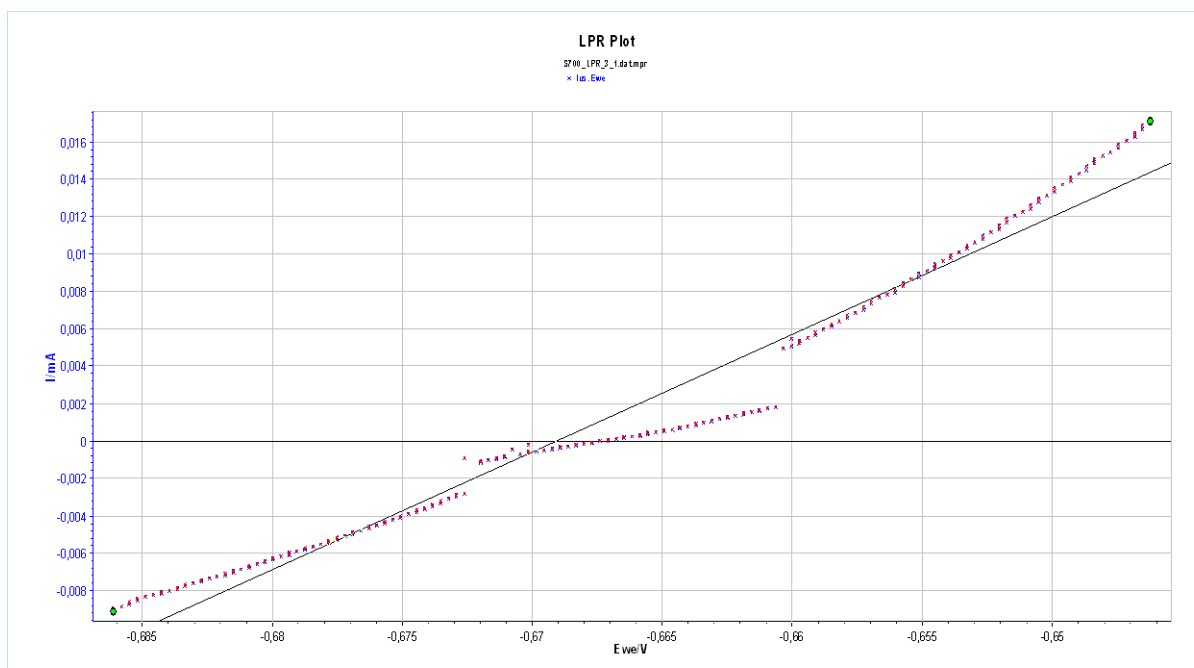
*Figure B.19: **S700** specimen – Potentiodynamic Polarization experiment (#3_1) on LPR method. **Blue dots**: experimental points, **Red dots**: fitted experimental points, **Black line**: fitted linear curve (slope=R_P^{-1}).*
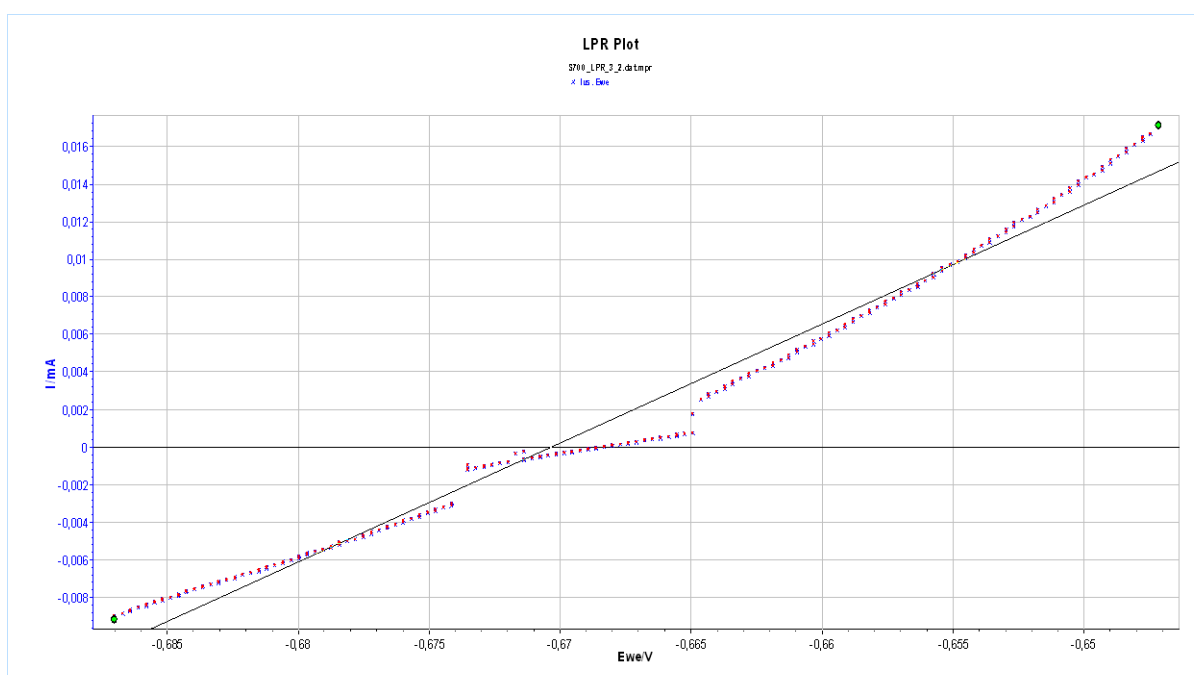
*Figure B.20: **S700** specimen – Potentiodynamic Polarization experiment (#3_2) on LPR method. **Blue dots**: experimental points, **Red dots**: fitted experimental points, **Black line**: fitted linear curve (slope=R_P^{-1}).*

B.3. Potentiodynamic Polarization - Tafel Extrapolation
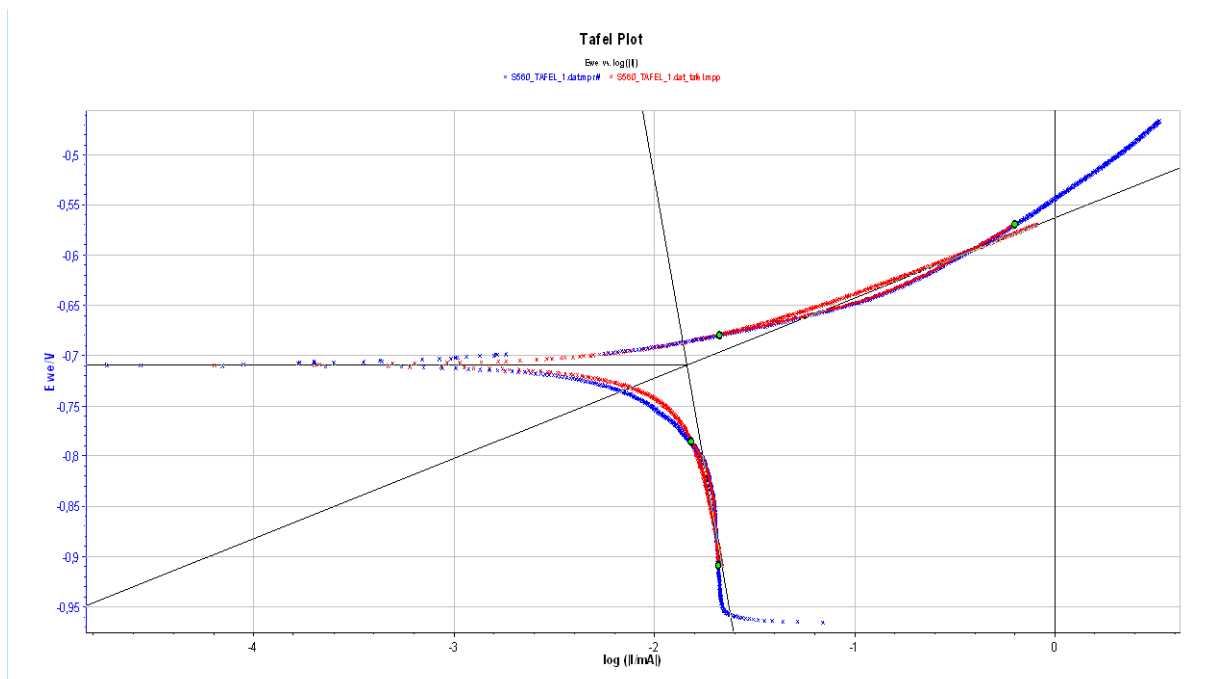
*Figure B.21: **S560** specimen – Potentiodynamic Polarization experiment (#1) with Tafel extrapolation method. **Blue dots**: experimental points, **Red dots**: fitted experimental points, **Black lines**: fitted extrapolated curves.*
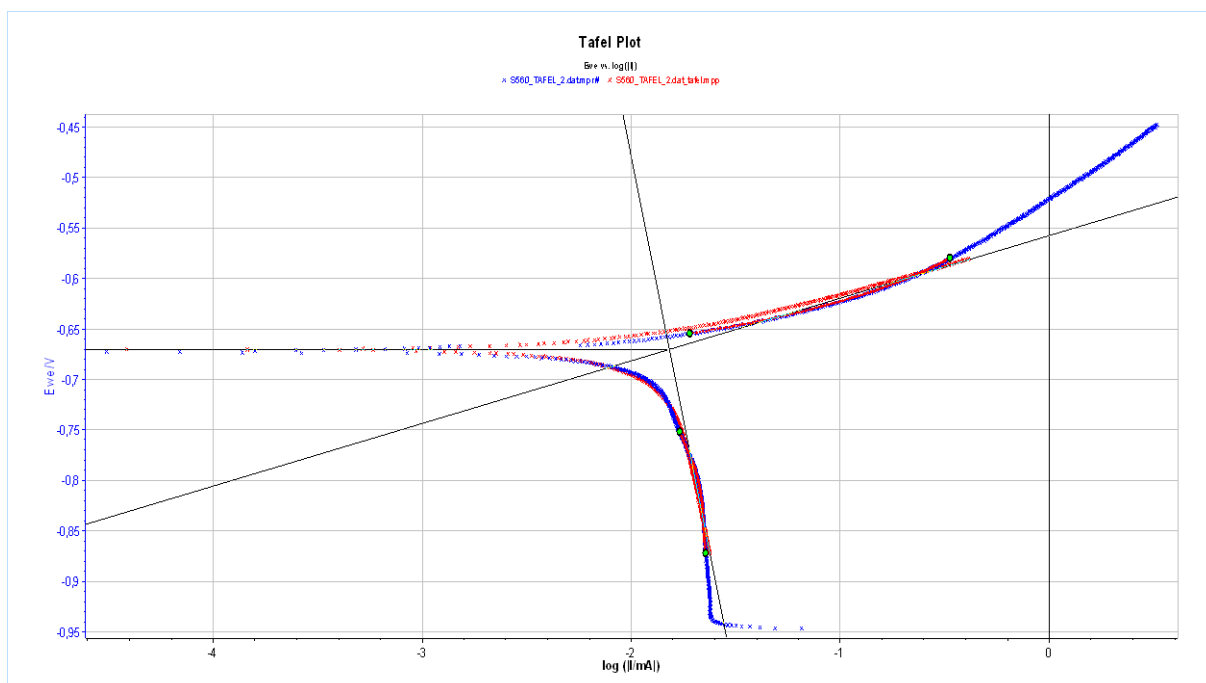
*Figure B.22: **S560** specimen – Potentiodynamic Polarization experiment (#2) with Tafel extrapolation method. **Blue dots**: experimental points, **Red dots**: fitted experimental points, **Black lines**: fitted extrapolated curves.*
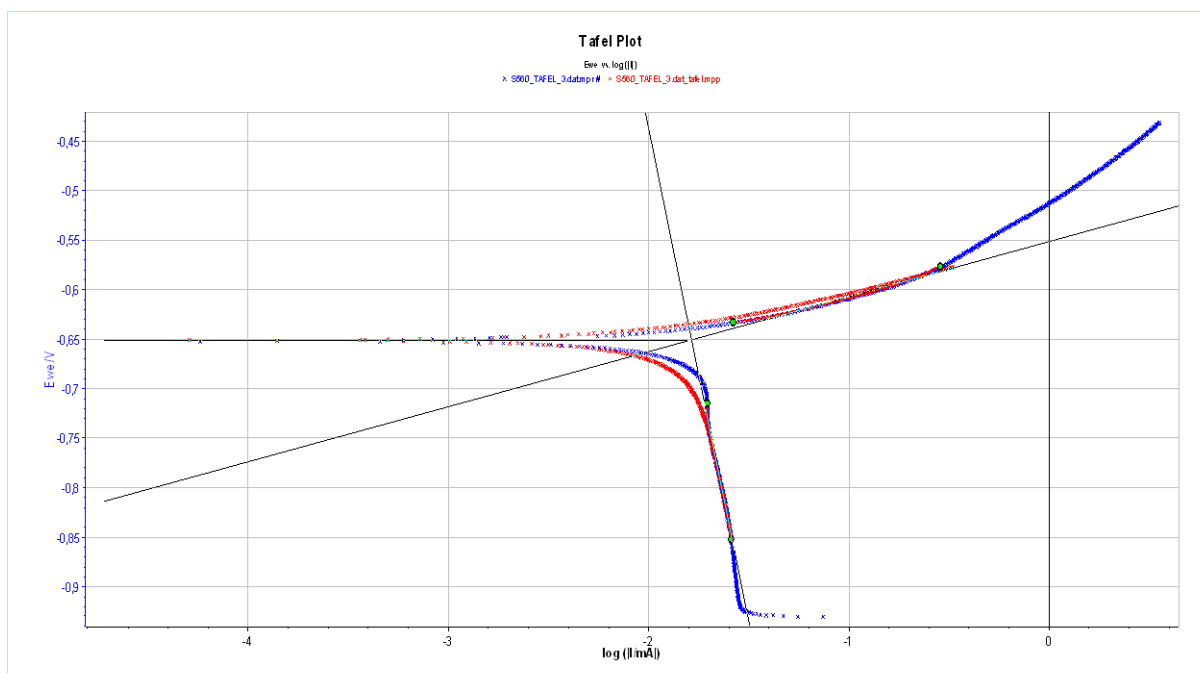
*Figure B.23: **S560** specimen – Potentiodynamic Polarization experiment (#3) with Tafel extrapolation method. **Blue dots**: experimental points, **Red dots**: fitted experimental points, **Black lines**: fitted extrapolated curves.*
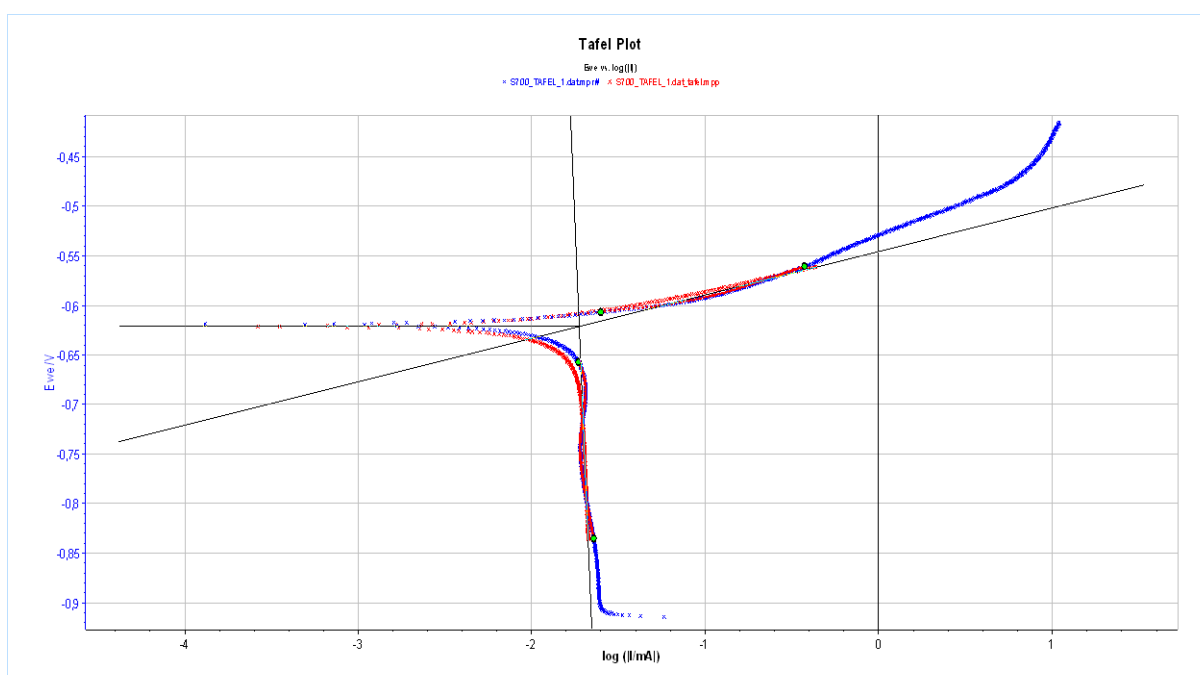
*Figure B.24: **S700** specimen – Potentiodynamic Polarization experiment (#1) with Tafel extrapolation method. **Blue dots**: experimental points, **Red dots**: fitted experimental points, **Black lines**: fitted extrapolated curves.*
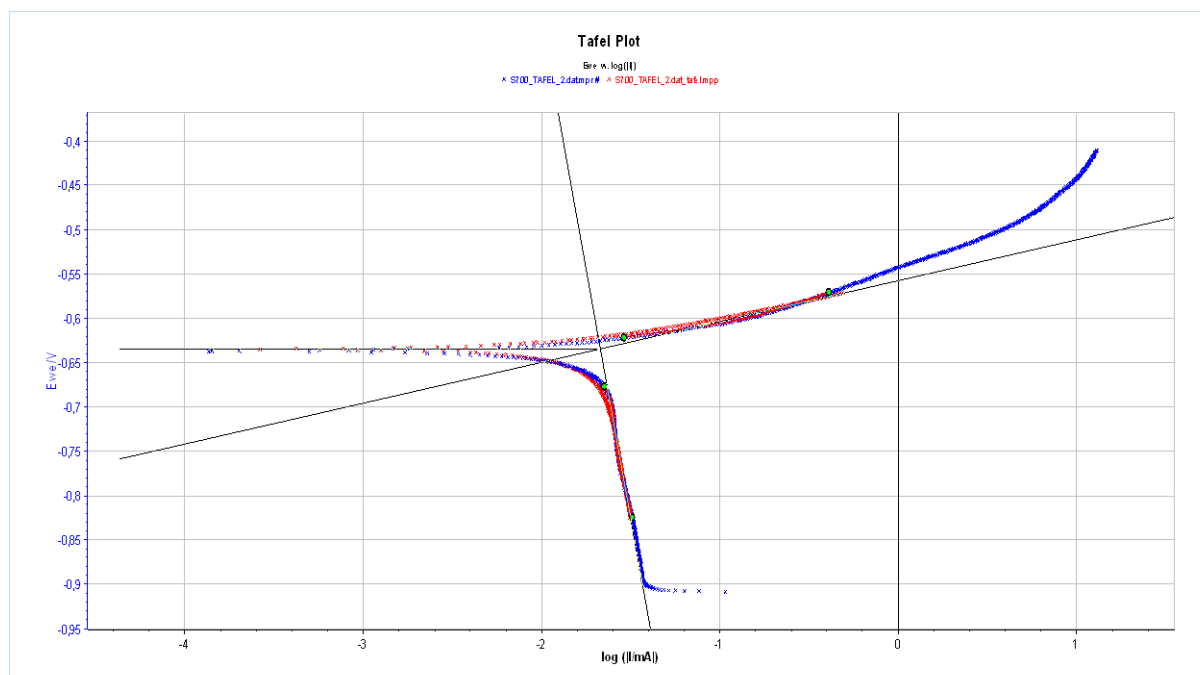
*Figure B.25: **S700** specimen – Potentiodynamic Polarization experiment (#2) with Tafel extrapolation method. **Blue dots**: experimental points, **Red dots**: fitted experimental points, **Black lines**: fitted extrapolated curves.*
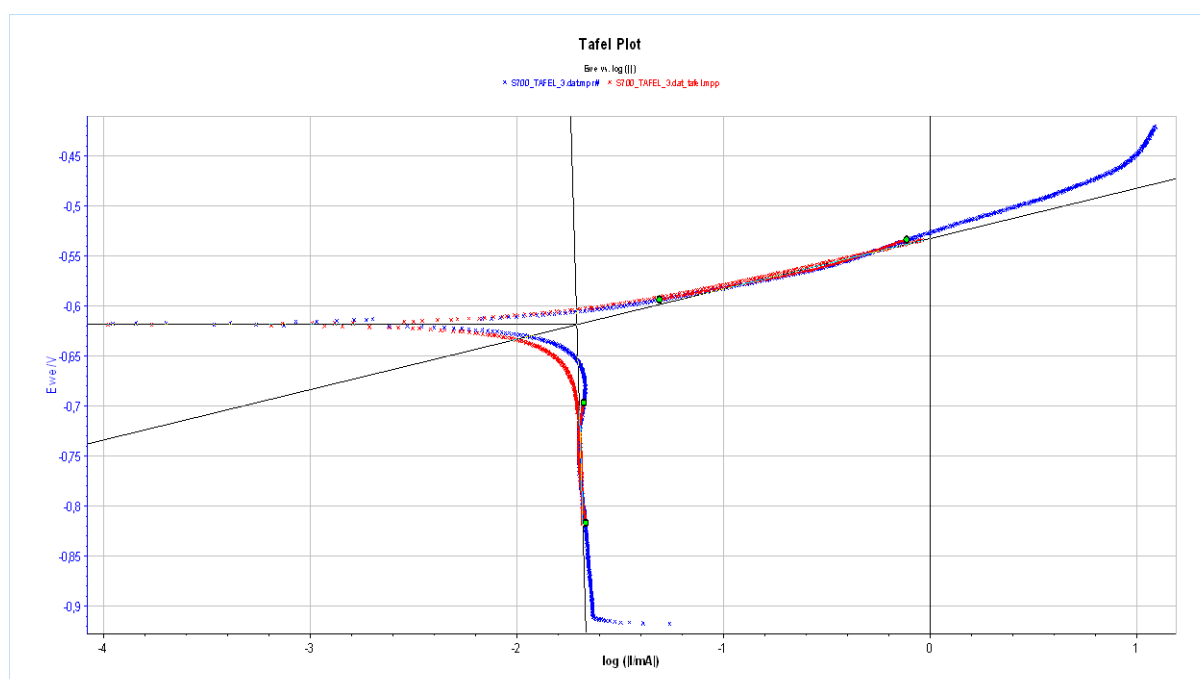
*Figure B.26: **S700** specimen – Potentiodynamic Polarization experiment (#3) with Tafel extrapolation method. **Blue dots**: experimental points, **Red dots**: fitted experimental points, **Black lines**: fitted extrapolated curves.*

B.4. Electrochemical Impedance Spectroscopy (EIS)

B.4.1. Three consecutive EIS experiment
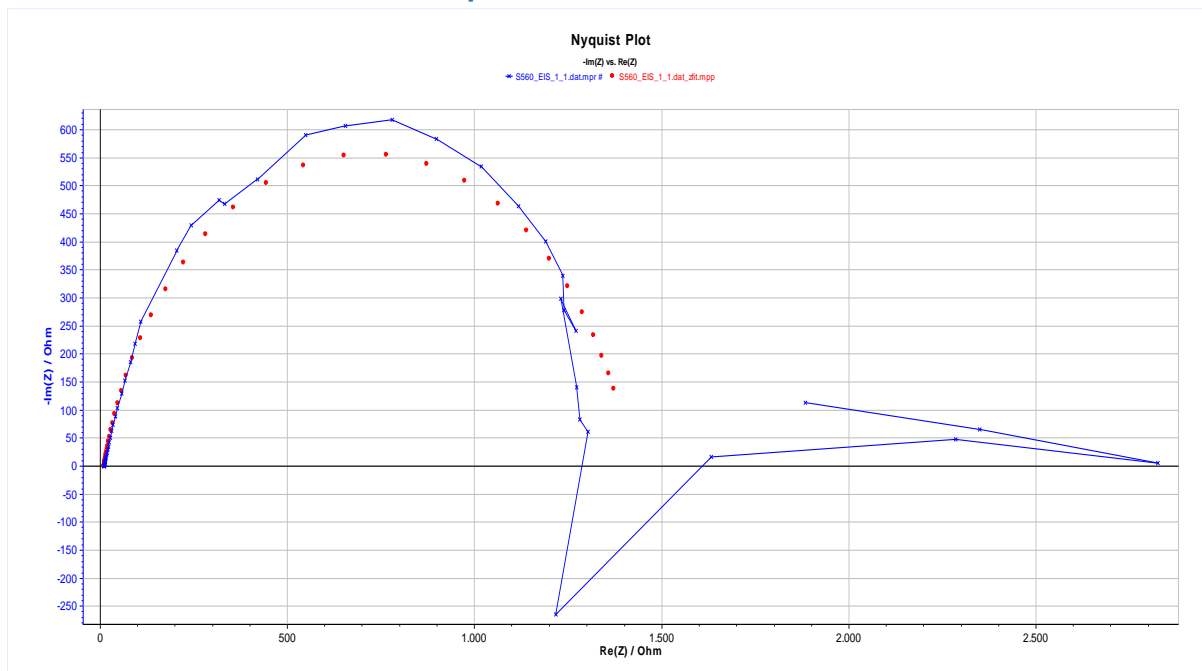
*Figure B.27: **S560** specimen – Nyquist plot of EIS experiment (1ˢᵗ cycle). **Blue line**: experimental points, **Red dots**: fitted points.*
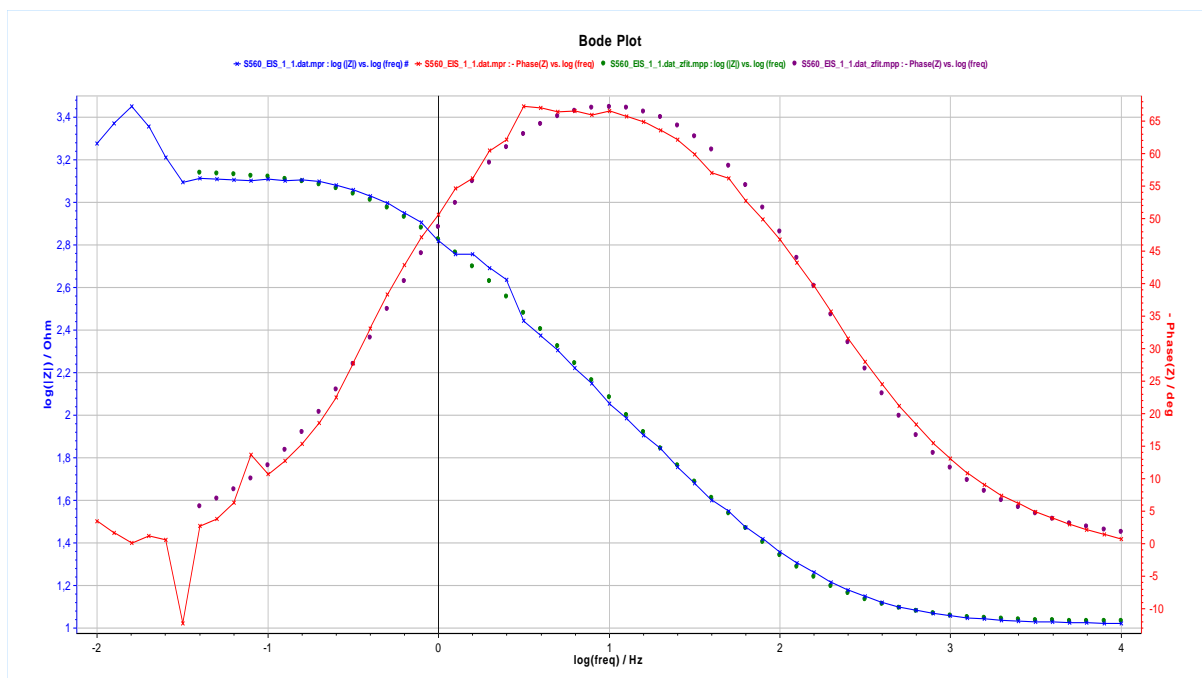
*Figure B.28: **S560** specimen – Bode plot of EIS experiment (1ˢᵗ cycle).*

***Blue line**: experimental points of log(|Z|), **Green dots**: fitted points.*

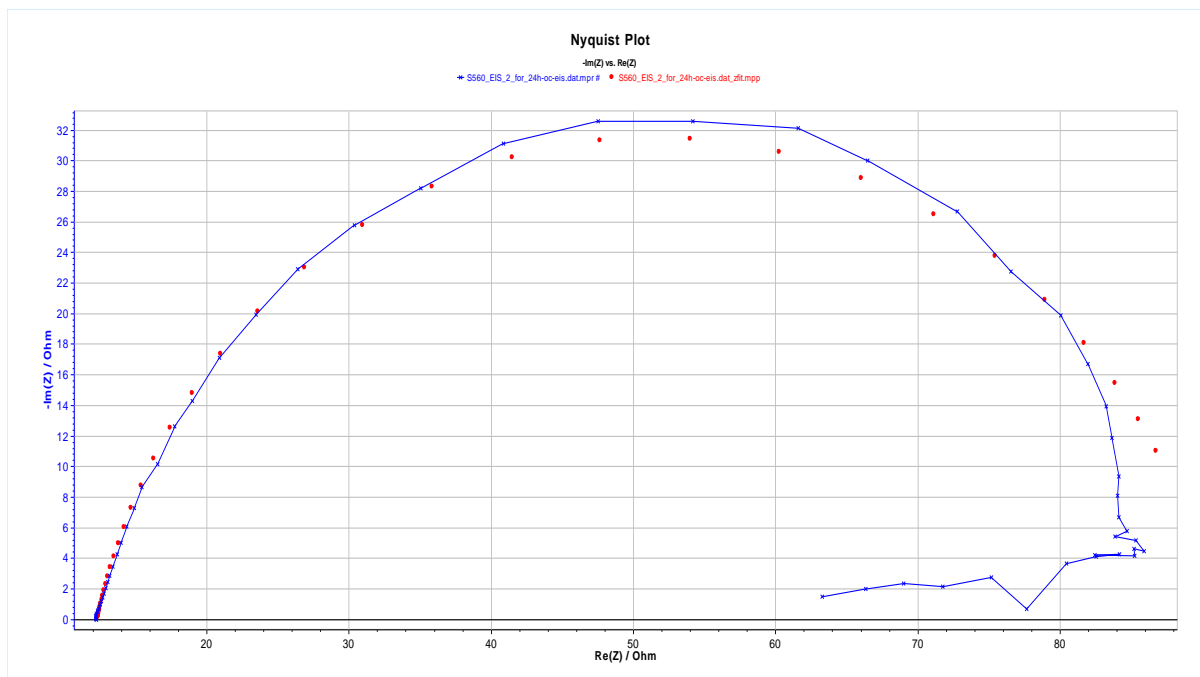***Red line**: experimental points of -phase(|Z|), **Purple dots**: fitted points.*
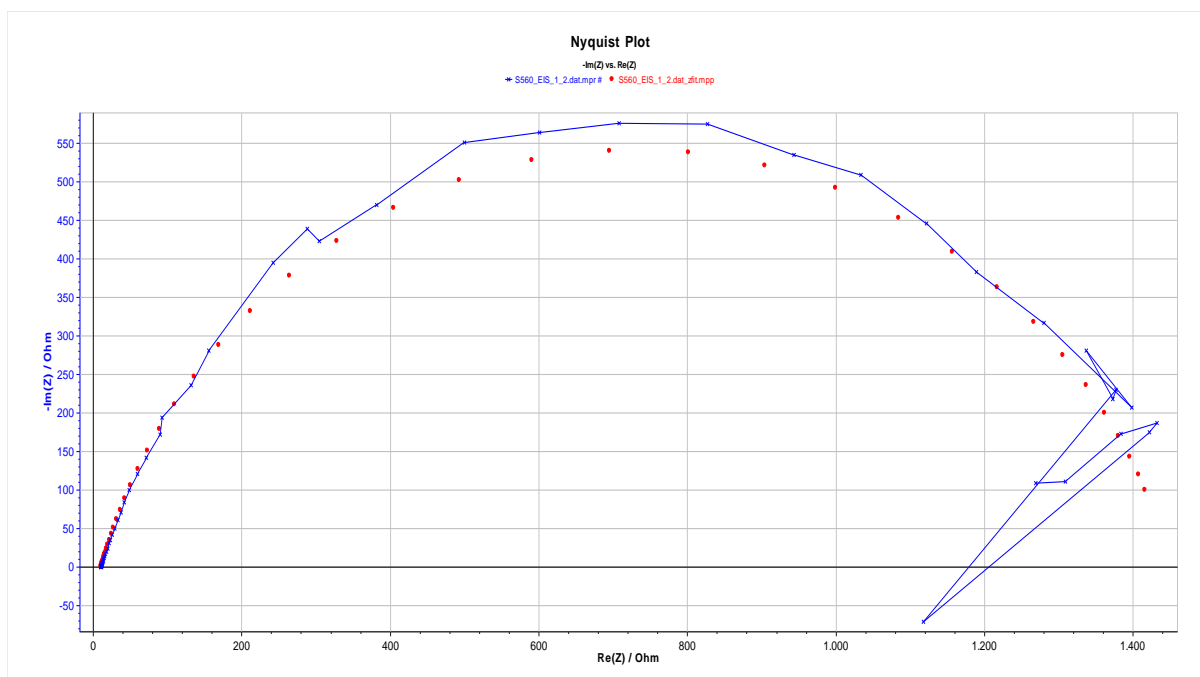
*Figure B.29: **S560** specimen – Nyquist plot of EIS experiment (2nd cycle). **Blue line**: experimental points, **Red dots**: fitted points.*
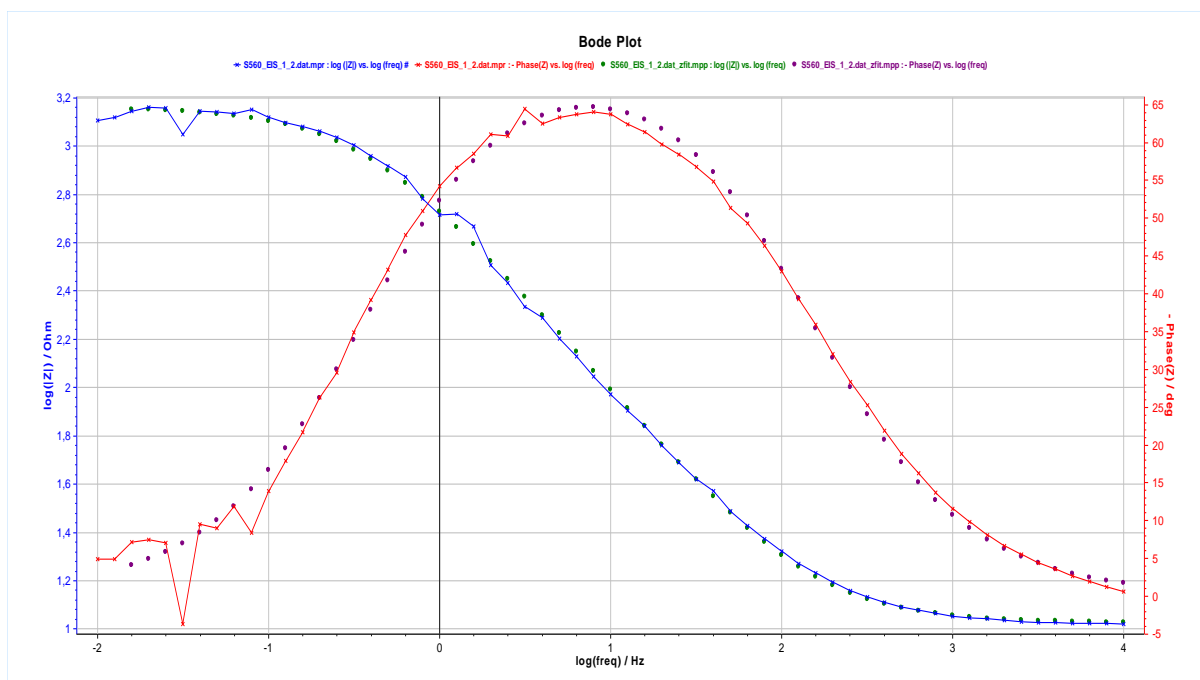
*Figure B.30: **S560** specimen – Bode plot of EIS experiment (2nd cycle).*

***Blue line**: experimental points of log(|Z|), **Green dots**: fitted points.*

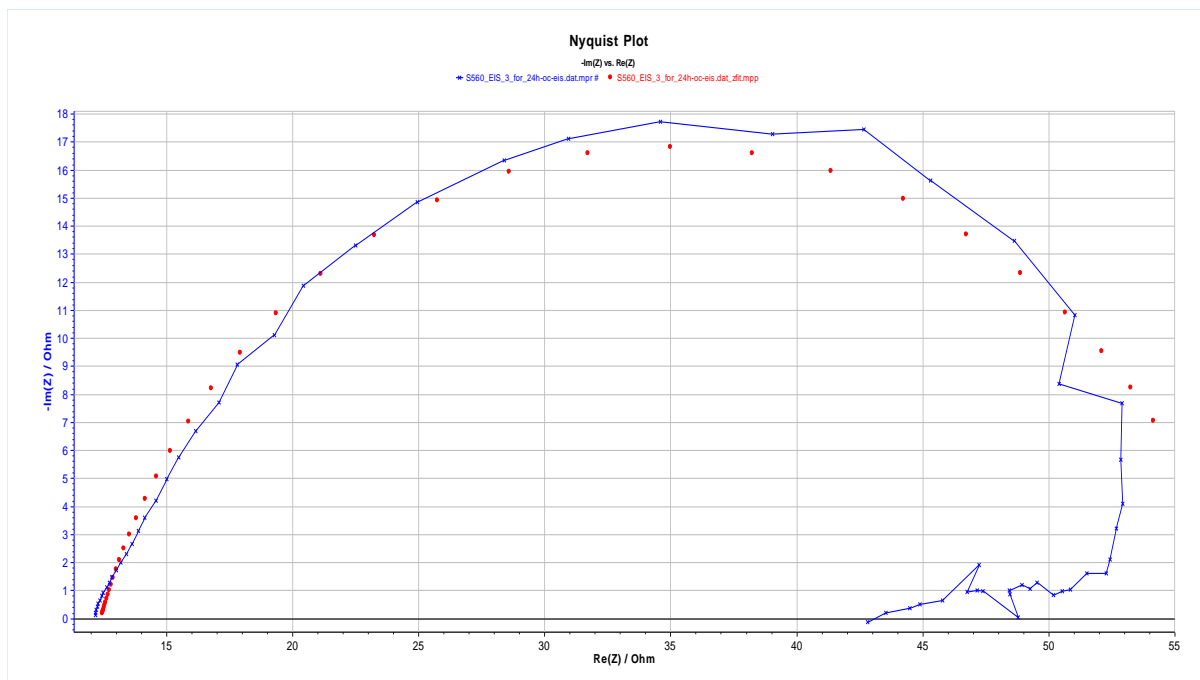***Red line**: experimental points of -phase(|Z|), **Purple dots**: fitted points.*
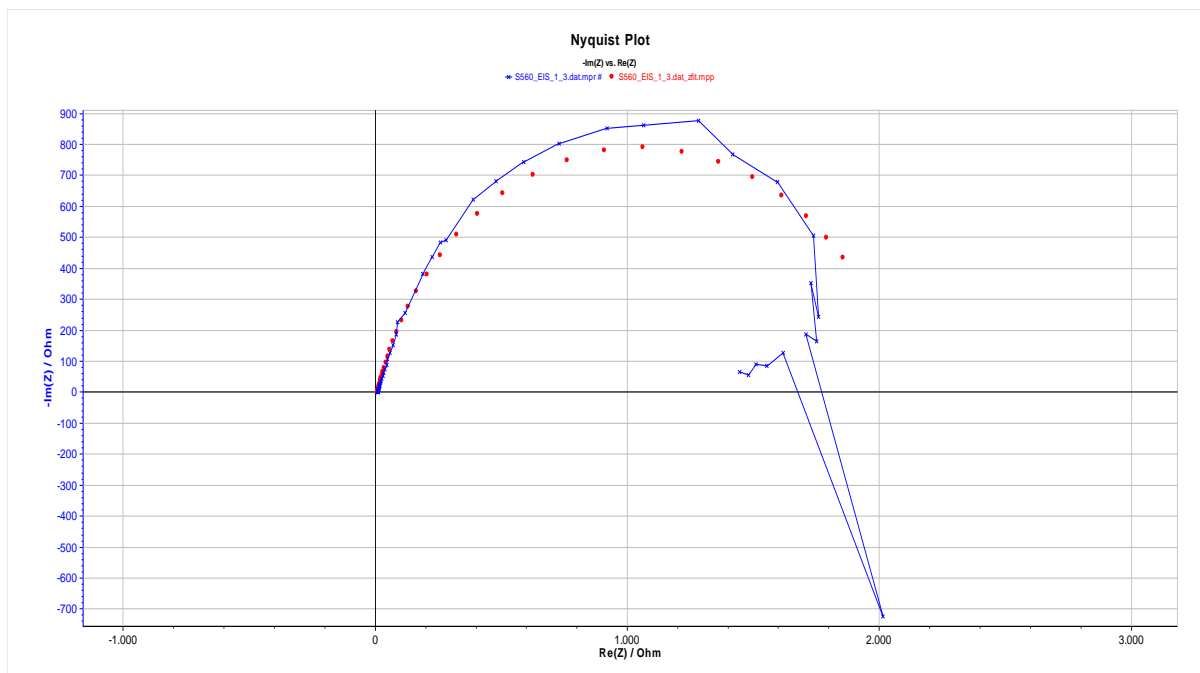
*Figure B.31: **S560** specimen – Nyquist plot of EIS experiment (3rd cycle). **Blue line**: experimental points, **Red dots**: fitted points.*
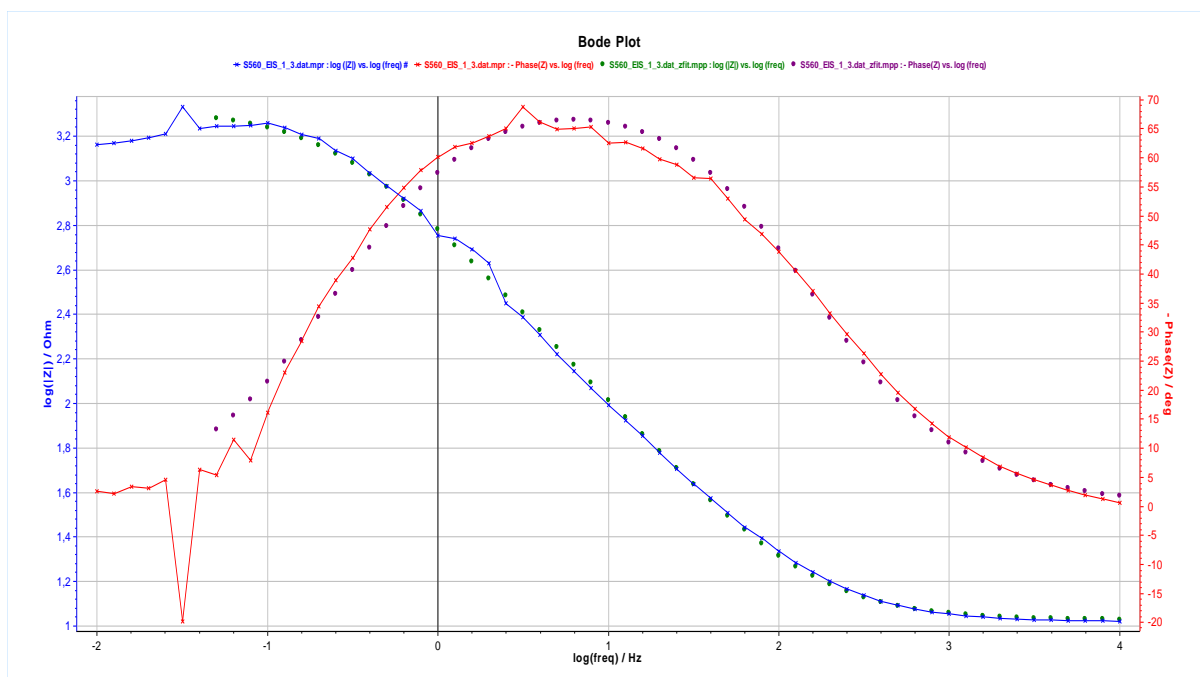
*Figure B.32: **S560** specimen – Bode plot of EIS experiment (3rd cycle).*

***Blue line**: experimental points of log(|Z|), **Green dots**: fitted points.*

***Red line**: experimental points of -phase(|Z|), **Purple dots**: fitted points.*
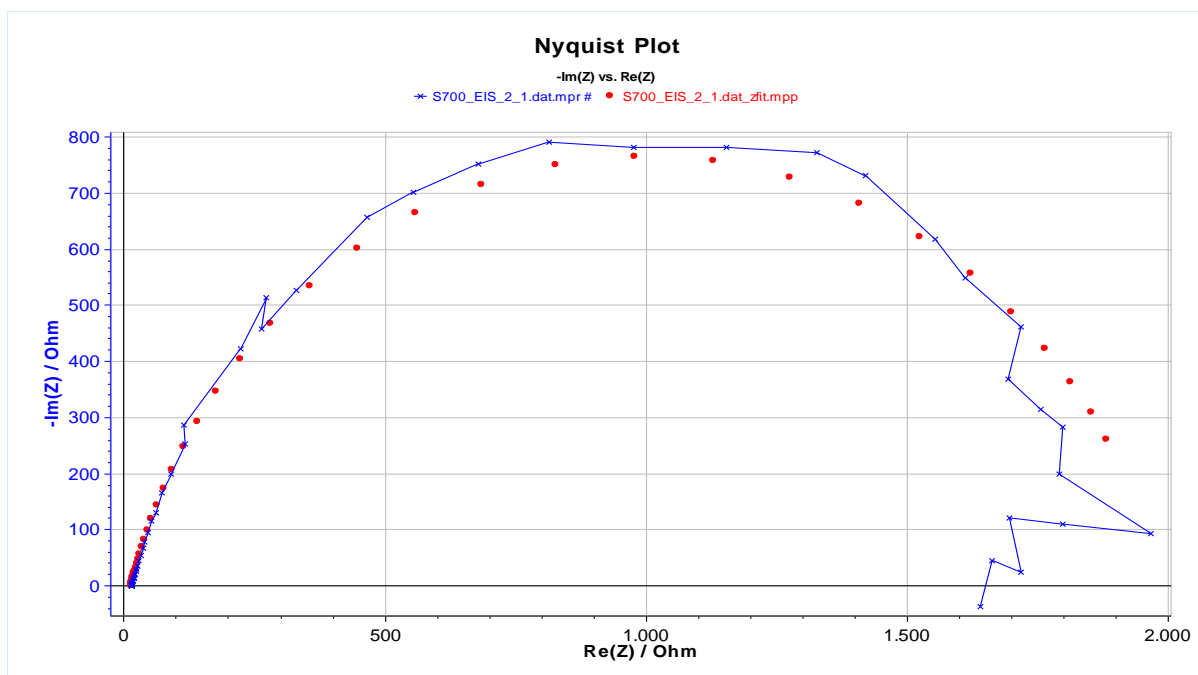
*Figure B.33: **S700** specimen – Nyquist plot of EIS experiment (1st cycle). **Blue line**: experimental points, **Red dots**: fitted points.*
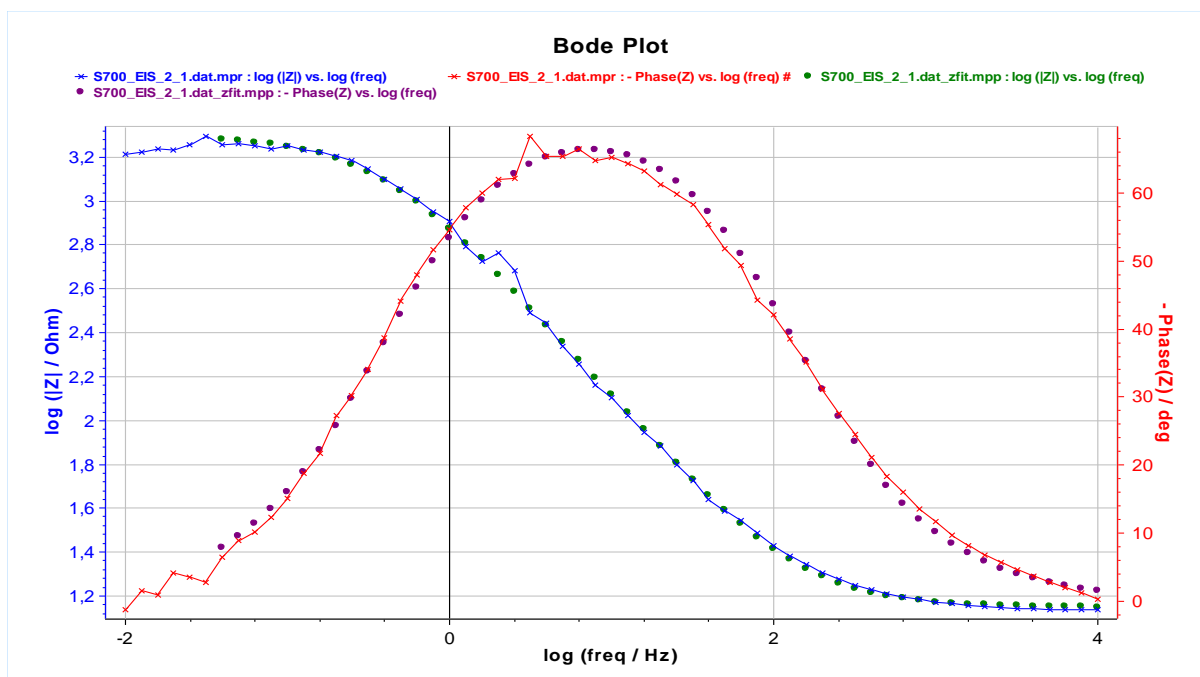
*Figure B.34: **S700** specimen – Bode plot of EIS experiment (1st cycle).*

***Blue line**: experimental points of log(|Z|), **Green dots**: fitted points.*

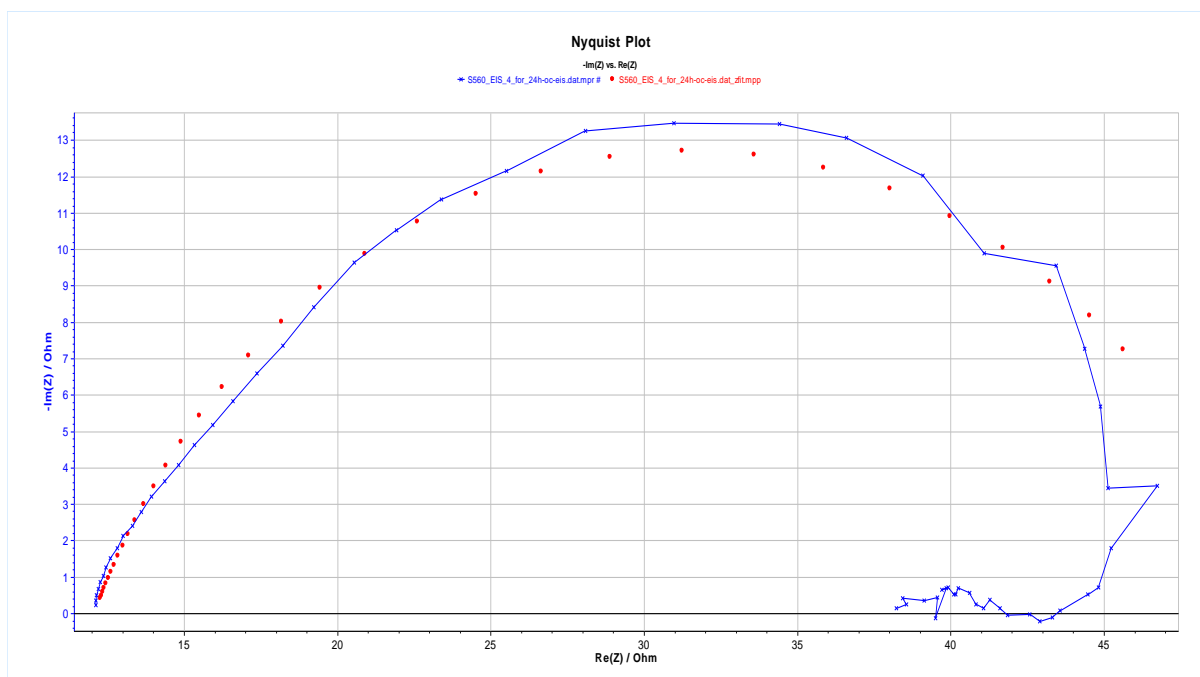***Red line**: experimental points of -phase(|Z|), **Purple dots**: fitted points.*
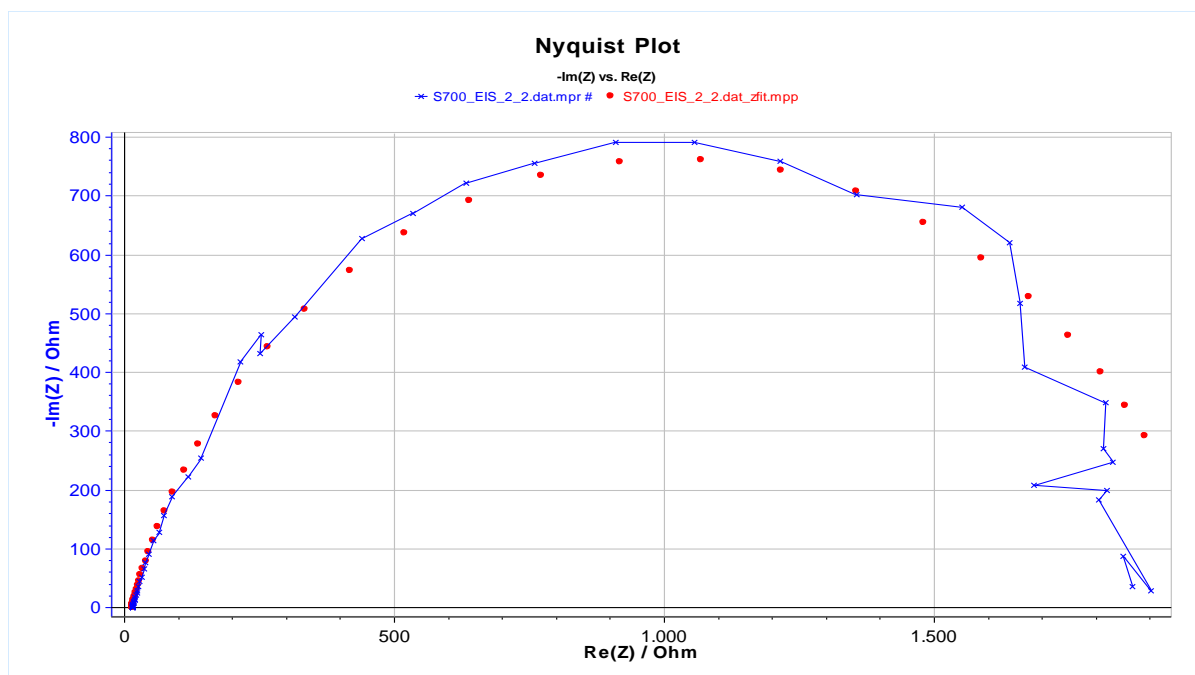
*Figure B.35: **S700** specimen – Nyquist plot of EIS experiment (2nd cycle). **Blue line**: experimental points, **Red dots**: fitted points.*
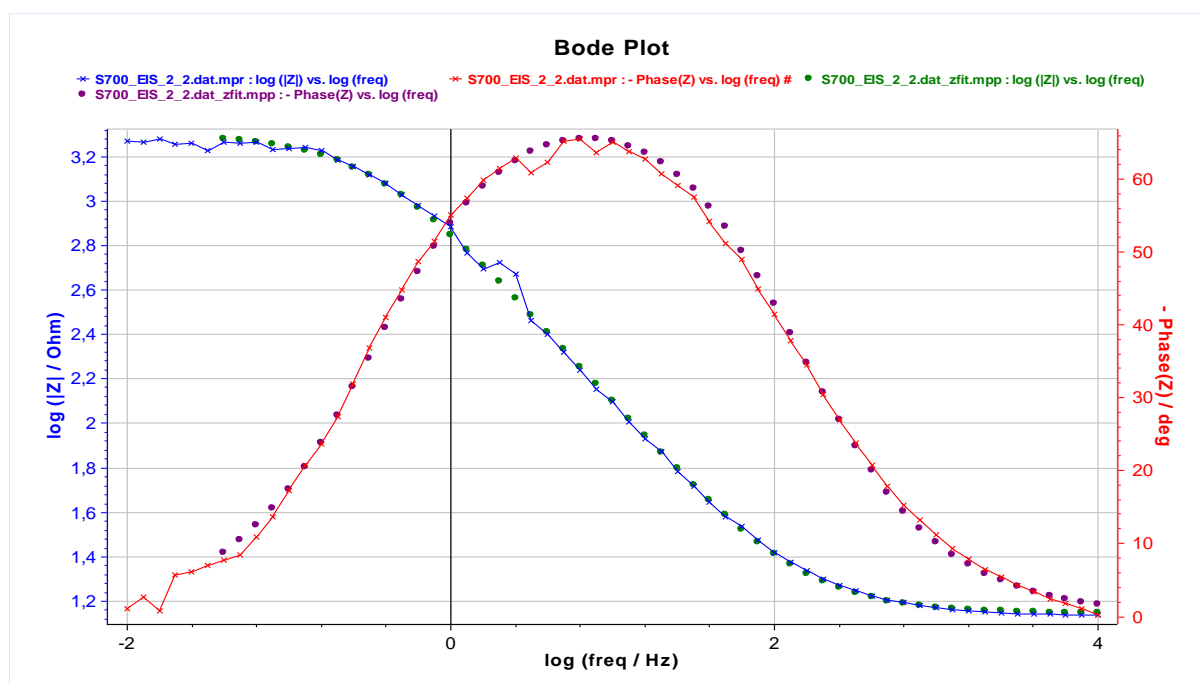
*Figure B.36: **S700** specimen – Bode plot of EIS experiment (2nd cycle).*

***Blue line**: experimental points of log(|Z|), **Green dots**: fitted points.*

***Red line**: experimental points of -phase(|Z|), **Purple dots**: fitted points.*
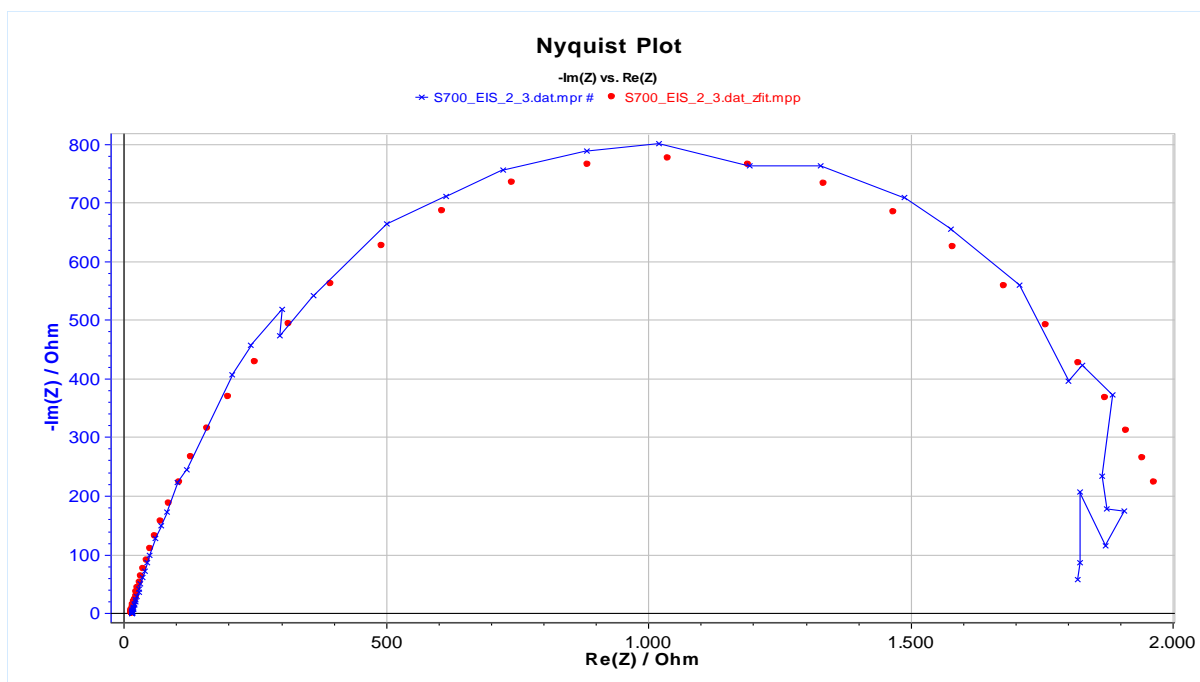
*Figure B.37: **S700** specimen – Nyquist plot of EIS experiment (3rd cycle). **Blue line**: experimental points, **Red dots**: fitted points.*
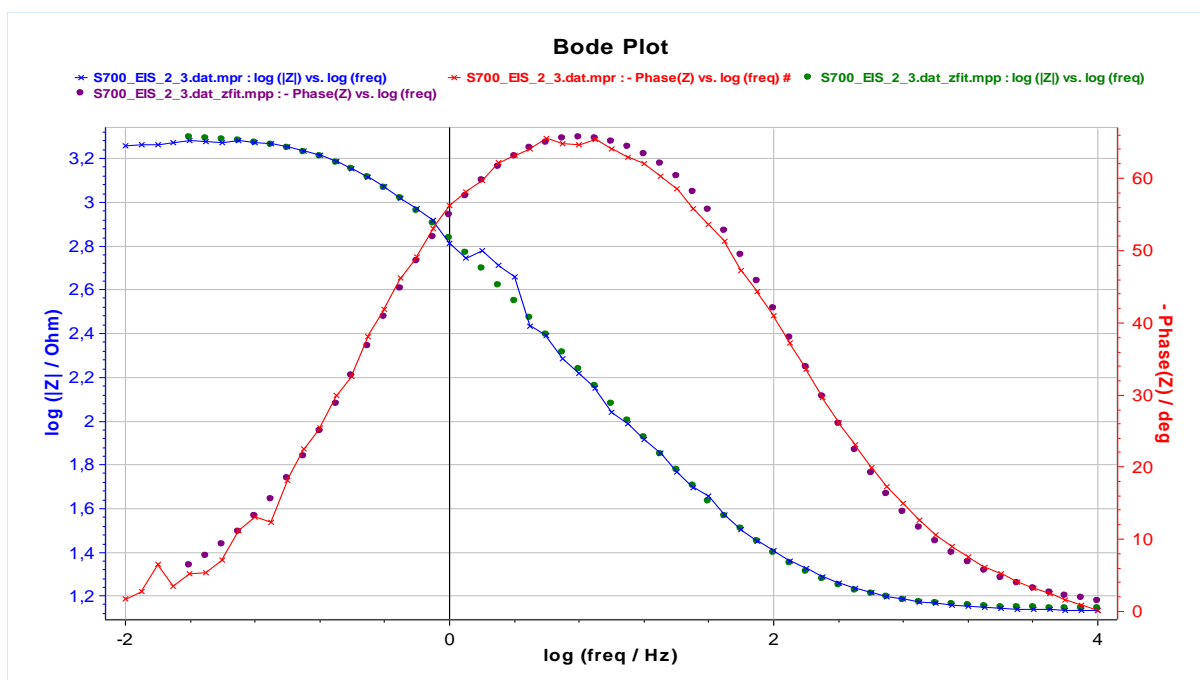
*Figure B.38: **S700** specimen – Bode plot of EIS experiment (3rd cycle).*

***Blue line**: experimental points of log(|Z|), **Green dots**: fitted points.*

***Red line**: experimental points of -phase(|Z|), **Purple dots**: fitted points.*
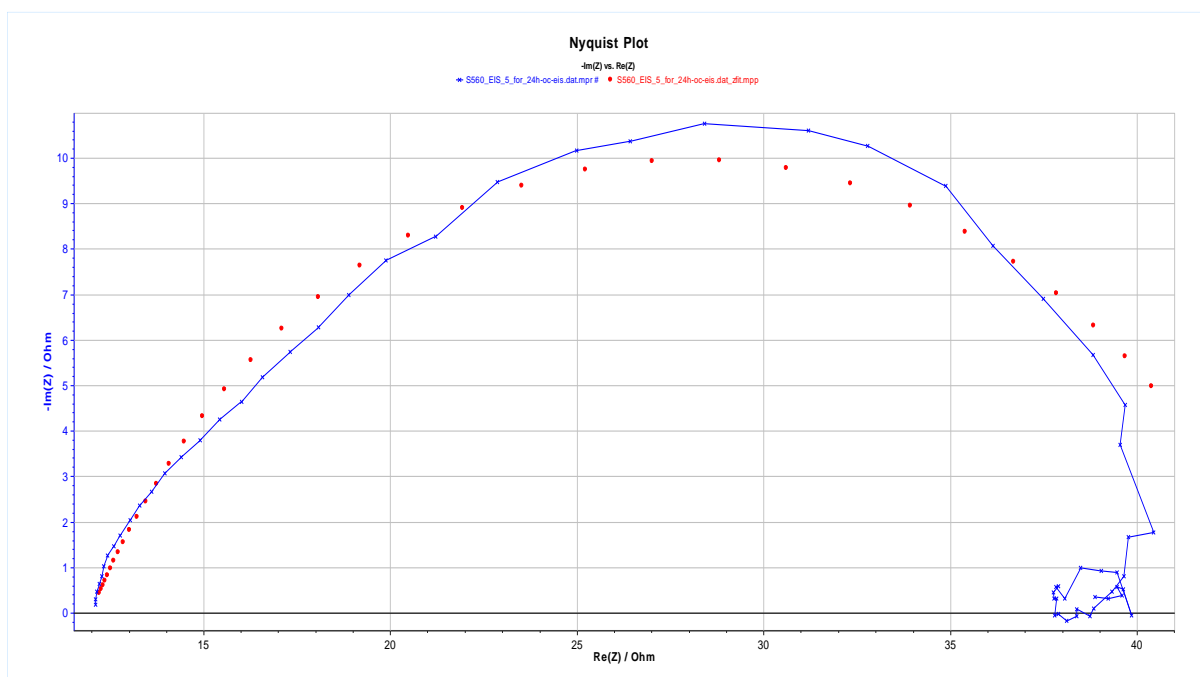
B.4.2. 24hour 6loop OC-EIS experiments
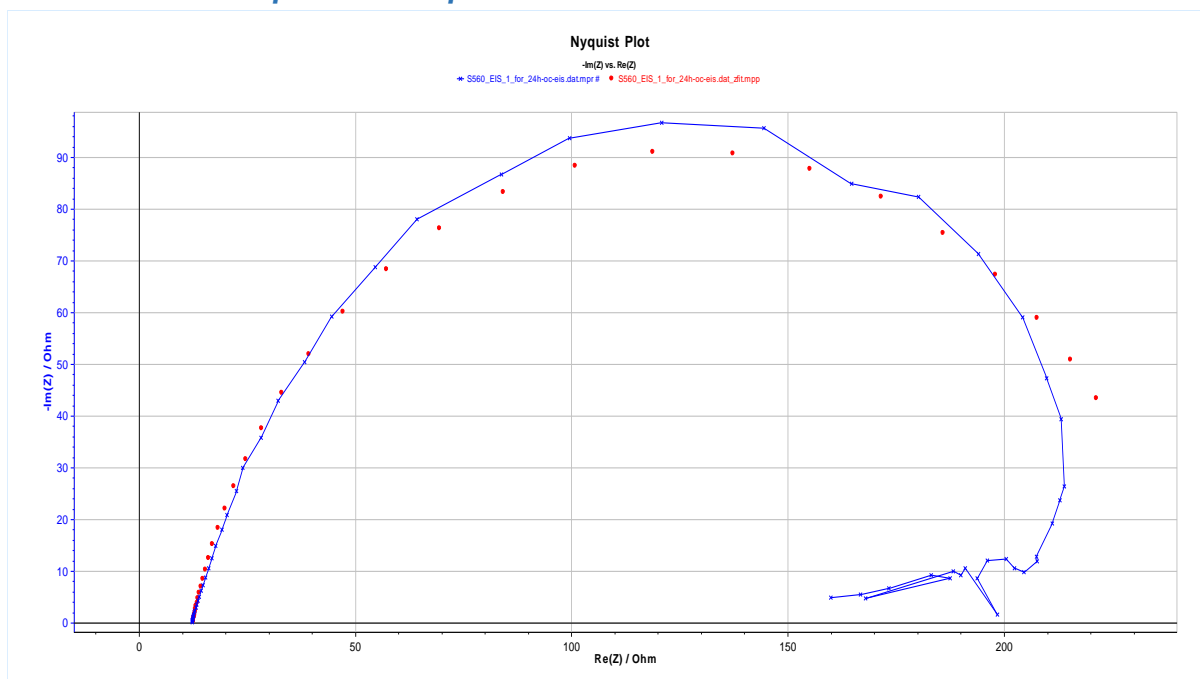
*Figure B.39: **S560** specimen – Nyquist plot of EIS (imposed at t=0h) of 24h 6loop OC-EIS experiment. **Blue line**: experimental points, **Red dots**: fitted points.*
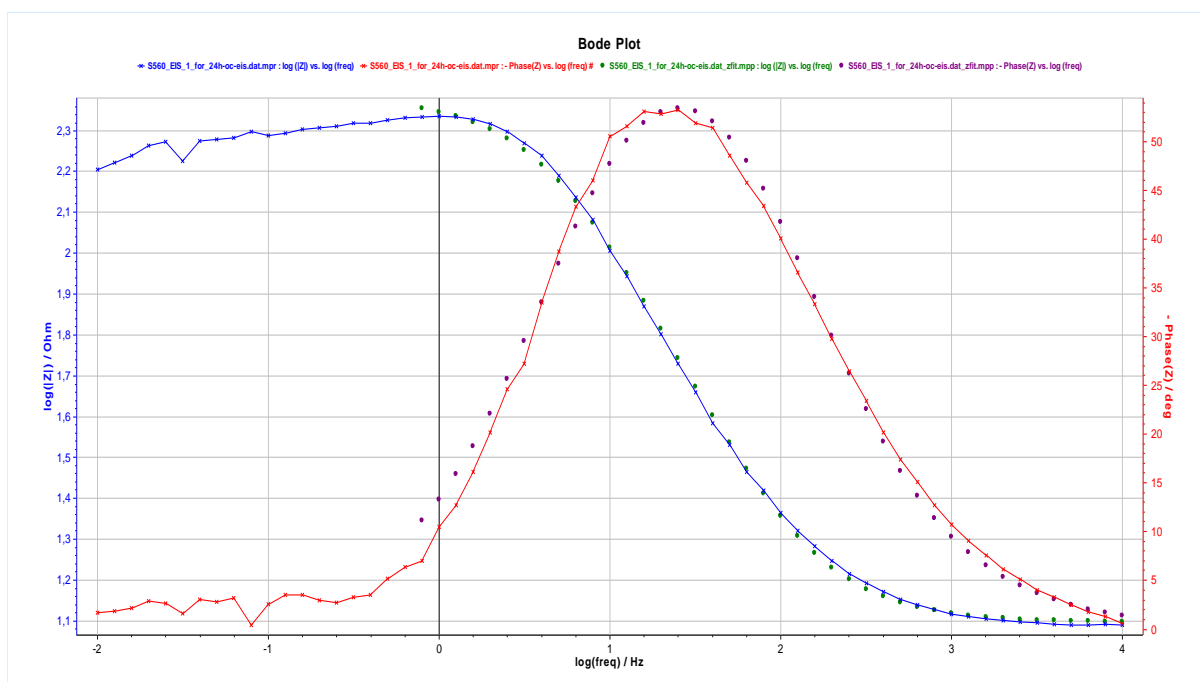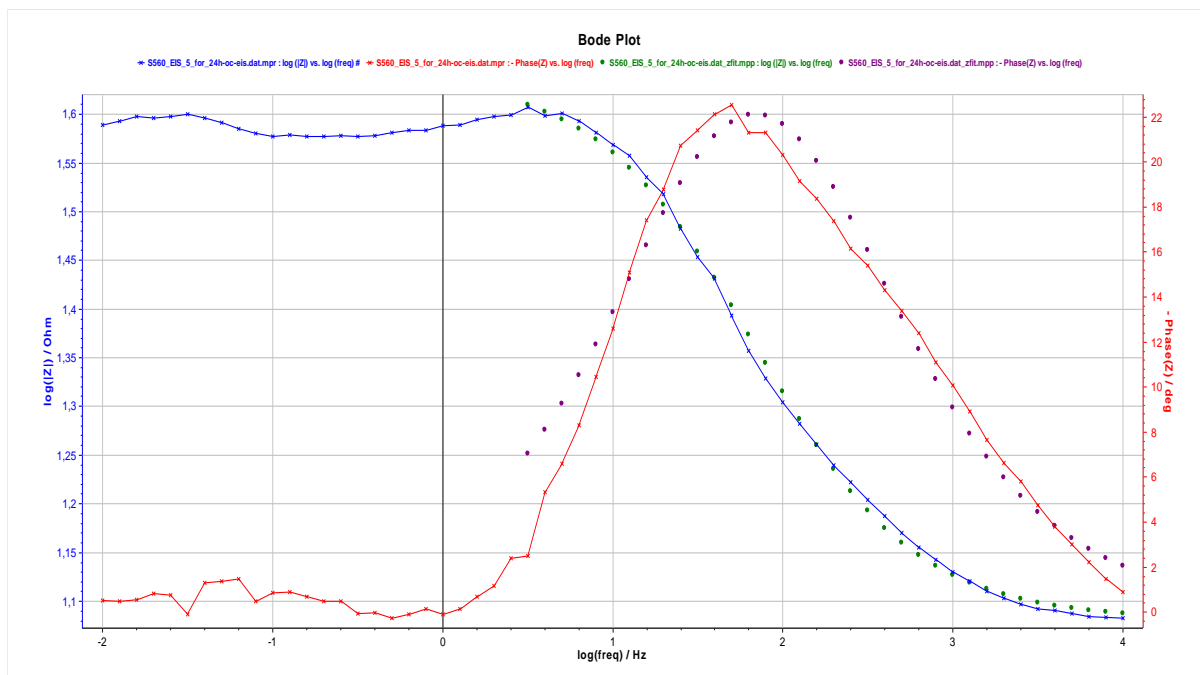

*Figure B.40: **S560** specimen – Nyquist plot of EIS (imposed at t=0h) of 24h 6loop OC-EIS experiment.*

***Blue line**: experimental points of log(|Z|), **Green dots**: fitted points.*

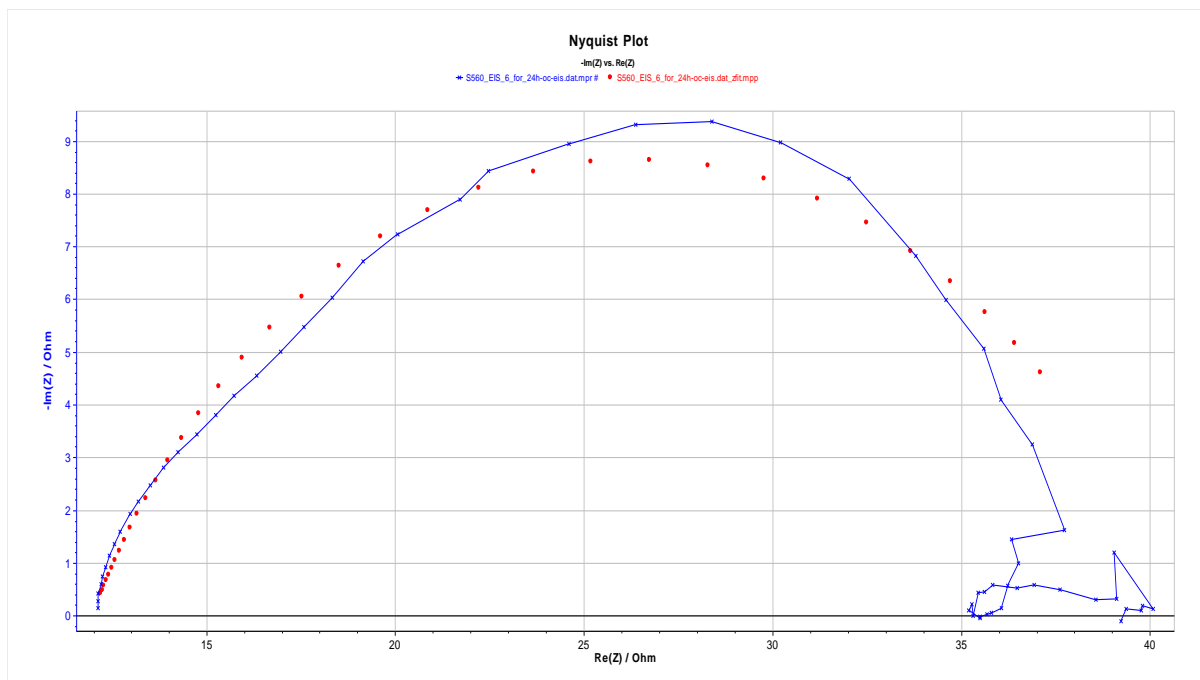***Red line**: experimental points of -phase(|Z|), **Purple dots**: fitted points.*

*Figure B.41: **S560** specimen – Nyquist plot of EIS (imposed at t=2h) of 24h 6loop OC-EIS experiment. **Blue line**: experimental points, **Red dots**: fitted points.*
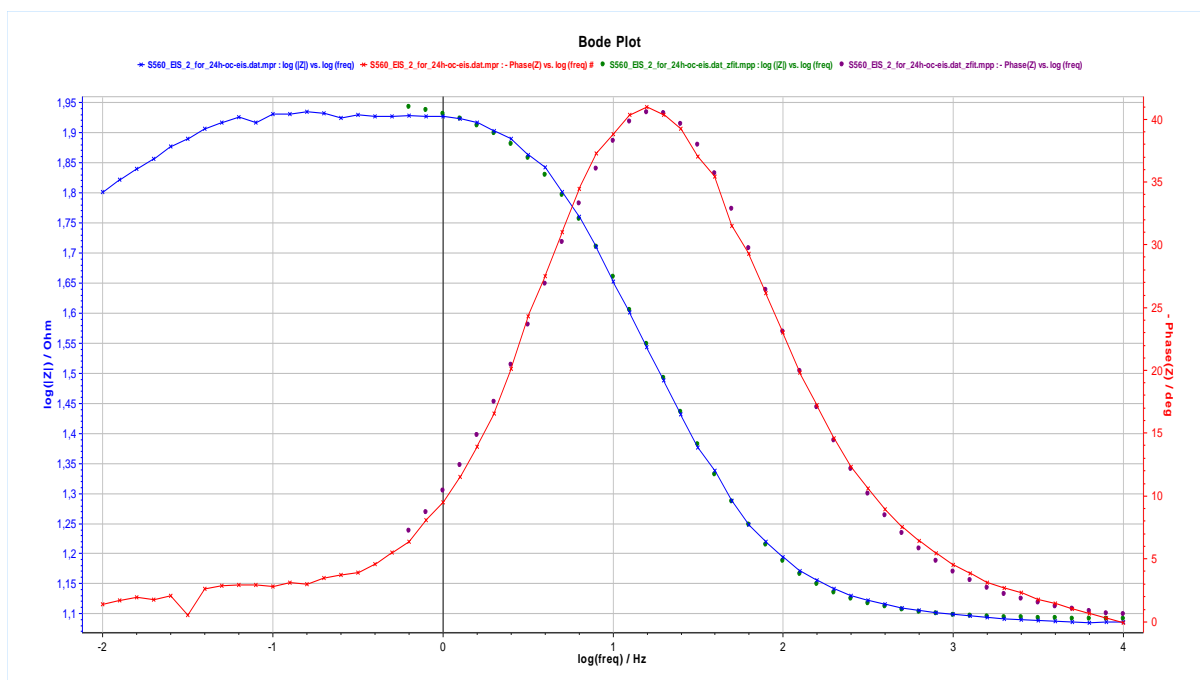
*Figure B.42: **S560** specimen – Nyquist plot of EIS (imposed at t=2h) of 24h 6loop OC-EIS experiment.*

***Blue line**: experimental points of log(|Z|), **Green dots**: fitted points.*

***Red line**: experimental points of -phase(|Z|), **Purple dots**: fitted points.*

*Figure B.43: **S560** specimen – Nyquist plot of EIS (imposed at t=4h) of 24h 6loop OC-EIS experiment. **Blue line**: experimental points, **Red dots**: fitted points.*
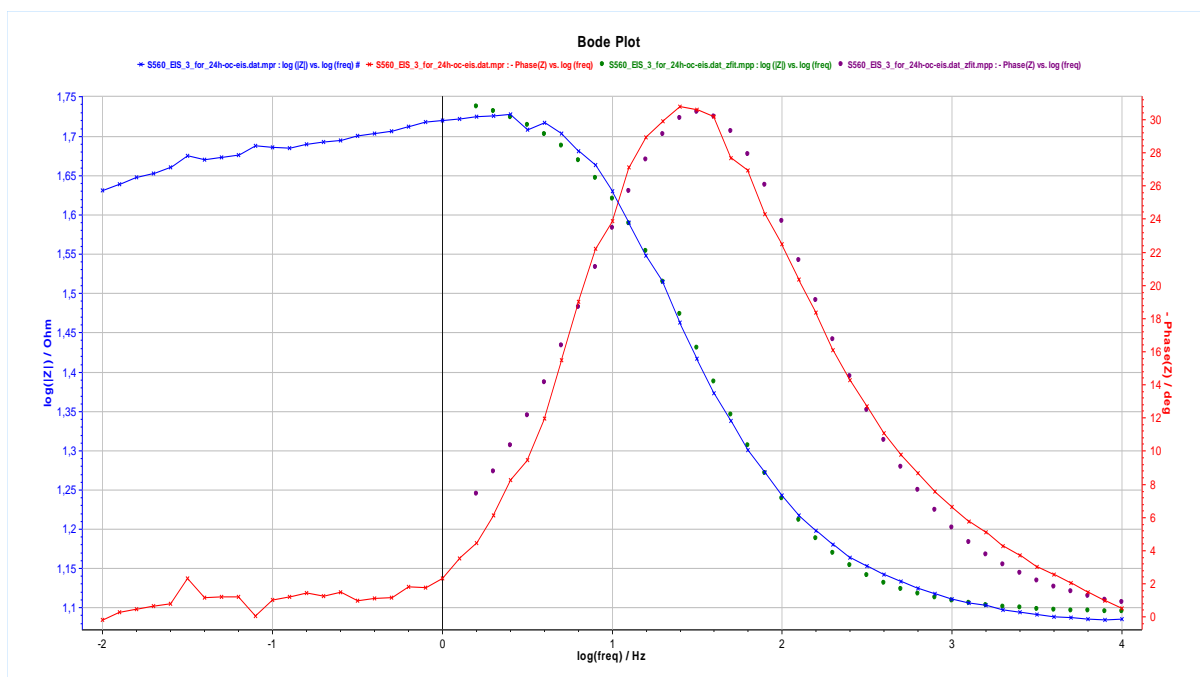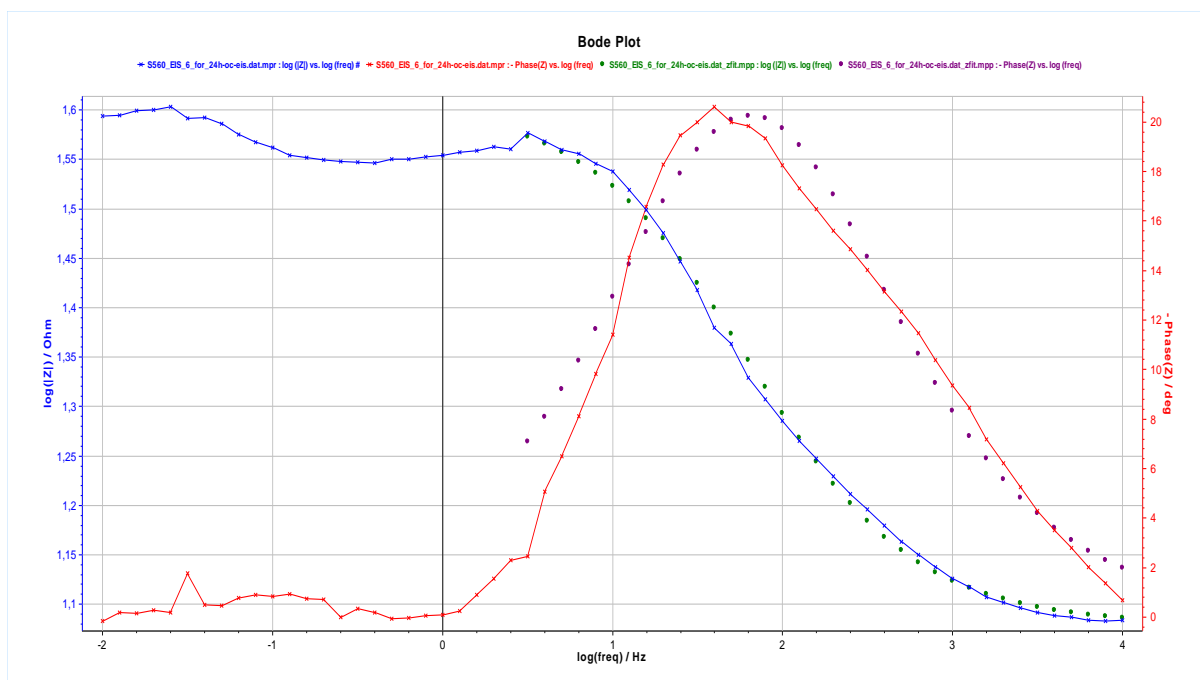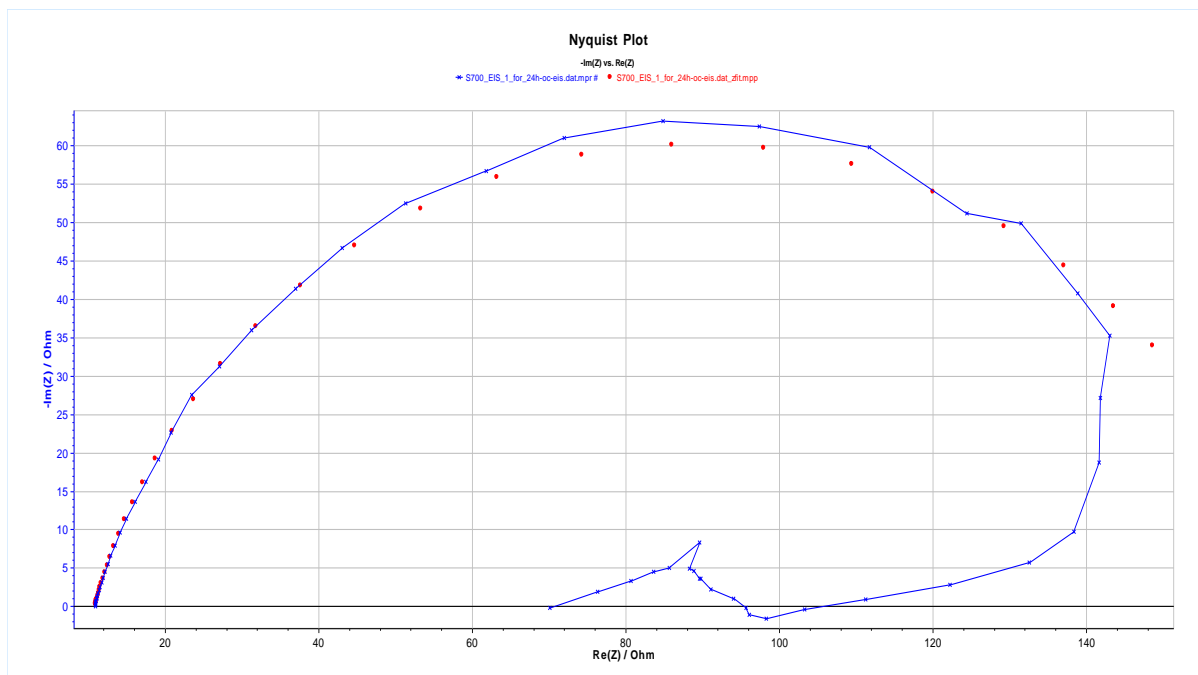

*Figure B.44: **S560** specimen – Nyquist plot of EIS (imposed at t=4h) of 24h 6loop OC-EIS experiment.*

__Blue line__: experimental points of log(|Z|), __Green dots__: fitted points.

__Red line__: experimental points of -phase(|Z|), __Purple dots__: fitted points.

Figure B.45: **S560** specimen – Nyquist plot of EIS (imposed at t=8h) of 24h 6loop OC-EIS experiment. **Blue line**: experimental points, **Red dots**: fitted points.
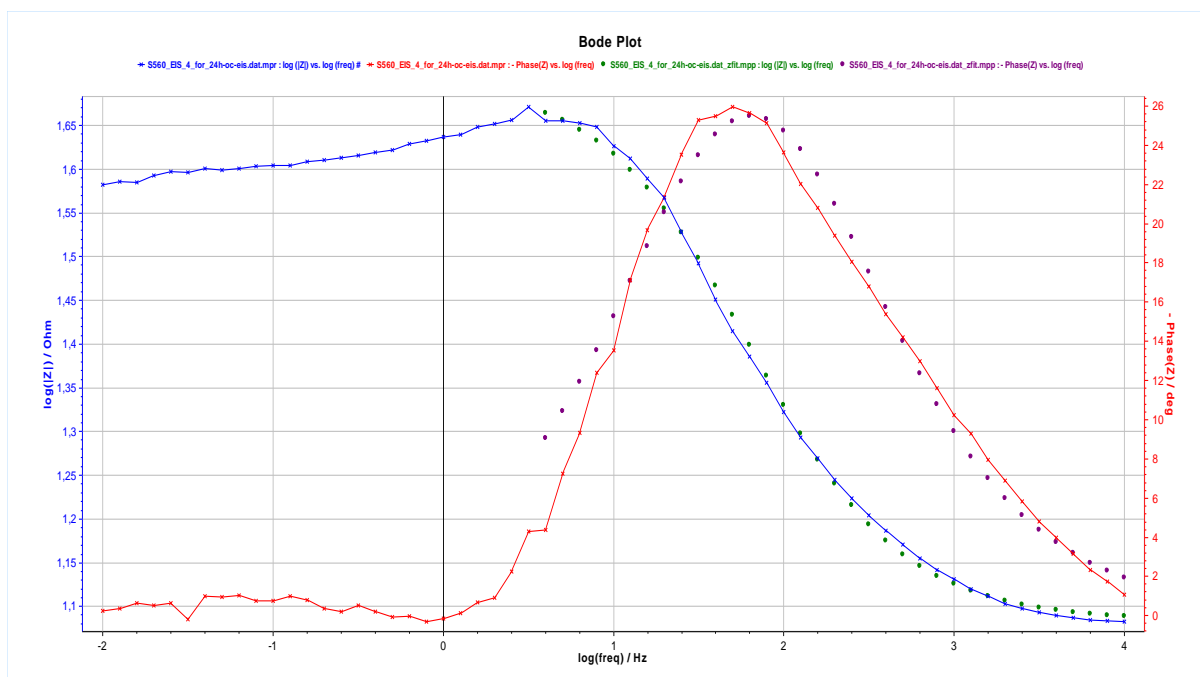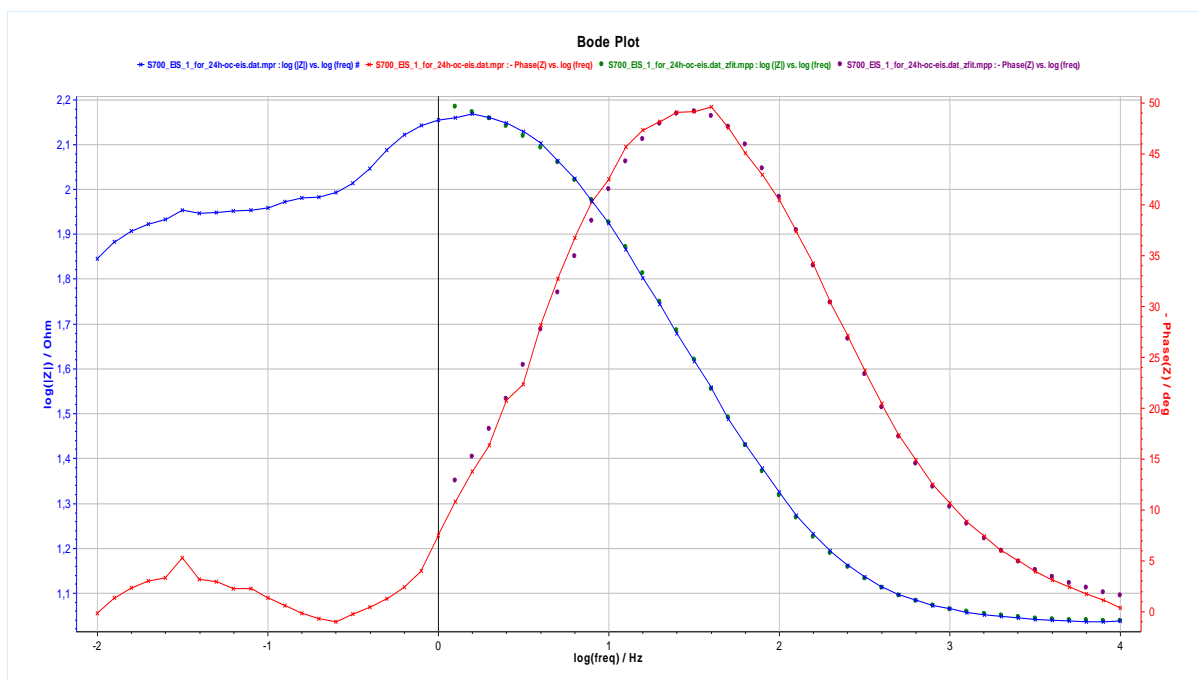

Figure B.46: **S560** specimen – Nyquist plot of EIS (imposed at t=8h) of 24h 6loop OC-EIS experiment.

Blue line: experimental points of log(|Z|), **Green dots**: fitted points.

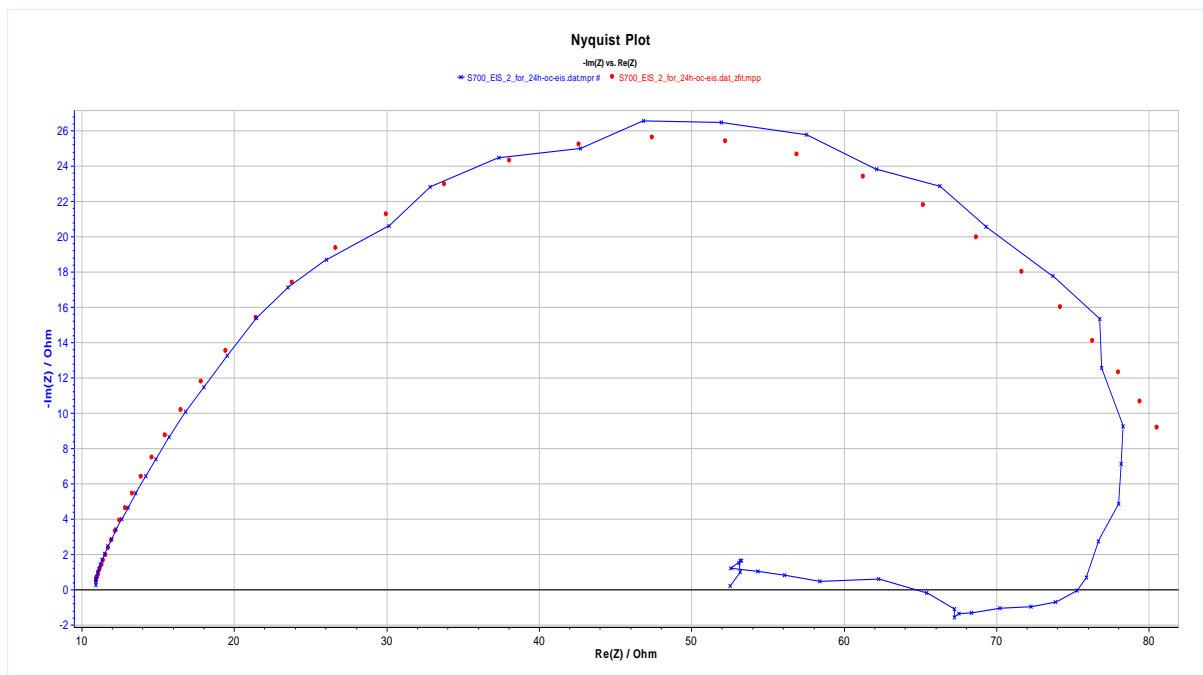**Red line**: experimental points of -phase(|Z|), **Purple dots**: fitted points.

*Figure B.47: **S560** specimen – Nyquist plot of EIS (imposed at t=16h) of 24h 6loop OC-EIS experiment. **Blue line**: experimental points, **Red dots**: fitted points.*

*Figure B.48: **S560** specimen – Nyquist plot of EIS (imposed at t=16h) of 24h 6loop OC-EIS experiment.*

***Blue line**: experimental points of log(|Z|), **Green dots**: fitted points.*

***Red line**: experimental points of -phase(|Z|), **Purple dots**: fitted points.*

*Figure B.49: **S560** specimen – Nyquist plot of EIS (imposed at t=24h) of 24h 6loop OC-EIS experiment. **Blue line**: experimental points, **Red dots**: fitted points.*
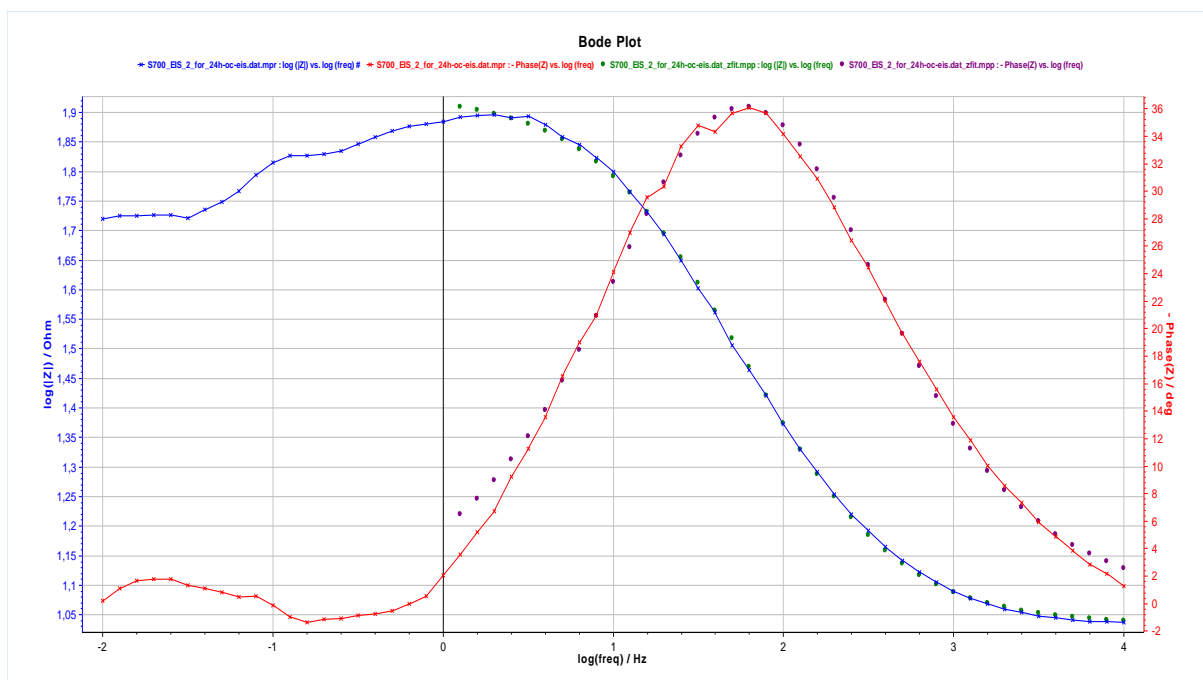

*Figure B.50: **S560** specimen – Nyquist plot of EIS (imposed at t=24h) of 24h 6loop OC-EIS experiment.*

***Blue line**: experimental points of log(|Z|), **Green dots**: fitted points.*

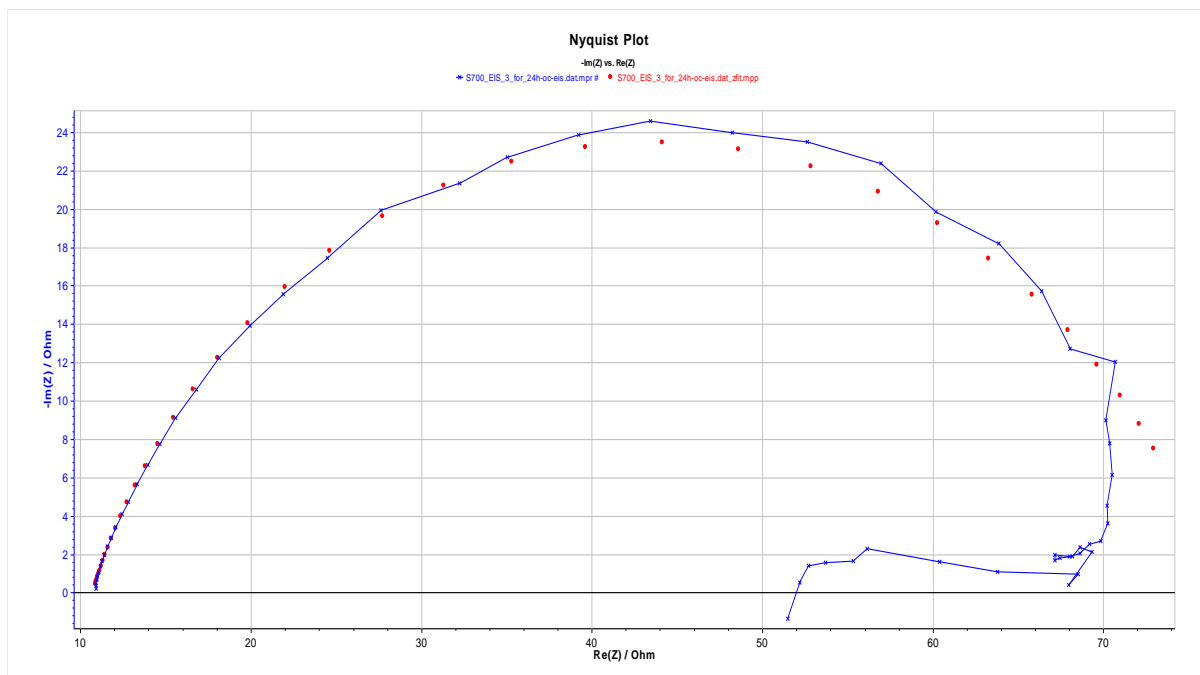***Red line**: experimental points of -phase(|Z|), **Purple dots**: fitted points.*

Figure B.51: **S700** specimen – Nyquist plot of EIS (imposed at t=0h) of 24h 6loop OC-EIS experiment. **Blue line**: experimental points, **Red dots**: fitted points.
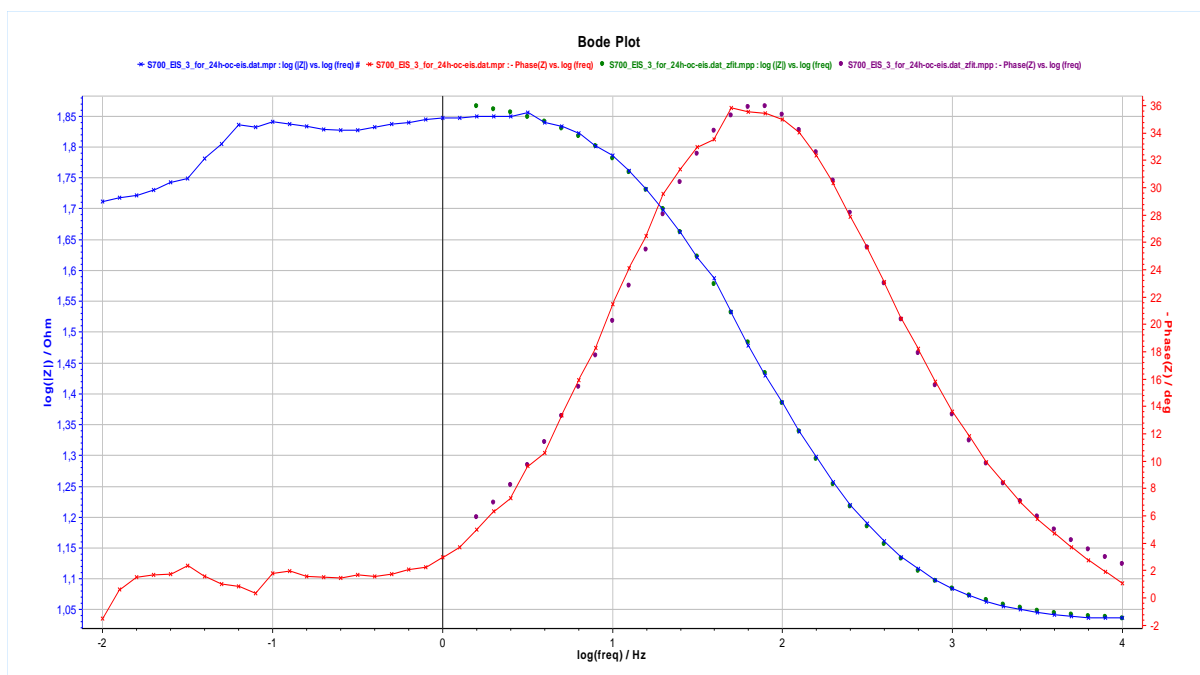

Figure B.52: **S700** specimen – Nyquist plot of EIS (imposed at t=0h) of 24h 6loop OC-EIS experiment.

Blue line: experimental points of log(|Z|), **Green dots**: fitted points.

Red line: experimental points of -phase(|Z|), **Purple dots**: fitted points.

Figure B.53: *S700* specimen – Nyquist plot of EIS (imposed at t=2h) of 24h 6loop OC-EIS experiment. **Blue line**: experimental points, **Red dots**: fitted points.

Figure B.54: *S700* specimen – Nyquist plot of EIS (imposed at t=2h) of 24h 6loop OC-EIS experiment.

Blue line: experimental points of log(|Z|), **Green dots**: fitted points.

Red line: experimental points of -phase(|Z|), **Purple dots**: fitted points.

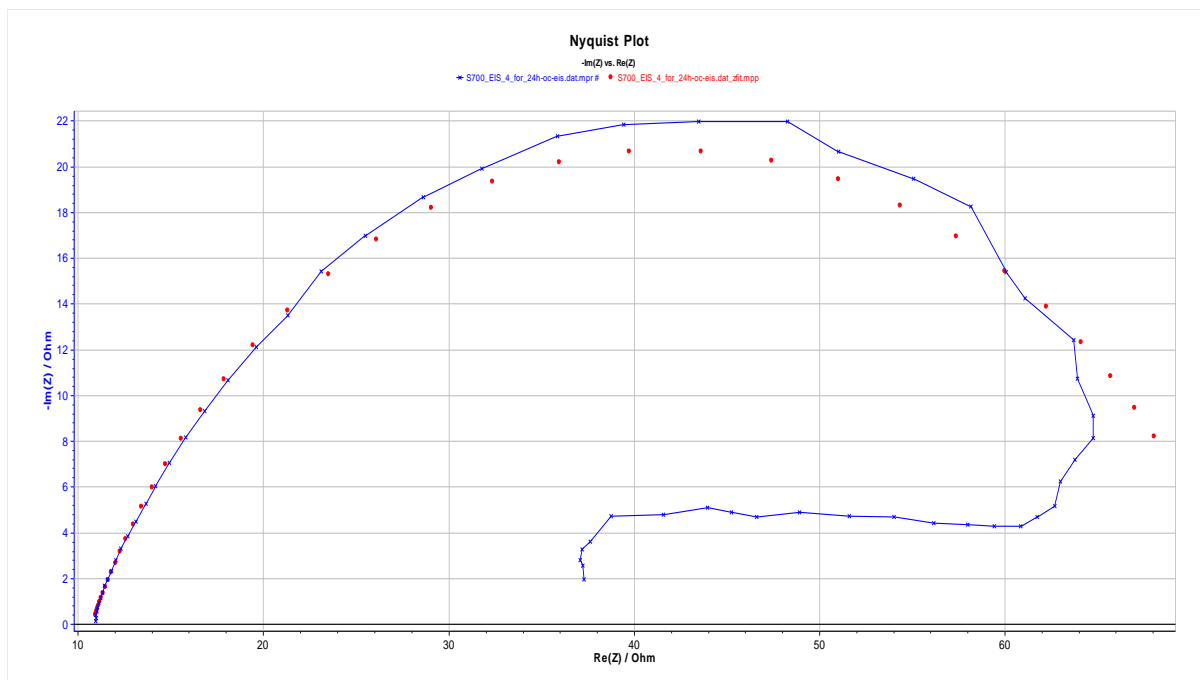Figure B.55: **S700** specimen – Nyquist plot of EIS (imposed at t=4h) of 24h 6loop OC-EIS experiment. **Blue line**: experimental points, **Red dots**: fitted points.
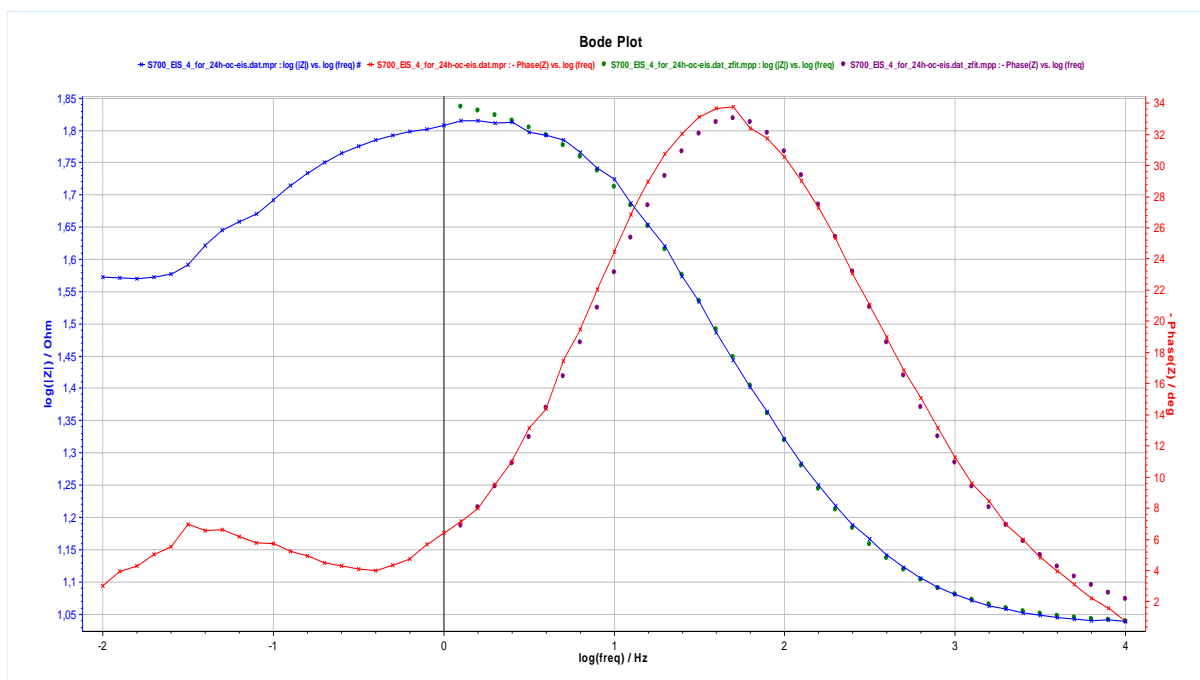

Figure B.56: **S700** specimen – Nyquist plot of EIS (imposed at t=4h) of 24h 6loop OC-EIS experiment.

Blue line: experimental points of log(|Z|), **Green dots**: fitted points.

Red line: experimental points of -phase(|Z|), **Purple dots**: fitted points.
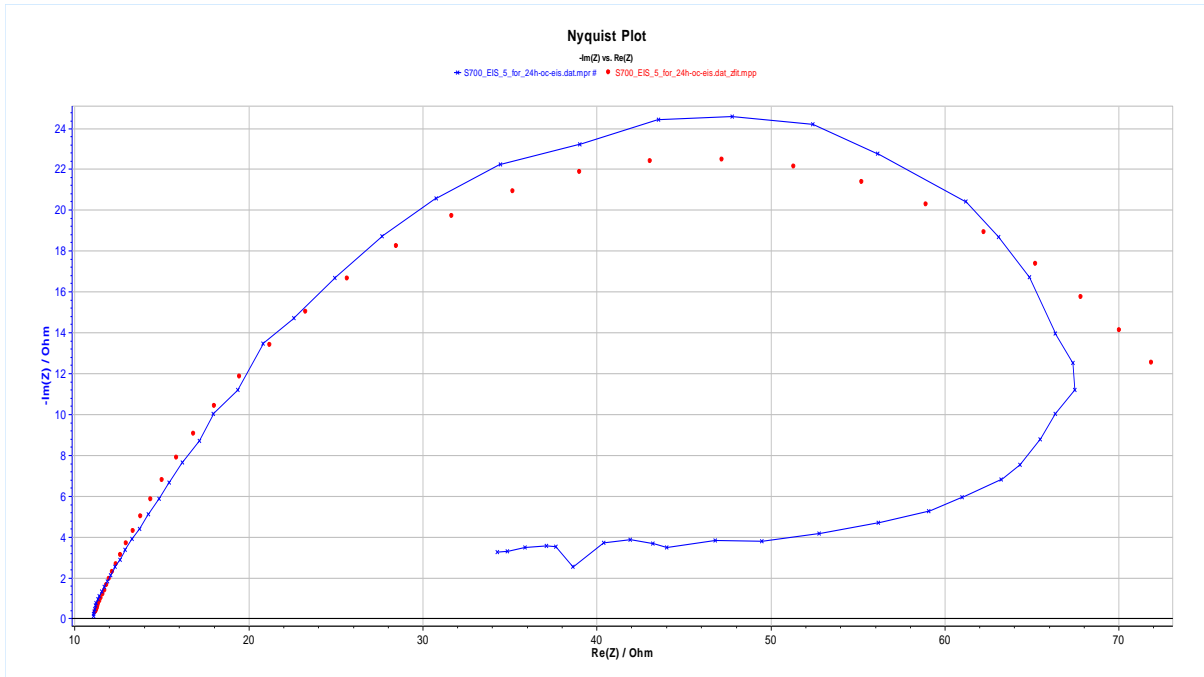
Figure B.57: **S700** specimen – Nyquist plot of EIS (imposed at t=8h) of 24h 6loop OC-EIS experiment. **Blue line**: experimental points, **Red dots**: fitted points.

Figure B.58: **S700** specimen – Nyquist plot of EIS (imposed at t=8h) of 24h 6loop OC-EIS experiment.

Blue line: experimental points of log(|Z|), **Green dots**: fitted points.

Red line: experimental points of -phase(|Z|), **Purple dots**: fitted points.

*Figure B.59: **S700** specimen – Nyquist plot of EIS (imposed at t=16h) of 24h 6loop OC-EIS experiment. **Blue line**: experimental points, **Red dots**: fitted points.*
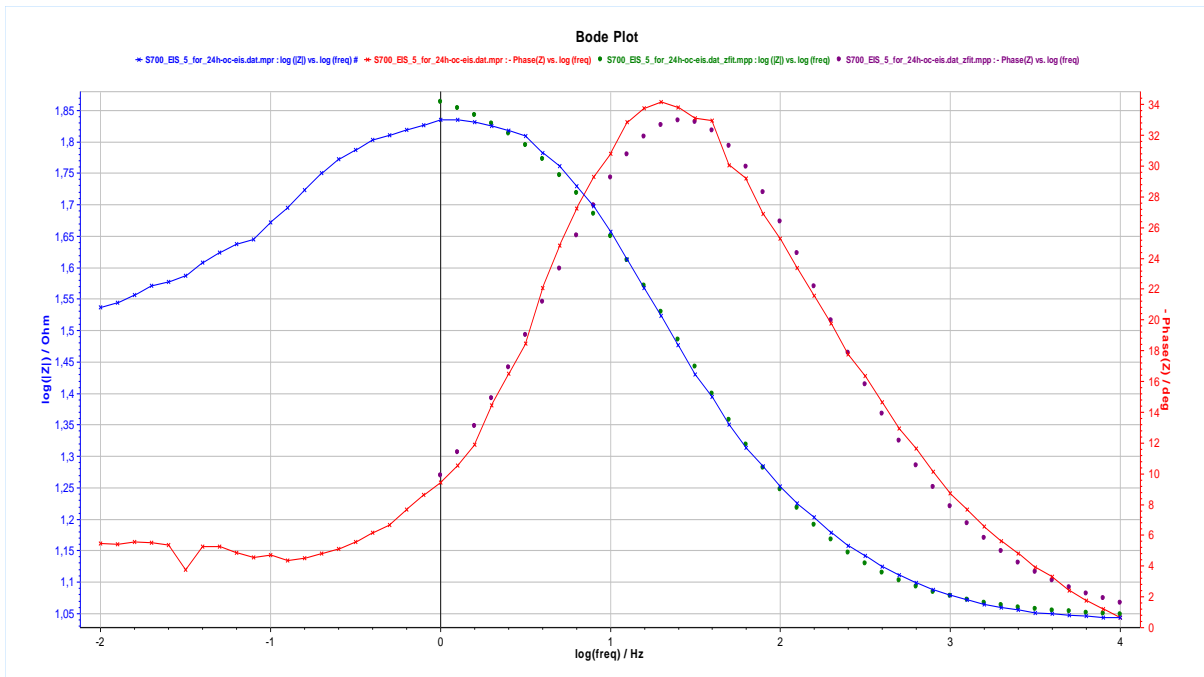

*Figure B.60: **S700** specimen – Nyquist plot of EIS (imposed at t=16h) of 24h 6loop OC-EIS experiment.*

***Blue line**: experimental points of log(|Z|), **Green dots**: fitted points.*

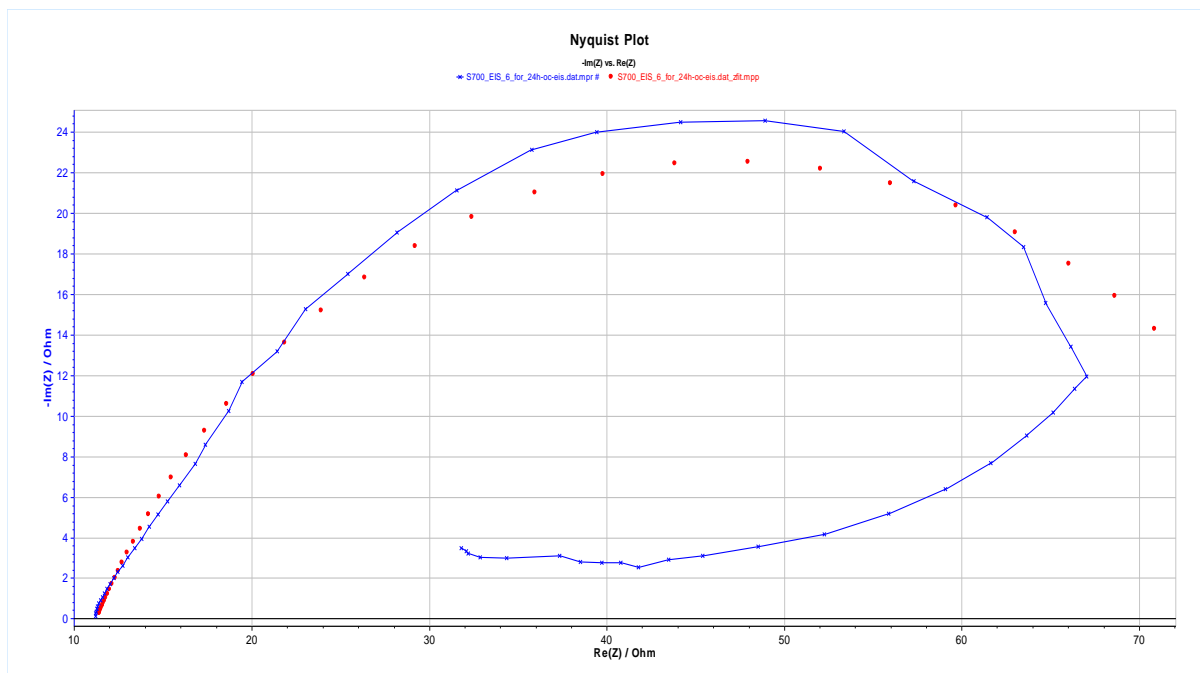***Red line**: experimental points of -phase(|Z|), **Purple dots**: fitted points.*

Figure B.61: *S700 specimen – Nyquist plot of EIS (imposed at t=24h) of 24h 6loop OC-EIS experiment. **Blue line**: experimental points, **Red dots**: fitted points.*
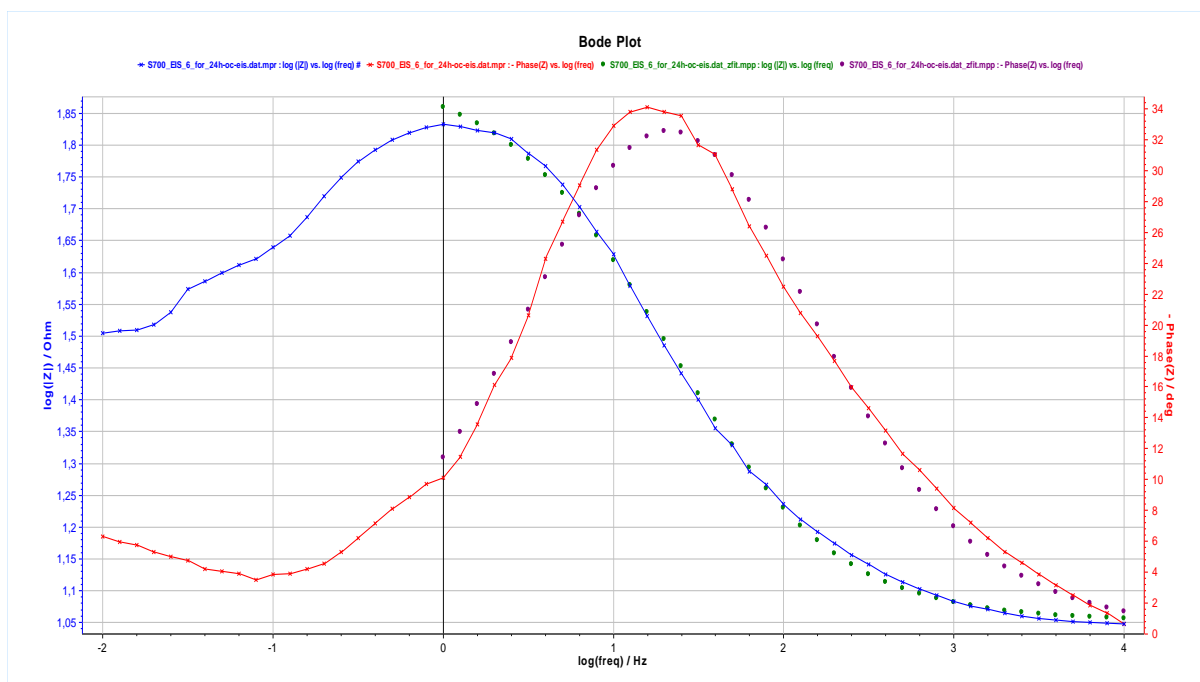

Figure B.62: *S700 specimen – Nyquist plot of EIS (imposed at t=24h) of 24h 6loop OC-EIS experiment.*

***Blue line**: experimental points of log(|Z|), **Green dots**: fitted points.*

***Red line**: experimental points of -phase(|Z|), **Purple dots**: fitted points.*